



University of
Nottingham

UK | CHINA | MALAYSIA

Experimental and Numerical Heat Transfer Investigation of Reverse Jet Impingement

Abdallah Ahmed

Thesis submitted to the University of Nottingham for
the degree of Doctor of Philosophy

June 2022

ACKNOWLEDGEMENTS

The successful completion of my thesis would not have been possible without the invaluable guidance provided by my esteemed advisors, the unwavering assistance of my friends and university staff, the constant support of my family and spouse, and the generous sponsorship from The Islamic Development Bank.

Foremost, I wish to express my utmost gratitude to my supervisor, Prof. Yuying Yan, for his exceptional mentorship, patience, attentiveness, and insightful advice throughout my doctoral studies. I would also like to extend my sincere appreciation to my laboratory colleague, Dr. Edward Wright, for his unrelenting support from the commencement of our collaboration, which enabled us to form a highly productive team. I am also indebted to the technical staff of the Built Environment Department, particularly Mr. Anthony Gospel, Mr. Daniel Cooper, and Mr. Carson Cheng, for their selfless assistance in the laboratory. Additionally, I am grateful to Dr. Alexandros Terzis from Stanford University, who provided me with guidance at the onset of this project.

Lastly, I wish to express my gratitude to my family and spouse. To my beloved mother, Ms. Fatimah Rajab, and father, Mr. Abdelaty Zaki, I offer my heartfelt thanks for your encouragement, trust, and unconditional support. To my dear wife, Ms. Sara Ibrahim, I am grateful for your unwavering companionship and support. Lastly, I extend my gratitude to my dear daughter, Jamila, and son, Mazen, for being my motivation to strive harder.

ABSTRACT

This project aimed to study heat transfer and flow in double wall aerofoil cooling using two primary studies: a novel jet impingement cooling geometry and a typical film cooling arrangement. Experimental testing with thermochromic liquid crystal validated numerical work using ANSYS Fluent.

A novel 'reverse' jet impingement geometry was developed to enhance heat transfer performance, comprising of a 'dimple' target enclosed within a cylindrical 'silo'. Experimental variations included Reynolds number range of 10,000 to 70,000, jet-to-target, crossflow condition, and an extended nozzle geometry. An overall enhancement of heat transfer was achieved with the novel geometry, with optimum jet to target spacing found at around 4 jet diameters, and some reduction in crossflow effects were observed.

A numerical investigation validated against experimental data for a novel 'reverse' jet impingement geometry was conducted. Optimizations in jet-to-jet and jet-to-target spacing were found, but no significant optimization of inlet condition was observed. The effect of outlet condition on discharge coefficient was significant, with an optimum nozzle length of 1 jet diameter for heat transfer enhancement. Staggered and inline dimples were shown to provide similar enhancements to heat transfer, significant compared to a traditional flat plate target.

Study evaluated heat transfer and discharge coefficients in a scaled cylindrical film cooling channel with varied Reynolds number, entry sharpness, inclination, and rotation angle.

PUBLICATIONS ARISING FROM THIS WORK

- **A. Ahmed**, E. Wright, J. F. Wright, Y. Yan, “Numerical Investigation of Slot Jet Reverse Impingement”, 17th UK Heat Transfer Conference (UKHTC2021), 4-6 April 2022, Manchester, UK.
- **A. Ahmed**, E. Wright, A. Terzis, Y. Yan, “Experimental Heat Transfer Investigation of Single Reverse Jet Impingement”, 17th UK Heat Transfer Conference (UKHTC2021), 4-6 April 2022, Manchester, UK.
- E. Wright, **A. Ahmed**, Y. Yan, J. Maltson, “Experimental Investigation of Entry Length Heat Transfer Coefficient Within Fan and Conical Shaped Film Cooling Channels”, 17th UK Heat Transfer Conference (UKHTC2021), 4-6 April 2022, Manchester, UK.
- **A. Ahmed**, E. Wright, F. Abdel-Aziz, Y. Yan, “Numerical Investigation of Heat Transfer and Flow Characteristics of a Double-Wall Cooling Structure: Reverse Circular Jet Impingement”, Journal of Applied Thermal Engineering, 189, 2021.
- E. Wright, **A. Ahmed**, Y. Yan, J. Maltson, L. A. Lopez, “Experimental and Numerical Heat Transfer Investigation of Impingement Jet Nozzle Position in Concave Double-Wall Cooling Structures” Journal of Heat Transfer Engineering, 2021.
- **A. Ahmed**, E. Wright, Y. Yan, “Numerical Investigation of Slot Jet Impingement: Comparison of Reverse and Flat Targets”, International Symposium on Numerical Methods in Heat and Mass Transfer 2020, 11-13 Dec, 2020, Ningbo, China.

NOMENCLATURE

CFD	Computational fluid dynamics
C_p	Specific heat, J/K.kg
C_d	Discharge coefficient
D	Dimple diameter, m
D_ω	Cross-diffusion term
d	Jet nozzle diameter, m
E	Total energy
G_{cf}	Crossflow mass flow rate
\tilde{G}_k	The generation of turbulence kinetic energy
G_ω	The specific turbulent dissipation rate of ω
H	Distance from jet nozzle to target surface, m
H_{cy}	Cylindrical tube height
H_{ex}	Vertical height of exit gap
h	Heat transfer coefficient, w/m ² .k
HSI	Hue, Saturation and Intensity colour model
HTC	Heat transfer coefficient, w/m ² .k
k	Thermal conductivity, w/m.K
l	Characteristic length, m
\dot{m}	Mass flow rate, kg/s
Nu	Nusselt number
Nu_{st}	Stagnation point Nusselt number
Nu_{avg}	Area average Nusselt number
$Nu_{overall}$	Overall average Nusselt number

P	Pressure, Pa
p	Pitch, or distance between jet nozzles in the x direction, m
r	Radial distance from the stagnation point, m
SST	Shear stress transport
Q	Heat transfer rate, W
Re	Reynolds number
RGB	Red, Green and Blue colour model
s	Radial surface distance from stagnation point, m
S_m	Source term
T	Temperature, K
T_i	Initial temperature, K
$T_{j,max}$	Maximum jet temperature, K
T_w	Wall temperature, K
T_f	Flow temperature, K
t	Time, s
t_{LC}	Liquid crystal activation time, s
TLC	Thermochromic liquid crystal
TIT	Turbine inlet temperature, K
V	Volume, m ³
v	Velocity, m/s
x	Streamwise Direction, m
Y_k	Dissipation due to turbulence of k
Y_ω	Dissipation due to turbulence of ω
y	Spanwise Direction, m
U	Uncertainty

u Velocity, m/s

Greek Symbols

α Thermal diffusivity, m²/s

δ Thickness, m

ε Rate of dissipation of the turbulent kinetic energy

ρ Density, kg/m³

τ_i Time constant, s

τ_{ij} Stress tensor

Γ_k Effective diffusivity of k

Γ_ω Effective diffusivity of ω

μ Dynamic viscosity, pa.s

η_{th} Thermal efficiency

θ Non-dimensional temperature, $(T - T_i)/(T_f - T_i)$

ν kinematic viscosity, m²/s

ω Specific rate of energy dissipation

Subscripts

c Central

e East direction

f Hot flow

i Initial

LC Liquid crystal

max Maximum

min Minimum

w West direction

TABLE OF CONTENTS

ACKNOWLEDGEMENTS	I
ABSTRACT	II
PUBLICATIONS ARISING FROM THIS WORK.....	III
NOMENCLATURE	IV
TABLE OF CONTENTS	VII
LIST OF TABLES	XI
LIST OF FIGURES	XI
Chapter 1. Introduction	1
1.1. Background of gas turbine cooling.....	1
1.2. Development of cooling technologies	5
1.3. Project aim and objectives	7
1.4. Thesis structure.....	9
Chapter 2. Literature Review	11
2.1. Single jet impingement.....	11
2.2. Multiple jet impingement	18
2.3. Jet impinging dimpled surface.....	23
2.4. Thermochromic liquid crystals (TCL).....	29
2.4.1. TLC aging.....	31
2.4.2. Lighting angle.....	31

2.4.3.	TLC thickness.....	32
2.4.4.	Bandwidth	33
2.5.	RGB and HSI colour Systems	33
2.6.	Summary.....	35
Chapter 3.	Experimental Methodology.....	37
3.1.	Introduction.....	37
3.2.	Transient Liquid Crystal Thermography Technique	38
3.3.	Calibration	41
3.4.	Experiment Setup and procedure.....	44
3.4.1.	Experiment setup.....	44
3.4.2.	Experimental procedure	47
3.5.	Data Reduction	48
3.6.	Summary.....	49
Chapter 4.	Single Reverse Jet Impingement.....	51
4.1.	Test section	51
4.2.	Results and discussions	52
4.2.1.	Recovery factor	53
4.2.2.	Nozzle-to-target effect.....	56
4.2.3.	Reynold number effect	59
4.2.4.	Discharge coefficient.....	60
4.3.	Uncertainty analysis.....	61

4.4.	Summary.....	65
Chapter 5.	Row Reverse Jet Impingement.....	66
5.1.	Test section.....	66
5.2.	Results and discussions.....	68
5.2.1.	Nozzle-to-target spacing effect.....	68
5.2.2.	Reynolds number effect.....	73
5.2.3.	Crossflow effect.....	76
5.2.4.	Nozzle configuration effect.....	81
5.2.5.	Discharge Coefficient.....	84
5.3.	Summary.....	86
Chapter 6	Array Reverse Jet Impingement.....	87
6.1.	Test section.....	87
6.2.	Results and discussion.....	89
6.2.1.	Jet-to-target spacing effect.....	89
6.2.2.	Reynolds number effect.....	93
6.2.3.	Discharge Coefficient.....	96
6.3.	Summary.....	98
Chapter 7.	Numerical Row and Array Reverse Jet impingement.....	99
7.1.	Numerical Procedure.....	99
7.1.1.	Fluid Dynamics governing equations.....	100
7.1.2.	Shear-Stress Transport (SST) k- ω Model.....	103

7.1.3.	Discretization of Governing Equations	104
7.1.4.	Flow solver algorithm	107
7.2.	Grid independency	111
7.3.	Turbulent model.....	112
7.4.	Row Reverse Jet impingement	114
7.4.1.	The Physical Problem and Boundary Conditions.....	114
7.4.2.	Results and Discussion	116
7.4.3.	Effect of nozzle to target spacing distance	124
7.4.4.	Summary	127
7.5.	Array Reverse Jet impingement.....	128
7.5.1.	The physical problem and boundary conditions.....	128
7.5.2.	Results and discussion.....	129
7.5.3.	Summary	150
Chapter 8.	Conclusions and future work.....	152
8.1.	Conclusions of current work.....	152
8.2.	Future work.....	156
REFERENCES	158
Appendix:	Experimental study on Film hole.....	175

LIST OF TABLES

Table 3.1 physical and thermal properties of acrylic Perspex	40
Table 5.1 Row reverse jet impingement study cases	68
Table 6.1 Array reverse jet impingement study cases	88
Table 7.1 Row jet impingement study cases	116
Table 9.1 Film hole study cases.....	176
Table 9.2 scheme of variations of inclination and rotation angles	177

LIST OF FIGURES

Figure 1.1 a) Closed-cycle gas turbine engine, and b) T-s diagram for the ideal Brayton cycle[1]	1
Figure 1.2 Influence of gas turbine compression ratio and inlet temperature on the thermal efficiency [2]	2
Figure 1.3 Evolution of gas turbine inlet temperatures, materials, and cooling technologies[4]	3
Figure 1.4 Development of cooling structure inside turbine blade [8].....	4
Figure 1.5 Gas turbine blade schematic with the common internal cooling system [5]	4
Figure 1.6 Schematic diagrams for the common gas turbine blade cooling systems: a) jet impingement[9], b)pin-fin cooling[10], c) rib turbulator[11], d) dimpled surface[12], and e) film cooling[13]	6
Figure 2.1 Different regions of a jet impingement flow[20]	12

Figure 2.2: Local Nusslet number distribution at the nozzle-to-plate spacing of $L/D=2$ [31].....	15
Figure 2.3 Multiple jet impingement crossflow schemes[38]: a) minimum crossflow, b) medium crossflow, and c) maximum crossflow.....	18
Figure 2.4: Dimple jet impingement velocity contours and streamlines at $D/D=0.318$, $Re=23,000$ and dimple depth ratio[62]: a) 0.1, b)0.2, and c)0.3	27
Figure 2.5: Flow velocity contours for Jet impinging on a dimpled target	29
Figure 2.6: Upstream and downstream Nusselt number contours for Jet impingement over a dimpled target.....	29
Figure 2.7 Liquid crystals colour plays	30
Figure 2.8 Illumination-viewing setup for TLCs calibrations[67]	32
Figure 2.9 TLC calibration techniques outputs: a)RGB, and b) HSI	35
Figure 3.1 Representative development of jet impingement target liquid crystal response over time.....	41
Figure 3.2 Schematic diagram of the liquid crystal calibration apparatus	43
Figure 3.3 Calibration of Liquid Crystals type R37C2W	43
Figure 3.4 Effect of the lighting conditions on the green colour intensity	44
Figure 3.5 Jet impingement cooling test rig	45
Figure 3.6.....	48
Figure 4.1 Diagram of jet and target plate: a) Flat target and b) Reverse target $H/d = 4$	52
Figure 4.2 Temperature response at the nozzle exit centre during a transient heat transfer test	52
Figure 4.3 Temperature profile at the nozzle exit.....	53

Figure 4.4 Wall temperature history at different 12 radial locations starting from the stagnation point at $Re = 50,000$ and $H/d=4$: a) Flat target and b) Reverse target.....	55
Figure 4.5 Radial distribution of recovery temperature: a) Flat target and b) Reverse target.....	56
Figure 4.6 Nusselt number distribution at $Re= 23,000$ and $D/d= 2.6 ,4 ,6$ and 8	57
Figure 4.7 Nusselt number comparison between flat and reverse surface: a) Nusselt number at the stagnation point, b) Average Nusselt number	59
Figure 4.8 Nusselt number distribution over dimpled surface at different Reynolds numbers, $H/d= 4$	60
Figure 4.9 Discharge coefficient for free jet, flat impingement and reverse impingement at $H/d = 6$	60
Figure 4.10 The discharge coefficient for reverse impingement at different Reynold numbers and nozzle-to-target distances.....	61
Figure 5.1 Sketch of row reverse jet impingement.....	67
Figure 5.2 Plenum vent valve and nozzles locker slider arrangement: a) before the experiment, b) during the experiment	67
Figure 5.3 Nozzle-to-target spacing distance influence on local Nu distribution at $Re= 30,000$	70
Figure 5.4 Nozzle-to-target spacing distance influence on Nu and average Nu distribution at $Re= 30,000$	72
Figure 5.5 Nozzle-to-target spacing distance influence on total average Nu distribution at $Re= 30,000$	73
Figure 5.6 Reynolds number influence on Nu distribution at $H/d= 4$	74

Figure 5.7 Reynolds number influence on average Nu distribution at $H/d= 4.75$	
Figure 5.8 Reynolds number influence on total average Nu distribution at $H/d= 4$	76
Figure 5.9 Different crossflow configurations: a) Minimum crossflow, b) Medium crossflow and c) Maximum crossflow.....	77
Figure 5.10 Crossflow influence on Nu distribution at $H/d= 4, Re= 30,000$...	78
Figure 5.11 Crossflow strength influence on average Nu distribution at $H/d= 4, Re= 30,000$	80
Figure 5.12 Crossflow strength influence on total average Nu distribution at $H/d= 4, Re= 30,000$	80
Figure 5.13 Different nozzle configuration: a) Square nozzle and b) Extended nozzle	81
Figure 5.14 Extended nozzle influence on local Nu distribution at $H/d= 4, Re= 30,000$	82
Figure 5.15 Extended nozzle influence on average Nu distribution at $H/d= 4, Re= 30,000$	83
Figure 5.16 Extended nozzle influence on total average Nu distribution at $H/d= 4, Re= 30,000$	84
Figure 5.17 Nozzle-to-target spacing distance influence on discharge coefficient at $Re= 30,000$	84
Figure 5.18 Reynolds number influence on discharge coefficient at $H/d= 4$...	85
Figure 5.19 effect of different crossflow schemes on the discharge coefficient	85
Figure 6.1 Sketch of array reverse jet impingement.....	87

Figure 6.2 Plenum vent valve and nozzles locker slider arrangement: a) before the experiment, b) during the experiment	88
Figure 6.3 Nozzle-to-target spacing distance influence on local Nu distribution at $Re= 30,000$	90
Figure 6.4 Nozzle-to-target spacing distance influence on average Nu distribution at $Re= 30,000$	92
Figure 6.5 Nozzle-to-target spacing distance influence on total average Nu distribution at $Re= 30,000$	93
Figure 6.6 Reynolds number influence on local Nu distribution at $H/d= 4$	94
Figure 6.7 Reynolds number influence on average Nu distribution at $H/d= 4$	95
Figure 6.8 Reynolds number influence on total average Nu distribution at $H/d= 4$	96
Figure 6.9 Nozzle-to-target spacing distance influence on discharge coefficient at $Re= 30,000$	97
Figure 6.10 Reynolds number influence on discharge coefficient at $H/d= 4$	97
Figure 7.1: A diagram of a control volume that illustrates the discretization of a scalar transport equation	105
Figure 7.2 The solution Method Overview of the pressure-based coupled algorithm	110
Figure 7.3 Grid independency analysis for 5 different element sizes at $Re=30,000$ and $H/d=4$	112
Figure 7.4 Comparing four turbulent models to experimental results at $Re=30,000$ and $H/d=4$	113

Figure 7.5 Cross-section views for reverse impinging jet arrangement with different nozzle configurations: a) square nozzle, b) extended nozzle and c) side view	115
Figure 7.6 Crossflow configuration effect on Nusselt number distribution: a) minimum crossflow, b) medium crossflow, and c) maximum crossflow	117
Figure 7.7 Crossflow configuration effect on averaged Nusselt number at $Re=23,000$ and $H/d=4$: a) dimples, b) cylinders	117
Figure 7.8 crossflow configurations effect on velocity contours at $Re=23,000$ and $H/d=4$: a) minimum crossflow, b) medium crossflow, and c) maximum crossflow	119
Figure 7.9 Effect of nozzle configuration on the area averaged Nusselt number at $Re=23,000$ and $H/d=4$: a) dimple, b) cylinder.....	120
Figure 7.10: Effect of nozzle configuration on pressure contour at $Re=23,000$ and $H/d=4$: a) square edged nozzle, b) extended nozzle	121
Figure 7.11 Effect of nozzle configuration on the velocity contour at $Re=23,000$ and $H/d=4$: a) square edged nozzle, b) extended nozzle	121
Figure 7.12 Effect of inlet orientation on the averaged Nusselt number at $Re=23,000$ and $H/d=4$: a) dimples, b) cylinders	123
Figure 7.13 Effect of inlet orientation on the velocity contours at $Re=23,000$ and $H/d=4$: a) top side inlet, b) left side inlet, c) right side inlet.....	123
Figure 7.14 Effect of Nozzle-to-target spacing distance on the averaged Nusselt number at $Re=23,000$: a) dimples, b) cylinders	125
Figure 7.15 Effect of Nozzle-to-target spacing distance on the velocity contours at $Re=23,000$: a) $H/d=1.6$, b) $H/d=3$, c) $H/d=5$, d) $H/d=7$	125

Figure 7.16 The relationship between the averaged discharge coefficient and a) crossflow configuration, b) Inlet flow configuration, c) nozzle-to-target spacing distance at $Re=23,000$.	126
Figure 7.17 Jet impingement arrangements: a) inline jet impingement, b) inline reverse jet impingement, and c) staggered reverse jet impingement	129
Figure 7.18 Target geometry influence on flow velocity contours at $H/d= 4$ and $Re= 30,000$	131
Figure 7.19 Target geometry influence on local Nu distribution at $H/d= 4$ and $Re= 30,000$	132
Figure 7.20 Comparison between the heat transfer and flat target heat transfer ratio (Q/Q_f) of inline and staggered jet arrangement at $H/d=4$, $Re= 30,000$	134
Figure 7.21 Comparison between average Nu of inline and staggered jet arrangement at $H/d=4$, $Re= 30,000$	134
Figure 7.22 Target geometry influence on discharge coefficient at $H/d= 4$, $Re= 30,000$	135
Figure 7.23 Number of jets influence on flow velocity contours at $H/d= 4$ and $Re= 30,000$	136
Figure 7.24 Number of jets influence on Nu contours at $H/d= 4$ and $Re= 30,000$	137
Figure 7.25 Number of jets influence on dimple average Nu at $H/d= 4$ and $Re= 30,000$	138
Figure 7.26 Number of jets influence on cylinder wall average Nu at $H/d= 4$ and $Re= 30,000$	138
Figure 7.27 Number of jets influence on discharge coefficient at $H/d= 4$ and $Re= 30,000$	139

Figure 7.28 Nozzle-to-dimple influence on flow velocity contours at $H/d= 4$ and $Re= 30,000$	140
Figure 7.29 Nozzle-to-dimple influence on Nu contours at $H/d= 4$ and $Re=$ $30,000$	141
Figure 7.30 Nozzle-to-dimple influence on dimple average Nu at $H/d= 4$ and $Re= 30,000$	141
Figure 7.31 Nozzle-to-dimple influence on cylinder wall average Nu at $H/d= 4$ and $Re= 30,000$	142
Figure 7.32 Nozzle-to-dimple influence on discharge coefficient at $H/d= 4$ and $Re= 30,000$	142
Figure 7.33 Reynolds number influence on flow velocity contours at $H/d= 4,$ $Re= 10,000$ and $70,000$	143
Figure 7.34 Reynolds number influence on Nu contours at $H/d= 4,$ $Re= 10,000$ and $70,000$	144
Figure 7.35 Reynolds number influence on dimple average Nu at $H/d= 4$ and $70,000$	145
Figure 7.36 Reynolds number influence on cylinder wall average Nu at $H/d=4$	145
Figure 7.37 Influence of Reynolds number on discharge coefficient at $H/d= 4$	146
Figure 7.38 Influence of crossflow channel height to nozzle on flow velocity contours at $H/d= 4,$ $Re= 30,000$	147
Figure 7.39 Influence of crossflow channel height to nozzle on Nu contours at $H/d= 4,$ $Re= 30,000$	148

Figure 7.40 The effect of crossflow channel height to nozzle diameter (h/d) on dimple the average Nu at $H/d= 4$, $Re= 30,000$	149
Figure 7.41 The effect of crossflow channel height to nozzle diameter (h/d) on cylinder average Nu at $H/d= 4$, $Re= 30,000$	149
Figure 7.42 Crossflow channel height to nozzle influence on discharge coefficient at $H/d= 4$, $Re= 30,000$	150

Chapter 1. Introduction

1.1. Background of gas turbine cooling

Gas turbine can be used in several applications of critical industries, for instance land-based power generation plants, liquified natural gas plants submarines and aircrafts propulsion. Gas turbine is a combustion engine that could convert heat energy from combustion fuels to mechanical energy in the form of shaft work according to Brayton cycle. The Basic gas turbine cycle consists of four essential processes, which are compression, heat addition, expansion then heat rejection as shown in Figure 1.1 a. The ideal cycle that represents the working fluid in the closed-cycle gas turbine engine is the Brayton cycle, as illustrated in Figure 1.1 b, which consists of four reversible processes: 1-2 Isentropic compression (compressor), 2-3 Constant-pressure heat addition (combustion chamber), 3-4 Isentropic expansion (turbine), and 4-1 Constant-pressure heat rejection (heat exchanger).

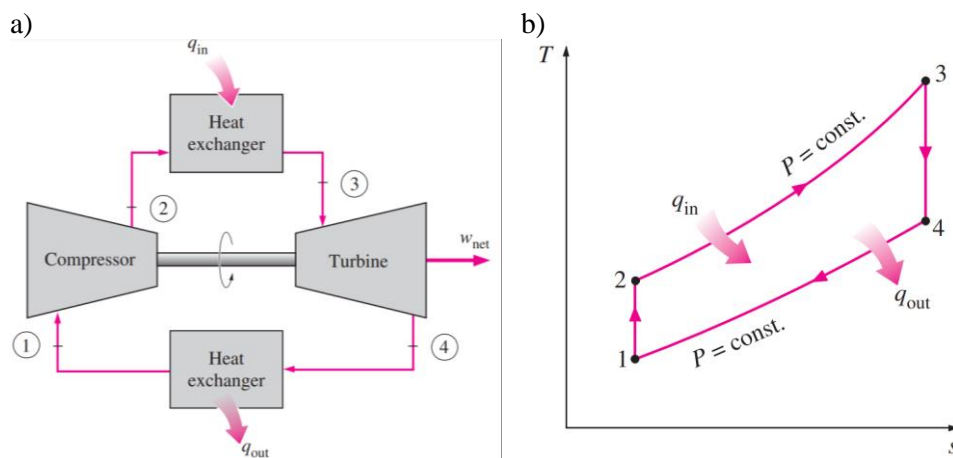


Figure 1.1 a) Closed-cycle gas turbine engine, and b) T-s diagram for the ideal Brayton cycle[1]

Brayton cycle overall thermal efficiency is derived as following [1][2]:

$$\eta_{th,Brayton} = 1 - \frac{T_1}{T_2} = 1 - \left(\frac{P_1}{P_2}\right)^{\frac{\gamma-1}{\gamma}} \quad \text{Equation 1.1}$$

According to Equation 1.1, gas turbine overall thermal efficiency could be improved by increasing turbine entry temperature. Figure 1.2 shows that the thermal efficiency of an actual gas turbine cycle increases by increasing the turbine inlet temperature[2]. Han et al.[3] pointed out that the turbine inlet temperature has been increased from no more than 900°C in the 1960s to around 1550°C at the present time.

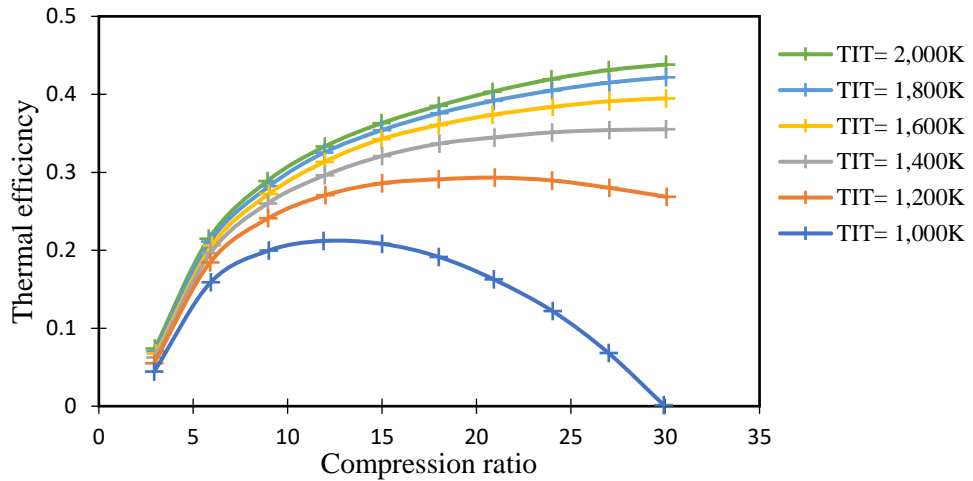


Figure 1.2 Influence of gas turbine compression ratio and inlet temperature on the thermal efficiency [2]

As shown in Figure 1.3, during the last thirty years there is a rapid increasing in the turbine entry temperature, as a result of applying advanced technology in manufacturing the cooling structure of the turbine blade[4]. the persistent evolution of coatings, high grade alloys, and internal cooling systems design which can preserve the blade structural integrity for longer life span.

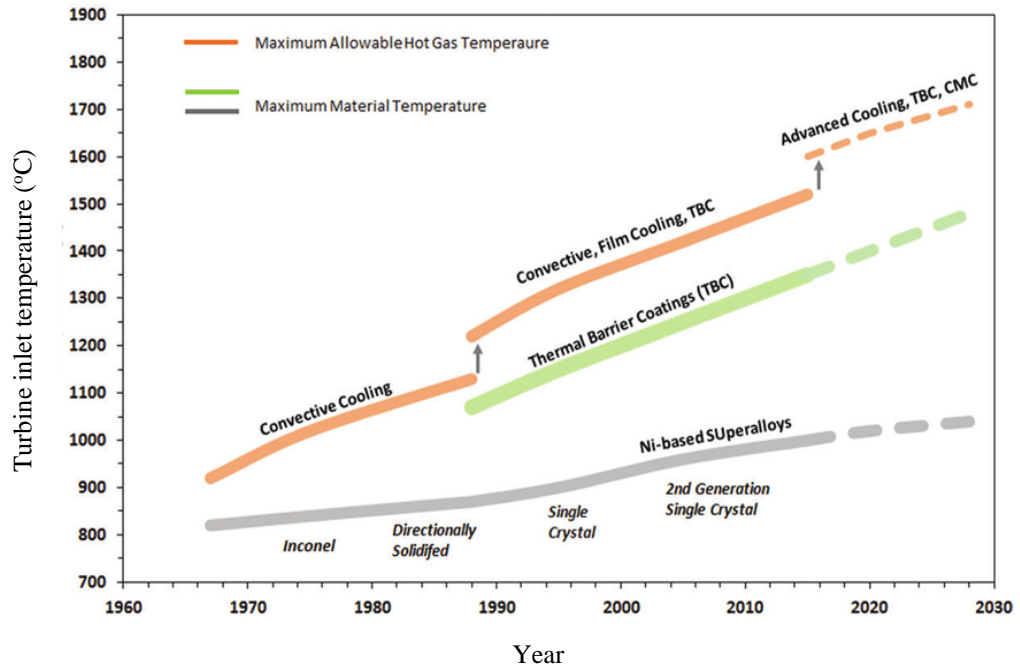


Figure 1.3 Evolution of gas turbine inlet temperatures, materials, and cooling technologies[4]

Gas turbine blade cooling structures have developed from single pass passage with film holes to sophisticated multi-pass passages attached with jet impingement, pin-fin and ribs structures, in addition to thermal barrier coating applied on blade external surface [5], as illustrated in Figure 1.4 and Figure 1.5. Takeishi [6] indicated that cooling technology enables turbine inlet temperature to increase by 25°C per year, whereas the achievement of super-alloy development technology limits by 10°C per year. Thus, for now, cooling technology development is more effective than thermal resistance materials for gas turbine improvement. To a large extent, it is expected in near future an advancement of using alternative fuels, which will induce more harsh working medium for gas turbine blade [7]. To capacitate gas turbine engines to withstand at such hostile environment, more efficient cooling structures are required for turbine blade to be durable and reliable.

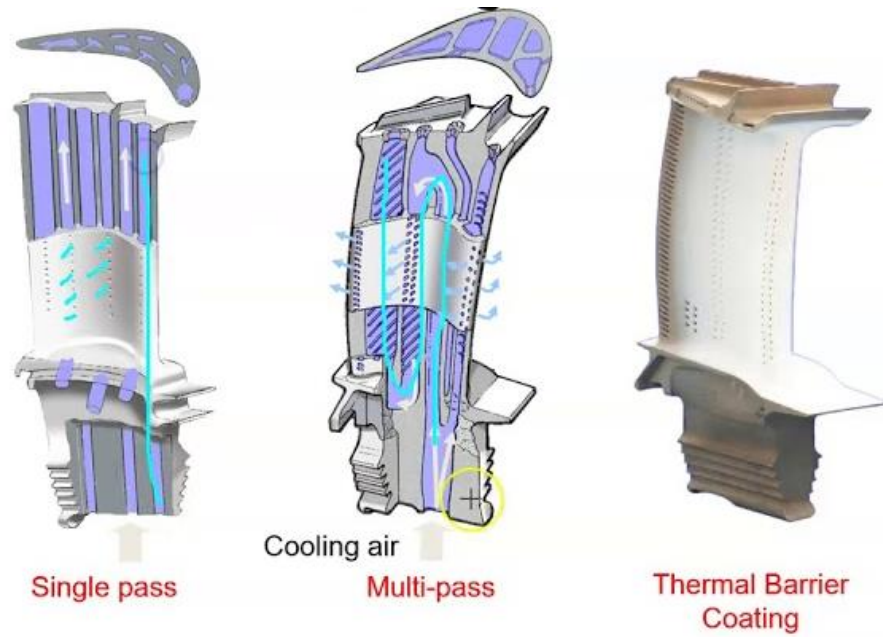


Figure 1.4 Development of cooling structure inside turbine blade [8]

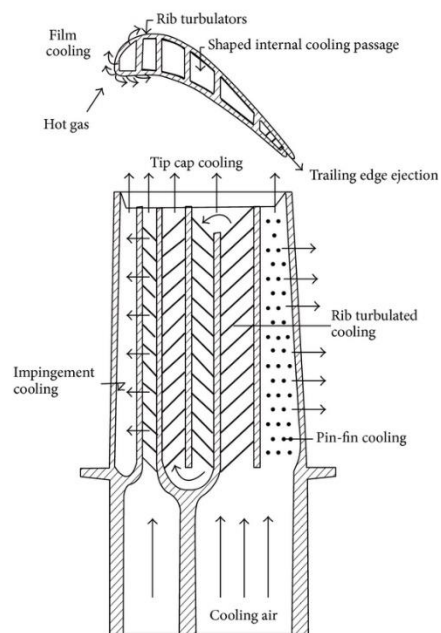


Figure 1.5 Gas turbine blade schematic with the common internal cooling system [5]

1.2. Development of cooling technologies

Gas turbine blade is cooled by compressed air which is extracted from the compressor last stages. On the other hand, that causes penalty on the cycle overall thermal efficiency, excepting that turbine entry temperature is sufficiently high so earnings exceed losses. Hence, the essential purpose of cooling techniques is to achieve the maximal overall cooling effectiveness at the minimal amount of cooling air. Han et al.[8] pointed out that the design of turbine blade cooling structure should guarantee that the maximum blade surface temperatures and temperature gradients during operation are less than the maximum allowed blade metal temperature and thermal stress. Therefore, advanced complex cooling techniques are crucial to avoid any local hot-spots and provide an effective cooling structure.

Four internal cooling techniques are presented in Figure 1.6, which includes jet impingement, pin-fin, dimples and rib-turbulator along with the external film cooling technique. All these designs cool down turbine blade by different approaches. Various parameters, including fabrication capability, determine suitable cooling techniques. Jet impingement is a single, row or array of high velocity jets which impact the target surface. Heat transfer could be enhanced by Pin-fin through interacting the flow between pins and disturbing flow boundary layer development. Dimple and Rib-turbulator have much the same cooling mechanism, which both boost heat transfer through turbulating the flow to prevent boundary layer development. Film cooling uses spent air from film holes to form a thin layer of air film to cover the turbine blade external surface against the extremely hot and turbulent gases.

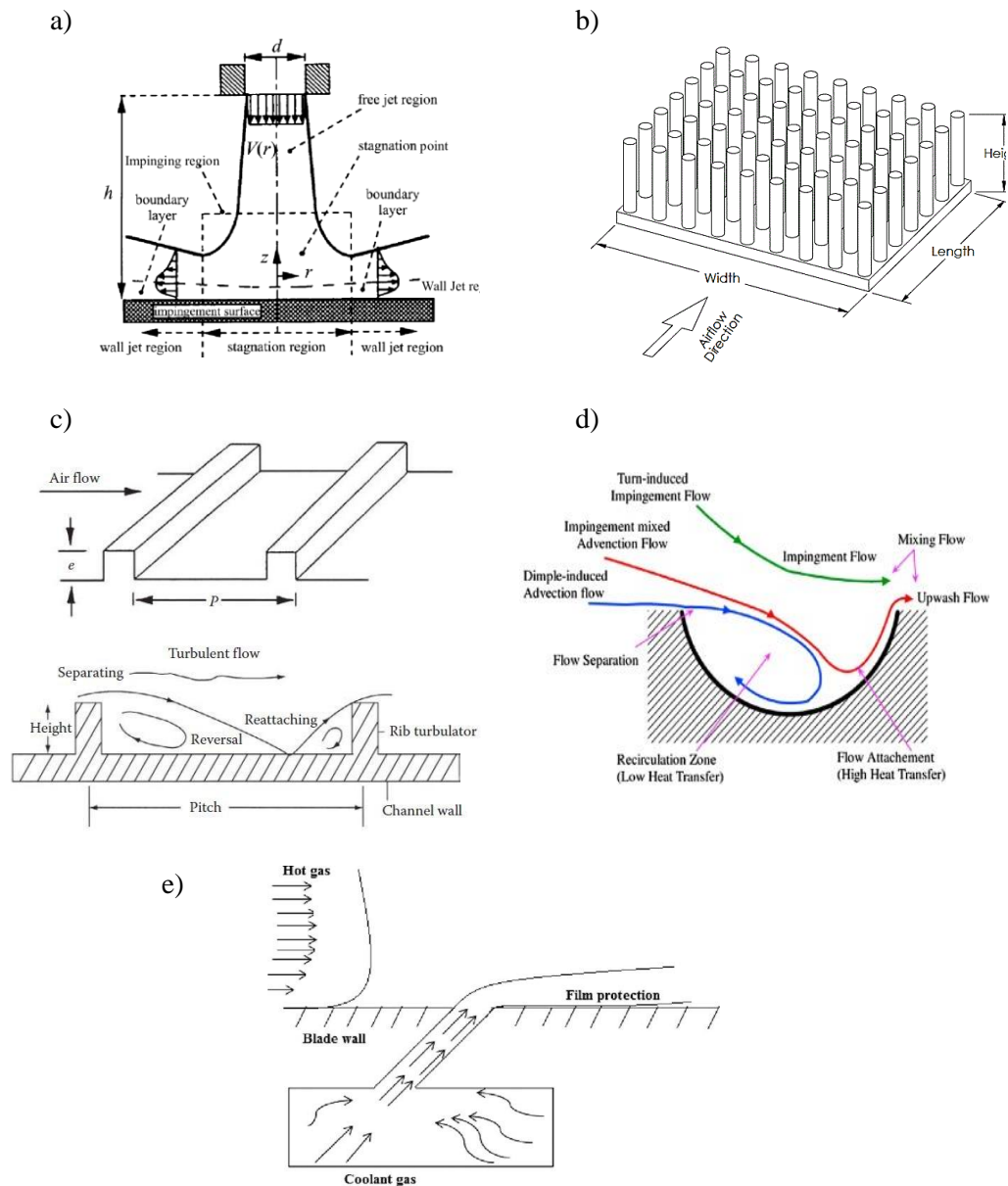


Figure 1.6 Schematic diagrams for the common gas turbine blade cooling systems: a) jet impingement[9], b) pin-fin cooling[10], c) rib turbulator[11], d) dimpled surface[12], and e) film cooling[13]

Cooling air is injected from blade platform into blade trailing edge and mid-chord. Air flows through serpentine passages with ribs and pin-fin attached in the mid-chord. part of cooling air in serpentine passages is delivered to the blade tip cap, and the rest cooling air is delivered for jet impingement at the blade leading edge. Finally, air is exhausted through small

holes distributed over the blade surface and concentrated mainly over the leading-edge area to create film cooling. A part of cooling air flows directly to the trailing edge and cools down the trailing edge through an array of pin-fins then spends out from exit slots, as shown Figure 1.5.

Great progress has been made in the field of blade cooling technologies during the past decades. Bunker[14] claimed the blade cooling structure in near future would move from macro scale to micro scale; from internal complex structure to internal simple structure, while with much more complex structure built near blade outer face; pushing the “battlefield” from blade inside to blade outer surface. However, that study has not included the pressure loss through this micro-channel[14]. It could be expected that channel with this scale of cross-sectional area would cause massive pressure loss. In addition, manufacture feasibility is another factor that needs to be taken into consideration. Several studies related to micro-channel cooling have been published[15][16][17].

1.3. Project aim and objectives

Recent improvements in metal Additive Manufacturing (AM) have allowed very complex internal channels to be manufactured by using the Laser Powder bed Fusion. That opens new horizons for structuring advanced configurations, such as double-wall configuration which is composed of an outer aerofoil wall and an inner support wall that are bonded to one another. The space between the two walls forms a channel for coolant flowing adjacent to the aerofoil wall. By means of the current additive manufacturing

technologies, more complicated cooling systems can be fabricated for achieving higher cooling effectiveness.

Therefore, the aim of this study is investigating the effectiveness of the reverse jet impingement as a novel and unexplored design. The potentials of this technique are achieving higher intensity of jets per unit area with minimal interfacing between jets and increasing the internal surface area which is exposed to the cooling air. The main objectives of this study are as follow:

- Conducting detailed analyses of the local heat transfer distributions for all internal surfaces of a single reverse jet impingement.
- Investigating the heat transfer distribution and the pressure drop of multiple reverse jet impingement with/without film cooling.
- Exploring the effect of crossflow on the heat transfer distribution in case of multiple reverse jet impingement.
- Studing the effect of the nozzle configuration and how it could eliminate the crossflow effect.
- Finding out the relationship between the nozzle-to-target spacing distance and the heat transfer rate.
- Studing how Renolds number affects heat transfer distribution and discharge coefficient.
- Examining the impact of jets number on the heat transfer distribution.
- Determining how the spent air chanel cross-section area influence the cross flow strength.
- Studing the local Nusselt number over a film cooling hole and how it depends on Renolds number.

- Testing different inlet configurations and measuring their effects on the heat transfer distribution and the pressure drop.
- Investigating the effect of the inclination and the rotation angles on the local heat transfer distribution along the film hole.
- Understanding the fluid dynamics characteristics of reverse jet impingement.

1.4. Thesis structure

Literature review has been done as demonstrated by Chapter 2 for the past and present experimental and numerical studies on the single and multiple jet impingement. In addition to, a detail review in the thermochromic liquid crystals and its calibration techniques. In Chapter 3, the experiment setup and the liquid crystals calibration apparatus have been discussed along with the experimental procedure and data reduction. A detailed investigation on Nusselt number distribution and the discharge coefficient for a single reverse jet impingement has been conducted. Evaluating the influence of the Reynolds number and nozzle-to-target spacing distance on heat transfer over the target surface (reverse jet impingement surface consists of hemispherical dimple and cylinder with the same diameter) and comparing with a flat target result is presented in Chapter 4. A row of reverse jet impingement has been studied experimentally in Chapter 5 to examine the effects of different crossflow schemes, Reynolds number and nozzle-to-target spacing distance on the local Nusselt number distribution and pressure drop. In Chapter 6 an array of reverse jet impingement with film hole cooling system has been investigated experimentally under a range of Reynolds number and Nozzle to target spacing

distance. Chapter 7 to some extent it is a repetition for Chapter 5Chapter 6 but by using the numerical technique. The main target from this chapter is to get more details about the fluid mechanics of the reverse jet impingement and performing some complicated study cases to avoid materials and manufacturing time wasting. Finally, Chapter 8 concludes the key findings and provides some suggestions for a potential reverse jet impingement future work. The effects of the rotation and inclination angles on a single film cooling hole is demonstrated in the appendix.

Chapter 2. Literature Review

This chapter provides an overview of the past and recent literature regarding the jet impingement. In this review, a focus will be placed on identifying the most significant factors that influence the jet impingement heat transfer. The first two sections discuss single and multiple jet impingement heat transfer. Then, some recent studies on jet impinging dimpled surface will be reviewed. Afterwards, several studies focusing on different Thermo-chromic Liquid Crystals (TLC) calibration techniques are summarized as well as demonstrating the factors which could affect the TLC accuracy.

2.1. Single jet impingement

Jet impingement method results in a high local heat transfer coefficient because the boundary layer around the stagnation zone is extremely thin. Therefore, heat exchange between the wall and the fluid is enhanced.

Several studies discussed the flow and heat transfer characteristics of a single jet impinging on a flat surface in a variety of configurations. A review of these studies can be found in Martin[18], Jambunathan et al. [19] and Viskanta[20]. It is therefore unnecessary to repeat these fundamental aerodynamic concepts and terminology here, and only a brief introduction will be provided for future reference. As illustrated in Figure 2.1, a single impinging jet forms a stagnation region on the target plate opposite to the nozzle outlet. The magnitude of the nozzle outlet velocity is almost uniform

inside a potential core. As the free jet develops, the potential core length generally extends from five to seven nozzle diameters based on the nozzle design. The jet is accelerated in a radial direction after striking the opposite wall, commonly referred to as a target plate. the maximum velocity is reached at about one nozzle diameter from the stagnation point. Beginning about two nozzle diameters from the stagnation point, a thin laminar boundary layer begins to develop, which becomes turbulent in the wall jet region. Heat transfer distributions over a target surface are greatly affected by the aerodynamic and thermal interactions between the jet and the target plate.

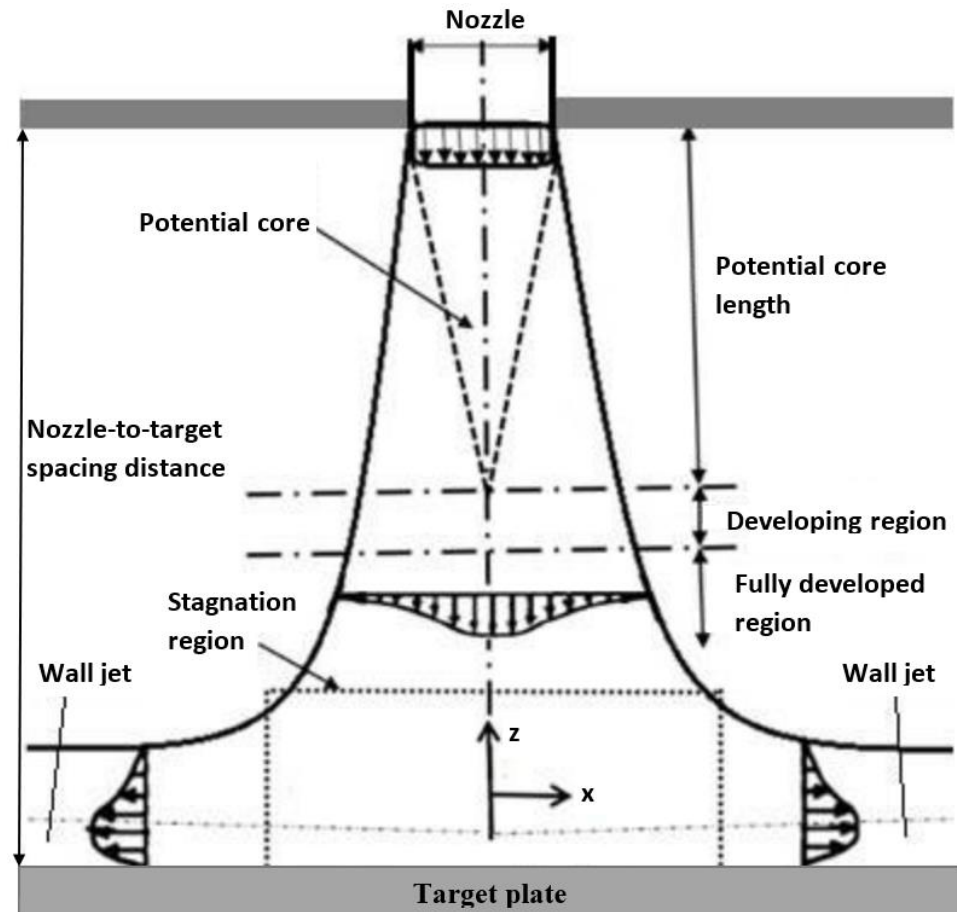


Figure 2.1 Different regions of a jet impingement flow[20]

In a study of jet impingement heat transfer, it was found that a power law relationship existed between heat transfer levels and flow conditions ($Nu=c.Re^m$). Goldstein et al.[21], which found that the value of the m exponent varied between 0.5 for laminar-stagnation point regions and 0.8 for turbulent-jet regions[22]. Furthermore, a considerable effect of the distance between the jet and the target plate (H/d) is also observed, especially for free impinging jets, as shown by the research of Blaugh and Shimizu[23]. When the nozzle-to-target spacing distance equals the jet potential core length (5-6 nozzle diameters), heat transfer towards the stagnation point is maximal. If the nozzle-to-target spacing distance is equal or less than two nozzle diameters, a secondary heat transfer peak will be produced about two nozzle diameters from the stagnation point. Popiel and Trass[24] have performed smoke flow visualisation experiments to demonstrate the local temperature distribution depends on the flow field, which contains vortical structures and strong recirculation zones.

Turbulent jet impingement was recognised to yield a higher heat transfer rate than laminar jets[25][26][27]. In comparing the heat transfer of laminar and turbulent jets, Donaldson et al.[26] found that turbulent heat transfer is 1.4-2.2 times greater than laminar heat transfer. At the stagnation point, Nusselt number is expressed as a function in Reynolds ($Nu_{st}=c.Re^m$). In the case of a laminar jet with a uniform exit velocity profile, the Reynolds number exponent m equals 0.5. In comparing the m values in various numerical and experimental studies, Polat et al.[28] found that there is a considerable scatter in the exponent values. Depending on whether the inlet velocity profile is parabolic or flat, m value varied between 0.23 and 0.67. Therefore, the velocity

profile shape at the nozzle exit should be taken into consideration before comparing experimental and numerical results.

Angioletti et al.[29] have studied the impact of the nozzle-to-target ratio on Nusselt number and found that, in case of $H/d > 4$, the peak Nusselt number lays at the jet stagnation point. The optimal spacing distance, H/d , appears to be the same as the jet potential core length. By the end of the potential core, the heat transfer coefficient falls as a result of velocity deterioration. A larger space between the impingement target and nozzle plate causes the heat transfer reduction as the jet flow can mix with the recirculation flow period it impinges the target surface. Jung-Yang and Mao-De[30] found that Nusselt number at the stagnation point is proportional to the jet Reynolds number raised to the power of 0.638 and inversely proportional to the Nozzle-to-target ratio raised to the power of 0.3. Jambunathan et al.[19] found that the Nusselt number at a radial distance from the stagnation point, r/d , greater than six diameters the heat transfer is independent on nozzle-to-target spacing distance up to 12 nozzle diameters.

Martin[18] pointed out that the local Nusselt number distribution pattern for nozzle-to-target ratio greater than five, appears such as a bell curve. The Nusselt number peak value locates at the stagnation point and the local distribution monotonically decreases, whereas for nozzle-to-target ratio less than four the distribution will have two peaks as shown in Figure 2.2. When the ratio of the nozzle size to the target is small, increasing the Reynolds number of the jet results in an increase in the second peak Nusselt number[31]. In fact, the second peak Nusselt number may become greater than the value of the first peak.

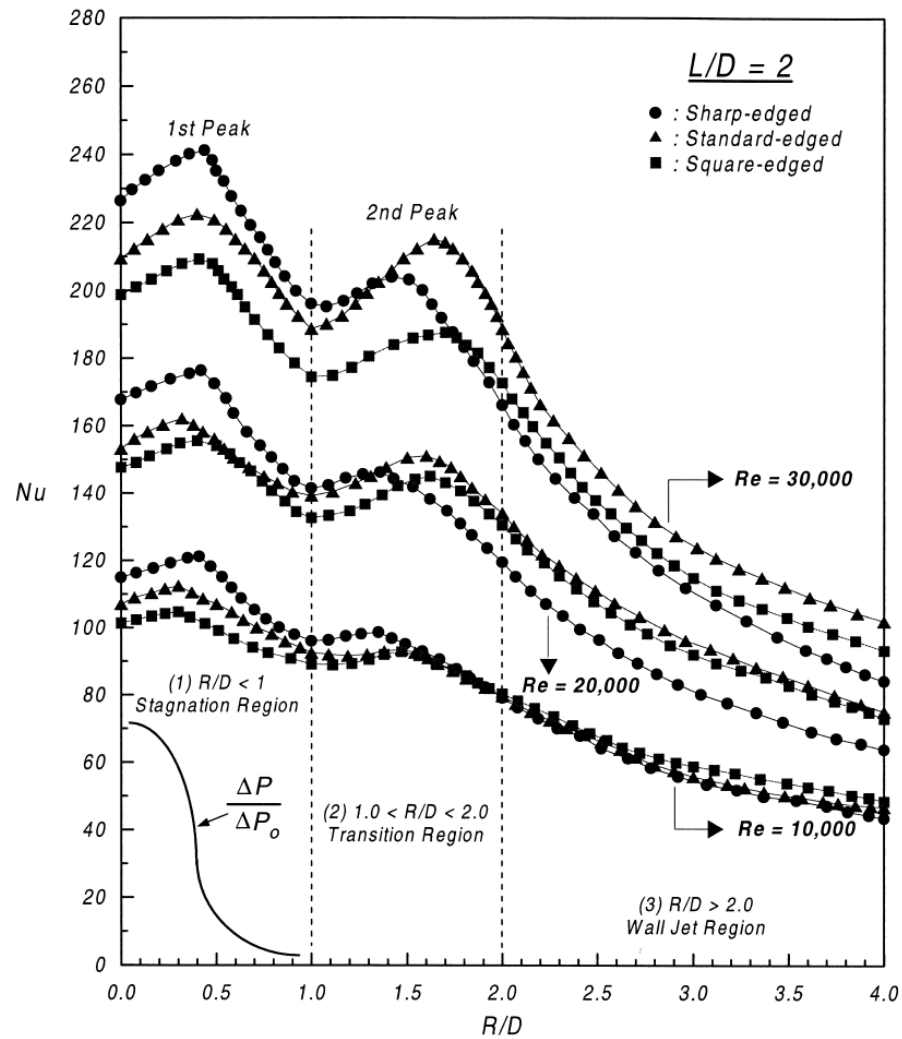


Figure 2.2: Local Nusselt number distribution at the nozzle-to-plate spacing of $L/D=2$ [31]

The influence of jet surrounding air entrainment on the Nusselt number has been studied by Obot et al.[32]. It has been found that nozzle shape has a significant effect on the surrounding air entrainment. The majority of the published jet impingement heat transfer studies state their jet nozzles configuration. However, in many applications, the sharp edge square nozzle configuration is generally preferable as a result of it is fabricated easily, particularly for the multi-jet arrangements.

Jambunathan et al.[19] reviewed experimental data of laminar and turbulent jet impingement with jet Reynolds numbers from 5,000 to 124,000, nozzle-to-target ratio from 2 to 16. They illustrated that the local Nusselt number correlations are expressed as a function of nozzle exit Reynolds number. On the other hand, the published empirical equations considered that Reynolds number exponent is a variable, and its value depends on the nozzle-to-target ratio and the displacement-to-nozzle ratio. In addition, the study concluded that if the displacement-to-nozzle ratio is higher than six, the heat transfer is independent of the distance between the nozzle and the target up to a distance of 12 nozzle diameters.

Garimella and Rice[33] studied experimentally the local Nusselt number distribution of a confined/unconfined jet impingement with Reynolds number from 4,000 to 23,000, and nozzle-to-target ratio from 1 to 14 and nozzle diameter from 0.79mm to 6.35mm. They found that the second Nusselt number peaks were approximately around two nozzle diameters from the stagnation point and they were more obvious at small nozzle-to-target ratios and large jet nozzle diameters, and as the nozzle-to-target ratio increases the second peak shift outwardly from the stagnation point. In addition to, at given nozzle-to-target ratio and Reynolds number the results showed that, the smaller nozzle diameters the higher Nusselt numbers attained and as the diameters enlarge the second peak becomes more obvious.

The majority of the jet impingement cooling systems applied in the industrial sectors are turbulent jet flow. Consequently, jet impingement numerical modelling is a challenging task to predict impinging jet heat transfer precisely. There is not a turbulence model has been generally approved to be

reliable to all numerical modelling cases, accordingly different turbulent models have been improved to predict heat transfer and fluid mechanics more accurately. There are some studies focused on comparing the capability of various turbulence models for impinging jets.

Chattopadhyay[34] studied the heat transfer of laminar impinging jet from annular and circular nozzles. It was found that the average Nusselt number from circular nozzle was about 20% higher than the annular nozzle and the local Nusselt number distribution shape over the impinging target was a function of Reynolds Number powered 0.55. Wang and Mujumdar[35] applied four $k-\omega$ models for heat transfer predicting of a two-dimensional turbulent slot impinging jet. The influence of turbulence model constants magnitudes has been investigated, and the numerical results have been evaluated by comparing them with experimental results.

Quan et al. [36] investigated the jet impingement heat transfer by using the $k-\varepsilon$ turbulent model. It was concluded that the nozzle-to-target spacing ratio equals five is the optimum spacing ratio. Badra et al.[37] applied different turbulent models and pointed out that the Shear Stress Transport (SST) $k-\omega$ turbulent model can perform very well in a Reynolds number range from 5,000 to 30,000. At nozzle-to-target ratio less than five, the first and second Nusselt number peaks were at displacement-to-nozzle 0.5 and 2, respectively. At spacing distance of six nozzle diameters, the Nusselt number at the stagnation point was the maximum and there is not second peak.

2.2. Multiple jet impingement

Multiple jet impingement differs from single jet impingement by the interface between jets flow. The strength of this interface is affected by the geometrical configuration of the jet array, such as nozzle-to-target spacing distance, nozzle-to-nozzle separation distance, and the effect of the generated crossflow from the upstream jets spent air as shown in the Figure 2.3.

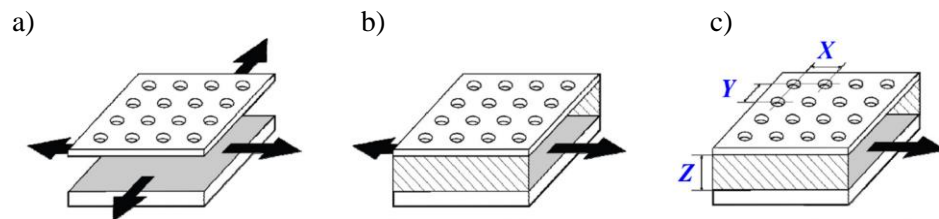


Figure 2.3 Multiple jet impingement crossflow schemes[38]: a) minimum crossflow, b) medium crossflow, and c) maximum crossflow

The crossflow strength is classified into the categories: minimum crossflow, medium crossflow, and maximum crossflow. This classification is based on the outlet configuration as illustrated in Figure 2.3. In the internal cooling systems of the gas turbine blade, maximum crossflow is common as a result of the spent flow orientation. Florschuetz et al.[39] developed an empirical correlation to estimate the average Nusselt number based on the heat transfer area geometries and flow configuration as shown below:

$$\overline{Nu} \propto f \left[Re, \left(\frac{G_{cf}}{G_j} \right), \left(\frac{X}{d} \right), \left(\frac{Y}{d} \right), \left(\frac{Z}{d} \right) \right] \quad \text{Equation 2.1}$$

Where G_{cf}/G_j is the mass flux ratio of crossflow mass flow rate and the impinging jet mass flow rate. Florschuetz et al.[39] empirical correlations, have been validated by Bailey et al.[40]. Generally, multiple jet impingement heat transfer attitude is the same as the single impinging jet are. Nusselt number directly proportional to Reynolds number ($Nu=c.Re^m$), where the local

Nusselt number exponent m value of m is agreed with single impinging jet. The exponent m value of averaged Nusselt number vary between 0.66 and 0.72 [39][40][41][42].

The geometry of the multiple jet impingement can be identified by nondimensional parameters, such as nozzle-to-target spacing distance ratio, nozzle-to-nozzle separation distance which is divided by the nozzle diameter. Along with the strength of the crossflow is another significant parameter that influences the heat transfer rates. Crossflow is a multiple jet impingement side-effect and strong crossflow is not desirable, because crossflow pushes the air jets stream-wise and reduces the strength of the impinging jet. A number of experiments and numerical studies conducted the heat transfer effectiveness and performance of multiple jet impingement, such as Goldstein and Behbahn[43], and Hollworth and Berry[44]. As in case of single jet impingement, flow from multiple jet impingement nozzles consists of three flow regions: free-jet, stagnation region, and wall-jet. Although that similarity, it is not practical to use the heat transfer data of single jet impingement in designing an array of jet impingement cooling system, because there are some flow mechanics differences as a result of the crossflow (Gao et al.[45]; Koopman[46]).

In case of array jet impingement, crossflow is an unavoidable side-effect. Several studies have examined how cross flow affects heat transfer. Florschuetz et al.[47] investigated the crossflow effect on the heat transfer of array jet impingement. the results showed that the crossflow reduces the heat transfer effectiveness of impinging jets. Moreover, increasing the mass flow rate of the crossflow dilutes the impinging jets intensity, consequently the

crossflow will dominate on the fluid flow and heat transfer. Huang et al.[41] observed that the direction of the crossflow affects the heat transfer of the impinging jets. The heat transfer peak takes place at the leading area where the crossflow has the contrary direction of the nozzles feeding flow. While in case of the crossflow has similar direction of the nozzles feeding flow, the heat transfer at the trailing section will be slightly more superior than the leading section. The study concluded that when allowing both directions for the air crossflow, heat transfer distribution became more uniform, and achieving higher overall heat transfer.

Some studies tried to remove the crossflow after impinging the target surface for the purpose of eliminating the crossflow effect. Hollwarth and Dagan[41], drilled holes with small diameter than the nozzles on the target plate at the same positions of impinging jet nozzles and the spaces in between. The overall heat transfer was 20-30% greater than the case of crossflow. Ekkad et al.[48] confirmed that the existence of film holes on the target plate improves the overall heat transfer. Yunfei et al.[49] investigated experimentally and numerically the characteristics of the heat transfer within a jet impingement array. Minimum, medium and maximum crossflow schemes have been applied. It has been demonstrated that the overall heat transfer of the maximum crossflow case was significantly lower than the other cases.

Metzger et al.[50] studied experimentally the effect of both the separation distances between nozzles and the nozzle-to-target spacing distance on the average heat transfer over the target plate. It was pointed out that increasing the nozzle-to-target spacing distance reduces the intensity of the crossflow. For nozzle-to-target spacing distances greater than eight nozzle diameters,

Freidman and Mueller[51] suggested that the optimum nozzle-to-nozzle separation distance value of four nozzle diameters for attaining the maximal heat transfer on the impinging surface. While Martin[18] observed that decreasing the nozzle-to-target spacing distance should accompanied with increasing the nozzle-to-nozzle separation distance to four eliminate the interference between adjacent jets. For instance, at nozzle-to-target spacing distance of 5.4 nozzle diameters, the optimum nozzle-to-nozzle separation distance is roughly seven nozzle diameters.

There is a number of experimental studies were concerned with analysing the effect of the nozzle patterns on the heat transfer performance. The inline pattern always demonstrates more effective performance than the staggered pattern. This trend was confirmed by Florschuetz et al.[47] and Metzger et al.[50]. In the case of the inline pattern, the spent flow has a straight route through the middle spanwise distance between the jets. Therefore, the impinging jets in the inline pattern are more preserved from the oncoming crossflow by the upstream jets. On the other hand, the crossflow affects the impinging jets more directly in the staggered pattern, which causes stronger diffusion and leads to divert jets from the impinging target and reduces the heat transfer effectiveness.

Badra et al.[37] performed numerical simulations for Multiple jet impingement. The numerical model has been evaluated against published experimental results. The numerical model validation demonstrated high degree of agreement between the numerical and experimental data when applying the SST $k-\omega$ turbulence model. Ashok Kumar and Prasad[52] conducted a numerical study on heat transfer of jet impingement row on a

concave surface with/without effusion holes. The pressure drop was found to be higher for configurations with only effusion holes as air outlet. A staggered arrangement of the impingement and effusion holes results in a significant increase in heat transfer by as much as 3.45 times that of an inline arrangement.

Zu et al.[53] have studied numerically the jet impingement heat transfer and applied seven turbulence models: standard, normalized and realizable $k-\epsilon$ model; standard and SST $k-\omega$ model; Reynolds Stress model; and the Large Eddy Simulation model. For Reynolds number from 10,000 to 30,000, nozzle-to-target spacing distance from 1 to 6 nozzle diameters, and impinging angle from 20° to 90° (jet impinges the target surface at impinging angle of 90°). It was observed that Large Eddy Simulation and SST $k-\omega$ turbulence models are reliable in predicting heat transfer and fluid flow; in particular, SST $k-\omega$ turbulent model is more recommended as it has the optimum compromise between the results accuracy and computational time. In addition to, they concluded that the optimal impinging angle occurred at 90° .

Craft et al [54] investigated the use of linear and non-linear eddy-viscosity models to predict the flow and heat transfer of a three-dimensional jet array impingement on a concave surface. The results showed that both models were able to broadly reproduce the mean flow field, but both underpredicted the levels of turbulence energy as the jets approached the curved surface and in the downwash regions. The use of standard wall-functions resulted in underpredicted heat-transfer levels around the jet impingement and a failure to capture the secondary Nusselt number peaks associated with the jet downwashes. The AWF results were highly sensitive to the approximation

adopted to represent wall-normal convective transport in this impingement-dominated flow. The proposed form was found to be numerically stable and to give broadly the correct peak Nusselt number levels, together with secondary peaks associated with the jet downwashes, although the overall heat transfer levels were somewhat underpredicted in these regions of the flow.

Iacovides et al [55] found out that rotation can have a significant impact on impingement cooling. Rotation can reduce the overall effectiveness of impingement cooling and can also lead to non-uniform heat transfer. The flow visualization studies suggest that rotation increases the spreading rate of the cooling jets, which can lead to variations in the spreading rates of different jets. The findings of this study have important implications for the design of blade-cooling passages.

2.3. Jet impinging dimpled surface

Lei et al.[56] investigated numerically the effect of dimple on enhancing the internal heat transfer of a double wall cooling structure. The jet flow is directly impinging on the dimple and released from the film holes after passing the double wall chamber. The Reynolds number range was from 10,000 to 70,000. The dimple depth and dimple diameter ratio was ranging from 0 to 0.4 and the dimple diameter and nozzle diameter ratio was varying from 0.5 to 3. It has been pointed out that the dimple can efficiently increase the heat transfer rate over the impingement surface as a result of reducing the thickness of the flow boundary layer and flow reattachment near the dimple rim especially at high Reynolds numbers. Moreover, at a large dimple depth, a heat transfer drop occurred due to the toroidal vortex which diverts the flow from the target

surface. The dimple depth and dimple diameter have a significant impact on the heat transfer performance.

Ravish et al.[57] studied experimentally the dimpled impinging target configuration in the heat transfer for a 3x3 array jet impingement. This study Reynolds number range was from 5,000 to 40,000, the nozzle-to-nozzle separation distance was three, four and five nozzle diameters, the dimples depth was 0.25 and 0.5 nozzle diameter, nozzle-to-target spacing distance was from one to six nozzle diameters, and dimple the diameter was equalled the nozzle diameter. It was reported that at nozzle-to-target spacing ratio less than three, the heat transfer performance over the flat target was better than the dimpled target. However, for nozzle-to-nozzle separation greater than three nozzle diameters, the dimpled surface performance was better than the flat surface. Moreover, the greatest heat transfer for the shallow dimple occurred at nozzle-to-nozzle separation distance five nozzle diameters.

The dimples arrangement pattern and the nozzles geometry have been experimentally investigated by Nevin C.[58]. The nozzle-to-target range was from two, six and ten, and all the experiments were conducted at Reynolds number 20,000. Results pointed out that the presence of the dimples produced higher heat transfer than the flat target. In all the cases of the study, the heat transfer performance of the inline pattern was slightly higher than the staggered pattern. The Nusselt number distribution at nozzle-to-target spacing distance six nozzle diameters was the optimum value.

The cooling performance and pressure drop of an array of jet impingement has been evaluated over a concave and convex dimpled target surface by Sun-

Min[59]. Among the four tested configurations (inline convex, staggered convex inline concave, and staggered concave) the staggered convex dimple array jet impingement showed the best heat transfer performance whereas the staggered-concave configuration showed the lowest pressure drop. A parametric study has been also performed on the staggered convex configuration with the dimple diameter to the jet diameter ratio. It was found that the dimple diameter to nozzle diameter ratio seven was the optimum value for achieving the highest area averaged Nusselt number.

Xing et al.[60] investigated experimentally the impinging jet heat transfer over a flat and dimpled target surface at different crossflow schemes. A 9x9 jet array impinging has been studied at Reynolds number range from 15,000 to 35,000. The nozzle-to-target spacing distance adjusted to be three, four and five nozzle diameters. Nusselt number distributions have been measured on the target surface using the transient liquid crystal technique. The narrow nozzle-to-target spacing distance three nozzle diameters produced the highest Nusselt number distribution for different crossflow schemes. The highest enhancement ratio was up to 12.3%. In all cases, the dimpled surface attained better heat transfer performance for the minimum crossflow scheme and at different nozzle-to-target spacing. Moreover, the ratio of the area averaged Nusselt number of the dimpled target and the flat target increases with increasing Reynolds numbers.

The heat transfer and flow of a circular jet impingement on a cuboid, concave and convex hemispheres were investigated numerically by Bolek et al.[61] The study has been performed for Reynolds number range from 4,300 to 23,000 and nozzle-to-target spacing distances two, six and nine nozzle

diameters. Different turbulence models have been compared with experimental data; the capability of the Shear Stress Transport $k-\omega$ in predicting the Nusselt number was the best. They confirmed that Nusselt number is proportional to Reynolds number, in regardless the shape of the impingement target surface. In comparison with the concave and convex hemispheres, impinging on the cuboid shape provides the highest Nusselt number distribution from the stagnation point to three nozzle diameters. Behind this region, the convex hemisphere shape produced the highest Nusselt number distribution.

A study Based on combined particle image velocimetry and numerical simulation, the heat transfer and flow characteristics of a single jet impingement over a dimpled target has been investigated by Xie et al.[62]. This study has been conducted for Reynolds number 5,000, 10,000 and 23,000, nozzle diameter to dimple diameter ratio 0.318, 0.5 and 1.045, dimple depth to dimple diameter ratio 0.1, 0.2 and 0.3, and fixed nozzle-to-target spacing distance two nozzle diameters. It has been observed that if the dimple depth to nozzle diameter increased to 0.3, the flow turning angle has increased up to 180 degrees. In that case, the wall jet flow completely leaves the target at the dimple rim and formed a large-scale toroidal vortex due to the centrifugal force of the deflected flow at the stagnation region, as shown in Figure 2.4. For the cases of nozzle diameter to dimple diameter 0.318 and 0.5, the area increasing enhanced the heat transfer performance, and the average Nusselt number increases with the increasing of dimple depth. The Nusselt number for the stagnation point was inversely proportional to the nozzle diameter to dimple diameter ratio.

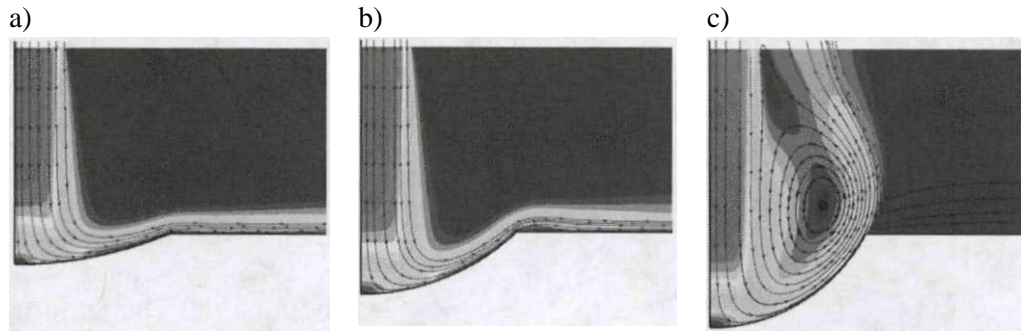


Figure 2.4: Dimple jet impingement velocity contours and streamlines at $D/D=0.318$, $Re= 23,000$ and dimple depth ratio[62]: a) 0.1, b)0.2, and c)0.3

Gm et al.[62] studied experimentally the jet impingement heat transfer on dimpled surface for a 4x12 jet array by applying the transient liquid crystal method. Measurements has been done for Reynolds numbers ranging from 4,850 to 18,300. The results pointed out that the Nusselt numbers for the flat target and dimpled target are about the same. However, the dimple target provided a better heat transfer rate because the heat transfer surface area of the dimpled target is greater compared with the flat target.

A numerical investigation of heat transfer characteristics of turbine leading edge with a combined dimpled and pin-fins cooling structure has been performed by Haifeng[63]. Nozzle-to-target spacing distance and target surface curvature under different Reynolds numbers and crossflow schemes were considered. The results showed that increasing the crossflow strength caused to reduce the jet cooling effectiveness, consequently, weaken the overall heat transfer performance. Large nozzle-to-target spacing distance improved the jet impingement cooling effectiveness for minimum crossflow, but for small and medium spacing distance cases the overall heat transfer will not recover as crossflow intensity get higher.

An experimental study on heat transfer for a 3x4 array jet impingement on concave/convex dimpled surface with effusion cooling has been performed by Shyy et al.[64]. That experimental study investigated the influence of effusion on the performance of the heat transfer for the array jet impingement by comparing the detailed Nusselt number measurements over the dimpled targets over Reynolds numbers range from 5,000 to 15,000 and nozzle-to-target spacing distance from 0.5 to 10. Three sets of Nusselt number for each dimpled surface at eccentricity between nozzle and dimple 0, 1/4, 1/2 has been measured. It was observed that Increasing of the nozzle-to-target spacing distance reduced the area averaged Nusselt number differences between the effusion and non-effusion cases for both convex and concave dimpled targets, while the heat transfer enhancement faded out as nozzle-to-target spacing distance increased. The highest area-averaged Nusselt number always emerged in all cases at eccentricity between nozzle and dimple 1/2 nozzle-to-nozzle separation distance over both dimpled target surfaces with effusions, while the averaged Nusselt number at eccentricity 0 and 1/4 gradually fall into close agreements as nozzle-to-target spacing distance increases from 0.5 to 10.

Abubakar et al.[65] investigated numerically the heat transfer enhancement and fluid mechanics for jet impingement with dimples, pin fins and rib turbulators. The area averaged heat transfer coefficient for the dimpled target surface was lower at all crossflow conditions and 26% lower at the highest crossflow strength. The dimpled surface heat transfer performance was lower than for the flat target or any of the targets with obstacles. This was due to that the crossflow resulted in deflection of the jet away from the target surface and increased the reverse flow in the gap, as illustrated in Figure 2.5.

This reduced local turbulent kinetic energy and heat transfer coefficient on the target surface at all crossflow intensities. For the downstream dimples the crossflow deflected the jets to impinging the flat target wall, so the dimple had no effect, as shown in Figure 2.6.

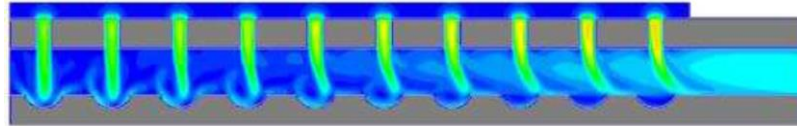
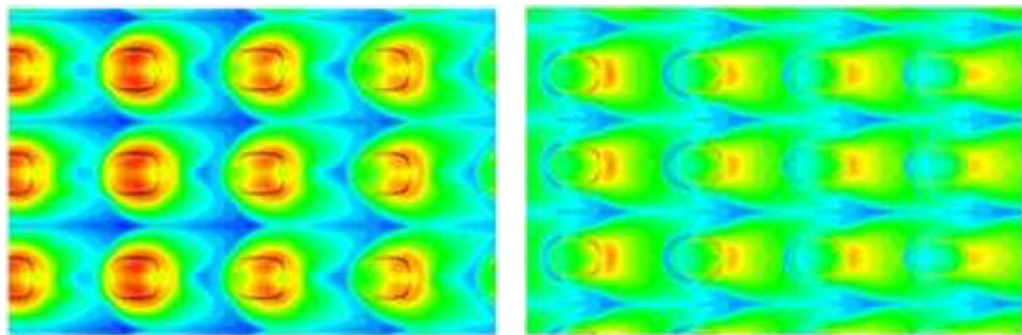


Figure 2.5: Flow velocity contours for Jet impinging on a dimpled target



Upstream

Downstream

Figure 2.6: Upstream and downstream Nusselt number contours for Jet impingement over a dimpled target

2.4. Thermochromic liquid crystals (TCL)

It has been found that thermochromic liquid crystals, scientifically called chiral or cholesteric nematic liquid crystals, are becoming increasingly popular in the experimental researches and industrial applications. TCL is widely used for heat transfer, such as in the current study, and flow visualisation experiments. TLC is a substance that exhibits a particular colours at specific temperatures . This liquid has a twisted molecular structure and it consists of organic chemicals that are optically active[65]. In the sense that all TLCs reflect incident white light selectively, they are better viewed over a background that does not reflect light, ideally black background.

Those mixtures susceptible to temperature change, as the TLC used in this study, begin as transparent, moving through the visible spectrum from red, yellow, green, blue, and violet with temperature increase, until they turn transparent again, as shown in Figure 2.7. A reversible colour change occurs in the course of cooling, and the sequence of colour change is reversed.

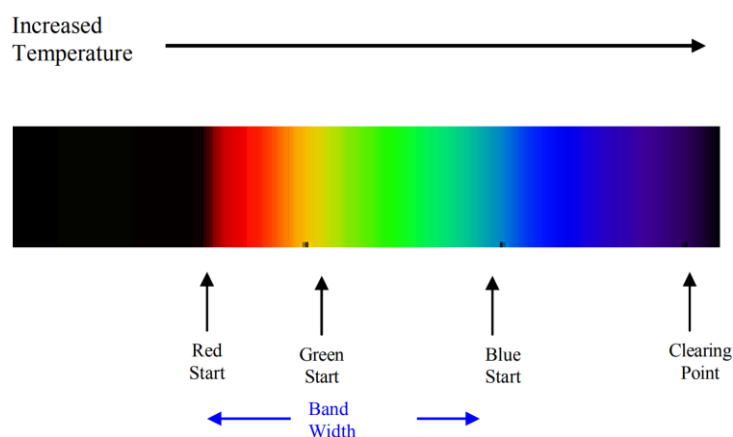


Figure 2.7 Liquid crystals colour plays

A colour play indicates the colour change properties of TLC. In this parameter, the colour of the TLC is specified at which temperatures it will change. The colour play provides either the red activation temperature or the mid-green activation temperature, the temperature unit ($^{\circ}\text{C}$) and the bandwidth. The bandwidth corresponds to the difference between the blue and red start temperatures. A red start temperature can be set from -30°C to 120°C , and a bandwidth from 1.0°C to 20°C . This depends on the colour play. On the basis of bandwidth, TLCs can be divided into two categories: wideband and narrowband. Wideband TLCs typically have bandwidth greater than 4°C whereas narrowband TLCs have bandwidth between 0.5 and 4°C [65].

TLC is available in different forms: solution, microencapsulated as aqueous slurries or coated sheets. TLC has characteristics that change depending on their use, so they must be used for a certain period of time in

order to retain their properties. TLCs used in the present study are in micro-encapsulated form providing 5-30 micron diameter capsules which protects the crystals and extends life. The detailed chemical and physical properties of liquid crystal is given by its provider LCRHallcrest[66]. The following are the major factors affecting the performance of thermochromic liquid crystals:

2.4.1. TLC aging

Using the TLC products extensively could reduce its accuracy. Manufacturers suggest that they should only be replaced after many months of use. However, the TLC coated layers were replaced after three months to make sure they are still accurate. With proper handling. Repeated use at elevated temperatures flow (+50° C) will accelerate degradation, as well as exposure to Ultraviolet light for long time [67][68].

Aging impact on TLC calibrations of R30C1W has been examined by Kakade et al. [34] on film TLC thicknesses of 15, 30 and 45 µm. The samples have been heated and maintained at 60 °C. After two hours the samples were cooled to 20 °C and then heated again for extra two hours at 60 °C. As a result of aging at an elevated temperature exceeding the clearing point temperature of the R30C1W TLC, It has been observed that hue occurs shifted towards higher temperatures at which was observed. The results of that study follow a similar trend to those of Wiberg and Lior [68].

2.4.2. Lighting angle

The lighting angle is determined by the angle formed between the camera axis and the light source, as shown in Figure 2.8. Rao and Zang[69]

recommend a lighting angle range from 20° to 27° in order to reduce measurement uncertainties. In their study, Kakade et al.[70] demonstrated that different illumination angles produced more pronounced effects on R30C5W TLC than on R30C1W TLC. Hence, narrowband TLCs are most suitable for viewing angles range from 0° to 40° in order to minimize the effects of varying lighting angle.

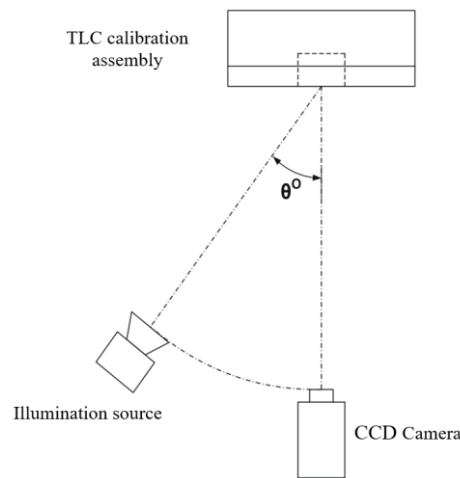


Figure 2.8 Illumination-viewing setup for TLCs calibrations[67]

2.4.3. TLC thickness

Coating thickness, also known as the film thickness, refers to the TLC layer thickness. Despite not being explicitly stated in the literature, TLC coating thickness generally refers to the dry film thickness. It is still unclear what the optimum thickness of TLC film should be, and the criteria for determining this are rather vague. As per Parsley [71] recommends a film thickness of 10 microns. In contrast, it is clear from previous studies [72][73][74] that measurements of coating thicknesses below $20\ \mu\text{m}$ are more susceptible to aging effects, signal noise, and colours quality degradation.

In this study, a clear TLC layer of a thickness of 30-50 microns was used. TLC layer thickness has a significant impact on the colours intensity. TLC coatings thinner than 10 microns degrade the intensities of the displayed colours and may cause noise to occur in the data.

2.4.4. Bandwidth

When the bandwidth of TLC is widened, the colour change sensitivity decreases, resulting in data noise, aging effect, hysteresis effect, and lower accuracy[69]. Narrow band crystals are not as affected as wide bandwidth by viewing angle[75]. Utilizing narrowband TLCs, which typically have bandwidths between 0.5 and 4 °C, is the simplest method of minimizing illumination disturbances. The narrow-band TLCs have been extensively used by numerous researchers[74][76][77] as a result of the fact that their calibrations are less influenced by variations in viewing angle and illumination intensity, as well as reflections that produce disturbance.

In light of this, it can be concluded that the technique is highly sensitive to environmental and boundary conditions. Hence, it is essential to handle Thin Layer Chromatography (TLC) with delicacy as its outcomes can be significantly influenced.

2.5. RGB and HSI colour Systems

Based on the changes in colour in the TLC layer, two different methods could be adopted to evaluate the temperature over the target surface. RGB method is associated with the red, green and blue intensity curves, while the

other method is associated with the hue value associated with the HSI model of colour. HSI stands for Hue, Saturation and Intensity. The RGB and HIS techniques will be discussed after the two colour systems have been briefly described.

RGB, which stands for red, green and blue light, is an additive system of colours in which all the other colours are formed by the addition of the these three. There is not an easy way to directly associate the colour information with temperature values. However, the peak intensities obtained from the intensity colour curves for the colour band can be associated with specific temperatures.

On the other hand, the term HSI refers to hue saturation and intensity. Considering that the interest in this experiment lies in determining the surface temperature, out of these three parameters, the hue value only would be used. Hue values for individual pixels indicate the surface temperature at the corresponding point. Due to the hue's characteristics, it can be used as a thermometer [78]. A calibration process [79] generates the hue curve, which shows the temperature on the target surface the TLC coated layer changes its colour.

In the case of the three-temperature problem (hot fluid temperature, initial temperature and wall temperature), two approaches have been proposed: by using the peak values from the intensity curves in the RGB colour model, alternatively, the full hue curve that can be gained from the HSI colour model.

Typical calibration results from both methods are presented in Figure 2.9. The RGB intensity method analyses the entire surface based on only the peak

values of each of the component colours. For the hue method, the hue curve may vary from point to point according to the surface temperature.

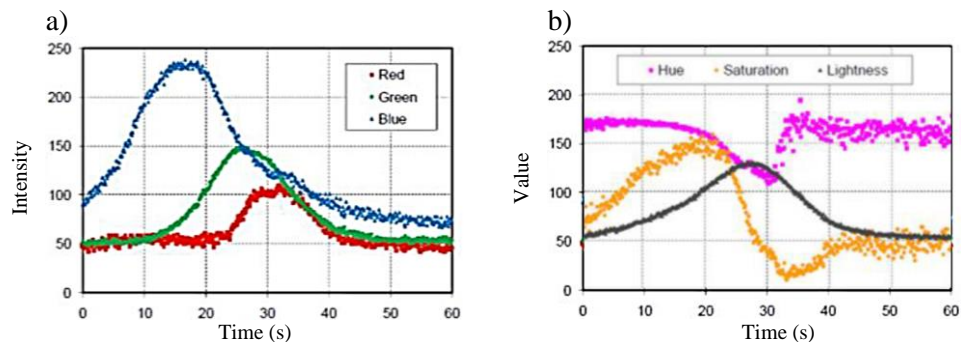


Figure 2.9 TLC calibration techniques outputs: a)RGB, and b) HSI

A previous study compared both approaches[80]. Based on a RGB colour model, the peak intensities that were obtained were more stable than those obtained from a hue curve. Accordingly, RGB method has been adapted in this study. As described in the following chapters, two variants of the method were tested.

2.6. Summary

The literature review chapter provides a comprehensive overview of single and multiple jet impingement techniques, and the effect of different parameters on heat transfer distribution. The limitations of conventional jet impingement techniques are discussed, including difficulty achieving uniform heat transfer due to crossflow. The use of multiple jets as a potential solution is noted, but with drawbacks such as increasing spacing distance and decreasing internal heat transfer area.

The literature review identifies a research gap in the need for a novel design that can overcome the limitations of conventional jet impingement techniques and proposes the use of reverse jet impingement. Advantages of this technique, such as overcoming cross-flow, reducing spacing distance between adjacent jets, and increasing internal heat transfer area are highlighted. The current study aims to contribute to the field by investigating the experimental and numerical heat transfer characteristics of reverse jet impingement and developing a prediction model to optimize design parameters for various applications.

Chapter 3. Experimental Methodology

3.1. Introduction

As aforementioned earlier in Chapter one, gas turbine blades depend heavily on cooling systems in order to function properly at operating temperatures above melting point. It is imperative that heat transfer coefficients be accurately determined in order to achieve accurate metal temperature prediction and cooling effectiveness. Experiments are essential in determining surface heat transfer coefficients. The cooling design process in the gas turbine industry is heavily based on correlations obtained by experiments that cover a large range of parameters and particular design aspects. Early techniques used thermocouples on thin-foil heaters to measure the coefficient of surface heat transfer and calculate it according to the equation presented below[81],[82]. In this case, the calculated heat transfer coefficient is the area-averaged coefficient of heat transfer. A staggered pin-fin matrix with various pin height to diameter ratios was measured using this technique by Brigham[81] and Vanfossen[82].

$$h = \frac{\dot{q}}{A. (T_w - T_f)} = \frac{\dot{q}_{gen} - \dot{q}_{loss}}{A. (T_w - T_f)} \quad \text{Equation 3.1}$$

Over time, mass-transfer analogies, such as the naphthalene sublimation method, became available to measure both local and averaged heat transfer coefficients on end-wall surfaces but without incorporating heat loss and axial conduction effects. Incropera and DeWitt[83] explain the principle of mass transfer analogy techniques, and Han et al.[3] provide examples of their use in heat transfer study on gas turbines.

In this project, transient liquid crystal thermography technique was used to measure heat transfer. Thermochromic liquid crystals are organic molecules that change colour with temperature. The molecules in these materials have a twisted molecular structure and exhibit an optical property in which they selectively reflect different colours when exposed to temperature changes. At a particular temperature, only one wavelength component is reflected. As a result, this phenomenon is called thermochromic. Liquid crystals are supplied in a microencapsulated form, providing a capsule with a diameter of approximately 5-30 microns, which protects the crystals and extends their useful life. A detailed description of liquid crystal's chemical and physical properties is provided by LCR Hallcrest[84].

3.2. Transient Liquid Crystal Thermography Technique

In general, thermochromic liquid crystal can be used in two ways to obtain heat transfer coefficient. The first is a steady state method, which uses liquid crystals to detect local heat transfer coefficients on the surface of a heater foil. 3-1. This method has been applied in various experimental setups as in the References [85][86]. An alternative method is the transient method which uses a semi-infinite solid model in 1D to calculate heat transfer coefficients[83]. A sudden change in temperature imposed on a test surface has been shown to induce transient 1D conduction within semi-infinite solids, as reported by Incropera and DeWitt[83]. In this instance of 1D conduction, Fourier's law is applicable where

$$\frac{\partial T}{\partial t} = \alpha \frac{\partial^2 T}{\partial x^2} \quad \text{Equation 3.2}$$

Initial condition,

$$\text{At } t = 0, \quad T(x,0) = T_i$$

Boundary condition,

$$\text{At } x = 0, \quad -k \left(\frac{dT}{dx} \right) = h(T_w - T_f)$$

A constant temperature flow was suddenly applied to the surface. However, the initial temperature did not change at an infinite distance from the surface.

$$\text{At } x \rightarrow \infty, \quad T(\infty, t) = T_i$$

The solution of the Fourier equation is given by Clifford et al.[87]

$$\frac{T_w - T_i}{T_f - T_i} = 1 - \exp\left(h^2 \cdot \frac{t_{LC}}{\rho \cdot C_p \cdot k}\right) \cdot \text{erfc}\left(h \cdot \sqrt{\frac{t_{LC}}{\rho \cdot C_p \cdot k}}\right) \quad \text{Equation 3.3}$$

It was stated by Simonich and Moffat [87] that the equation needs to be modified with the help of superposition and Duhamel's theorem, as ideal step-change in air temperature is not achievable in practice. As a consequence of the Duhamel theorem, Equation 3.7 becomes

$$T_w - T_i = \sum_{i=1}^N \left[(T_{f,i} - T_{f,i-1}) \left[1 - \exp\left(h^2 \cdot \frac{t_{LC} - t_i}{\rho \cdot C_p \cdot k}\right) \cdot \text{erfc}\left(h \cdot \sqrt{\frac{t_{LC} - t_i}{\rho \cdot C_p \cdot k}}\right) \right] \right]$$

$$\text{Equation 3.4}$$

To determine wall temperature, a single colour such as green or red is used because these two colours are easily recognizable. In a liquid crystal colour display, Camci et al[88] have found that the hue value of colour is typically

monotonic with temperature as a function of the temperature range. The calibration process will be described in detail in the following section.

In this project, transient liquid crystal technique combined with maximum green colour intensity calibration method mentioned by Terzis et al.[89] is adopted. The heat transfer coefficient can be found by solving Equation 3.8. Calibration of maximum green intensity to temperature has been performed and is presented in 3.3. All test specimens are made from Plexiglas, whose thermal properties are listed in Table 3.1. Due to Plexiglas's low thermal conductivity, the semi-infinite solid model can be used for a definite period of time before thermal pulses penetrate the wall.

$$t \leq \frac{\delta^2}{4\alpha} \quad \text{Equation 3.5}$$

Where t represents the experiment duration, δ represents the wall thickness and α represents the wall material thermal diffusivity. The test sections have different thicknesses but the smallest thickness is 10mm to extend the experiment duration to 3.5 minutes to keep the semi-infinite assumption unviolated.

Table 3.1 physical and thermal properties of acrylic Perspex

Property	
Thickness, δ	≥ 0.01
Density, ρ	1100 kg/m ³
Specific Heat, C_p	1470 J/K.kg
Thermal Conductivity, k	0.19 W/m.K
Thermal Diffusivity, α	1.175e ⁻⁷ m ² /s

The experimental setup and procedures for transient liquid crystal are described in Sections 3.4. Finally, data reduction will be discussed in Section 3.5 with parameters used in this project.

3.3. Calibration

Liquid crystals that are temperature sensitive are widely used in a variety of applications. Among these are improving the transient liquid crystal experimental techniques (Baughn[90], Ireland and Jones.[91] and Wang *et al.*[92]) image processing techniques (Abu Talib *et al.*[93], Wang *et al.*[94] and Wilson *et al.*[95]), liquid crystal calibration techniques (Chan *et al.*[96], Hay and Hollingsworth[97], and Camci *et al.*[88]) and data reduction techniques (Chen *et al.*[98]). A narrow band TLC was used in this study experimental work as well as a single colour peak intensity calibration technique to mark the temperature over the target surface then calculating heat transfer coefficients.

When a sudden change in fluid temperature is applied to the test section, the TLC coating is used to observe the delayed surface temperature response with a high speed digital colour camera, as illustrated in Figure 3.1.

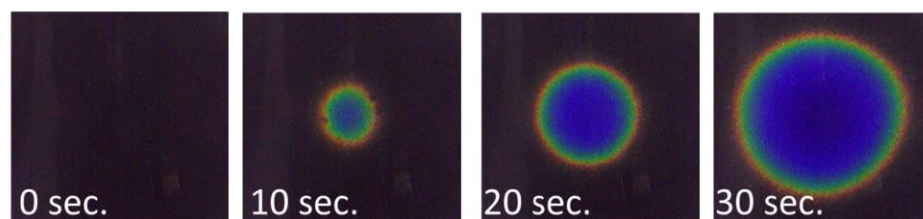


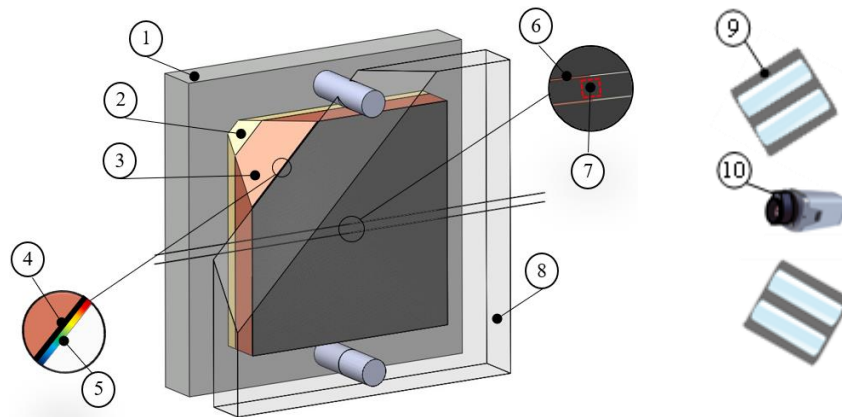
Figure 3.1 Representative development of jet impingement target liquid crystal response over time

The wall temperature can be indirectly measured with the use of thermochromic liquid crystals. This method was developed as a result of an understanding of the relationship between the temperature and a distinct indication event of the TLC. An indication event is produced when a liquid crystal is heated to a particular temperature within a certain range of temperature and is able to gradually exhibit all colours of the visible spectrum. TLC with an activation temperature of 37 °C and a bandwidth of 2 °C (from red colour start to blue colour start) has been used in this project. A sprayable TLC type R37C2W was purchased from Hallcrest Ltd.

For TLC calibration, there are two main techniques. First, Hue method is adapted from the HSI colour model, and it is based on hue value. Second, the methods of maximum intensity based on RGB camera channels. Previous studies have shown that using the maximum green intensity method, the heat transfer coefficient calculation results are less sensitive to illumination and view angle[99].

Figure 3.2 presents a schematic of the calibration setup. The test model used for the calibration is made of a copper plate painted with black backing paint then coated with a film layer of TLC. Two T-type thermocouples, butt-welded bare wire 0.075mm diameter, were mounted over the copper plate with 3mm separation distance between each other. An acrylic sheet cover the TLC to replicate test conditions. The calibration process was relatively simple. The copper plate was slowly heated to increase the temperature of the TLC coated face uniformly to the colour play temperature range of the TLC. About 2 °C before the TLC activation temperature, pictures recording is started at intervals of 500ms. The calibration process ends after watching all the TLC colour play.

Then, the recorded pictures are chromatically analysed only inside the area of interest. The area of interest is about 3mm x 3mm in the middle of the copper plate and between the two thermocouples thermocouple junctions. temperature was taken as the average between thermocouples.



1- Substrate 2- Electric heater 3- Copper plate 4- Black coating 5- Liquid crystals layer 6- T-type thermocouple 7- Area of interest 8- Acrylic sheet 9- Lighting unit 10- Camera

Figure 3.2 Schematic diagram of the liquid crystal calibration apparatus

In Figure 3.3, the RGB channels are demonstrated. Since Green channel provides maximum intensity at a certain temperature, it is used in calibrating the TLC.

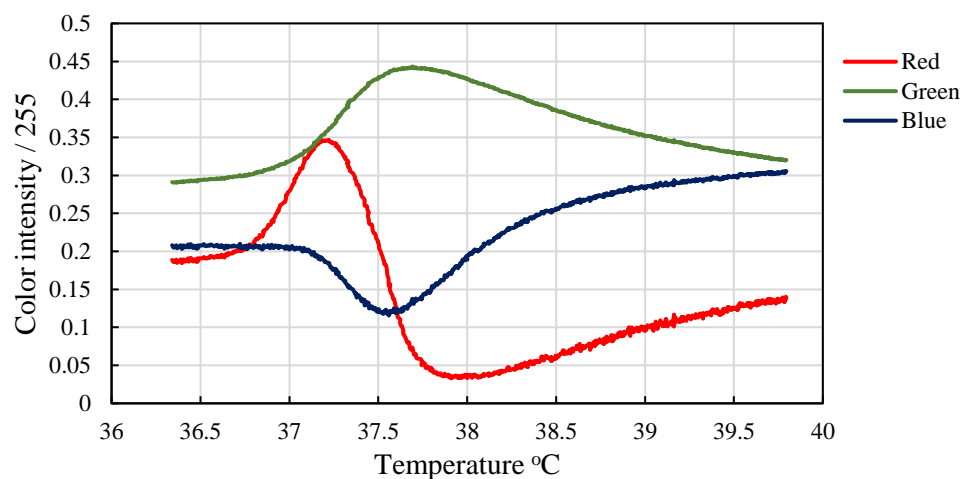


Figure 3.3 Calibration of Liquid Crystals type R37C2W

The majority of the test sections have a curved surface, such as dimples and cylinders. So it is not easy to achieve a uniform light intensity over the rest section. Therefore, it is imperative to ensure that TLC maximum green colour intensity temperature is not affected by the variation of the lighting intensity, as shown in Figure 3.4.

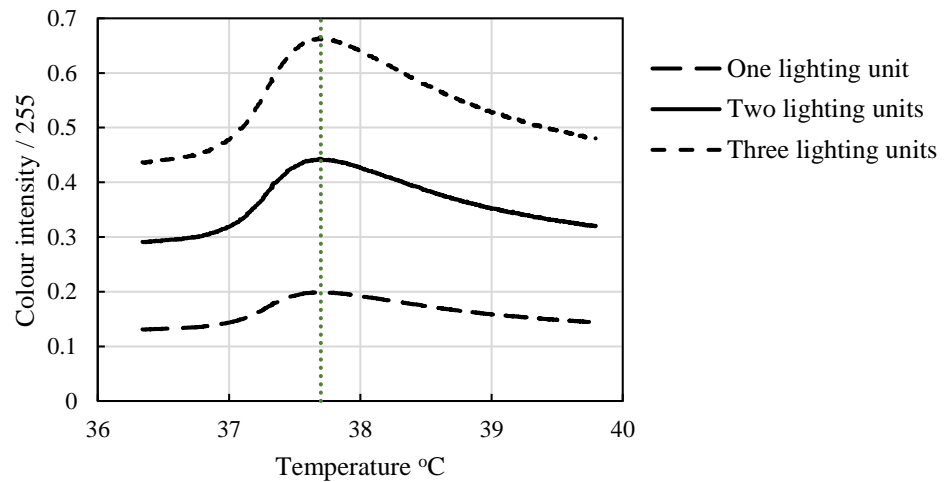


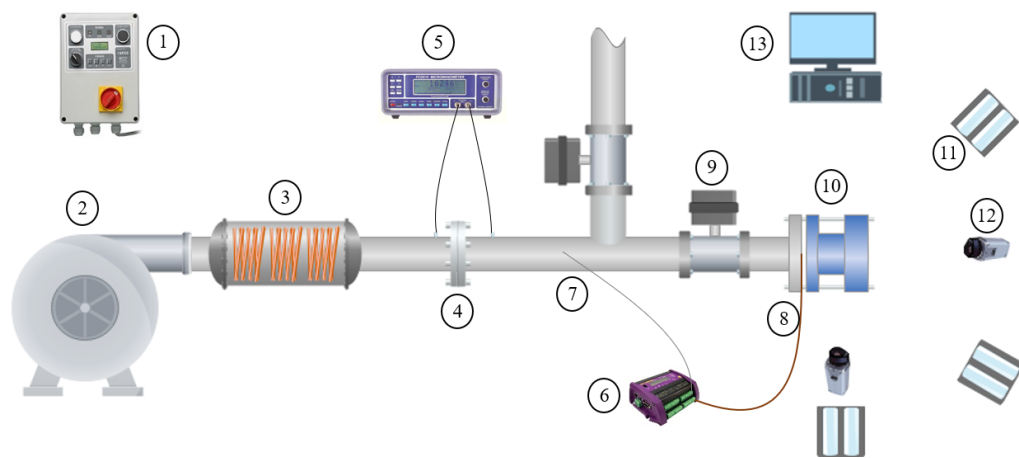
Figure 3.4 Effect of the lighting conditions on the green colour intensity

3.4. Experiment Setup and procedure

3.4.1. Experiment setup

A schematic layout of the experimental apparatus is shown in Figure 3.5. Inlet air is supplied by a 5.5kW blower, with motor inverter for blower speed control. Air flow from air blower is then ducted through three 2kW inline heaters for heat addition. An ISO5167 standard sharp edged orifice plate is installed at 20D downstream of the heater to ensure developed flow[100]. The orifice and the pipe diameters were 45mm and 90mm, respectively. Pressure values are obtained using a micro manometer, and pressure difference is utilised to obtain accurate mass flow conditions. Following the orifice plate, a

3-wire platinum thermal resistance meter is installed to monitor air temperature for determining air properties when mass flow rate through orifice plate is calculated as well as observing when air temperature becomes steady. At a location $6D$ downstream of orifice plate, a bypass (T-junction) is connected and controlled by two fast-action pneumatic valves. The T-junction and pneumatic valve assembly enable the incoming flow to divert between either exhaust ducting during heating up the air, or into test section when the temperature of the heated air becomes stable. For all test sections, there is a T-type thermocouples, butt-welded bare wire 0.075mm diameter, mounted over every single nozzle, whereas the thermocouple junction is located at the nozzle outlet centre.



- | | | |
|------------------------|----------------------------|--------------------|
| 1- Motor control panel | 6- Data acquisition system | 10- Test section |
| 2- Air blower | 7- RTD | 11- Lighting unite |
| 3- Electric heaters | 8-Thermo-couple | 12- Camera |
| 4- Orifice meter | 9- Pneumatic valves | 13- Computer |
| 5- Micro-manometer | | |

Figure 3.5 Jet impingement cooling test rig

While the rotation effect is an important consideration in gas turbine blade cooling design[101], it has been neglected in this study for several reasons. One reason is that neglecting the rotation effect simplifies the used test rig. Additionally, focusing on evaluating the cooling techniques or geometries, and neglecting the rotation effect can help isolate the effects of these factors.

For use of a semi-infinite model, a requirement of sudden temperature change against the test surface must be satisfied. Initially, flow is diverted away from test rig, and out of the laboratory whilst being heated until a steady state temperature. A variable speed motor controls pressure drop through the orifice meter to ensure an equivalent mass flow to the specific geometry section being tested. After the continuous air flow reaches the steady desired temperature, giving signal to the valves, they react within 0.3-0.4 seconds to divert the flow into the test section, satisfying the step-change temperature condition. A 20-40micron TLC layer is present on the target plate, then coated in an additional 40microns of black backing coating to ensure visibility of the TLC activation. As the model surface temperature changed, the transient wall temperature manifests as a local activation and transition of the TLC colour bands. The camera is installed and focused on the target surface. Accurate and coordinated measurement of air temperature and the colour change time response is very important key to reliable data.

3.4.2. Experimental procedure

Transient liquid crystal technique works by applying a sudden temperature change to the surface, creating a transient condition where the temperature changes rapidly. As the temperature changes, the liquid crystal coating responds by changing colour, and the resulting colour pattern can be captured using a camera. The colour pattern can then be analysed to determine the temperature distribution on the surface. These experimental procedures were also considered in this study.

1. Turning on the blower and increasing the blower speed until getting the desired mass flow rate.
2. Turning on the electric heaters, the number of used electric heaters depends on the required air temperature.
3. Adjusting the lighting units and the camera(s) settings.
4. When the air temperature becomes stable, activate the camera and start temperature recording of the nozzle thermocouples.
5. Altering the direction of the airflow through actuating the pneumatic valves to direct the flow of heated air towards the designated test section.
6. Waiting until the blue colour covers the test section surface entirely, then stop camera and thermocouples recording.
7. Actuating the pneumatic valves in order to redirect the flow of heated air to outside the laboratory room.
8. Turning off the electric heaters and the lighting units.
9. Waiting until the air cool down around 40 °C and then turning off the blower.

3.5. Data Reduction

Calculating the mass flow rate of air passing through the above-mentioned orifice plate by:

$$\dot{m} = \frac{\pi}{4} \cdot C_d \cdot \varepsilon \cdot d^2 \cdot \sqrt{\frac{2 \cdot \rho \cdot \Delta P}{1 - \beta^4}} \quad \text{Equation 3.6}$$

In the following equation, P is the pressure difference as determined by a manometer, and β is the geometric diameter ratio of 0.4994 (D/d, duct diameter divided by opening size). ε is the expansibility factor for air, which is 1, for the incompressible fluid in this instance. Based on the Stolz equation as dictated by ISO-5167[102], C_d is the discharge coefficient of the orifice plate

$$C_d = 0.5959 + 0.312 \cdot \beta^{2.1} - 0.015839 \cdot \beta^3 - 0.184 \cdot \beta^8 + 0.0029 \cdot \beta^{2.5} \cdot \left(\frac{10^6}{Re}\right)^{0.75} + \frac{0.039 \cdot \beta^4}{1 - \beta^4} \quad \text{Equation 3.7}$$

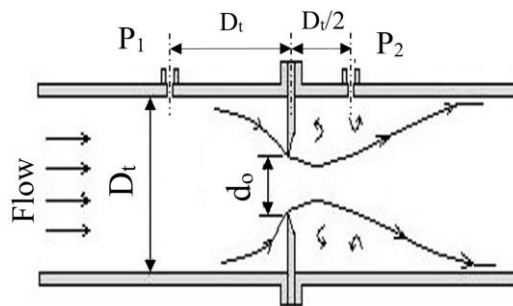


Figure 3.6: Orifice meter schematic diagram

Equation 3.9 denotes the Reynolds number at the orifice plate determined by the diameter of the orifice plate. A previous PhD student at GTHTL in Nottingham calibrated the orifice plate[103]. Reynolds number is commonly calculated as follows:

$$Re = \frac{\rho \cdot \bar{V} \cdot d}{\mu} \quad \text{Equation 3.8}$$

Assuming that \bar{V} is the mean velocity across channel flow cross-sections and D is the hydraulic diameter. This study utilizes mass flow rate to determine the Re number. Consequently, the Re number changes as follows:

$$Re = \frac{4 \cdot \dot{m}}{\pi \cdot d \cdot \mu} \quad \text{Equation 3.9}$$

For the channel cross-section, \dot{m} is the mass flow rate.

Furthermore, the heat transfer coefficient will be shown as a Nusselt number. Nusselt number is defined as follows:

$$Nu = \frac{h \cdot d}{k} \quad \text{Equation 3.10}$$

3.6. Summary

Chapter 3 outlines the experimental methodology employed in this study. The chapter begins with an introduction and proceeds to provide an in-depth description of the transient liquid crystal thermography technique used to collect data. The calibration process is also presented in detail to ensure precise and reliable data collection. Moreover, the experiment setup and procedure are comprehensively explained, including the hardware and instrumentation used, as well as a detailed account of the experimental procedure. Finally, the chapter concludes with a discussion of the data reduction process, which involves converting raw data into meaningful results. The implementation of these techniques enables accurate data collection, facilitating further analysis and interpretation. Overall, this chapter offers a meticulous account of the

experimental methodology, which serves as the cornerstone of the subsequent chapters in this thesis.

Chapter 4. Single Reverse Jet Impingement

This chapter presents the results of the experimental investigation of single reverse jet impingement, which is a common cooling technique used in many engineering applications. The chapter begins with a detailed description of the test section used for the study, including the hardware and instrumentation employed. Subsequently, the chapter presents the results and discussions, focusing on four key factors that affect the performance of the cooling technique: the recovery factor, nozzle-to-target effect, Reynold number effect, and discharge coefficient. The results of each factor are analysed and discussed in-depth to provide insights into the effectiveness of the cooling technique. The chapter also includes an uncertainty analysis to evaluate the reliability of the results obtained. Overall, this chapter provides valuable insights into the performance of single reverse jet impingement and contributes to the broader understanding of cooling techniques in engineering applications.

4.1. Test section

Figure 4.1 shows two primary variations of geometry tested in the present study, i.e. flat and reverse impinging targets. In both configurations, the nozzle diameter, d , remains constant. Radial target surface distance from the jet stagnation point, s , is shown. The nozzle-to-target spacing, H , is the distance between the nozzle exit and the stagnation point. Figure 4.1a shows the flat plate geometry. Figure 4.1b shows the reverse jet impingement geometry, where the target geometry is made up of a ‘dimple’ surface of diameter D , and a cylindrical tube height H_{cy} .

Where, $D/2$ is the vertical distance from stagnation target to cylinder wall start, and H_{ex} is the vertical height of exit gap for the spent flow. During this study H_{ex} equals one nozzle diameter, and D equals 3.2 nozzle diameters, therefore, to maintain the ‘dimple’ geometry, a minimum H/d condition is set at 2.6. H_{ex} and D are constants throughout the experimental work. Accordingly, H change is regulated by H_{cy} change.

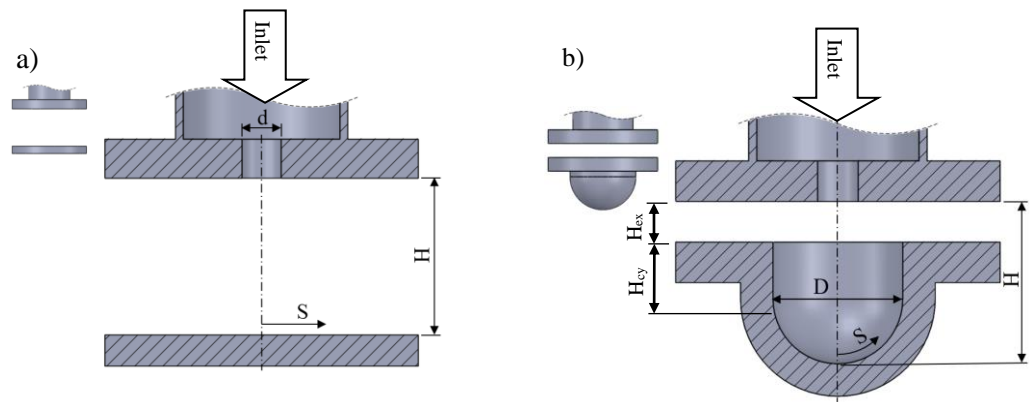


Figure 4.1 Diagram of jet and target plate: a) Flat target and b) Reverse target $H/d = 4$

4.2. Results and discussions

Figure 4.2 shows the temperature step taken from nozzle exit. Transient analysis shows that the temperature step was fast enough relative to the first liquid crystal activation ($\sim 30s$), and hence, no correction for Duhamel’s principle or thermocouple thermal inertia is necessary[104].

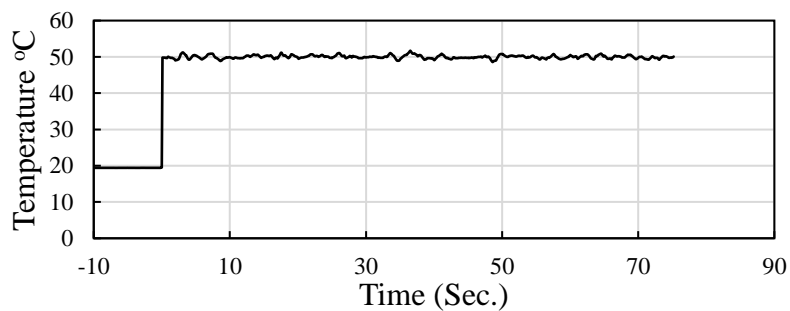


Figure 4.2 Temperature response at the nozzle exit centre during a transient heat transfer test

Figure 4.3 shows the nozzle exit temperature profile which was measured by using a very fine thermocouple. The temperature is normalised by the maximum jet temperature $T_{j,max}$ and the initial wall temperature T_i . The results for two different Reynolds numbers, 23,000 and 50,000, fall into the same profile. The maximum temperature appears at the jet centre. It is apparent that some heat transfer occurs between hot air before the nozzle and the relatively cool ambient air, through the pipe wall. This conduction tends to cool the hot air boundary layer as it flows toward the nozzle plate.

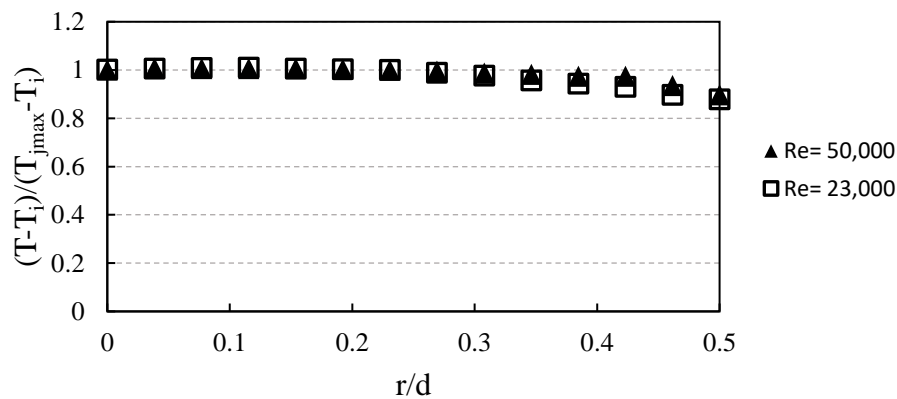


Figure 4.3 Temperature profile at the nozzle exit

4.2.1. Recovery factor

Popiel et al. [9] employed a heated jet with an ambient temperature plate in contrast to most previous studies of impinging jet heat transfer. For the incompressible flow, whether the plate is heated or cooled with respect to the jet temperature, the heat transfer characteristics remain the same. There exist two cases of the surrounding fluid temperatures: one when it is equal to the temperature of the jet, and another when it is equal to the temperature of the plate. In both cases, the heat transfer distributions were different. It was noted that the surrounding fluid was entrained into the jet when the jet impinged on

the plate. As a result of the thermal entrainment, the distribution of temperature in the jet is altered which affect the heat transfer between the impinging jet and the target plate. Several experiments and analytical studies have been conducted on the thermal entrainment effect on impinging jet heat transfer [105][106].

According to them, entrainment is an inherent characteristic of all jets, including the ambient temperature jets with heated plates. Goldstein et al. [106] concluded that when the local recovery temperature is used as the reference temperature in the definition of the heat transfer coefficient, the heat transfer coefficient is independent of the relative magnitudes of nozzle exit temperature and ambient temperature. Consequently, heat transfer coefficients for jet impingement at ambient temperatures, which have been extensively investigated, can be used for jets at temperatures other than the ambient fluid temperature provided that the adiabatic wall temperature of the surrounding fluid is known.

Figure 4.4 shows the results of transient temperature measurements when the heated jet is suddenly allowed to impinge on the plate. Temperatures are measured through 12 T-type thermocouples of 0.2mm diameter at 12 separate radial locations from the stagnation point, each at a discrete circumferential distance. Figure 4.4 demonstrates the temperature step for these thermocouples at $Re = 50,000$ and $H/d = 4$. Each temperature profile shows a nearly logarithmic increase in time. Eliminating the surrounding air entrainment in the reverse target helped to achieve stability and higher recovery factor than the flat target.

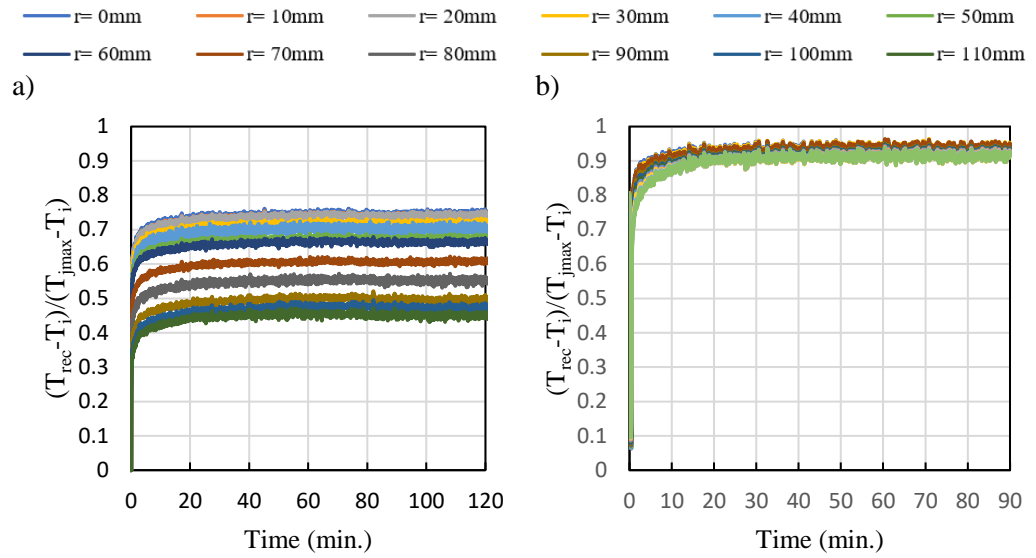


Figure 4.4 Wall temperature history at different 12 radial locations starting from the stagnation point at $Re = 50,000$ and $H/d=4$: a) Flat target and b) Reverse target

The recovery temperature radial distributions are shown in Figure 4.5 for Reynolds number 30,000 and different nozzle-to-target spacing distances. The adiabatic steady-state condition has been achieved after 60 minutes and 30 minutes for the flat target and the reverse target, respectively. For the flat target, the recovery factor decreases with increasing the nozzle-to-plate distance or at large radial distances from the stagnation point as a result of increasing the room air entrainment as shown in Figure 4.5a. While in case of the reverse geometry, the recovery factor does not depend on the nozzle-to-target spacing distance as well as the recovery factor higher than 90%.

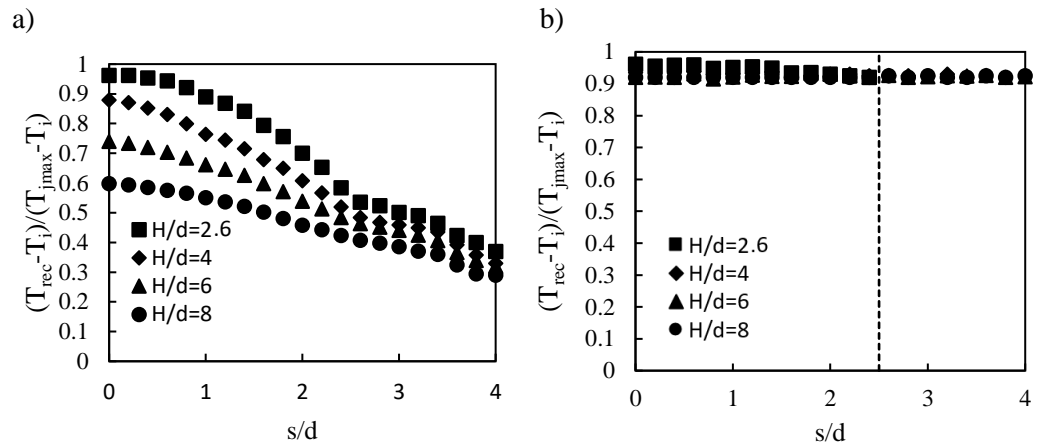


Figure 4.5 Radial distribution of recovery temperature: a) Flat target and b) Reverse target

4.2.2. Nozzle-to-target effect

To analyse the effects of the novel reverse jet impingement geometry on heat transfer distribution, four different nozzle-to-plate distances (i.e. $H/d = 2.6, 4, 6,$ and 8), at a jet Reynolds number of $23,000$ are compared with a flat plate target, as shown in Figure 4.6 a and b. Figure 4.6 compares the Nusselt number distribution from the point of stagnation to a distance of 2.5 nozzle diameters. This methodology is intended to provide a direct comparison for the heat transfer within this ‘dimple’ section, but negates any additional heat transfer resulting from extended ‘reverse jet’ cylinder walls. Nusselt number distribution over the reverse jet cylinder is shown in Ahmed et al. [107].

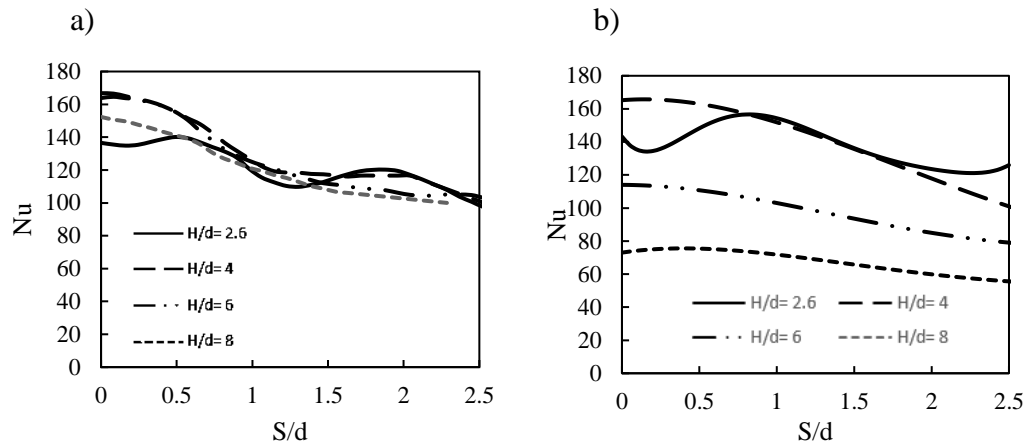


Figure 4.6 Nusselt number distribution at $Re=23,000$ and $D/d=2.6, 4, 6$ and 8

Significant variation in Nusselt number distribution and magnitude area seen between the flat and the reverse targets. Figure 4.6a shows the effect of H/d on the flat geometry, and whilst variation in Nu distribution profile vary, there is relatively little change in magnitude. When studying the equivalent Nu distributions for the reverse jet geometry, Figure 4.6b shows that for $H/d = 2.6$ and 4 the changes are also mainly apparent in the Nusselt number distribution profile, but for $H/d = 6$ and 8 there is an obvious reduction in the magnitude of Nu number distribution.

The overall Nusselt number show only minimal variation with radial distance, due to the nondimensionalisation effect of the recovery temperature. Nusselt numbers decrease monotonically along the radial direction with the maximum at stagnation point for long nozzle to-plate distance, $H/D = 6$ and 8 . For $H/D = 4$, the second maximum in Nusselt number appears around two diameters away from the stagnation point. Amano [108] attributed the second peak to high near wall turbulent kinetic energy around $r/D = 2$. The high near wall turbulent intensity at $r/D = 2$, is also shown in Figure 4.6. Sparrow et al. [109] attributed this to transition from laminar to turbulent boundary layer.

When an impinging jet is targeted at a dimple surface, it is recognised that after the wall jet exits the dimple, there is an opening and sharp turn in the flow, this causes acceleration and an eddy to form, this effect is significant enough to cause the increase in local Nu, and is the phenomena which drives the unique heat transfer enhancement seen in Figure 4.6b for $H/d = 2.6$, at location $S/d = 2.5$. This effect is not seen for the larger H/d ranges, as the wall has a transition to the reverse jet cylinder walls.

Figure 4.7a shows the Nusselt number at the stagnation point for both the flat and reverse targets with nozzle-to-plate distances, $H/d = 2.6, 4, 6, 8$, and Reynolds number, $Re = 23,000$. Stagnation Nusselt number values for $H/d = 2.6$ and 4 are almost identical for both the flat and reverse jet targets. However, for nozzle-to-plate spacing, $H/d > 4$, there is an exponential decrease in the stagnation point Nusselt number for the reverse target relative to the flat target. As it is expected that the jet potential core length in case of the reverse jet impingement is about 4 nozzle diameters.

Figure 4.7b depicts the mean Nusselt number observed across the entire surface area of the "dimple". The findings suggest that the influence of the nozzle-to-target distance on the heat transfer averaged over the surface of a flat target is minimal.

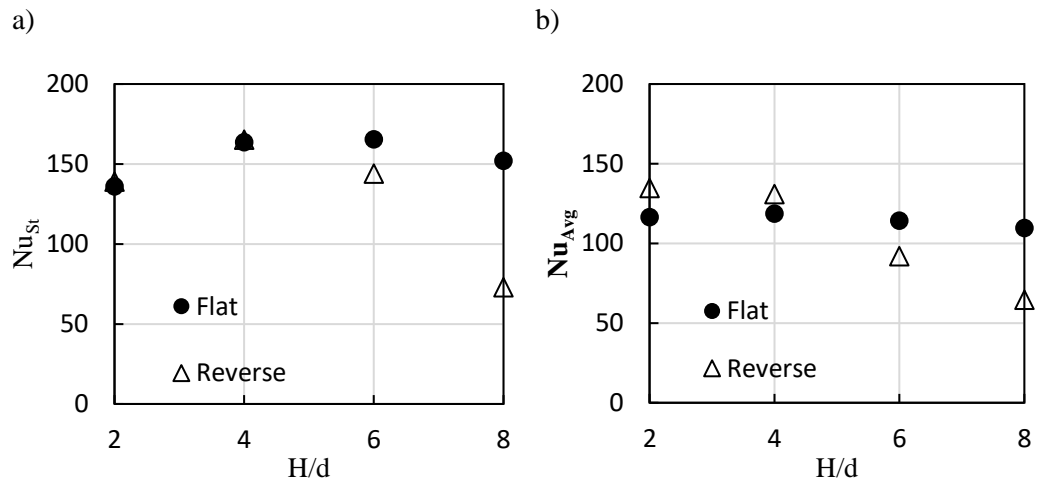


Figure 4.7 Nusselt number comparison between flat and reverse surface: a) Nusselt number at the stagnation point, b) Average Nusselt number

At $H/d < 6$ the area weighted average Nusselt number for the reverse target is higher than of the flat target. At $H/d = 6$ the area weighted average Nusselt number for the reverse target is almost identical to the flat target area weighted average Nusselt number. Whilst at $H/d > 6$ the area average Nusselt number for the reverse target starts to decrease sharply relative to the flat target area weighted average Nusselt number. In the next Chapter 7 the CFD work will help in interpreting the sharp decrease in the area average Nusselt number for the reverse impingement by presenting the flow mechanics.

4.2.3. Reynold number effect

Nusselt number variation over a Reynolds number range, $Re = 30,000 - 60,000$, is shown in Figure 4.8. As seen in other jet impingement cooling schemes, Nusselt number is proportional to Reynolds number ($Nu_{st} = c \cdot Re^m$). based on the presented data the Reynolds number m exponent equals 0.51.

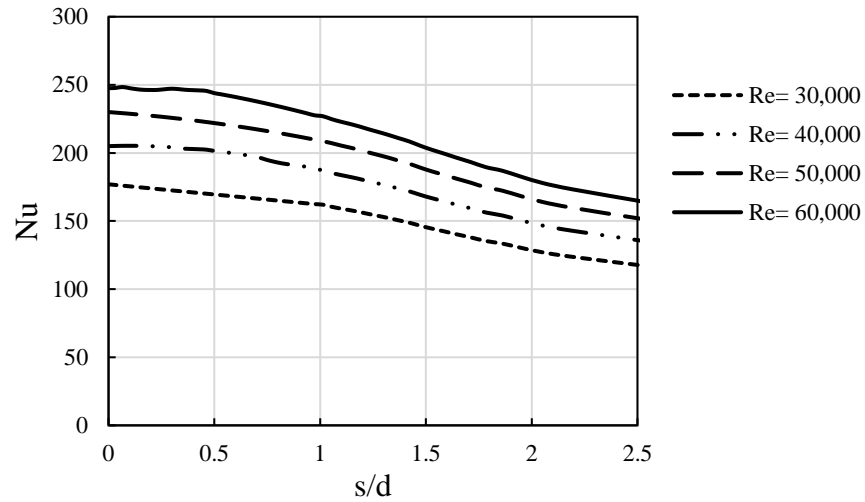


Figure 4.8 Nusselt number distribution over dimpled surface at different Reynolds numbers, $H/d = 4$

4.2.4. Discharge coefficient

Discharge coefficient for varying target configurations, and a wide range of Reynolds number ($Re=20,000-60,000$) is demonstrated in Figure 4.9. The discharge coefficients for all geometry variations have the same trend. The discharge coefficient of the flat plate is also very similar in magnitude to the free jet. The discharge coefficient values for the reverse impingement are less than the flat plate by a range of 0.01-0.02, and values for the independent dimple result in the lowest recovery, on average 0.03-0.04 lower.

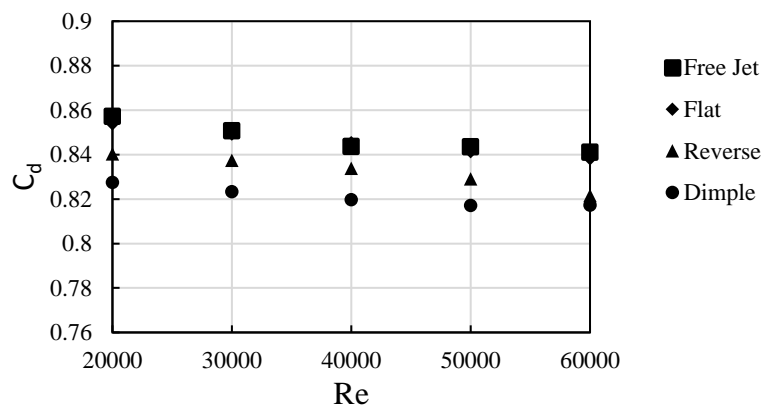


Figure 4.9 Discharge coefficient for free jet, flat impingement and reverse impingement at $H/d = 6$

Figure 4.10 shows the effect of the nozzle-to-plate distance on the discharge coefficient for just the reverse impingement over the same Reynolds range as Figure 4.9, but with variation in H/d . The discharge coefficient values for the reverse impingement at $H/d= 8$ and 6 are the comparable, but the discharge coefficients for $H/d= 4$ and 2.6 are lower by $0.01-0.02$ and $0.04-0.06$, respectively.

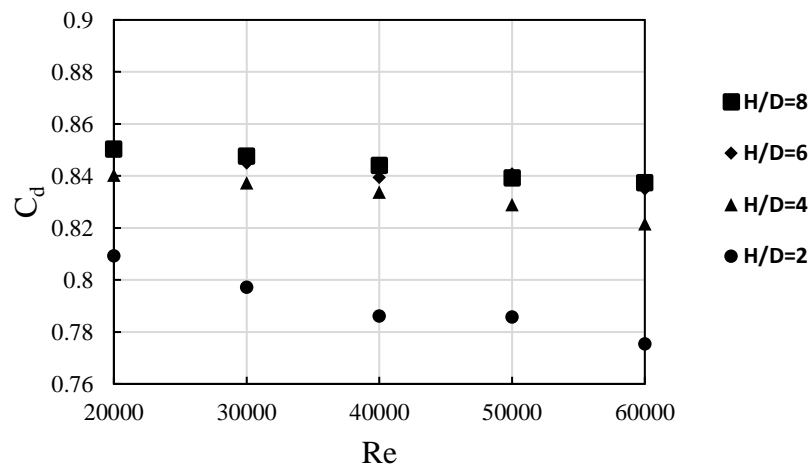


Figure 4.10 The discharge coefficient for reverse impingement at different Reynold numbers and nozzle-to-target distances

4.3. Uncertainty analysis

The heat transfer uncertainty calculations were based on 95% confidence levels according to Moffat [110]. For calculating the Nusselt number uncertainty, the individual uncertainty terms of the independent variables in Equation 3.3 have been combined using the Root-Sum-Square approach.

The formulation of the one-dimensional transient heat conduction equation for a semi-infinite plate can be expressed in the following manner by utilizing non-dimensional parameters:

$$\theta = 1 - e^{\beta^2} \operatorname{erfc}(\beta) \quad \text{Equation 4.1}$$

Where

$$\theta = \frac{T_w - T_i}{T_f - T_i}, \quad \beta = h \sqrt{\frac{t_{LC}}{b}} \quad \text{and} \quad b = \rho c k \quad \text{Equation 4.2}$$

According to Equation 3.3, the calculated heat transfer coefficient depends on the flow temperature, wall temperature, initial temperature, the activation time, and the thermal properties of the material in the model.

$$U_{\beta}^2 = \left(\frac{\partial \beta}{\partial \theta} U_{\theta} \right)^2 \quad \text{Equation 4.3}$$

$$U_{\theta}^2 = \left(\frac{\partial \theta}{\partial T_w} U_{T_w} \right)^2 + \left(\frac{\partial \theta}{\partial T_i} U_{T_i} \right)^2 + \left(\frac{\partial \theta}{\partial T_f} U_{T_f} \right)^2 \quad \text{Equation 4.4}$$

$$U_h^2 = \left(\frac{\partial h}{\partial \theta} U_{\theta} \right)^2 + \left(\frac{\partial h}{\partial T_w} U_{T_w} \right)^2 + \left(\frac{\partial h}{\partial b} U_b \right)^2 \quad \text{Equation 4.5}$$

The calculation of the heat transfer coefficient uncertainty (U_h) at a specific measurement point can be determined by substituting Equation 4.2, 4.3 and 4.4 into Equation 4.5:

$$U_h^2 = \left(\frac{\partial h}{\partial \theta} \right)^2 \left[\left(\frac{\partial \theta}{\partial T_w} U_{T_w} \right)^2 + \left(\frac{\partial \theta}{\partial T_i} U_{T_i} \right)^2 + \left(\frac{\partial \theta}{\partial T_f} U_{T_f} \right)^2 \right] + h^2 \left[\left(\frac{1}{2t_{LC}} U_{t_{LC}} \right)^2 + \left(\frac{1}{2b} U_b \right)^2 \right] \quad \text{Equation 4.6}$$

$$U_h^2 = \left(\frac{\partial h}{\partial \theta} \right)^2 \left[\left(\frac{1}{T_f - T_i} U_{T_w} \right)^2 + \left(\frac{T_w - T_f}{(T_f - T_i)^2} U_{T_i} \right)^2 + \left(\frac{T_w - T_i}{(T_f - T_i)^2} U_{T_f} \right)^2 \right] + h^2 \left[\left(\frac{1}{2t_{LC}} U_{t_{LC}} \right)^2 + \left(\frac{1}{2b} U_b \right)^2 \right] \quad \text{Equation 4.7}$$

Based on Equation 3.10, the Nusselt number depends on the heat transfer coefficient, characteristic length, and air thermal conductivity. Nevertheless, the uncertainties associated with the characteristic length and air thermal conductivity can be omitted from consideration, as their values are markedly smaller than the uncertainty attributed to the heat transfer coefficient. Consequently, the Nusselt number uncertainty may be expressed as follows:

$$U_{Nu} = \frac{l}{k} U_h \quad \text{Equation 4.8}$$

The uncertainties of the independent factors which affect the heat transfer coefficient calculation are the liquid crystal temperature ± 0.1 °C, the target initial temperature ± 0.2 °C, the hot air temperature ± 0.4 °C, the liquid crystals colour change time ± 0.1 S, and the thermal properties of the Perspex ± 28.8 J/m² °C S^{0.5}. By substituting all the above independent variables uncertainties in Equation 4.7, the relative uncertainty for the heat transfer coefficient and the Nusselt number equal 8.5% and 8.8%, respectively.

The Nusselt number uncertainty calculation for Equation 3.3 was previously performed. However, since this equation does not incorporate the velocity parameter, the calculated uncertainty does not account for the uncertainty associated with the Reynolds number. Hence, it is crucial to understand the relationship between the uncertainty of the Nusselt number and the uncertainty of the Reynolds number. The following correlation presents the Nusselt number as a function of Reynold number and nozzle-to-target spacing [111]:

$$Nu = 0.641Re^{0.566} \left(\frac{H}{d}\right)^{-0.078} \quad \text{Equation 4.9}$$

Assuming that the nozzle-to-target uncertainty is zero to determine to what extent the Reynold number uncertainty is significant for the Nusselt number uncertainty calculation.

$$U_{Nu} = \frac{\partial Nu}{\partial Re} U_{Re} = 0.363Re^{-0.444} \left(\frac{H}{d}\right)^{-0.078} U_{Re} \quad \text{Equation 4.10}$$

The uncertainty of Reynolds number has been calculated following the guidelines provided in ISO 5167-1[102] and ISO 5167-2 [112]. Reynold number uncertainty equals ± 500 at Reynold number 30,000 and nozzle-to-target spacing equals 6. By substituting in Equation 4.10, the relative uncertainty for the Nusselt number equals 0.9%.

By conducting a comparison between the two values of the calculated Nusselt number uncertainty, it is observed that despite the absence of the velocity parameter in the Equation 3.3, the resultant uncertainty is deemed acceptable. This is due to the negligible impact of Reynold number uncertainty on the Nusselt number uncertainty.

4.4. Summary

An experimental study was conducted to assess the effectiveness of a novel reverse jet impingement geometry and comparing the results with the flat target jet impingement, utilising the thermochromic liquid crystal technique. Overall, there is an enhancement of heat transfer uniformity to a dimple target surface, and additional heat transfer rate as the wall jet can transition to the ‘silo’ cylindrical wall. An optimum H/d was identified at $H/d = 4$, and Nusselt number was found to increase monotonically with Reynolds number. In addition to that the discharge coefficient is inversely proportional to the nozzle-to-target spacing distance. The calculated relative uncertainty of the Nusselt number is 8.6%.

Chapter 5. Row Reverse Jet Impingement

This chapter focuses on the use of row reverse jet impingement as a heat transfer enhancement technique. The chapter begins by describing the test section used for the experiments. This is followed by an in-depth discussion of the results and findings, which are presented in five sub-sections. The first sub-section examines the effect of nozzle-to-target spacing on heat transfer, while the second sub-section looks at the impact of Reynolds number. The third sub-section explores the influence of crossflow, while the fourth sub-section investigates the effect of nozzle configuration. The fifth and final sub-section analyses the discharge coefficient. The chapter concludes by summarizing the key findings and offering insights into the potential applications of row reverse jet impingement in heat transfer enhancement.

5.1. Test section

The modular test piece system has been developed to allow for multiple configurations of impingement geometry to be tested in a scaled, but realistic experimental simulation, as illustrated in Figure 5.1.

The test section comprises of an inlet from the fan and heater rig exit tube, into a large plenum. Within the plenum the pressure and temperature of the air will allow for a uniform flow through the extent of the test piece being investigated.

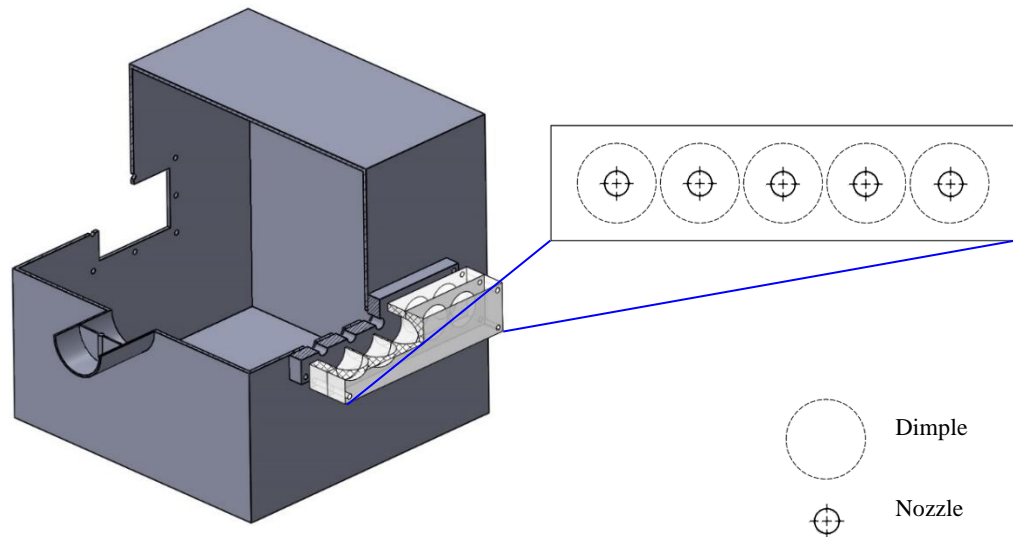


Figure 5.1 Sketch of row reverse jet impingement

The plenum is connected to a vent valve and the nozzles inlet is covered by a sliding locker. To ensure that the heated air temperature will remain hot especially at the beginning of running the test, the vent valve is opened and the sliding locker locks the nozzles inlet to scavenging the cold air from the plenum space and replacing it with hot air, as shown in Figure 5.2.

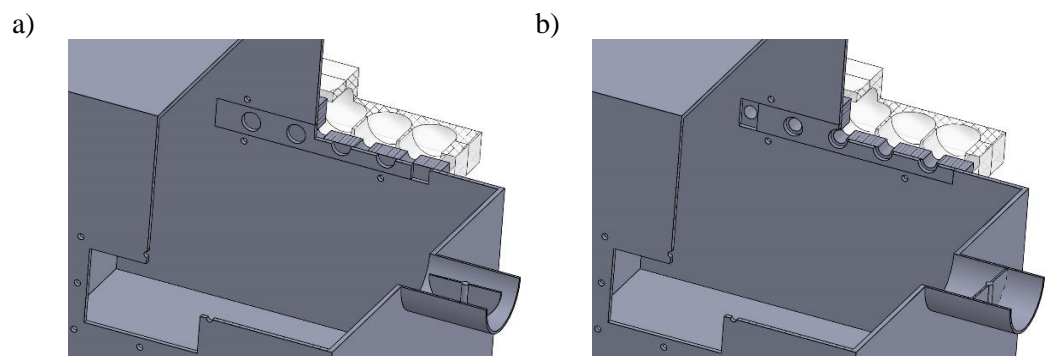


Figure 5.2 Plenum vent valve and nozzles locker slider arrangement: a) before the experiment, b) during the experiment

Table 5.1 Row reverse jet impingement study cases shows the primary variations of reverse jet impingement tested, independent variables assessed here include the effect of nozzle-to-target spacing distance from 2.6 to 8,

Reynolds number between 15,000 and 45,000, the impact of exit condition driven crossflow effects, and the implementation of a novel extended nozzle to reduce these crossflow effects.

Table 5.1 Row reverse jet impingement study cases

	H/d	Re	Crossflow	Nozzle configuration
1	2.6	30,000	Minimum	Square edged
2	4	30,000	Minimum	Square edged
3	6	30,000	Minimum	Square edged
4	8	30,000	Minimum	Square edged
5	4	15,000	Minimum	Square edged
6	4	45,000	Minimum	Square edged
7	4	30,000	Medium	Square edged
8	4	30,000	Maximum	Square edged
9	4	30,000	Medium	Extended
10	4	30,000	Maximum	Extended

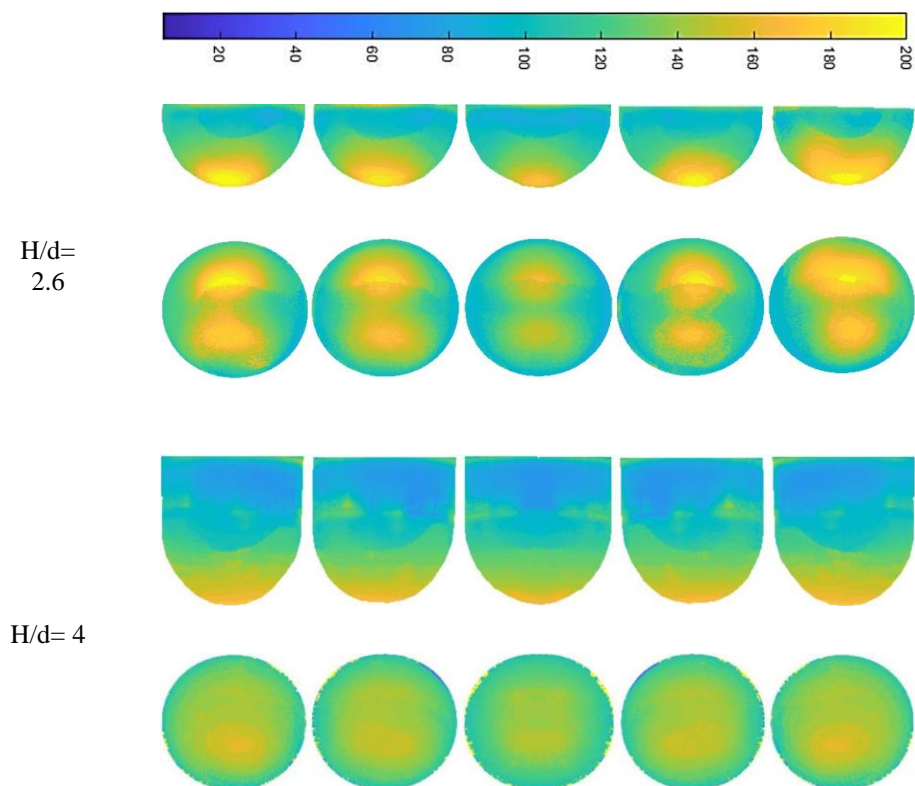
5.2. Results and discussions

5.2.1. Nozzle-to-target spacing effect

For a given mass flow, one of the most fundamentally significant geometry variations associated with jet impingement is the jet to target spacing ratio, as a potential core is present post-nozzle exit, the heat transfer achieved is very dependent on its relative interaction with the target surface. This effect is well understood in literature, for both flat, concave, and dimpled surface, it was key to verify this in the novel reverse impinging jet geometry.

The distribution of heat transfer shows a traditional form, in proximity of the stagnation point, the highest magnitude of heat transfer is observed as the potential core turns against the target surface, subsequently, a wall jet develops, with thickening boundary layer, and therefore decreasing magnitude of Nusselt number. Clear modification of this peak is seen, with a ‘peanut’ shape forming from the secondary flows, as illustrated in Figure 5.3. Overall, this distribution is largely independent of H/d , but magnitude decreases with increasing the spacing distance.

Secondary flows are shown clearly by the ‘peanut’ shape high intensity Nu zones, these secondary flows are caused by the crossflow outlet condition within the geometrical constraint of the reverse target ‘silos,’ and drive the local distributions of heat transfer.



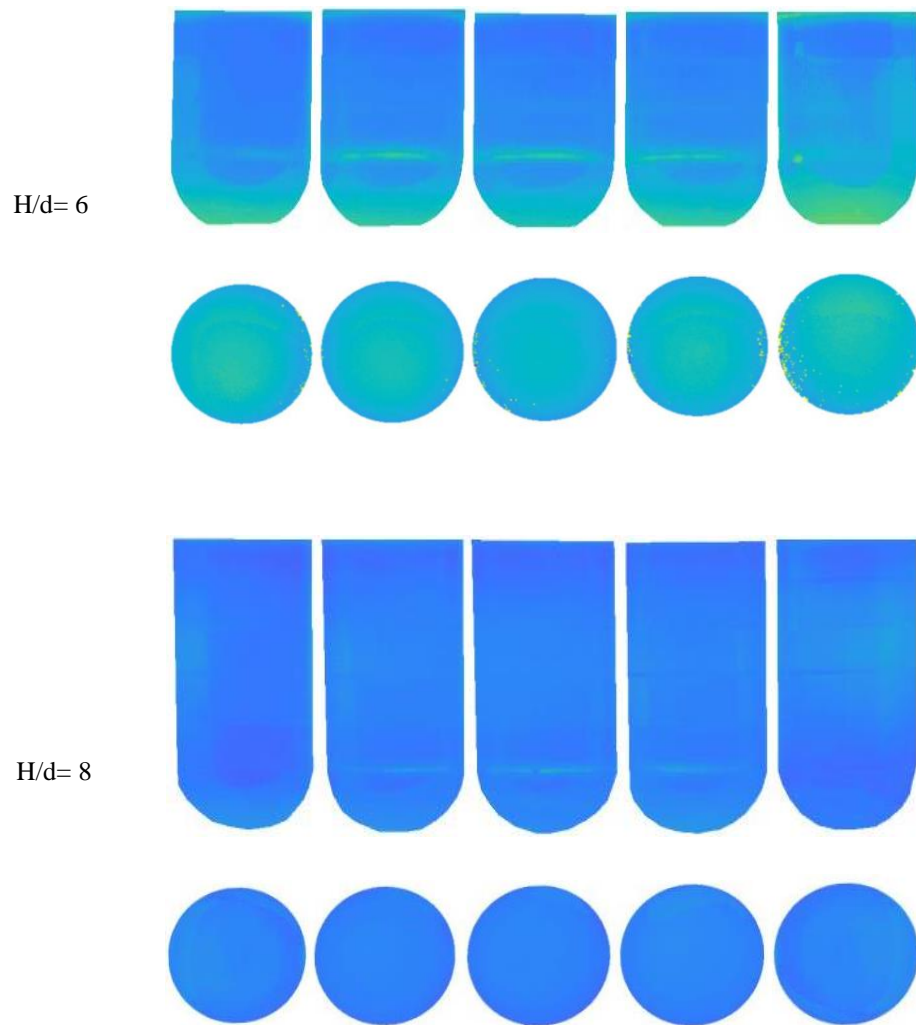


Figure 5.3 Nozzle-to-target spacing distance influence on local Nu distribution at $Re= 30,000$

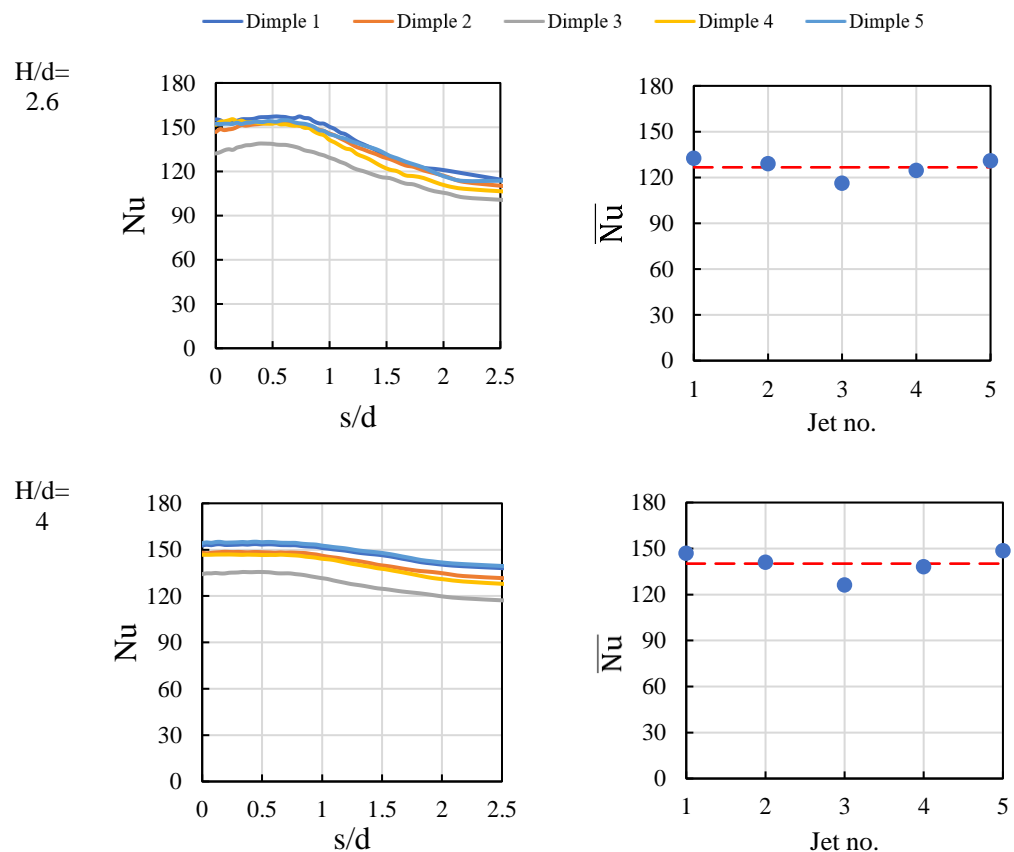
When plotting the average Nusselt number relative to the distance along the target surface from the stagnation point, s/d , plots were generated for an average of the 5 jets to understand the effect of the geometry on the stagnation point, and development of the wall jet boundary layer, as shown in Figure 5.4. The overall average Nu for each jet target was also plotted, to demonstrate the variation between jet targets, which demonstrates the overall Nu performance.

The region of highest Nu is seen between s/d of 0 – 1, around the stagnation region, followed by a decrease as the wall jet develops along the

dimple surface. The most significant decrease is observed in the $H/d = 2.6$ case, where the Nu magnitude decreases by 20% from $s/d = 0.5$, to $s/d = 2.5$, compared to just 7% for a H/d of 4.

Plots show that the outer nozzles, closest to the spent flow exits have highest Nu , this is likely due to the relatively large pressure difference over the jet nozzles in proximity to the outlets.

At optimum H/D of 4, which is generally consistent with the optimum spacing for a jet impinging arrangement, the variation between individual nozzle targets becomes greater, and more uniform with decreasing or increasing H/d .



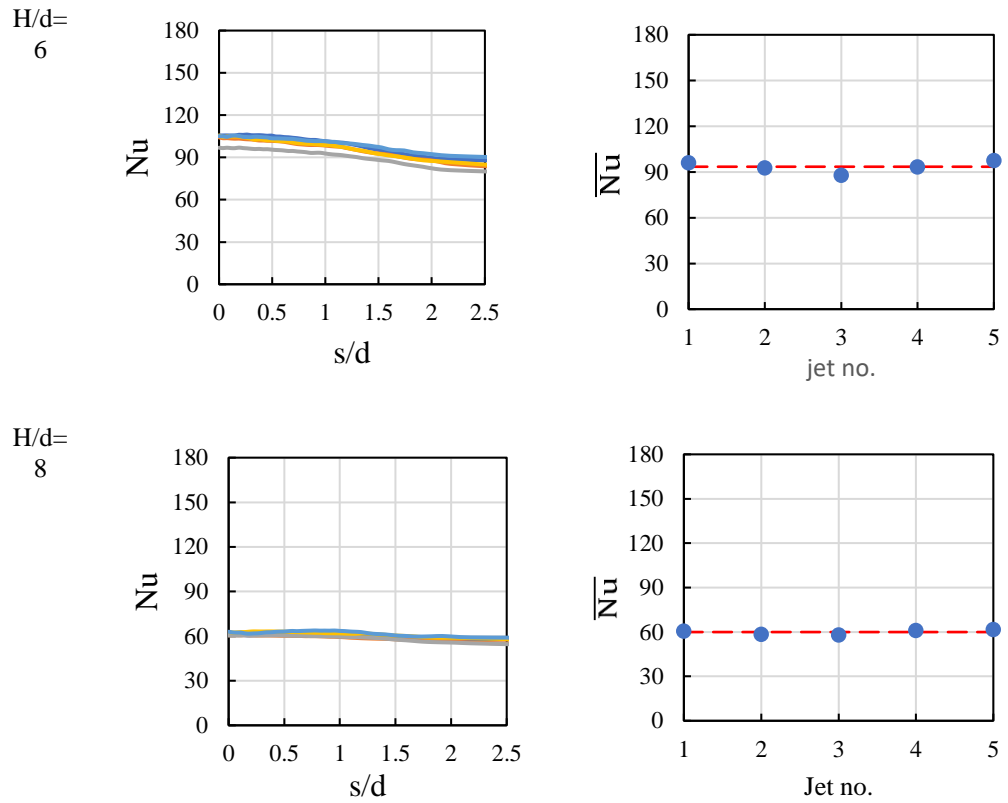


Figure 5.4 Nozzle-to-target spacing distance influence on Nu and average Nu distribution at $Re= 30,000$

A comparison of the five dimples overall average Nu at different nozzle-to-target spacing distances, $H/d= 2, 4, 6$ and 8 , is presented at Figure 5.5. As it clear for $H/d= 2$ and 4 the Nusselt numbers at the stagnation region, $s/d \leq 1d$, are typically the same. While in the jet wall region, $s/d \geq 1d$, the nozzle-to-target spacing ratio of 4 obtained higher Nusselt number distribution. While as the spacing distance ratio between the nozzle and the target the Nusselt number started to deteriorate. This deterioration is a result of that the potential core in the reverse jet impingement is about four nozzle diameters.

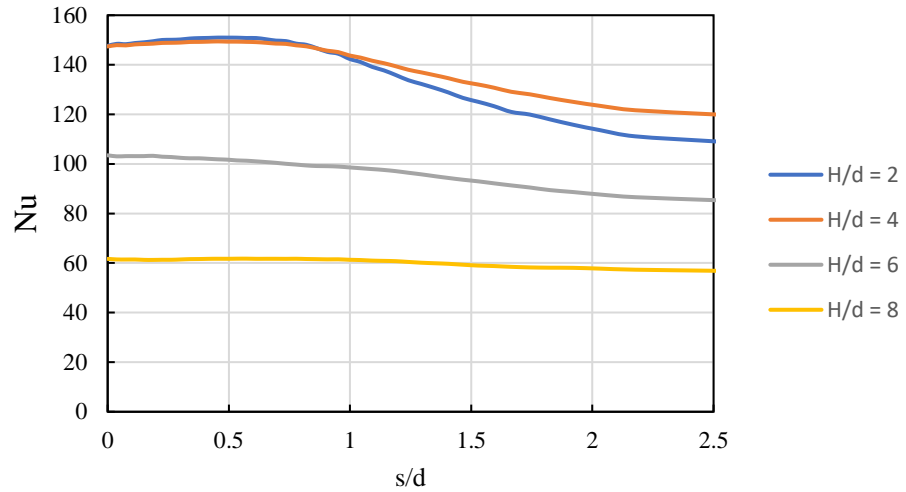


Figure 5.5 Nozzle-to-target spacing distance influence on total average Nu distribution at $Re = 30,000$

5.2.2. Reynolds number effect

The effect of Reynolds number on Nusselt number distribution and magnitude was investigated for the novel reverse jet impingement design. Consistent with literature on more conventional impingement target design, there is a monotonic increase of Nu with Re, however similar distribution against each dimple target and cylinder walls is observed independent of Re, As illustrated in Figure 5.6.

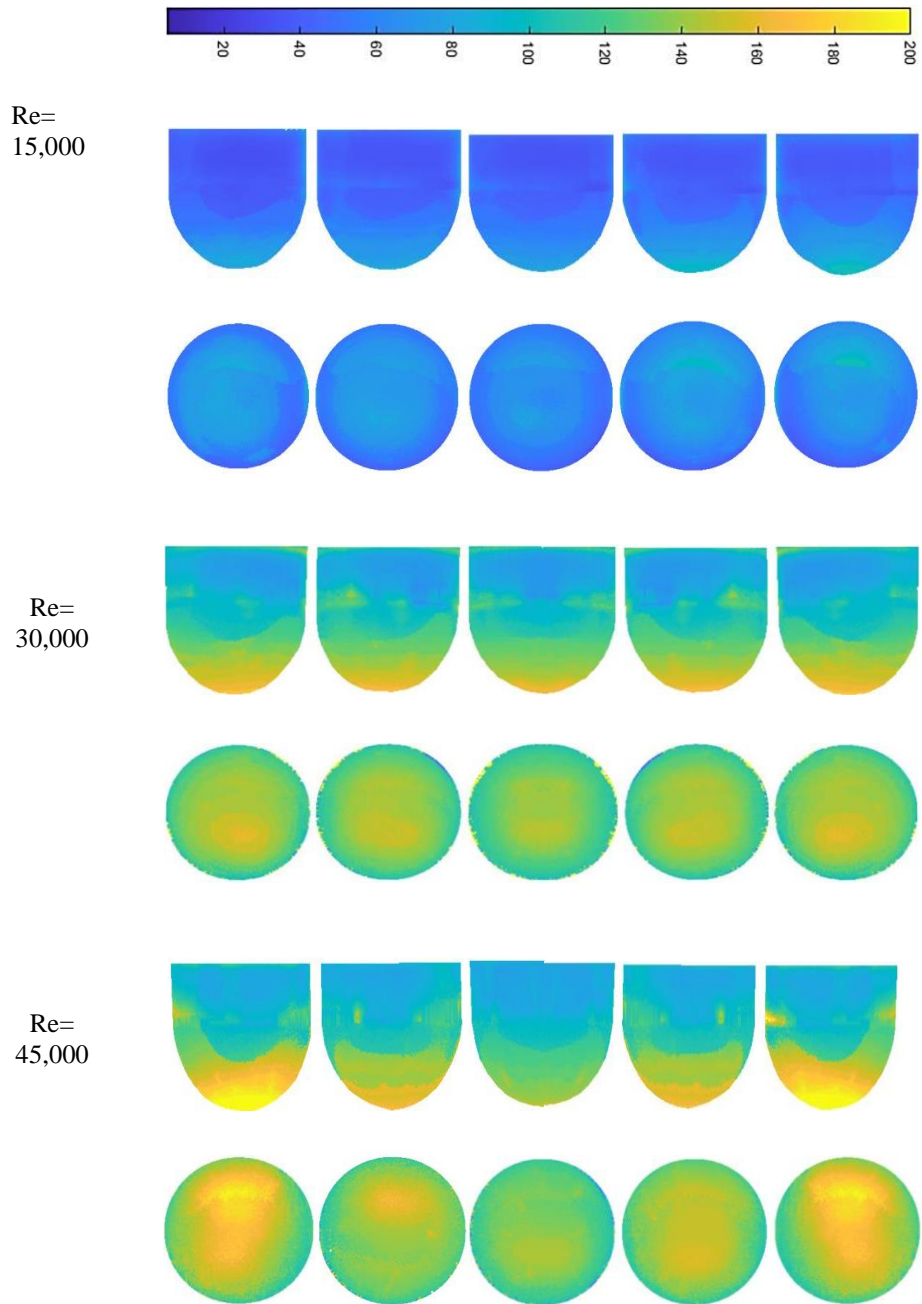


Figure 5.6 Reynolds number influence on Nu distribution at $H/d=4$

Although distribution in individual targets is consistent, the Nu variation between jets becomes more significant for turbulent flow, as shown in Figure 5.7, with a 15% spread of jet variation for 30,000 Re, compared to a variation of just 6% for the lower Re of 15,000.

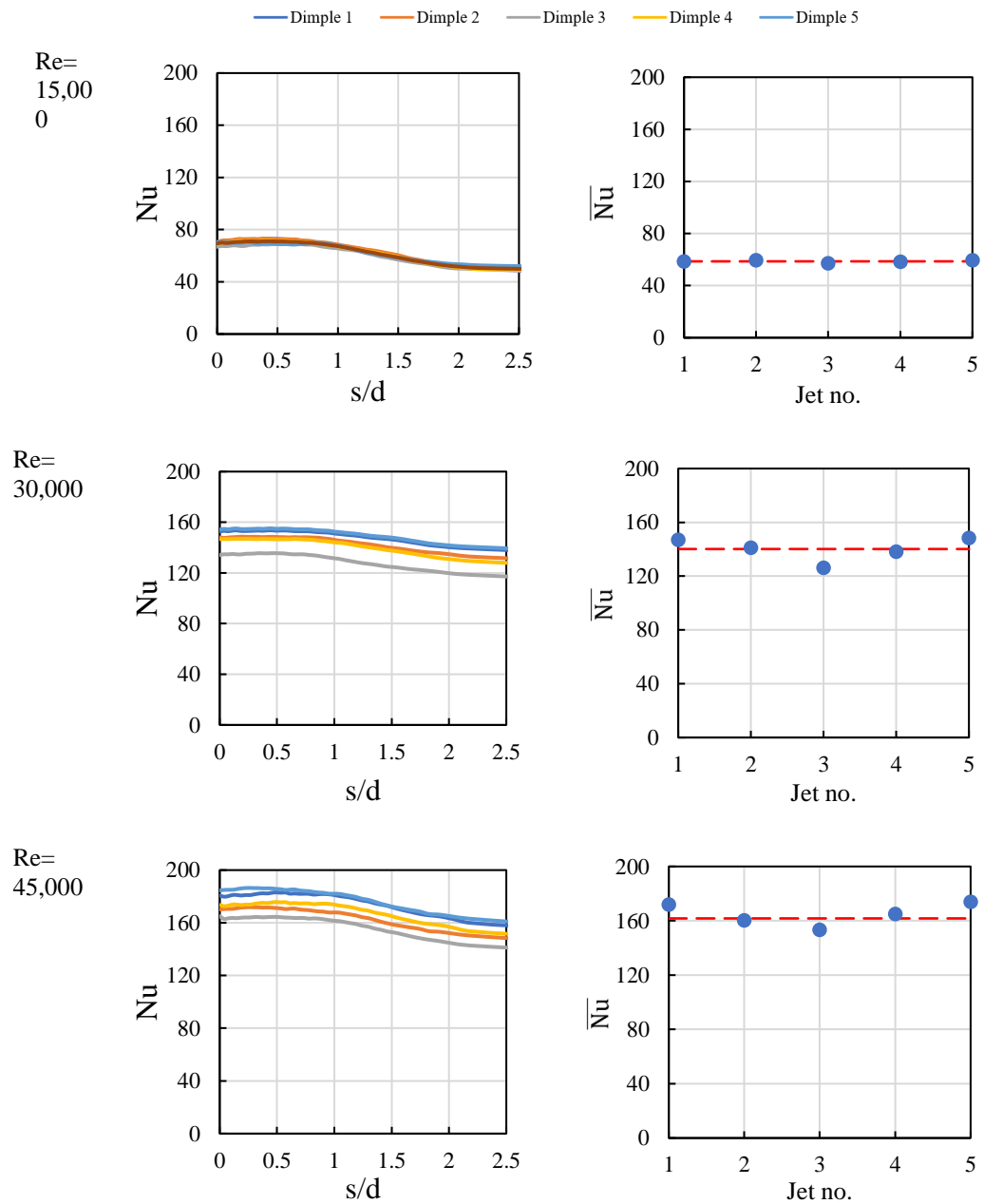


Figure 5.7 Reynolds number influence on average Nu distribution at $H/d = 4$

Figure 4.8 demonstrates that the s/d trend of Nusselt number is independent of Reynolds number, but increases monotonically with Reynolds number ($Nu_{st} = c \cdot Re^m$). Based on the current data, the Reynolds number m exponent value equals 0.49.

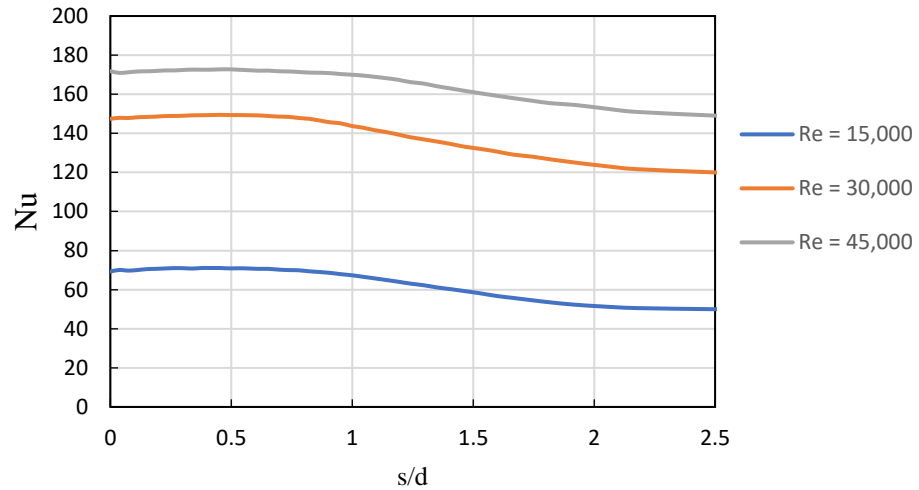


Figure 5.8 Reynolds number influence on total average Nu distribution at $H/d=4$

5.2.3. Crossflow effect

The effect of crossflow was assessed with varying outlet direction conditions that could be expected in typical applications, the minimum crossflow case is shown in Figure 5.9a, where all outlet directions are opened, representative of a double-wall mid-chord application. The intermediate crossflow case is shown in Figure 5.9b, where all flow exits from the left and right ends of the impingement row, such as in a nozzle guide vane, and the maximum crossflow case is shown in Figure 5.9c, where all flow must exit from the left of the impingement row, typical of a rotating blade situation.

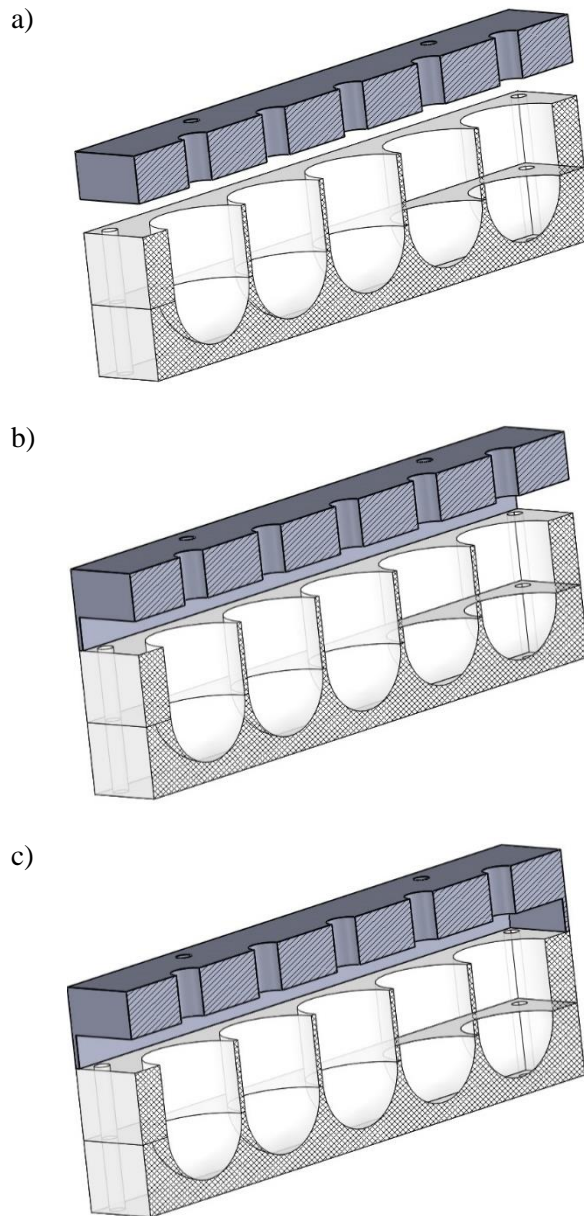


Figure 5.9 Different crossflow configurations: a) Minimum crossflow, b) Medium crossflow and c) Maximum crossflow

Nusselt number contour plots of these crossflow variations show that the crossflow has a cumulative effect in deflection the jet away from its central target location, as shown in Figure 5.10. In both the medium and maximum crossflow cases, this cumulative deflection can be seen as an enhancement of heat transfer against the side wall in the crossflow direction.

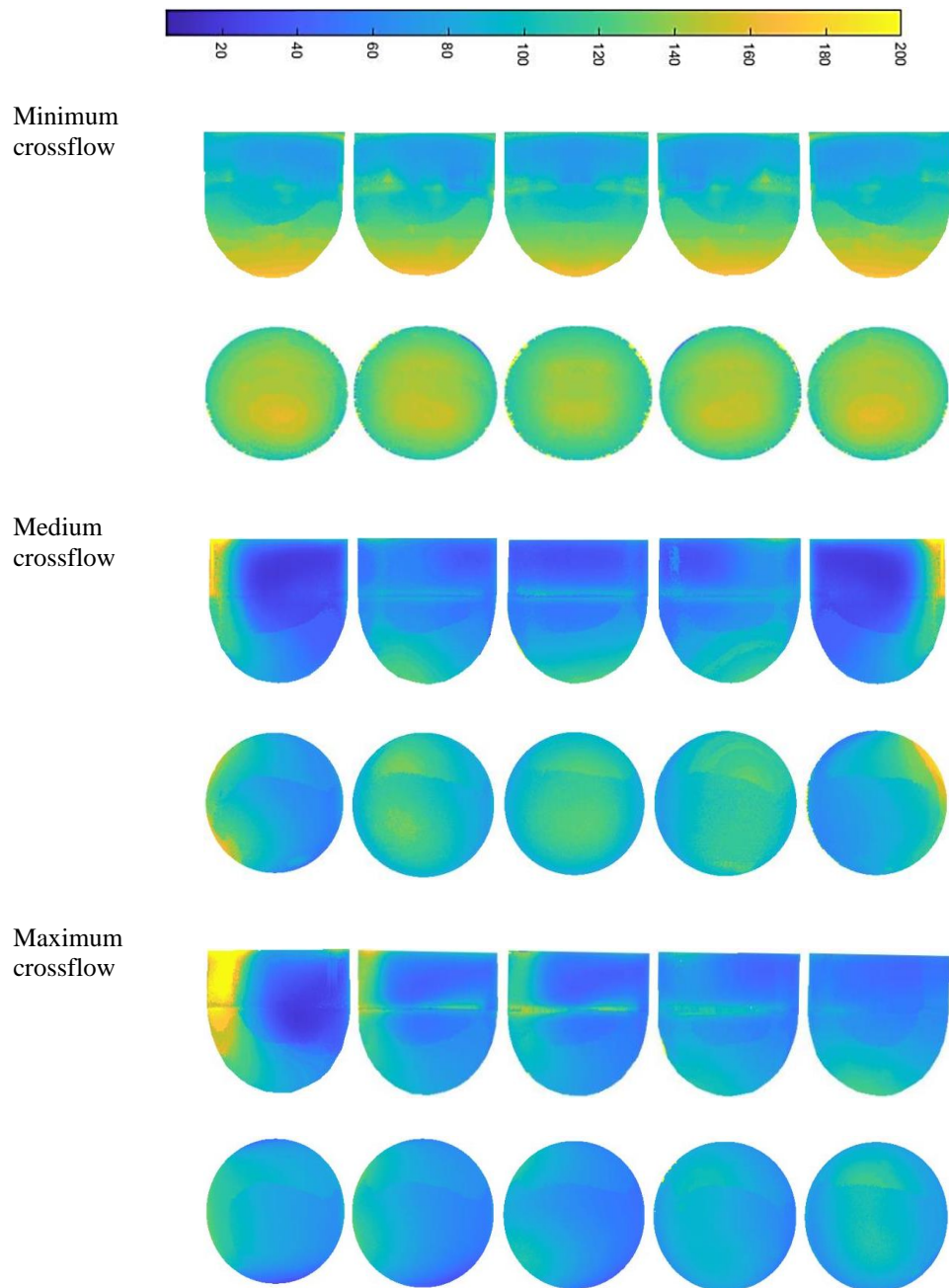


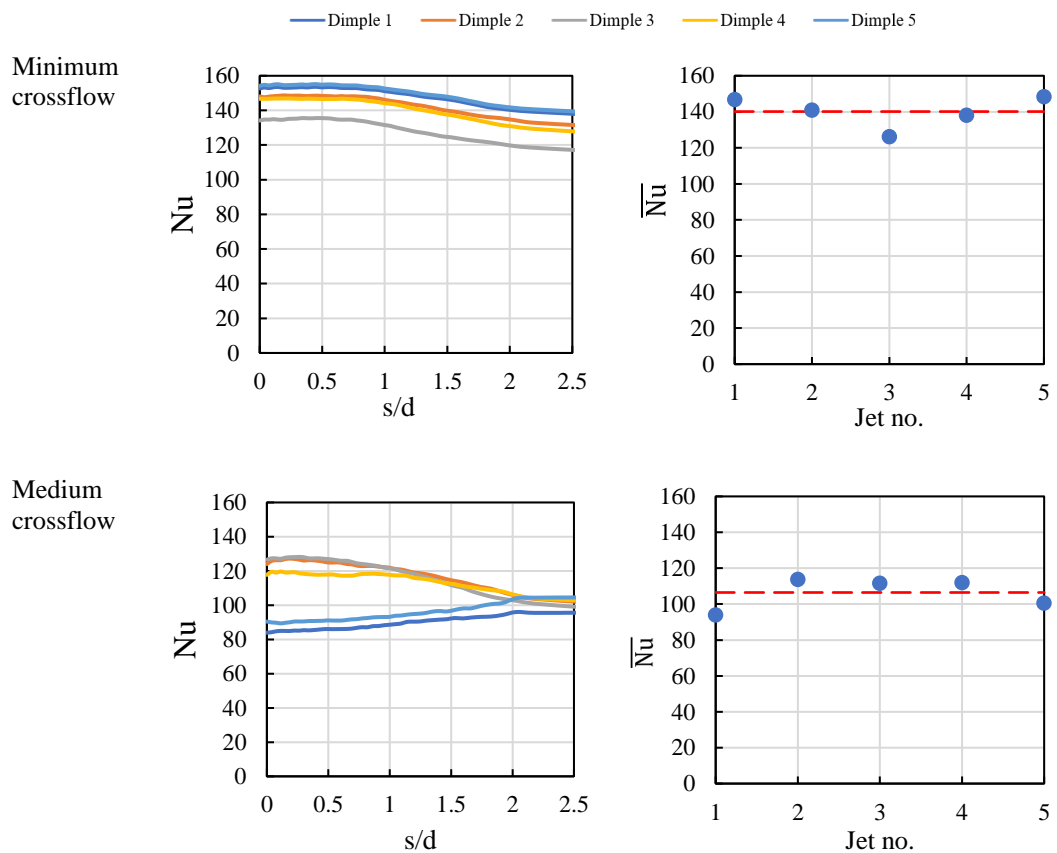
Figure 5.10 Crossflow influence on Nu distribution at $H/d= 4$, $Re= 30,000$

Figure 5.11 shows that the effects of a medium crossflow are a relatively diminished heat transfer effect on the targets closest to the crossflow exit. It can also be seen that the stagnation point Nu, i.e. $s/d = 0$, is reduced to the lowest local Nu, and the jet is with similar magnitude against the cylinder walls, due to the jet being ‘pressed’ against one of these walls, we can also

assume that this effect is highly biased towards the crossflow direction, providing a non-uniform cooling effect.

Due to the reduced crossflow channel area compared to a typical row target, the pressure drop over these crossflow channels is relatively large, where multiple jet flows must cumulate and exit from a single or reduced number of outlets, a relatively large variation in target plenum pressures exists. Therefore, the effective pressure drop over nozzles in proximity to the outlets is increased, producing a larger local mass flow, and Reynolds number.

In the maximum crossflow case, we can observe that this diminished heat transfer is compensated by the cumulative crossflow of all 5 jets, here we see a very significant enhancement of heat transfer against the outlet crossflow wall.



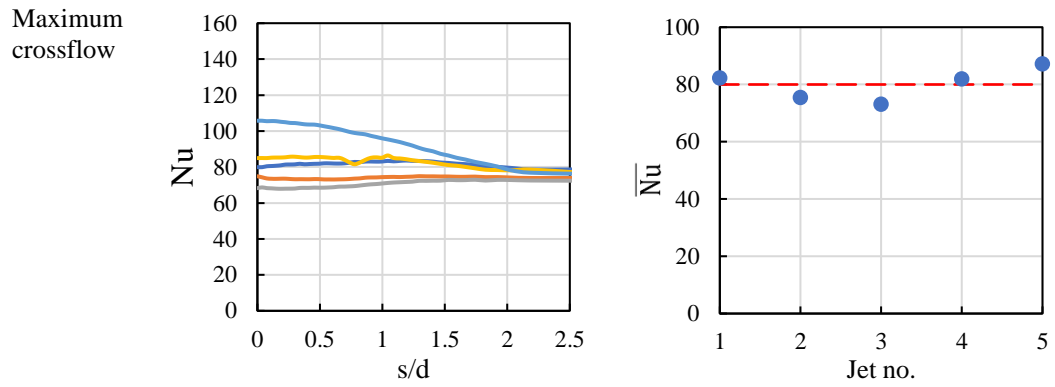


Figure 5.11 Crossflow strength influence on average Nu distribution at $H/d=4$, $Re=30,000$

Overall, the effects of crossflow diminish the impingement effect in the centre of each target, and lead to a reduction in s/d averaged Nu for the entire impingement target surface, as presented in Figure 5.12.

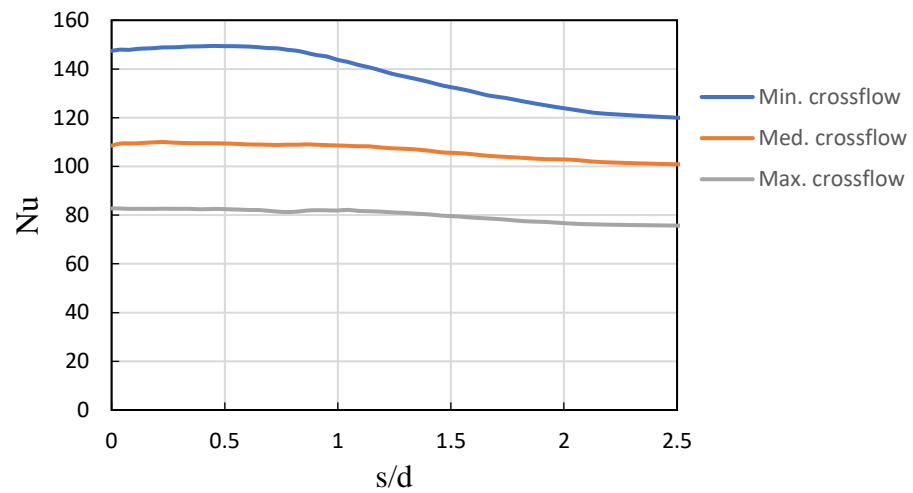


Figure 5.12 Crossflow strength influence on total average Nu distribution at $H/d=4$, $Re=30,000$

5.2.4. Nozzle configuration effect

To reduce the effects of crossflow further, a novel nozzle arrangement was constructed, here, the nozzle is extended as a tube into the crossflow path, where the cumulative mass flow can become significant in deflecting the jet and is shown in Figure 5.13.

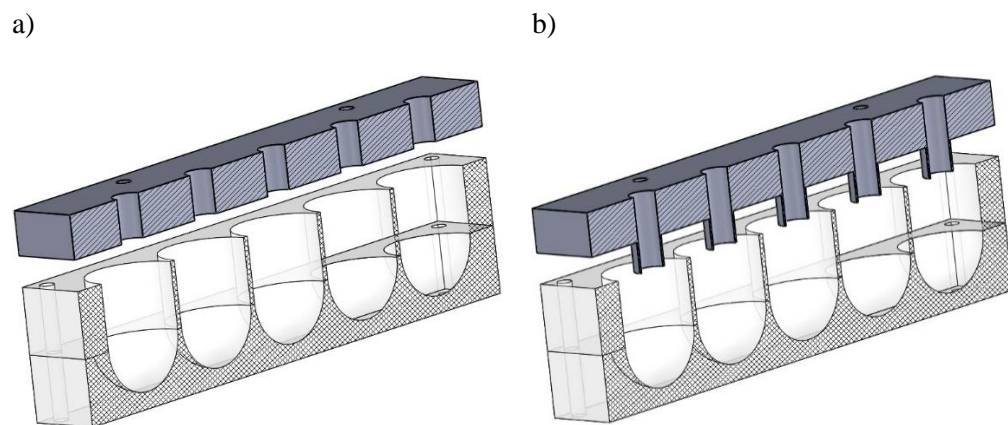


Figure 5.13 Different nozzle configuration: a) Square nozzle and b) Extended nozzle

It has been observed that the utilization of an extended nozzle results in a reduction of impingement flow deflection, thereby facilitating the visualization of the effects of a larger pressure drop on the variation of Nusselt number between the jets. However, despite this improvement, the relative Reynolds number difference between the jet nozzles remains significant, as depicted in Figure 5.14. It is noteworthy that as the number of jets used with the same terminal crossflow outlet increases, this discrepancy in relative Reynolds number will become even more prominent.

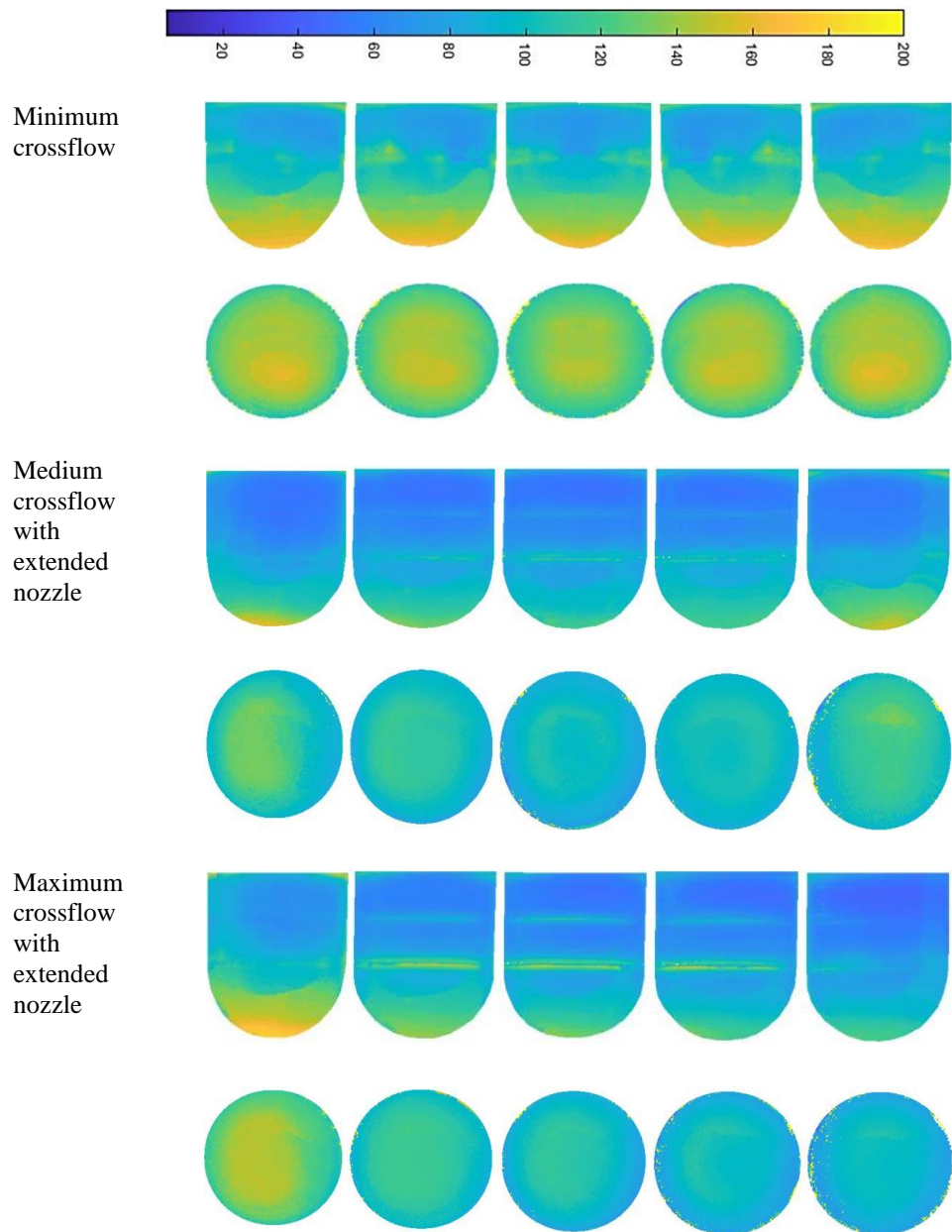


Figure 5.14 Extended nozzle influence on local Nu distribution at $H/d= 4$, $Re= 30,000$

The maximum crossflow case shows a larger enhancement of Nu for the jet closest to the exit, this is likely due to a relatively large pressure drop over the nozzle consequently higher mass flow rate, and therefore enhanced Re, as shown in Figure 5.15. Showing variation of Nu between jets of 17% for the minimum crossflow case but a clear diminishment of Nu of 22% from jet 1 to jet 5 for the maximum crossflow case.

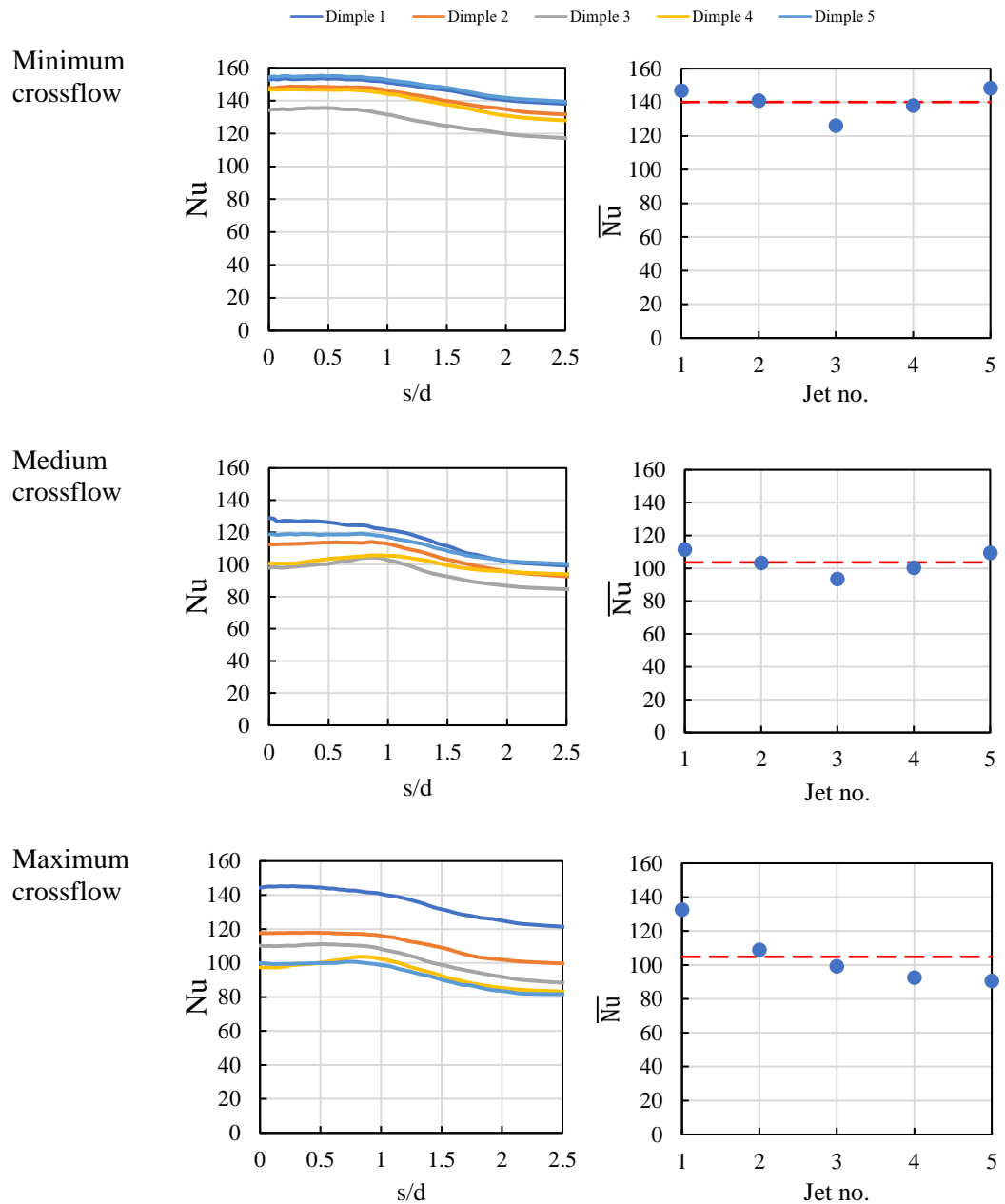


Figure 5.15 Extended nozzle influence on average Nu distribution at $H/d=4$, $Re=30,000$

Here, the medium and maximum crossflow cases are shown to be almost identical in overall magnitude along s/d for the average of all 5 nozzles, as shown in Figure 5.16, but with very significant variations in local Nu distribution and distribution between jet averages, as illustrated in Figure 5.15.

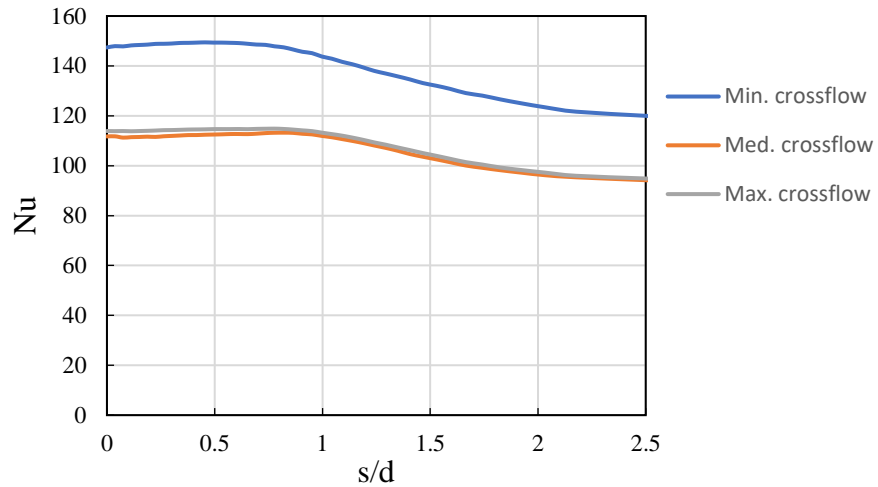


Figure 5.16 Extended nozzle influence on total average Nu distribution at H/d=4, Re= 30,000

5.2.5. Discharge Coefficient

Discharge coefficient is shown to increase with H/d, from 70% at H/d = 2, to 75% above H/d = 6, as presented in Figure 5.17. This increase in discharge coefficient is associated with the larger target plenum providing less pressure drop as the spent air flows to the outlet of the test sections. The interaction between the mid-potential core and the target for H/d of 2.6 also has a reducing impact on Cd.

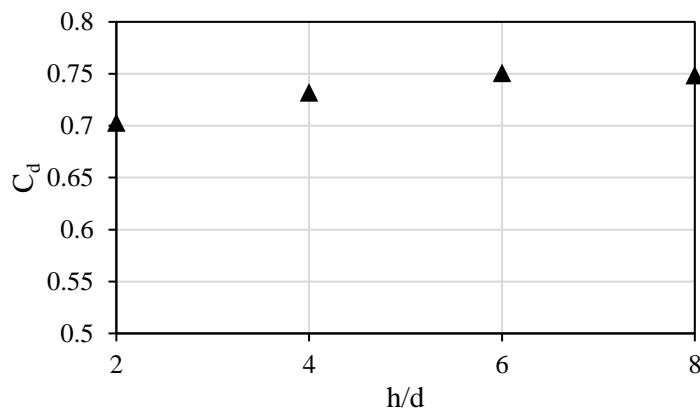


Figure 5.17 Nozzle-to-target spacing distance influence on discharge coefficient at Re= 30,000

Discharge coefficient is shown to increase with Reynolds number for a $H/d = 4$, from 69% at 15,000 Re, to 77% at 45,000 Reynolds number, as illustrated in Figure 5.18.

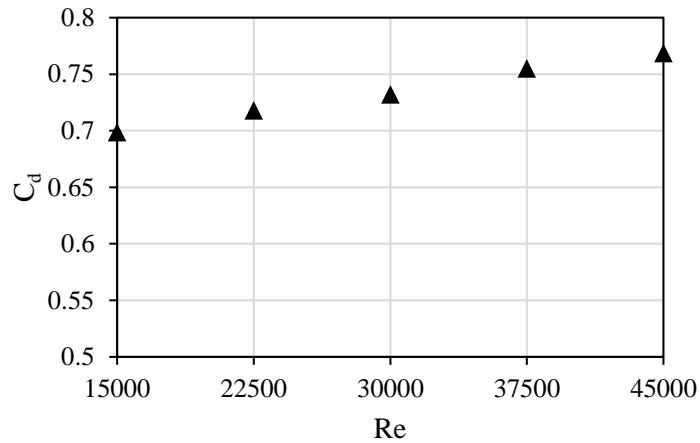


Figure 5.18 Reynolds number influence on discharge coefficient at $H/d= 4$

Discharge coefficient is shown to decrease with crossflow, this is due to the downstream flow restriction after the impingement function. In addition to, the extended nozzle provide higher discharge coefficient than the square edge nozzle in all crossflow schemes, as shown in Figure 5.19.

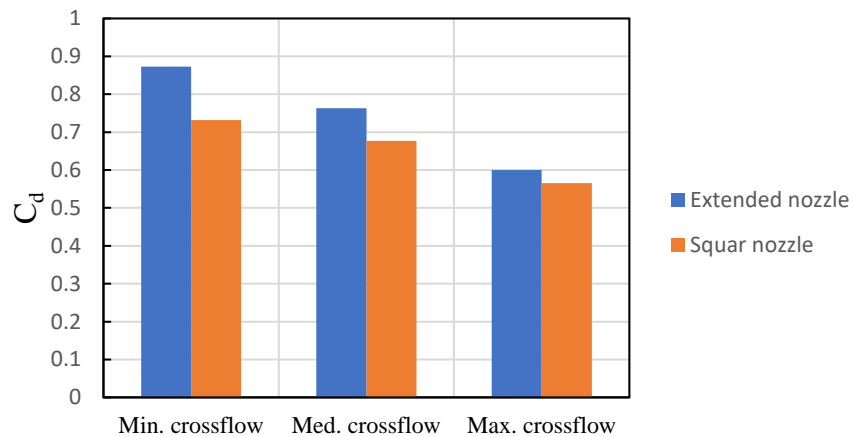


Figure 5.19 effect of different crossflow schemes on the discharge coefficient

5.3. Summary

Overall, there is an enhancement of heat transfer consistent to a dimple target surface, and additional heat transfer performed as the wall jet can transition to the ‘silo’ cylindrical wall. An optimum H/d was identified at $H/d = 4$, and Nusselt number was found to increase monotonically with Reynolds number.

Crossflow impacts the distribution of Nusselt number between each jet in the row, and the relatively large pressure drops generated over the crossflow channels cause an enhancement in the heat transfer for the impingement target closest to the outflow locations, becoming more significant when a maximum crossflow condition is imposed.

Implementing an extension to the nozzles through the crossflow channels reduced negative effects of crossflow, especially the effects of jet deflection, but the effects of pressure drop variation remained significant.

Discharge coefficient was shown to increase with larger H/d , and also increase with Reynolds number. Moreover, the extended nozzle causes lower pressure drop than the square nozzle in all different crossflow schemes.

Chapter 6. Array Reverse Jet Impingement

Beyond a single nozzle, or row of nozzles, many applications exist where a larger target area requires cooling. Impingement cooling arrays are common for such requirements. This section explores the application of reverse jets to this problem.

6.1. Test section

The plenum is maintained from the impinging row test section to generate a uniform temperature and pressure condition at the inlets, and the modular nozzle and target arrangement allows for the installation of a cooling array.

The array consists of seven staggered nozzles of equal diameter, each nozzle is surrounded by 6 film outlets, as shown in Figure 6.1. Central film outlets are proportionally larger to allow spent air from neighbouring jets. Outer film holes are smaller as they are connected to fewer jets each.

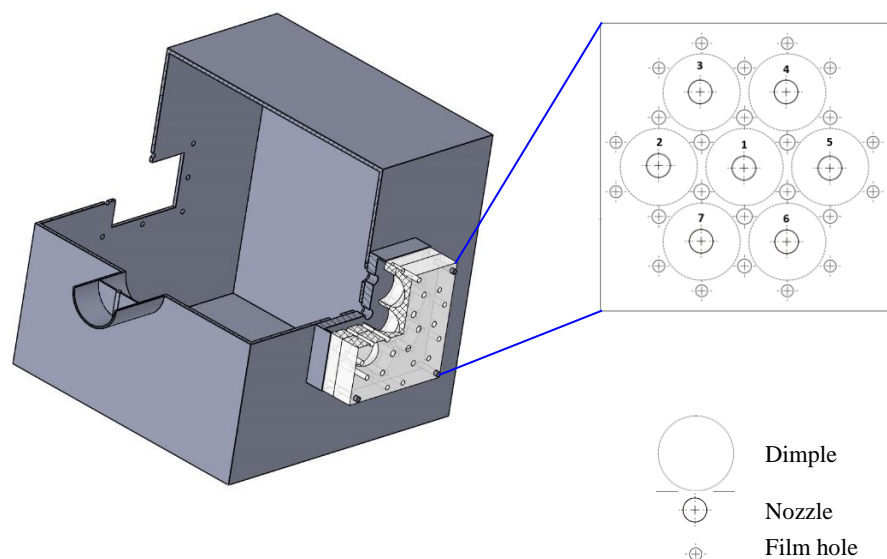


Figure 6.1 Sketch of array reverse jet impingement

As was the case with the row jet impingement, the plenum is connected to a vent valve and the nozzles are closed by a sliding locker to scavenge the cold air from the plenum room before the start of the test to keep the air jet temperature hot and steady throughout the experiment, as previously discussed in Section 5.1.

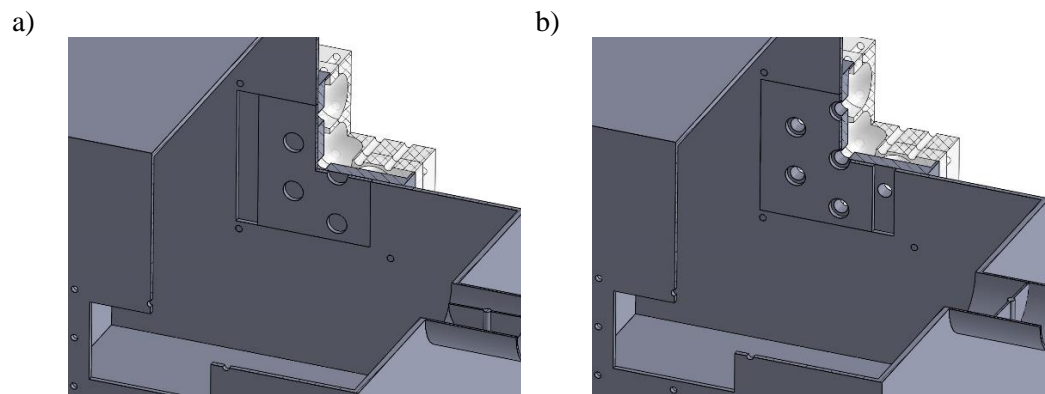


Figure 6.2 Plenum vent valve and nozzles locker slider arrangement: a) before the experiment, b) during the experiment

Experimental tests conducted for the reverse impingement array evaluated a range of jet to target spacings, H/d from 2.6 to 8, and Reynolds number between 20,000 – 40,000. The overall test schedule for this study is shown in Table 6.1.

Table 6.1 Array reverse jet impingement study cases

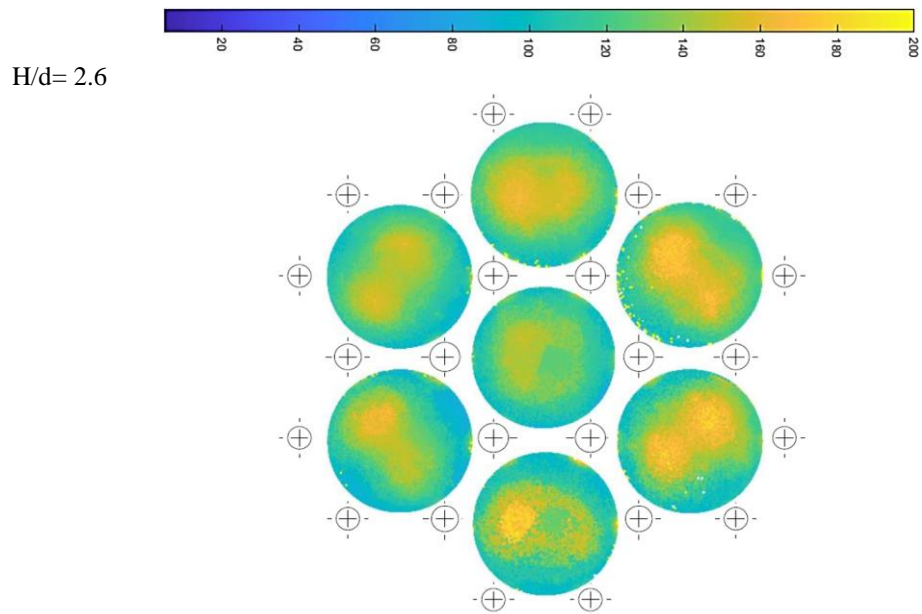
	H/d	Re
1	2.6	30,000
2	4	30,000
3	6	30,000
4	8	30,000
5	4	20,000
6	4	40,000

6.2. Results and discussion

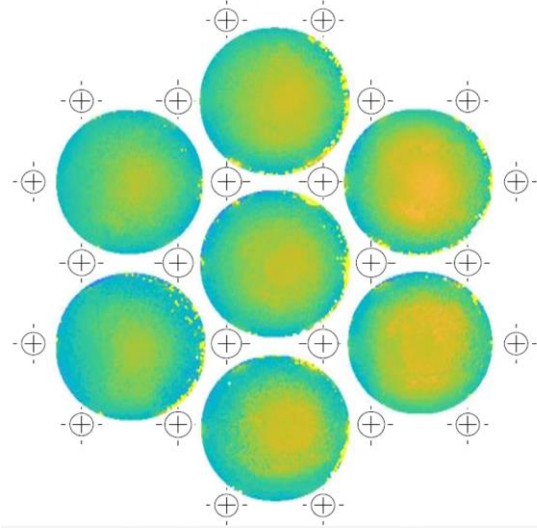
6.2.1. Jet-to-target spacing effect

When assessing the distribution of Nusselt number across all seven target surfaces, as shown in Figure 6.3, it can be observed that the central target has no ‘peanut’ shape distribution, this was previously recognised to be a function of the outlet flow directions secondary flow effects, and here is consistent with the lack of a single or dual vector of outlet flow, instead travelling radially outward in six directions.

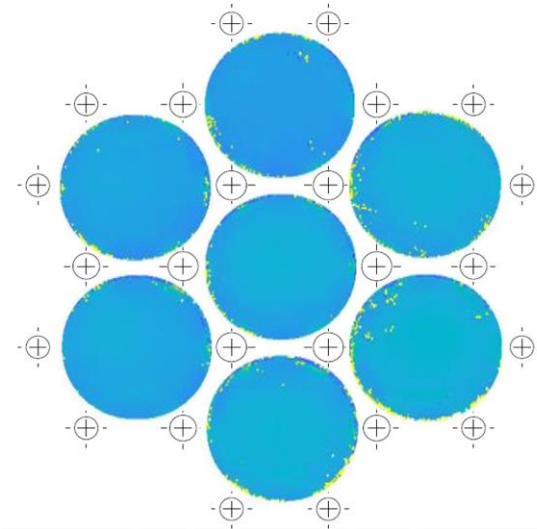
When focussing on the outer six targets, the Nusselt number distribution is consistent with row crossflow direction ‘peanut’ shape secondary flows, with clear vectors of outflow direction.



H/d= 4



H/d= 6



H/d= 8

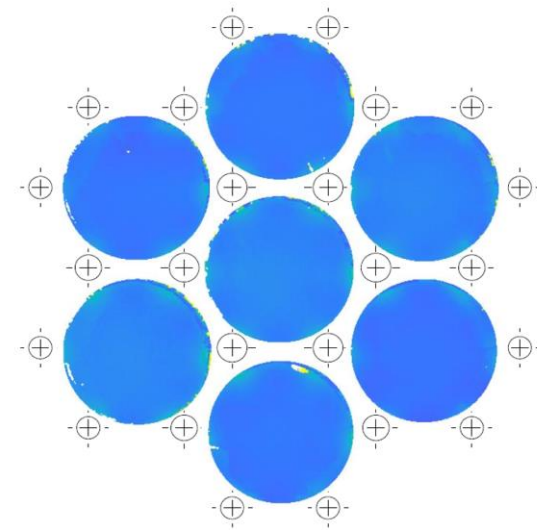


Figure 6.3 Nozzle-to-target spacing distance influence on local Nu distribution at $Re= 30,000$

Plots were produced of radial average Nusselt number as a function of radial distance, s , from the stagnation point. Figure 6.4 shows the radial distribution of average Nusselt number for each of the seven nozzles, and an overall average Nusselt number for each.

At the lower H/d value of 2.6, targets show a local Nusselt number minimum at the stagnation point, this is previously recognised in the reverse jet impinging row arrangement, is likely impacted by effects previously observed by Jambunathan et al.[19].

At $H/d = 4$, the peak Nusselt number for each target is at the stagnation point, with less impact from the secondary flows, and with more variation between the seven jets observed, but a very similar overall average Nu value across the seven targets to $H/d = 2.6$.

At $H/d = 6$, the stagnation point is again the location of the maximum Nusselt number observed, with a decreased variation between the seven jets, and a significantly decreased overall heat transfer.

At $H/d = 8$, the Nu is very level and consistent from the stagnation point to $s/d = 1.5$, then an increase is observed to Nusselt number maxima at $s/d = 2$, this is due to the influence of the film extraction outlet holes.

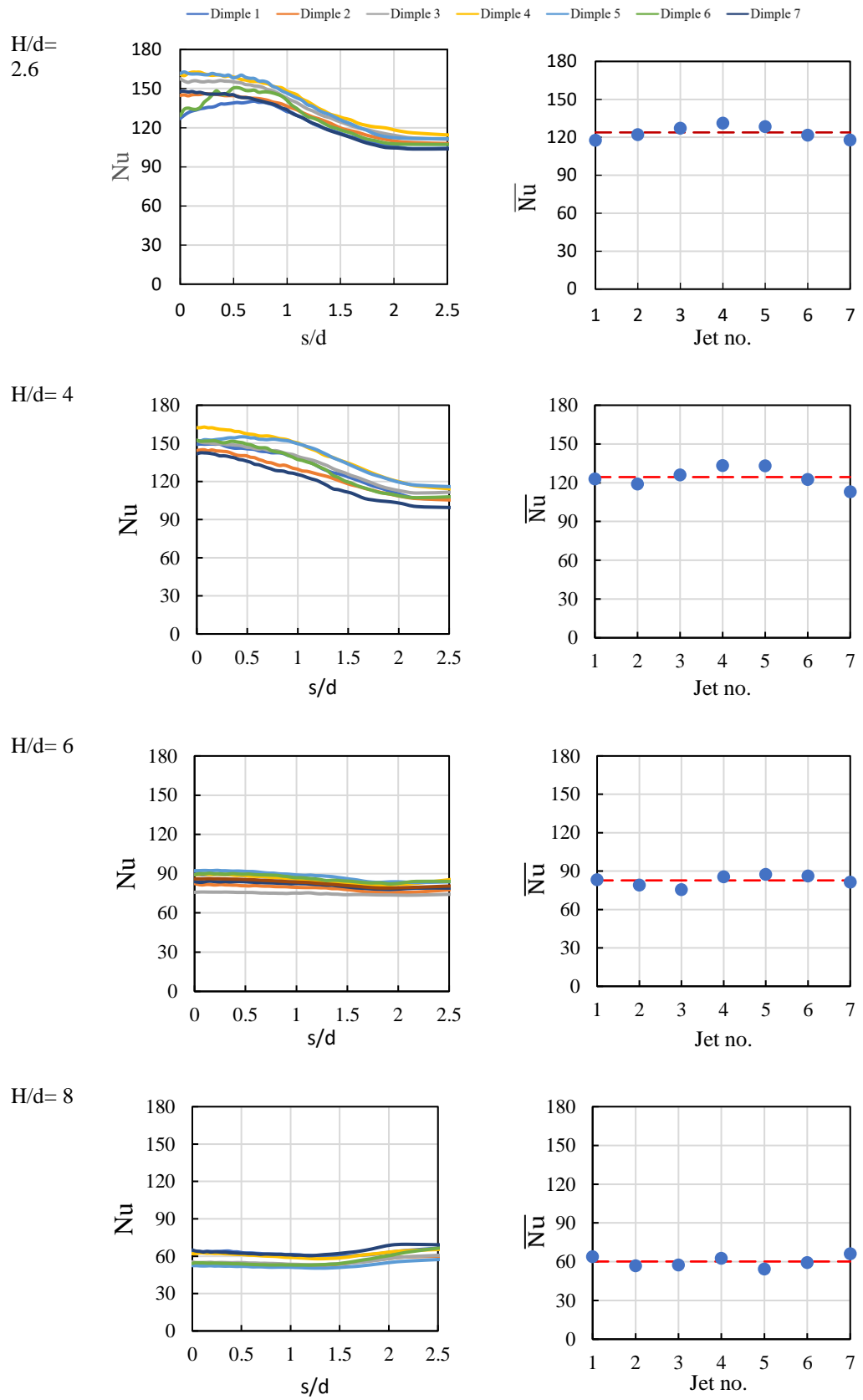


Figure 6.4 Nozzle-to-target spacing distance influence on average Nu distribution at $Re = 30,000$

When averaging the s/d varied Nusselt number distributions for all seven targets of each jet to nozzle distance variation, as illustrated in Figure 6.5, it can be observed that the $H/d = 2$, and $H/d = 4$ demonstrate similar distributions and magnitude of Nusselt number in this array configuration. s/d Nusselt number distributions for $H/d = 6$ and 8 show decreasing magnitudes, and a less severe enhancement in the stagnation point.

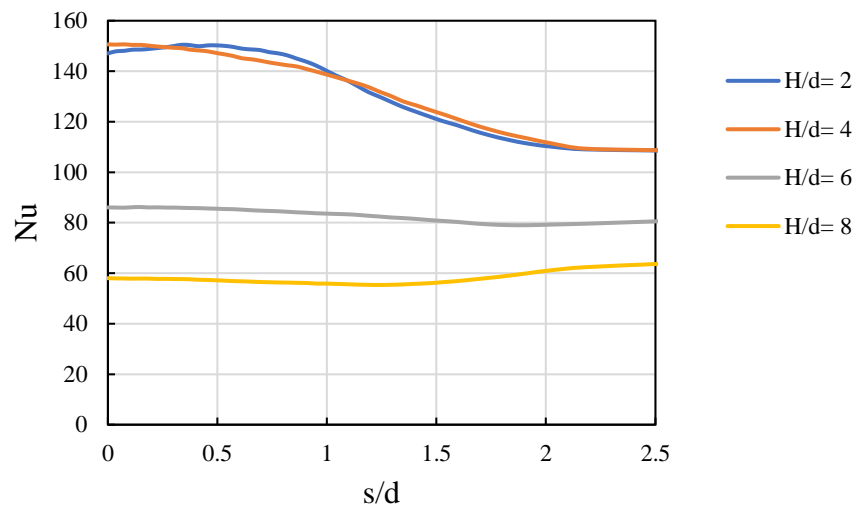


Figure 6.5 Nozzle-to-target spacing distance influence on total average Nu distribution at $Re = 30,000$

6.2.2. Reynolds number effect

The effect of Reynolds number on the Nusselt number distribution and magnitude was assessed between $10,000 Re$ and $30,000 Re$ for $H/d = 4$. Plots of Nu distribution are shown in Figure 6.6 and are consistent with literature on jet impingement arrays. Nusselt number is observed to increase monotonically with Reynolds number, whilst distributions gradient remains largely independent of the turbulence.

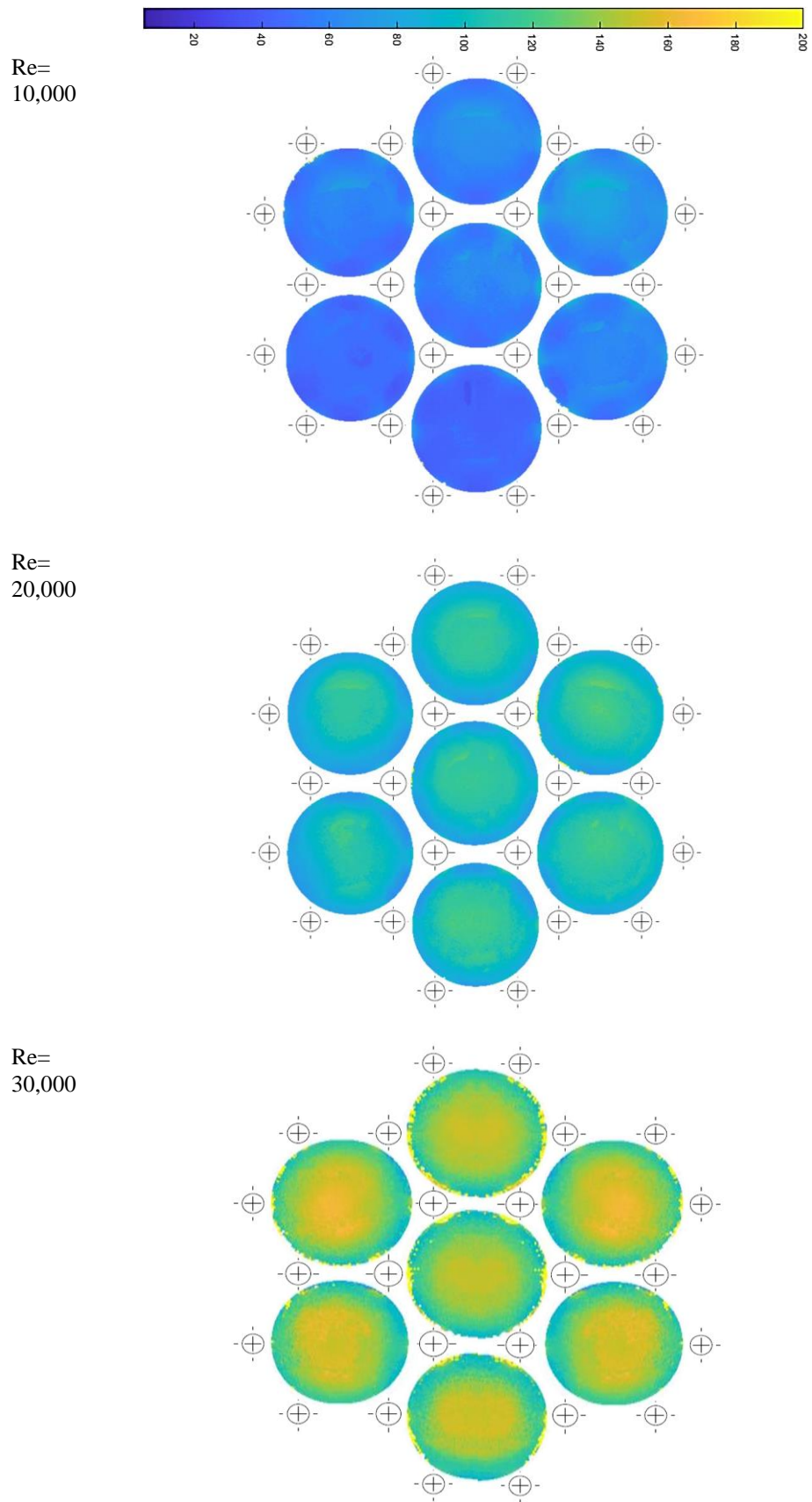


Figure 6.6 Reynolds number influence on local Nu distribution at $H/d= 4$

At $Re = 10,000$, the relative magnitude of the stagnation point Nu is observed to be less enhanced than at higher Reynolds number flows, as shown in Figure 6.7. The relative variation in overall Nusselt number between the seven jets is seen to not vary significantly between the Reynolds number range of 10,000 to 30,000, but the overall average Nusselt number for each array is seen to increase as Reynolds number increases.

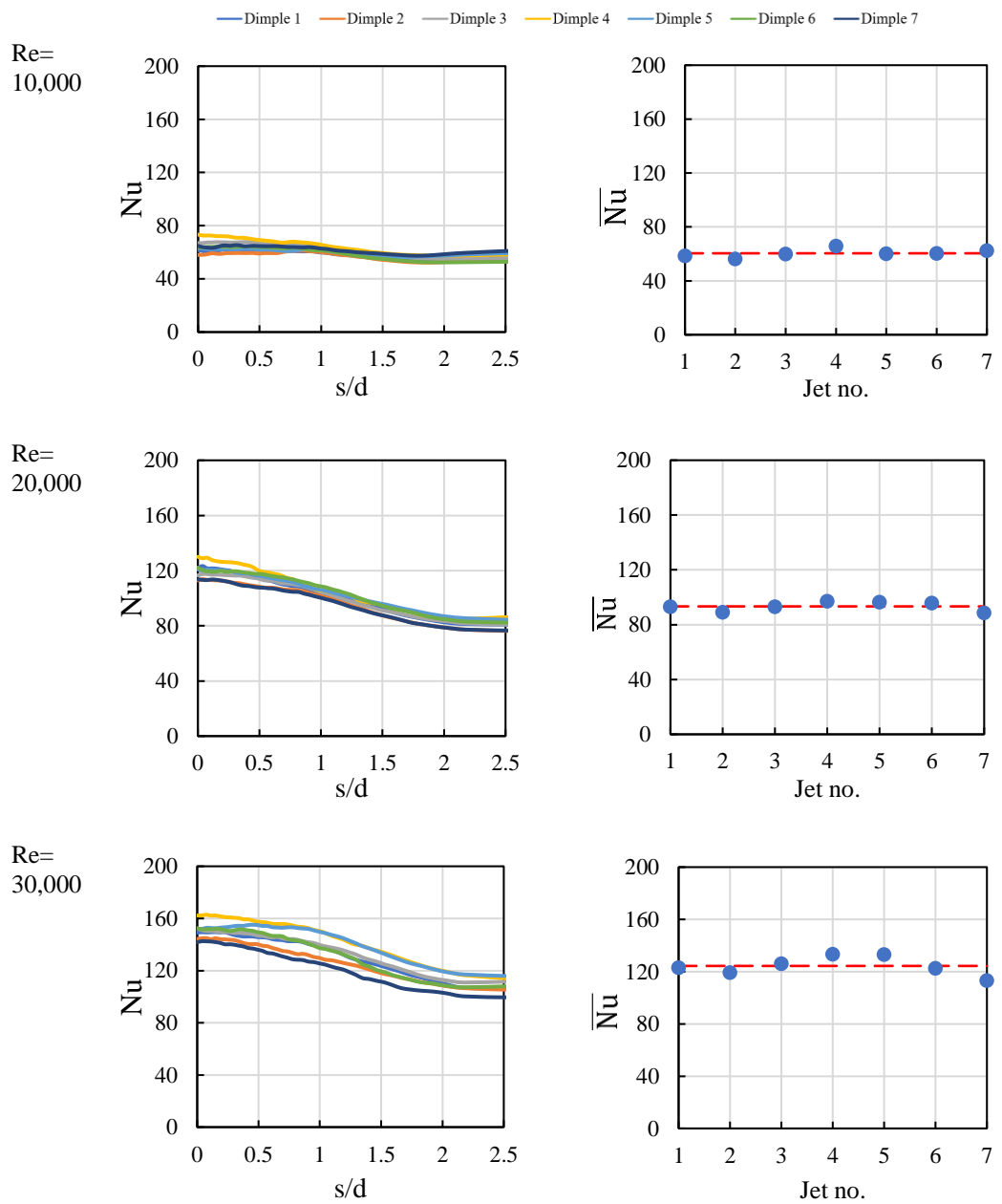


Figure 6.7 Reynolds number influence on average Nu distribution at $H/d = 4$

When averaging the Nusselt number distributions for all seven targets as shown in Figure 6.8, it can be observed that the Nu distributions demonstrate different trends for 20,000 to 30,000 Re, but that at 10,000 Re, the stagnation point has a minor enhancement of heat transfer. This is likely due to the transitional turbulence as the jet enters the larger volume and once the stagnation point is reached at $H/d = 4$. The Nusselt number distribution, in the three cases, is proportional to the Reynolds number ($Nu = c \cdot Re^m$) and the m exponent value equals 0.76.

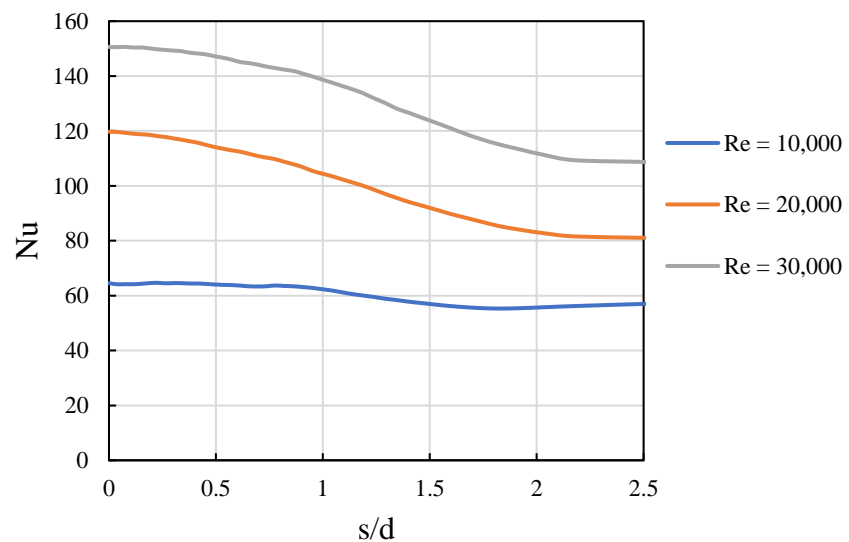


Figure 6.8 Reynolds number influence on total average Nu distribution at $H/d = 4$

6.2.3. Discharge Coefficient

When assessing the effect of H/d on overall Discharge coefficient at 30,000 Reynolds number, Discharge coefficient can be observed not to vary significantly with varying h/d for the reverse jet impinging array, decreasing from 54% at $H/d = 2.6$ to 53% at $H/d = 8$, as shown in Figure 6.9.

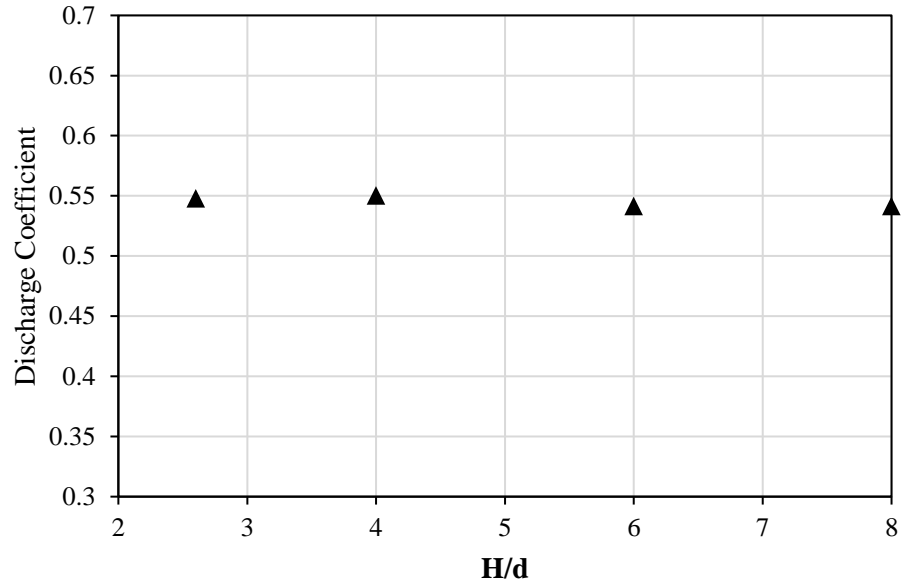


Figure 6.9 Nozzle-to-target spacing distance influence on discharge coefficient at $Re = 30,000$

For the reverse jet impingement array at a H/d of 4, there is a slight increase in discharge coefficient from 53% at 15,000 Re , to 55% at 30,000 Re , but significant increase is observed in discharge coefficient after 30,000 Re , reaching 62% at 37,500 Re , as shown in Figure 5.10.

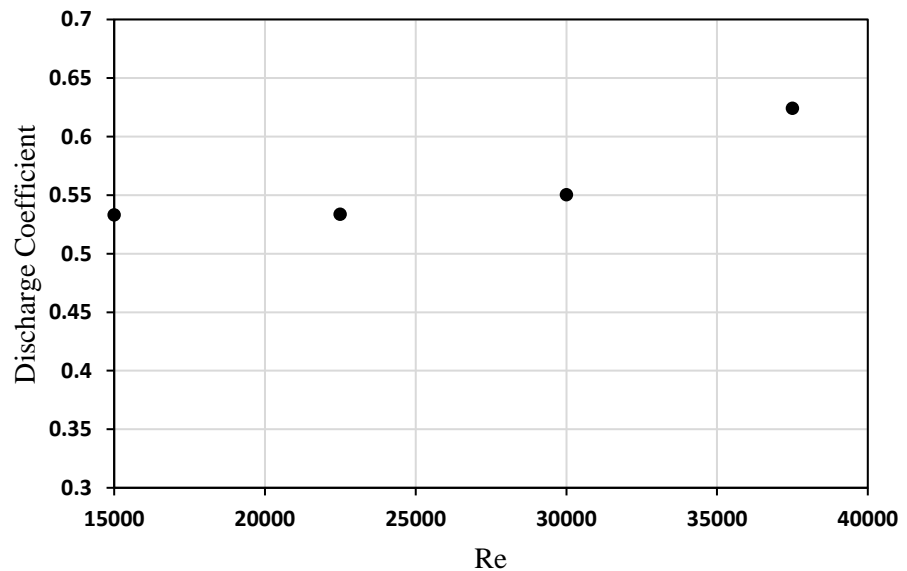


Figure 6.10 Reynolds number influence on discharge coefficient at $H/d = 4$

6.3. Summary

Overall, there is an enhancement of heat transfer consistent to a dimple target surface, and additional heat transfer performed as the wall jet can transition to the ‘silo’ cylindrical wall. An optimum H/d was identified between $H/d = 2.6 - 4$, and Nusselt number was found to increase monotonically with Reynolds number.

The presence of film outlet holes between nozzle ‘silos’ is key to minimising the effects of crossflow, and some crossflow was still observed to impact the distribution of Nusselt number on the target surfaces of the outer six jets. Discharge coefficient was shown to be independent of H/d , and increase with Reynolds number.

Chapter 7. Numerical Row and Array Reverse

Jet impingement

Chapter 7 of this book presents a comprehensive analysis of Numerical Row and Array Reverse Jet Impingement. The chapter initiates with an exposition of the Numerical Procedure employed in the study, coupled with an exploration of Grid Independency and the Turbulent Model. The chapter subsequently delves into the phenomenon of Row Reverse Jet Impingement, elucidating the Physical Problem and Boundary Conditions, followed by a rigorous analysis of Results and Discussion. Additionally, the chapter investigates the Effect of Nozzle to Target Spacing Distance on this phenomenon and draws a conclusive remark. Finally, the chapter delves into the Array Reverse Jet Impingement, and sequentially presents the Physical Problem and Boundary Conditions, Results and Discussion, and a Concluding statement. This chapter aims to furnish readers with a thorough understanding of the phenomenon of Reverse Jet Impingement and its effects on target surfaces.

7.1. Numerical Procedure

This study utilized the commercial CFD software ANSYS Fluent 19.2 to provide a comprehensive interpretation of the heat transfer and flow field within the cooling structure of the reverse jet impingement and validated against experimental heat transfer distribution results from Chapter 5 and against an additional experimental Thermochromic Liquid Crystal model of a

single reverse jet impingement nozzle and target for Nusselt number distributions, basic flow and pressure drop measurements.

Using three-dimensional numerical computations, the governing equations have been solved [113]. As a function of air temperature, air properties have been defined. Convergence was achieved using coupled schemes for pressure-velocity coupling, which was defined as the residuals of u , v , w , p , k , and ω being less than 10^{-4} , while the residuals of energy were set less than 10^{-6} , and the average Nusselt number and intake pressure have been observed during the computations to ensure that they reached steady states.

The following sections provide an overview of the governing equation, the finite-volume discretization process, and the solution algorithm.

7.1.1. Fluid Dynamics governing equations

The bedrock of computational fluid dynamics (CFD) resides in the foundational governing equations of fluid dynamics, namely, the continuity equation, the momentum equation, and the energy equation. These equations embody mathematical representations of three essential physical principles that serve as the underlying basis for the entire field of fluid dynamics.

7.1.1.1. Continuity equation

The continuity equation, or conservation of mass, is a fundamental concept in physics. Asserting that within a given domain, the total mass remains constant over time - mass is neither created nor destroyed. The continuity equation can be expressed in the following form[114]:

$$\frac{\partial \rho}{\partial t} + \frac{\partial(\rho u_i)}{\partial x_i} = S_m \quad \text{Equation 7.1}$$

Where ρ is the density, t is the time, u is the velocity, x is the direction, and S_m is the source term.

$$u = \bar{u} + \acute{u} \quad \text{Equation 7.2}$$

Where \bar{u} is the mean velocity and \acute{u} is the fluctuating velocity

Equation 7.1 represents the comprehensive formulation of the mass conservation equation, applicable to both incompressible and compressible flows. The term S_m is a source term, and it corresponds to the mass contribution from the dispersed second phase, such as the vaporization of liquid droplets, in addition to any custom-defined sources.

For steady state, single phase and incompressible flow model, the continuity equation could be simplified to

$$\frac{\partial \bar{u}_i}{\partial x_i} = 0 \quad \text{Equation 7.3}$$

7.1.1.2. Momentum equation

The conservation of momentum is a core principle in physics, alongside the conservation of mass. Momentum is defined as the product of an object's mass and its velocity. The conservation of momentum asserts that, within a given domain, the total momentum remains constant. Momentum is neither created nor destroyed but can only be altered through the influence of forces, as described by Newton's laws of motion. The conservation of momentum is mathematically described by[114]:

$$\frac{\partial(\rho u_i)}{\partial t} + \frac{\partial(\rho u_j u_i)}{\partial x_j} = -\frac{\partial P}{\partial x_i} + \frac{\partial \tau_{ij}}{\partial x_j} \quad \text{Equation 7.4}$$

Where P is the static pressure, τ_{ij} is the stress tensor. The stress tensor τ_{ij} is given by

$$\tau_{ij} = \mu \left(\frac{\partial \bar{u}_i}{\partial x_j} + \frac{\partial \bar{u}_j}{\partial x_i} \right) - \rho \overline{u_i u_j} \quad \text{Equation 7.5}$$

Where μ is the dynamic viscosity.

Simplify:

$$\frac{\partial(\rho \bar{u}_j \bar{u}_i)}{\partial x_j} = -\frac{\partial \bar{P}}{\partial x_i} + \frac{\partial \tau_{ij}}{\partial x_j} \quad \text{Equation 7.6}$$

7.1.1.3. Energy Equation

The conservation of energy, in conjunction with the conservation of mass and the conservation of momentum, constitutes a fundamental principle in physics. Within a specific domain, the total energy remains constant, and energy is not created nor destroyed. While energy can undergo conversion from one form to another, the overall energy within the domain remains constant, as postulated by the first law of thermodynamics. The energy equation can be expressed mathematically in the following form:

$$\frac{\partial \rho E}{\partial t} + \frac{\partial(\rho u_j E)}{\partial x_j} = \frac{\partial P}{\partial t} + \frac{\partial}{\partial x_j} \left(k \frac{\partial T}{\partial x_j} \right) + \frac{\partial(\tau_{ij} u_i)}{\partial x_j} \quad \text{Equation 7.7}$$

where E is the total energy.

Simplify:

$$\frac{\partial(\rho u_j E)}{\partial x_j} = \frac{\partial}{\partial x_j} \left(k \frac{\partial T}{\partial x_j} \right) + \frac{\partial u_i \tau_{ij}}{\partial x_j} \quad \text{Equation 7.8}$$

7.1.2. Shear-Stress Transport (SST) k- ω Model

Menter [115] introduced the shear-stress transport (SST) k- ω model with the aim of combining the robustness and accuracy inherent in the k- ω model's formulation, which performs well in the near-wall region, with the free-stream independence exhibited by the k- ϵ model in the far field. This is accomplished by transforming the k- ϵ model into a k- ω formulation. The SST k- ω model exhibits similarities to the standard k- ω model in its fundamental framework and formulation but incorporates several refinements, incorporating the following enhancements:

- Both models are combined using a blending function. This function has a value of one near the wall, activating the standard k- ω model, and a value of zero away from the surface, activating the transformed k- ϵ model.
- In the SST model, a damped cross-diffusion derivative term is added to the ω equation. This term is important for accurately representing and describing different flow phenomena. The definition of turbulent viscosity is adjusted to consider the transport of turbulent shear stress.
- The SST model uses specific modelling constants, which are selected carefully to ensure its effectiveness and accuracy in capturing flow characteristics and phenomena. The proper choice of these constants is crucial for achieving reliable and realistic simulations in computational fluid dynamics.

The SST k- ω model shares a similar mathematical form with the standard k- ω model. Both models exhibit resemblances in their overall structure and

equations, with certain refinements and additional terms incorporated in the SST k- ω model to enhance its performance and applicability to a wider range of flow scenarios.

Turbulent kinetic energy (k) equation:

$$\frac{\partial}{\partial t}(\rho k) + \frac{\partial}{\partial x_i}(\rho k u_i) = \frac{\partial}{\partial x_j} \left(\Gamma_k \frac{\partial k}{\partial x_j} \right) + \tilde{G}_k - Y_k \quad \text{Equation 7.9}$$

Specific energy dissipation (ω) equation:

$$\frac{\partial}{\partial t}(\rho \omega) + \frac{\partial}{\partial x_i}(\rho \omega u_i) = \frac{\partial}{\partial x_j} \left(\Gamma_\omega \frac{\partial \omega}{\partial x_j} \right) + G_\omega - Y_\omega + D_\omega \quad \text{Equation 7.10}$$

Within these equations, \tilde{G}_k denotes the generation of turbulence kinetic energy resulting from mean velocity gradients. G_ω represents the the specific turbulent dissipation rate of ω . Γ_k and Γ_ω correspond to the effective diffusivity of k and ω , respectively. Y_k and Y_ω refer to the dissipation due to turbulence of k and ω , respectively. D_ω accounts for the cross-diffusion term.

7.1.3. Discretization of Governing Equations

Equation discretization entails the conversion of integral equations or partial differential equations into algebraic equations. The discretization of the governing equations of fluid dynamics involves reformulating these equations in a manner that enables their application in computational fluid dynamics.

ANSYS Fluent divides the computational domain into a number of small control volumes. The transport equation is then integrated over each control volume, and the resulting integral is converted into a discrete equation. This discrete equation expresses the conservation law for the quantity being

transported on a control-volume basis. The control-volume-based technique is a powerful tool for solving fluid flow and heat transfer problems.

The discretization of governing equations can be most effectively explained by considering the conservation equation for the transport of a scalar quantity, which we will denote by ϕ . This is shown by the following integral equation written for an arbitrary control volume, V :

$$\oint \rho \phi u \cdot dA = \oint \Gamma_{\phi} \nabla \phi \cdot dA + \int_V S_{\phi} dV \quad \text{Equation 7.11}$$

Where ρ is density, u is velocity vector, A surface vector, Γ_{ϕ} is diffusion coefficient for ϕ , $\nabla \phi$ is gradient of ϕ , S_{ϕ} is source of ϕ per unit volume, and V is cell volume.

Every cell or control volume within the computational field applies Equation 7.11. The two-dimensional triangular cell illustrated in Figure 7.1 serves as a prime example of these control volumes.

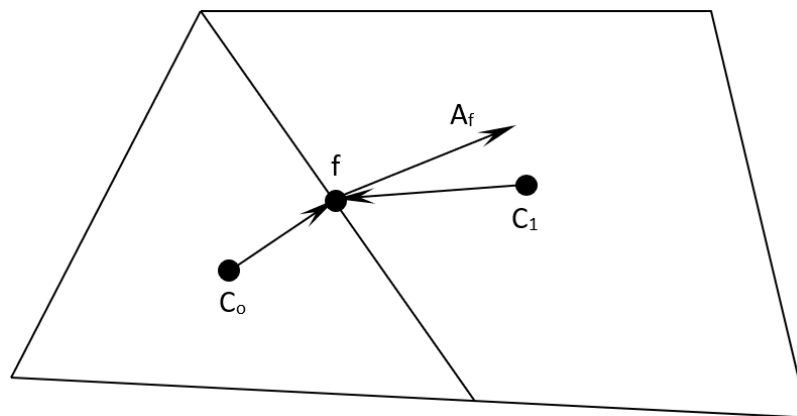


Figure 7.1: A diagram of a control volume that illustrates the discretization of a scalar transport equation

When Equation 7.11 is discretized for a specific cell, it results in:

$$\sum_f^{N_{faces}} \rho_f u_f \phi_f \cdot A_f = \sum_f^{N_{faces}} \Gamma_\phi \nabla \phi_f \cdot A_f + S_\phi V \quad \text{Equation 7.12}$$

Where N_{faces} is number of faces enclosing cell, ϕ_f value of ϕ convected through face f , $\rho_f u_f \cdot A_f$ is mass flux through the face, and A_f is face area.

Equation 7.12, the discretized scalar transport equation, incorporates an unknown scalar variable ϕ located at the cell's centre and unknown quantities in the cells surrounding it. In most instances, this equation is non-linear in relation to these variables. A rendition of Equation 7.12 in a linearized form can be scripted as

$$a_p \phi = \sum_{nb} a_{nb} \phi_{nb} + b \quad \text{Equation 7.13}$$

Where the subscript nb denotes the neighbouring cells, while a_p and a_{nb} represent the linearized coefficients for ϕ and ϕ_{nb} , respectively.

The count of neighbouring cells for each one is influenced by the configuration of the mesh, and it typically corresponds to the number of faces that surround the cell, however cells at the boundary are exceptions.

The discrete values of the scalar ϕ are saved at the centre of each cell, as depicted by c_0 and c_1 in Figure 7.1. Meanwhile, the convection terms in Equation 7.12 necessitate the face values ϕ_f , which must be interpolated from the values at the cell centres. This interpolation is achieved via an upwind scheme. Upwinding signifies that the face value ϕ_f is calculated from data in the cell which is upstream, or 'upwind' with respect to the direction of the normal velocity mentioned in Equation 7.12. ANSYS Fluent provides the

option to select from a range of upwind schemes such as first-order upwind, second order upwind, power law, and QUICK.

To achieve second-order accuracy, quantities at cell faces are calculated employing a multidimensional linear reconstruction method[115]. This technique guarantees higher-order accuracy at cell faces by expanding the cell-centred solution around the cell centroid through a Taylor series. Hence, when second order upwinding is chosen, the face value ϕ_f is determined using the subsequent formula:

$$\phi_f = \phi + \nabla\phi \cdot r \quad \text{Equation 7.14}$$

Where ϕ and $\nabla\phi$ are the cell centre value and its gradient in the upstream cell respectively, while r is the displacement vector from the centre of the upstream cell to the face centre. This equation mandates the computation of the gradient $\nabla\phi$ in every cell.

7.1.4. Flow solver algorithm

In this study, the pressure-based solver has been employed as the chosen method for solving the flow field. The pressure-based solver is commonly utilized for low-speed flows with Mach numbers below 0.3 and incompressible flows. On the other hand, the density-based solver is typically employed for high-speed flows and compressible flows, where the density variations significantly impact the flow behaviour. The decision to use the pressure-based solver in this study aligns with the nature of the flow being investigated, considering its low speed and incompressible characteristics.

Regardless of the chosen method (pressure-based or density-based), ANSYS Fluent utilizes a control-volume-based technique to solve the governing integral equations for mass and momentum conservation, as well as energy and other scalar quantities like turbulence. This technique involves the following components:

1. Dividing the computational domain into discrete control volumes or cells.
2. Applying the conservation equations, such as mass, momentum, and energy, to each control volume.
3. Discretizing the equations using numerical schemes to convert them into algebraic equations.
4. Solving the resulting algebraic equations iteratively to obtain the solution for each control volume.
5. Interpolating and extrapolating the solution values across the control volumes to obtain the continuous representation of the flow field.

By employing this control-volume-based approach, ANSYS Fluent is able to accurately solve the governing equations and provide numerical solutions for various flow and scalar variables within the computational domain.

7.1.4.1. Pressure-based solver

In the pressure-based solver, the pressure field is determined by solving a pressure or pressure correction equation, while the velocity field is obtained from the momentum equations[116]. In contrast, the density-based solver uses the continuity equation to obtain the density field, and the pressure field is determined from the equation of state.

ANSYS Fluent offers two pressure-based solver algorithms for computational simulations: Segregated algorithm solver and coupled algorithm solves. In this study, the coupled scheme has been utilized due to its advantages in achieving a robust and efficient implementation for steady-state flows in a single phase. Compared to segregated solution schemes, the coupled scheme offers superior performance in terms of accuracy and computational efficiency. By adopting the coupled scheme, this study aims to benefit from its favourable characteristics and ensure reliable results for the analysed steady-state flow problems.

7.1.4.2. The pressure-based coupled algorithm

In contrast to the segregated algorithm, the pressure-based coupled algorithm in ANSYS Fluent solves a coupled system of equations that includes the momentum equations and the pressure-based continuity equation. The iterative process of the coupled algorithm follows the steps depicted in Figure 7.2 and outlined below:

1. Update fluid properties, including density, viscosity, and specific heat, based on the current solution. This also includes updating the turbulent viscosity (diffusivity) if turbulence modelling is applied.
2. Solve the momentum equations and the pressure-based continuity equation simultaneously. This involves using the updated values of velocity, pressure, and face mass fluxes.
3. Correct the face mass fluxes, pressure, and velocity field using the pressure correction obtained from the previous step.
4. Solve additional equations for scalars, such as turbulent quantities, and energy, using the current values of the solution variables.

5. Update the source terms that arise from interactions among different phases or components, such as the source term for the carrier phase due to discrete particles.
6. Check for convergence of the equations. If the convergence criteria are not met, repeat steps 1 to 5.

These steps are repeated until the convergence criteria are satisfied, ensuring a reliable and accurate solution.

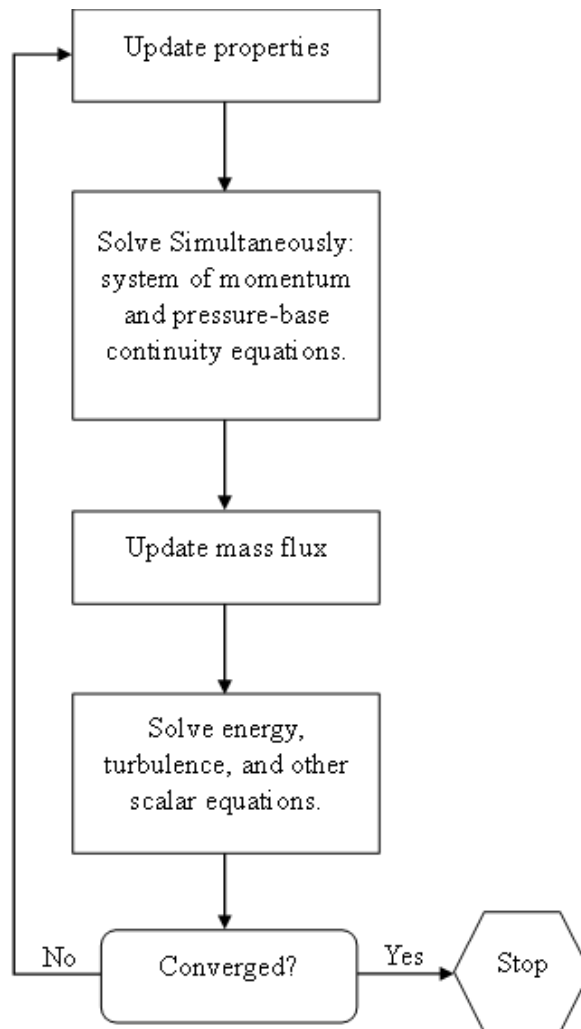


Figure 7.2 The solution Method Overview of the pressure-based coupled algorithm

7.2. Grid independency

A grid independence study was conducted to ensure that the mesh resolution was independent of the results obtained. Tetrahedral volume meshes were utilised during the study and generated using the ANSYS Meshing tool. For the grid independency study, five meshing grids of different element sizes were trailed in sequence: 1, 2, 3, 4, and 5mm. It was calculated that the first layer thickness would be 0.004 mm with an expansion ratio of 1.2, so that the maximum value of the Y plus local on each grid resolution is less than 1.0, and that the skewness value is not greater than 0.8 over the five resolutions. In numerical simulation, the Y+ value represents the distance of the first computational node from the surface of a solid object, normalized by the molecular viscosity of the fluid and the velocity gradient at the surface. A Y+ value of less than one indicates that the first computational node is located very close to the wall and is inside the laminar sublayer. This is important because in the laminar sublayer, the flow is essentially linear and viscous, and turbulence has not yet developed.

Figure 7.2 demonstrates the average Nusselt number results, as well as the discharge coefficients for five meshing grids. By using the Richardson extrapolation method[117], the extrapolation value for an infinitesimal grid (i.e., element size \approx 0mm) was calculated. According to the infinitesimal grid extrapolated values, the deviation of the discharge coefficient as well as the averaged Nusselt number and the discharge coefficient are less than 1% for the 1mm, and 2mm grids. Thus, in order to reduce computational time, a 2mm grid has been adopted.

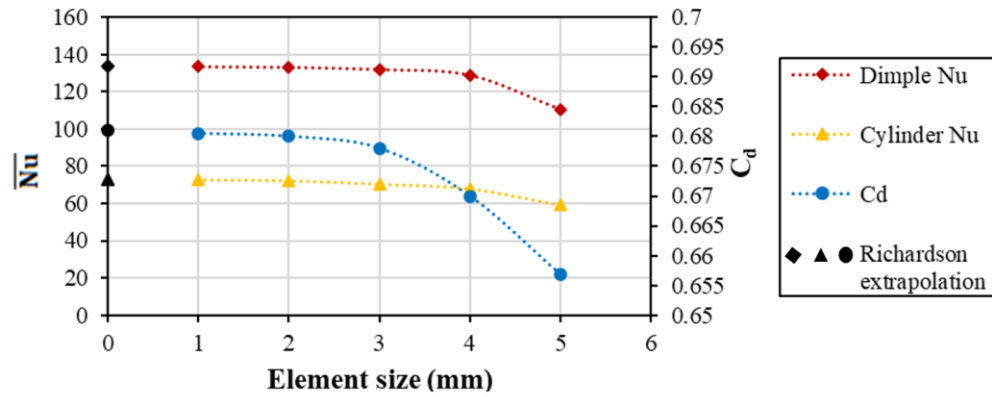


Figure 7.3 Grid independency analysis for 5 different element sizes at $Re=30,000$ and $H/d=4$

7.3. Turbulent model

The Reynolds-Averaged Navier-Stokes (RANS) approach is a mathematical modelling technique widely used in fluid dynamics to simulate turbulent flows. It solves the Navier-Stokes equations by time-averaging the flow variables, which separates the mean flow quantities from the turbulent fluctuations. This approach allows turbulence to be modelled using additional equations, known as turbulence models, which describe the turbulent transport of momentum, energy, and other quantities. The RANS approach is particularly suitable for practical engineering applications, where turbulent flow behaviour is complex and where Direct Numerical Simulation (DNS) is computationally prohibitive. RANS has proven to be an essential tool in computational fluid dynamics (CFD), enabling accurate prediction of mean flow quantities, and the capture of turbulence effects, including the Reynolds stress and other turbulence quantities. Despite its limitations, the RANS approach remains an essential tool for studying and understanding turbulent flows in various engineering and scientific applications.

A comparison of the standard $k-\omega$ [118], and SST $k-\omega$ [119], standard $k-\epsilon$ [120], and Realizable $k-\epsilon$ [121], turbulence models was conducted to assess their ability to predict the heat transfer performance and flow characteristics in reverse jet impingement structures. Figure 7.3 illustrates the comparison between the four turbulent models numerical results and the experimental results for the dimple average Nusselt number. SST $k-\omega$ turbulent model results are generally the closest to the experimental results more than the other turbulence models. In addition to, it is extensively documented in similar literature that SST $k-\omega$ turbulent model was validated with great accuracy to experimental results. Consequently, the SST $k-\omega$ model has been chosen for all further modelling in this study. The same turbulence model has been used in several previous work[122][123].

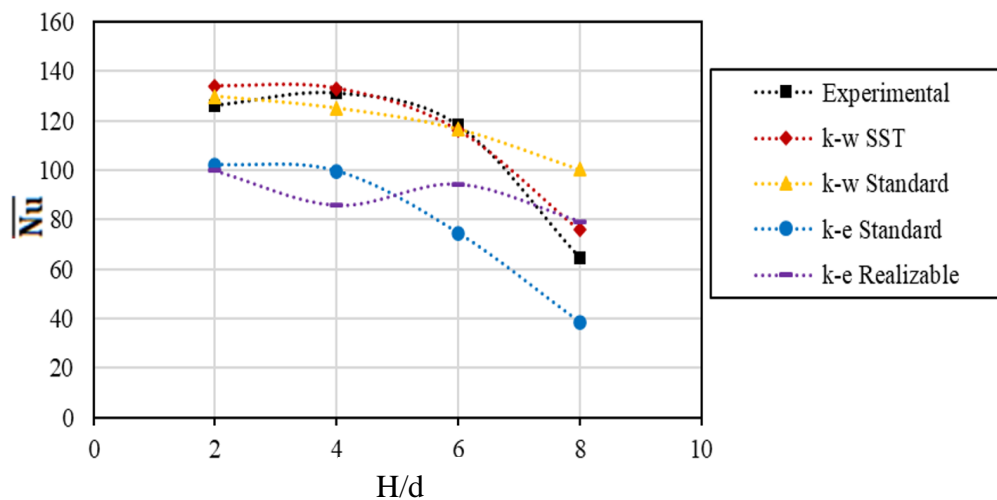


Figure 7.4 Comparing four turbulent models to experimental results at $Re=30,000$ and $H/d=4$

7.4. Row Reverse Jet impingement

7.4.1. The Physical Problem and Boundary Conditions

In this study, the working fluid modelled is air, which is directed evenly towards the row of five square edged jet impingement nozzles, after each jet nozzle, a reverse jet target is modelled, as presented in **Figure 7.5**. Nozzle diameter, d for all jets is 25mm, the jet-to-jet separation distance equals 3.4 nozzle diameters, the crossflow channel height and the nozzle plate thickness both equal one jet diameter. All nozzles are concentric with the reverse jet 'silos'. The reverse jet target system comprises a hollow cylinder and a hemispherical dimple. The diameter of the cylinder and the dimple is the same, D , and equals 3.2 nozzle diameters. For the purpose of setting the same average jet Reynolds number for all study cases, the mass flow rate of air is constant for each case, $Re = 23,000$. Several variables, such as the orientation of the inlet and outlet flow, as well as the distance from the nozzle to the target surface, can be evaluated to quantify how they affect the flow characteristics.

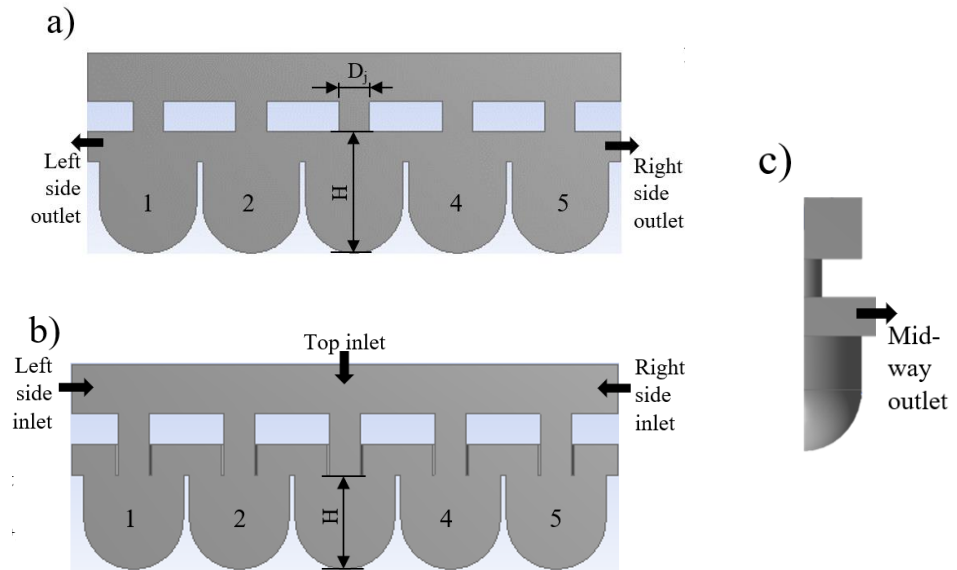


Figure 7.5 Cross-section views for reverse impinging jet arrangement with different nozzle configurations: a) square nozzle, b) extended nozzle and c) side view.

For inlet conditions, the temperature is set to 298K and the turbulence intensity to 10%. Zero-gauge pressure is set as the outlet boundary condition. At the target surface, 1000 W/m^2 of heat flux is applied. Other walls are subjected to adiabatic conditions, and all walls are subjected to a non-slip shear condition. The inlet conditions can be varied between a uniform flow from the top, left or right of the inlet plenum, to simulate arrangements in different specific applications. The outlet conditions can again be varied between the left, right, and midway outlets, for variations in the outlet crossflow. To replicate the results obtained in Chapter 5, the effects of an extended nozzle were also modelled numerically. The overall numerical test schedule for this study is detailed in

Table 7.1.

Table 7.1 Row jet impingement study cases

	Crossflow	Nozzle	Inlet	H/d
1	Max.	Square	Top	3
2	Med.	Square	Top	3
3	Min.	Square	Top	3
4	Max.	Extended	Top	3
5	Max.	Extended	Left	3
6	Max.	Extended	Right	3
7	Max.	Extended	Top	1.6
8	Max.	Extended	Top	5
9	Max.	Extended	Top	7

7.4.2. Results and Discussion

7.4.2.1. Effect of crossflow

The effect of crossflow was investigated using the sharp square edged nozzles and top inlet conditions with the three outlet crossflow configurations. Figure 7.6 presents the Nusselt number distributions results on the target dimple and the cylindrical side walls surfaces. Figure 7.6 and Figure 7.5. Show the local and average Nusselt number distribution, respectively. The objective was to determine how crossflow mechanisms contribute to the overall cooling effect.

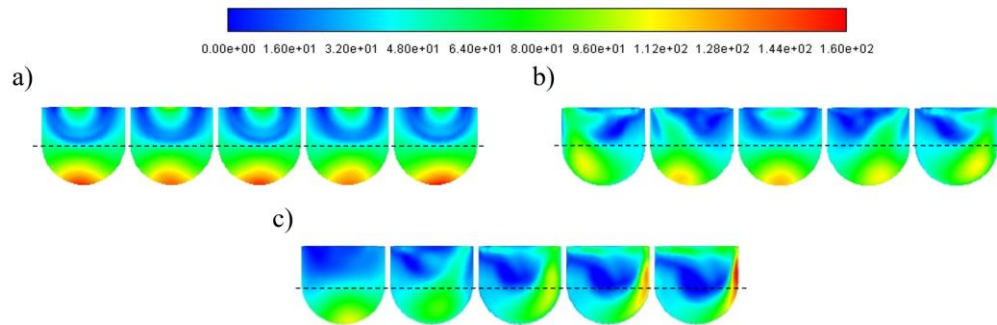


Figure 7.6 Crossflow configuration effect on Nusselt number distribution: a) minimum crossflow, b) medium crossflow, and c) maximum crossflow

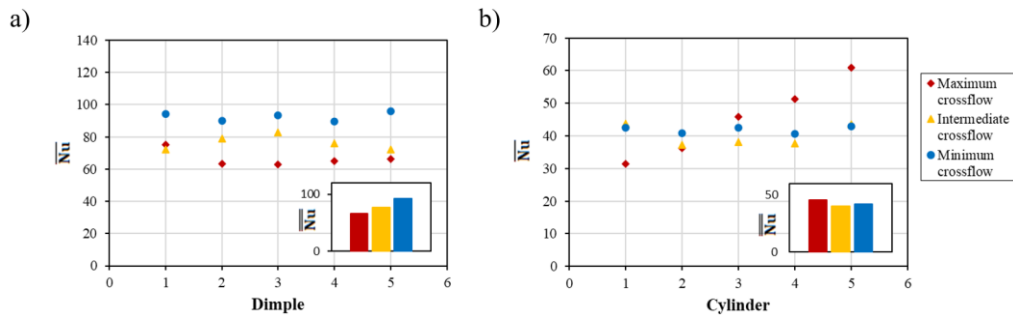


Figure 7.7 Crossflow configuration effect on averaged Nusselt number at $Re=23,000$ and $H/d=4$: a) dimples, b) cylinders

When the impinging jet exits the nozzles, it impinges upon the target , which is exposed to the stagnation region of the jet, which results in the highest heat transfer throughout the geometry. A wall jet is formed when the flow continues radially outwards and flows parallel to the surface of the cylinder as it travels towards the outlets. Using the 'dimple' surface as a specific example, it can be seen that when crossflow is increased, average heat transfer across the whole array is reduced by 17% for intermediate crossflow conditions, and by 28% for maximum crossflow conditions. Although a reduction in average is observed when crossflow is present, only very little variation in Nusselt number is seen between each of the five 'dimples', especially in the minimum crossflow case, where deviation is uniform and below 2%. The velocity contours in Figure 7.8a offer a simple explanation for this heat transfer uniformity between individual jets for the crossflow

minimum condition. The highest heat transfer is observed in the central, 3rd jet of the intermediate crossflow condition, followed by 7% decreases in Nu for each jet in the direction of the crossflow exits. A similar conclusion can be drawn from the velocity flow fields shown in Figure 7.8b.

According to the maximum crossflow case, the maximum heat transfer can be observed in jet 1, which experiences the least amount of crossflow, but for jets 2 to 5, a deviation of just 2.3% can be seen, and there is no decrease in 'dimple' heat transfer as crossflow increases towards the outlet. An inversely proportional relationship exists between two contributing factors that may explain the lack of diminished heat transfer. Firstly, an increased crossflow has the effect of deflecting the jet away from the stagnation point at the dimple concave, resulting in a reduced Nusselt number. A second effect, which negates the loss, is that because of the arrangement of the outlet, a downward pressure gradient is formed within the target cavity, which decreases from jet 1-5. This results in a greater pressure drop over jets 4 and 5, which in turn results in a higher velocity, and therefore a higher Reynolds number. In due course, this increased jet Re will result in an increased nu. The combination of the effects of the crossflow, and jet to jet Re variation mitigate each other's effect when the exit is located to the right of the test section. This results in a 'dimple' heat transfer (Figure 7.8c).

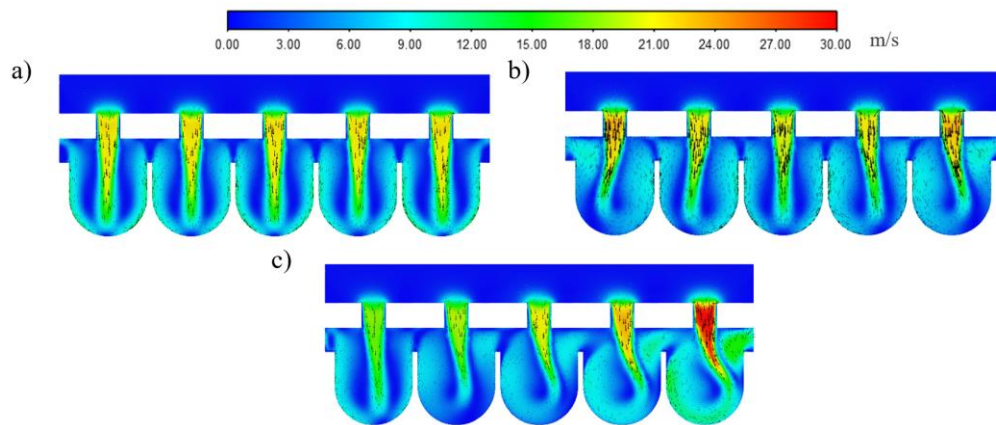


Figure 7.8 crossflow configurations effect on velocity contours at $Re=23,000$ and $H/d=4$: a) minimum crossflow, b) medium crossflow, and c) maximum crossflow

As the air impinges on the 'dimple' surface, it flows towards the exits and crosses the side walls of the cylinder, which enhance heat transfer. In contrast to the initial impingement mechanism, the slightly cooler fluid now develops a thicker boundary layer against the wall, resulting in a lower average Nu value for this surface, as shown in the difference between the average Nu values for the dimpled and cylindrical surfaces in Figure 7.5.

While the numeric value for Nu for the 'cylinder' is 46% lower than for Nu for the 'dimple', the average heat transfer coefficients for both intermediate and minimum crossflows are similar (Figure 7.6). Similarly, both the minimum crossflow case and the intermediate case again demonstrate uniform Nu across jets, with the intermediate case now demonstrating a very similar, but opposite increase in Nu of $\approx 7\%$ as subsequent jets move in the crossflow direction. It has been previously discussed that the impinging jets closest to the crossflow outlets move the impingement force away from the centre of the concave 'dimple' and towards the sides of the 'cylinder' (Figure 7.8).

Analysis of the wall heat transfer effect of the cylinder in the maximum crossflow case indicates that the effect is significantly different. As shown in Figure 7.6, the average Nu increases significantly with crossflow direction. Nu increases by 93% from jet 1 to jet 5. The cylinder Nu at jet 5 is found to be only 9% lower than that of the dimple. Based on the analysis, it appears that the high Nu in this region is caused by jet deflections towards the sidewalls, and the increased Re previously discussed, shown in Figure 7.8c, and a large swirl effect. Swirling occurs as a result of the jet being displaced from the centre, causing the jet to travel along the right-hand wall of the cylinder, around the concave dimple, and back up the left-hand wall before exiting the cylinder. The flow along the 'cylinder' wall will have a relatively high velocity, Re, and therefore Nu as compared to the typical case in which impingement initially leads to localised stagnation.

7.4.2.2. Effect of nozzle configuration

The nozzle was extended to be level with the crossflow channel to reduce the crossflow effects which were observed with the basic, sharp-edged nozzle. This was also tested experimentally in Chapter 5. As can be seen in Figure 7.9, extended nozzles are highly effective in eliminating crossflow effects on Nu.

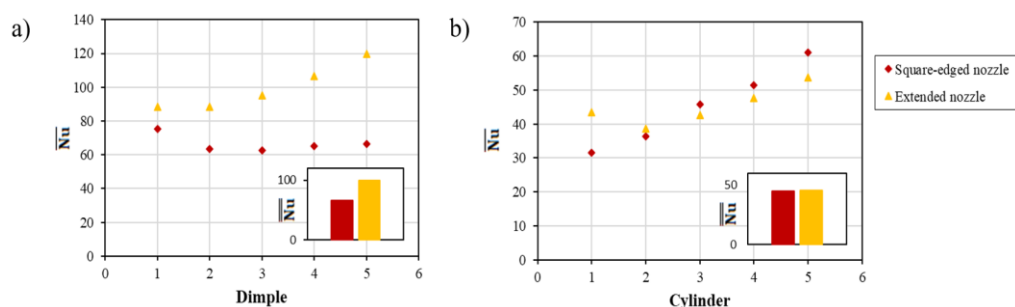


Figure 7.9 Effect of nozzle configuration on the area averaged Nusselt number at Re=23,000 and H/d=4: a) dimple, b) cylinder

For the purpose of reproducing a typical arrangement, we set an inlet on top and an outlet on the right during this batch of testing. Due to this, a higher ΔP will be observed above the jet nozzles in proximity to the outlet as illustrated to Figure 7.10. Variation in ΔP between successive jets generally results in a higher Re and, consequently, a higher Nu in subsequent jets.

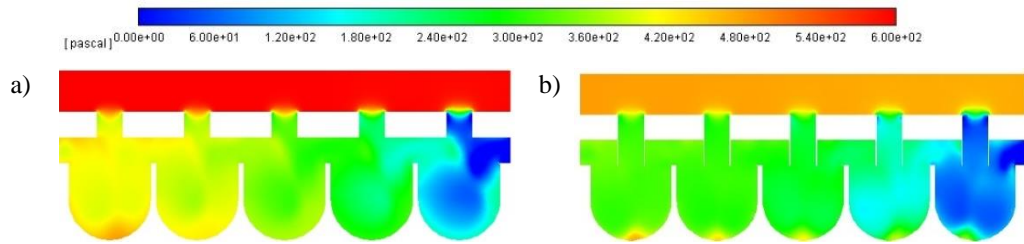


Figure 7.10: Effect of nozzle configuration on pressure contour at $Re=23,000$ and $H/d=4$: a) square edged nozzle, b) extended nozzle

As illustrated in Figure 7.11, the combination of crossflow effects from jets 1 to 5 offsets this ΔP effect, resulting in a relatively level Nu between the 5 jet targets. Further analysis of this 'cylinder' surface shows that subsequent crossflow effects deflect the jet core away from its natural target at the dimple and speed it up toward the walls of the cylinder. The deflection results in an unexpected increase in 'cylinder' wall Nu from jets 1 to 5, as shown in Figure 7.9b, which reduces 'dimple' surface heat transfer.

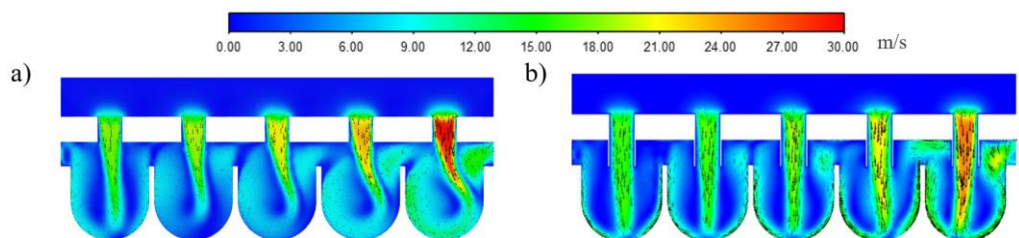


Figure 7.11 Effect of nozzle configuration on the velocity contour at $Re=23,000$ and $H/d=4$: a) square edged nozzle, b) extended nozzle

By extending the nozzle geometry, the Nusselt number is increased by an average of 50% at the dimple surface (Figure 7.9a). The ΔP effect, which results in higher Nu of jets near the outlet, is unaffected by the extension of the nozzle, while crossflow effects are virtually eliminated. Consequently, the most dramatic increases in Nu are observed in jets closest to an outlet location, although all jets exhibit an increase in Nu.

By reducing the crossflow 'deflection' of the jet towards the cylinder walls, the extended nozzle has an adverse effect on the 'cylinder' wall heat transfer (Figure 7.9b). Due to the extended nozzle jet's primary objective of increasing the Nu on target 'dimple' surfaces, it is only possible to observe an increase in Nu at the wall of the 'cylinder' that is a fraction of 1% and, therefore, is not statistically significant.

The extended nozzle demonstrated extraordinary ability to mitigate crossflow effects, providing an overall Nusselt number improvement of 50% over the basic nozzle design.

7.4.2.3. Effect of inlet configuration

Several simulations were conducted with variations in the inlet configuration in order to determine the effect of inlet configuration on the extended nozzle. Air was injected from the top, right side, or left side. In all simulations, the extended nozzle was used, as well as the maximum crossflow scenario in which all air exits from the right side outlet.

Nu values on the cylinder are 47.4% lower on average than those on the dimple section in all cases. Due to the ΔP effect, both the dimple surface as

well as the cylinder surface have higher Nu values in subsequent jets in a crossflow direction.

According to Figure 7.12, jet 5 was the highest Nu due to its high Re in all configurations and locations. The increased Re was caused by the ΔP effect due to its proximity to the outlet, particularly when a high-pressure inlet is also located nearby. As shown in Figure 7.13b, the simplest flow path has the left-side inlet and right-side outlet to accommodate the pressure gradient decreasing from left to right through the jets. As a result of this more even pressure gradient, average Nu slightly increases, although the highest Nu values are produced at jets 5. This lack of high Nu at jet 1 close to the inlet is a result of an increased crossflow over the jet 1 nozzle inlet in the main plenum.

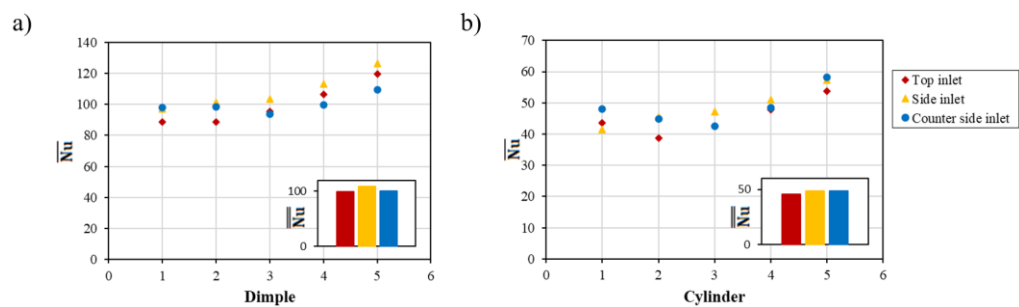


Figure 7.12 Effect of inlet orientation on the averaged Nusselt number at $Re=23,000$ and $H/d=4$: a) dimples, b) cylinders

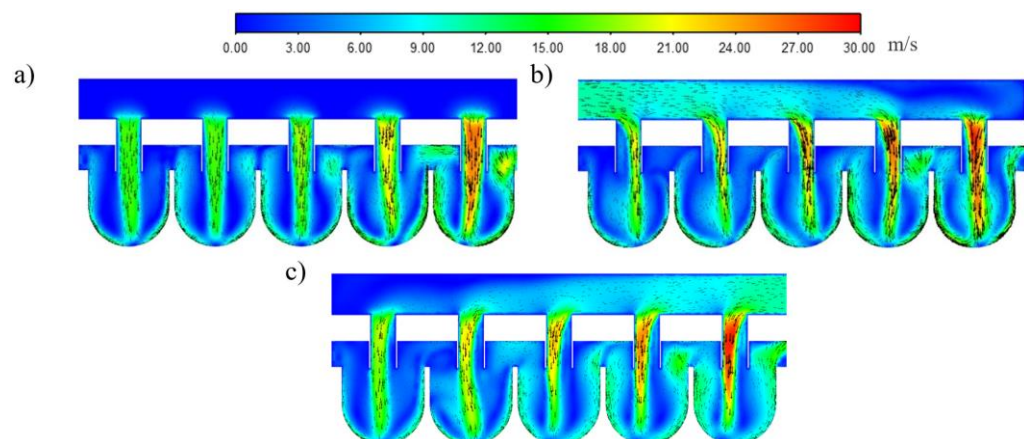


Figure 7.13 Effect of inlet orientation on the velocity contours at $Re=23,000$ and $H/d=4$: a) top side inlet, b) left side inlet, c) right side inlet

There was no significant advantage to any of the three variations of the inlet orientation. Since the flow path from the left side outlet to the right-side inlet was simple, Nu values on the left side inlet were marginally higher.

7.4.3. Effect of nozzle to target spacing distance

Lastly, to optimize the heat transfer in this geometry arrangement, the distance between the nozzles and target surface was examined. Considering that the independent variable in this study was the spacing between the nozzle and the target, a 'pipe' type nozzle with a constant 'top' inlet and 'maximum crossflow' right side outlets was used. The work was done using four variations of H/d , namely $H/d = 3, 5, 7$ and the theoretical minimum of $H/d = 1.6$, in which the wall length of the cylinder is set to zero and only the dimple remains.

A study of Nu distributions at the 'dimple' surface for $H/d = 1.6, 3, 5$ and 7 confirmed the general trend of increased Re and consequently Nu in the crossflow direction, as illustrated in Figure 7.14 and Figure 7.15. Based on the $H/d = 7$ case, Nu values were significantly lower, with a diminishing heat transfer in the crossflow direction. The flow analysis indicates that the potential core of the jet had trouble stagnating at the 'dimple' target surface at jet 1, with crossflow deflection reducing this property even more. The $H/d = 5$ case also showed some diminishment effect, although this was relatively insignificant.

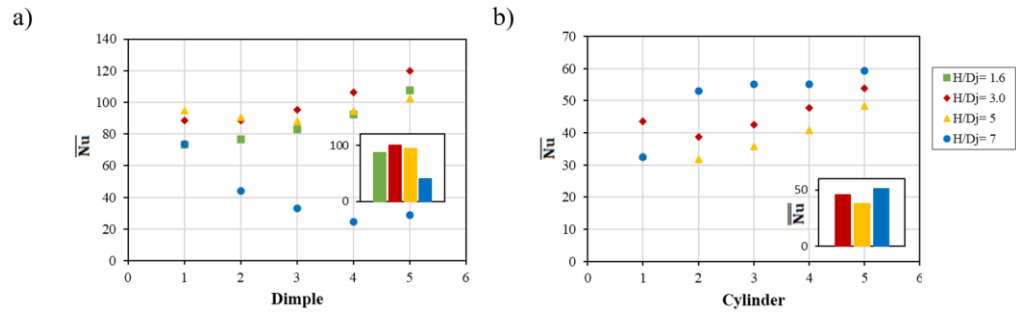


Figure 7.14 Effect of Nozzle-to-target spacing distance on the averaged Nusselt number at $Re=23,000$: a) dimples, b) cylinders

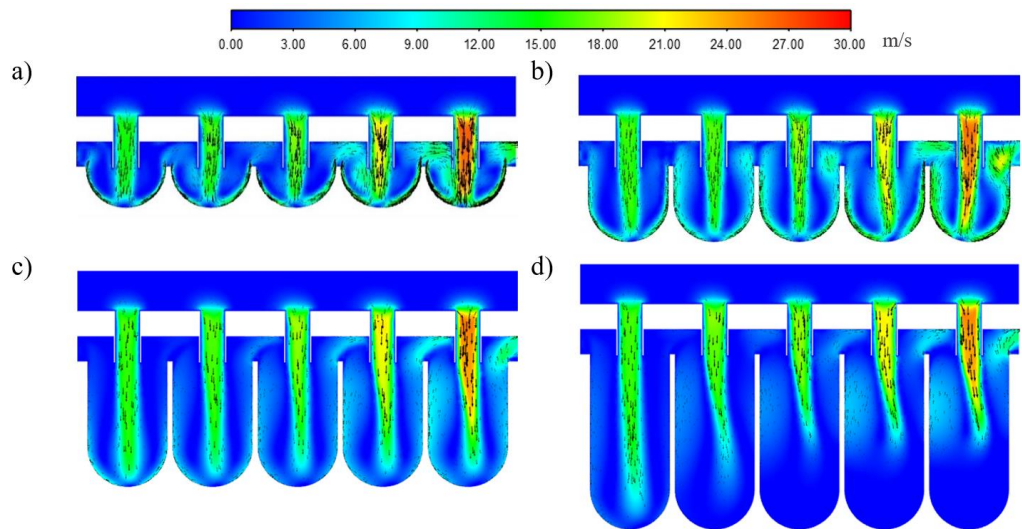


Figure 7.15 Effect of Nozzle-to-target spacing distance on the velocity contours at $Re=23,000$: a) $H/d=1.6$, b) $H/d=3$, c) $H/d=5$, d) $H/d=7$

It was observed that the optimum impingement heat transfer against the ‘dimple’ surface occurred at $H/d = 3$, with Nu values 15%, 6%, and 144% higher than those at $H/d = 1.6, 5$, and 7 , respectively. Accordingly, an optimal spacing distance is near the $H/d = 3$ nozzle-to-target spacing distance.

It is important to note that a larger heat transfer surface will promote greater levels of heat transfer overall when considering the additional heat transfer that is contributed by the cylinder wall portion of the reverse jet impingement geometry. On the average, Nu wall values for cylinders are half the magnitude of those for ‘dimples’. Despite the absence of target surface impingement stagnation in the $H/Dj = 7$ case, it is expected that the cylinder

walls will observe the highest velocity flow, which will result in a higher localised heat transfer, particularly at the edges of the cylinder.

Considering both dimple surface and cylindrical surface heat transfer effects, it has been determined that the $H/D_j = 3$ case provides the best overall heat transfer.

7.4.3.1. Discharge coefficient

For the potential flow combinations of the geometry, a final numerical study was conducted in order to determine the discharge coefficient. Figure 7.16a illustrates that an increase in flow area at the outlet leads to an increase in the discharge coefficient. The Figure 7.16b shows that there is very little change in C_d following modification of the inlet location. The top inlet condition is the highest, while the counter inlet is the lowest.

It is observed that the discharge coefficient varies very little with variation in H/d as shown in Figure 7.16 c, where slightly higher C_d values are observed as H/d increases due to less interference from the typically high-pressure stagnation zone generated at lower H/d values.

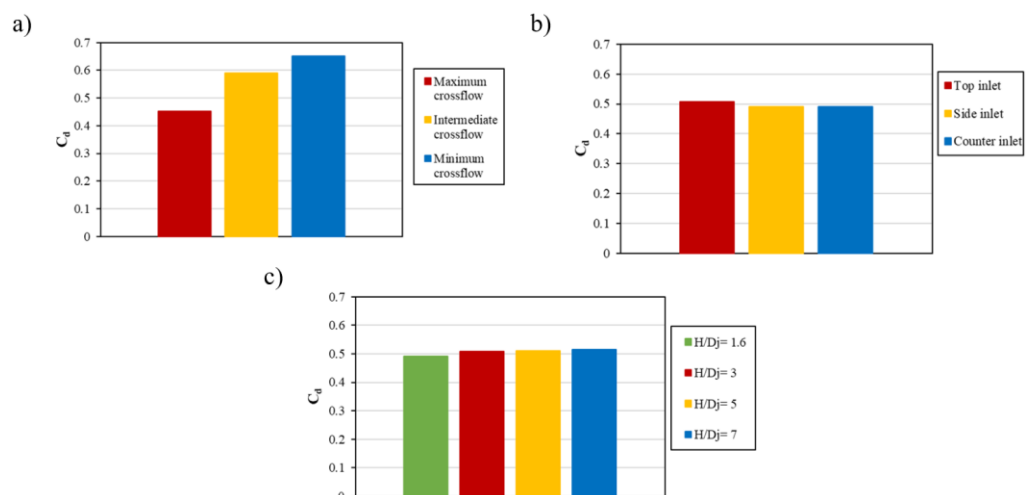


Figure 7.16 The relationship between the averaged discharge coefficient and a) crossflow configuration, b) Inlet flow configuration, c) nozzle-to-target spacing distance at $Re=23,000$.

7.4.4. Summary

CFD was used to analyse a novel reverse jet impingement geometry. For procedural optimization of the arrangement, variations of the nozzle geometry, inlet geometry, and outlet conditions were tested in order to increase its effectiveness.

- Initial testing indicated that crossflow effects were still significant in the reverse jet impingement geometry.
- Extending nozzle to the level of the crossflow channel significantly decreased the crossflow effect and enhanced the heat transfer.
- Variation of inlet orientation was analysed in detail, but no significant improvement in the heat transfer was found.
- Different nozzle-to-target spacing distance has been investigated and the optimum spacing distance is around three jet diameters.
- The most significant variable in determining the nozzle discharge coefficient was the crossflow configuration, where a maximum outlet flow area generated the highest discharge coefficient.

Based on the results of the numerical study, an extended nozzle was determined to be the optimal reverse jet impingement arrangement. Due to its high resistance to crossflow, this design can be applied to a wide range of inlet and outlet configurations.

7.5. Array Reverse Jet impingement

Developing and validating against the experimental work conducted in Chapter 6, a numerical study was conducted on the reverse jet impingement in an array configuration, utilising a similar methodology as utilised in Row Reverse Jet impingement7.4.

7.5.1. The physical problem and boundary conditions

For this numerical study, two variations of jet impingement array target were numerically evaluated; inline and staggered, as shown in Figure 7.17 b and c respectively. These were also referenced against a flat plate baseline target, as shown in Figure 7.17 a.

The nozzle configuration for this study was chosen as extended nozzles, to provide the introduced protection against the negative effects of crossflow, and is shown in Figure 7.17. The outlet for flow is the maximum crossflow condition, and is to the right of each test section, to simulate extreme crossflow effects.

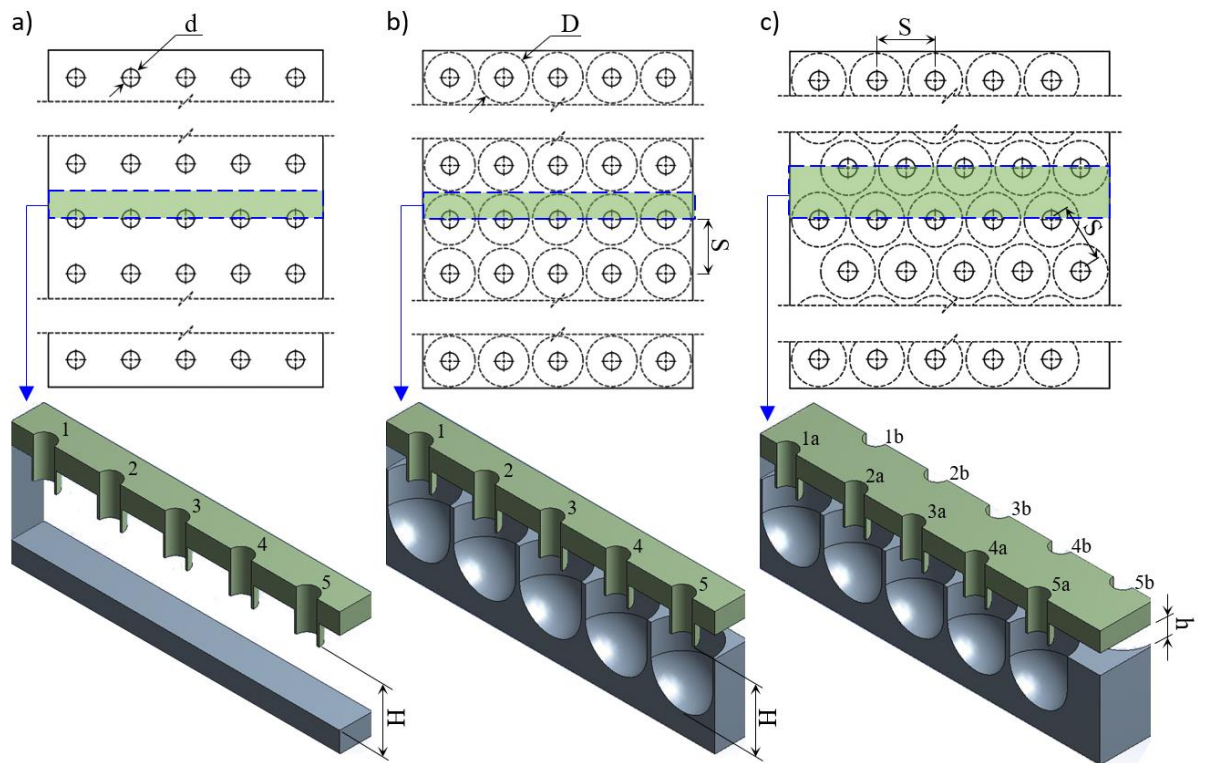


Figure 7.17 Jet impingement arrangements: a) in-line jet impingement, b) in-line reverse jet impingement, and c) staggered reverse jet impingement

7.5.2. Results and discussion

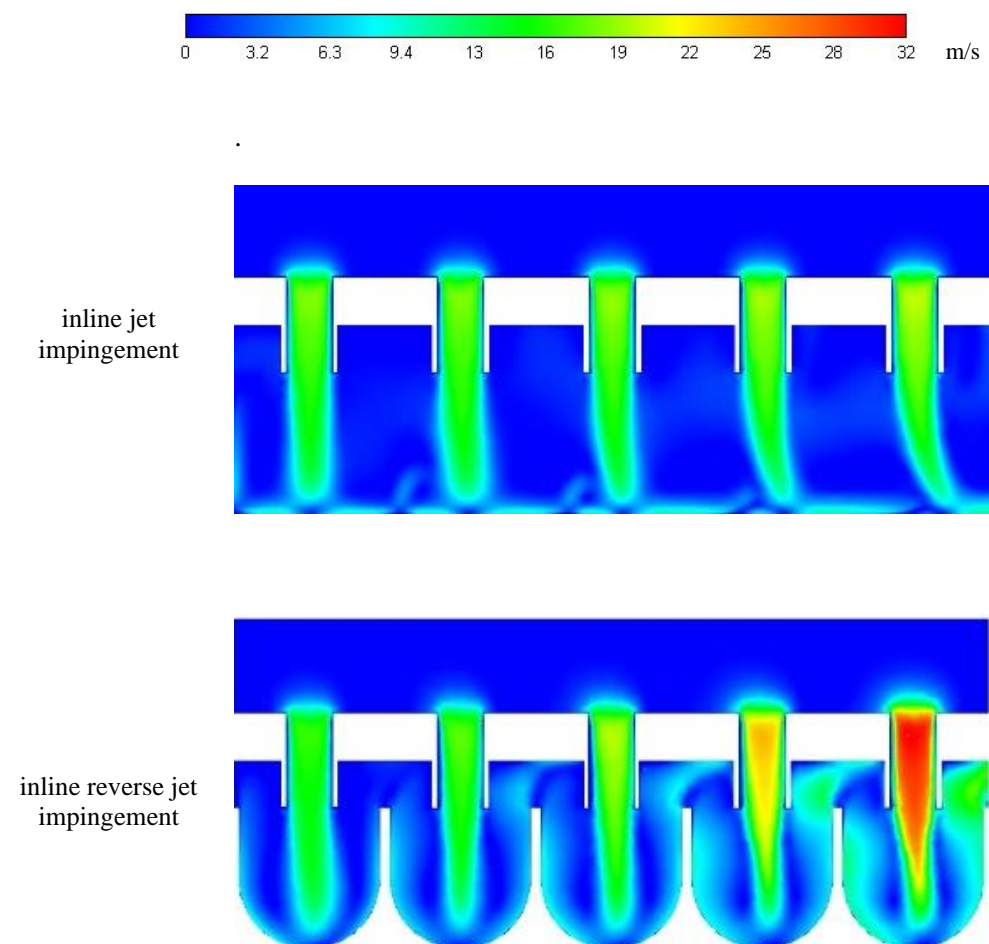
7.5.2.1. Flat, in-line vs. staggered

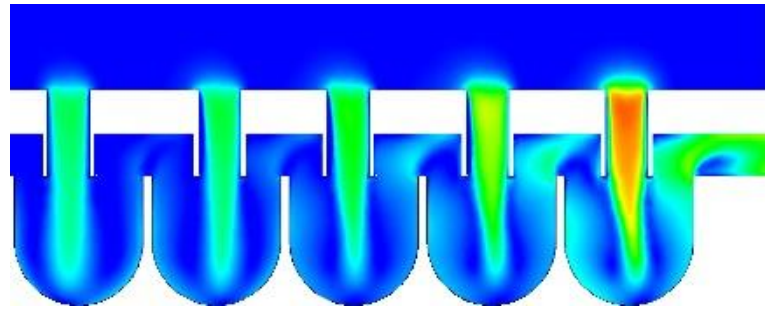
The influence of crossflow is observable across all examined geometries, as evidenced by the progressively higher jet deflection angles from the intended dimple concave minimum as the number of impinging jets increases. This behaviour can be attributed to the accumulation of spent impingement flow in the target plenum, which is believed to cause the observed deviations from the intended jet configuration.

When observing the characteristics of the deflection, Figure 7.18, for the flat plate target, the fifth jet, can be seen to have continuous crossflow deflecting force through the entire height from its nozzle to the target,

producing a continued deflection. When studying the characteristics of the jet deflection for both inline and staggered targets, the deflection can be seen to only have a deflective force closer to the nozzle exit. This produces an overall improvement in resistance to jet deflection from crossflow.

The variation in velocity between the five jets is seen to be more significant in reverse jet impingement designs, due to the relatively decreased outflow cross-sectional area for spent air between jets, and at the outlet. This reduced cross-section produces a larger pressure drop over these crossflow channels, and therefore the relative pressure drop over the nozzles closest to the outlet are larger.





staggered reverse
jet impingement

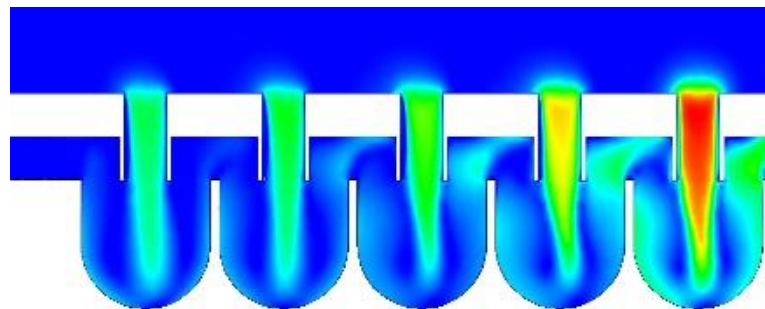


Figure 7.18 Target geometry influence on flow velocity contours at $H/d= 4$ and $Re= 30,000$

Figure 7.19 shows the distribution of Nusselt number on the constituent target faces of each geometry. The inline jet impingement against a flat plate shows the crossflow deflection effects on each subsequent jet. It can be observed that secondary flows form as the spent air migrates away from the stagnation point, and towards the side wall. The fountain region disappears with subsequent jets, as the upstream wall jet cannot overcome the spent air crossflow.

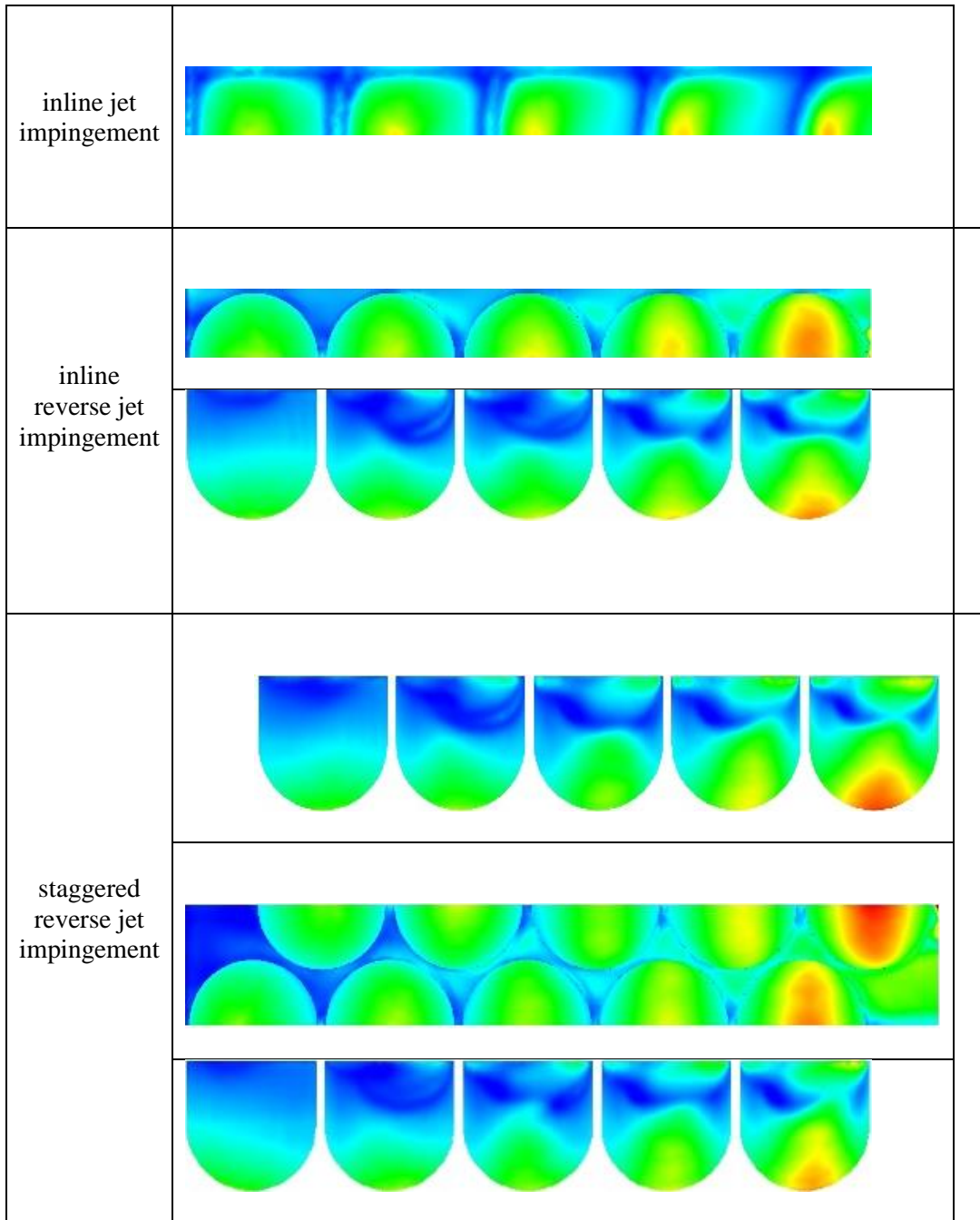
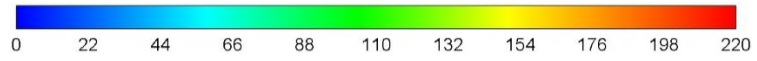


Figure 7.19 Target geometry influence on local Nu distribution at $H/d=4$ and $Re=30,000$

Figure 7.20 shows the heat transfer enhancement of the inline and staggered reverse jet impingement array relative to the flat target assessment. The heat transfer enhancement is broken down into three heat transfer surfaces; the initial impingent target ‘dimple’, the side wall ‘cylinder’ surfaces, and the ‘Upper face’ surface at the top of each silo.

This figure shows that the overall enhancement to heat transfer rate is significant for the reverse jet impingement proposed design. The majority of heat transfer in each reverse variation is focussed on the dimple surface, in proximity to the stagnation point, with additional heat transfer occurring as the wall jets pick up heat from the cylindrical ‘silos,’ the relative distribution between the cylinder and dimple surfaces remains consistent between jets, showing that the deflection in this case does not affect the jets’ ability to target the dimple surface. The increase in overall heat transfer enhancement with jet number is due to the relatively increased pressure drop, and therefore a variation in the effective Reynolds numbers between the five jets.

Limited heat transfer occurs on the top ‘upper face’ surface of the cylinder walls, and is dominated by the Reynolds number, and therefore flowrate through the crossflow and outlet gaps. As the crossflow channels maintain constant cross-section between all jets, the air velocity increases with increasing mass of spent air and is reflected as an increasing Nusselt number on the upper face with increasing jet number.

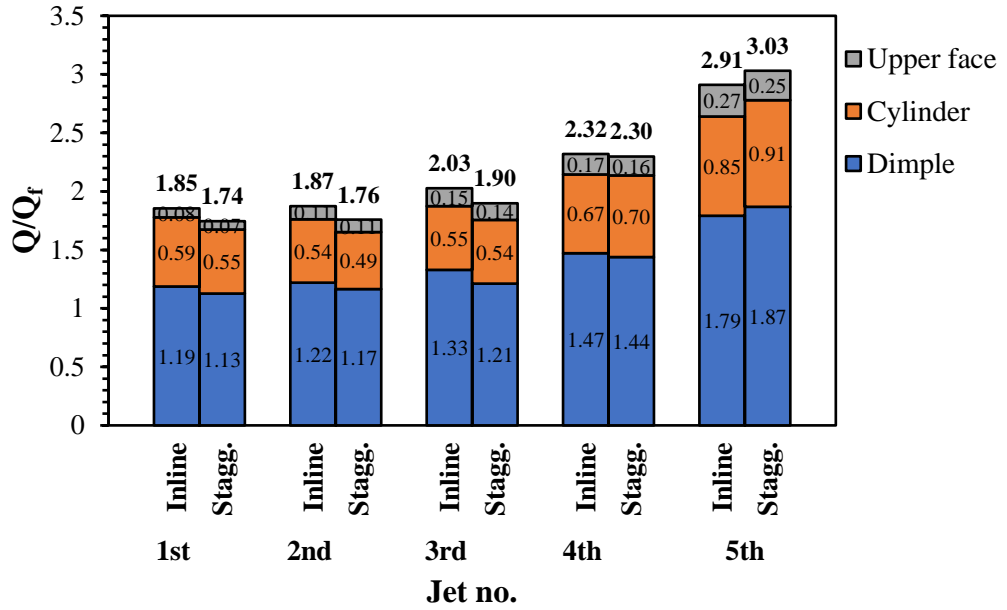


Figure 7.20 Comparison between the heat transfer and flat target heat transfer ratio (Q/Q_f) of inline and staggered jet arrangement at $H/d=4$, $Re= 30,000$

Figure 7.21 shows the effects of crossflow on subsequent jet targets for both the baseline flat target case, and for the constituent dimple and cylinder faces for both the inline and staggered reverse jet impingement at a Reynolds number of 30,000 and H/d of 4.

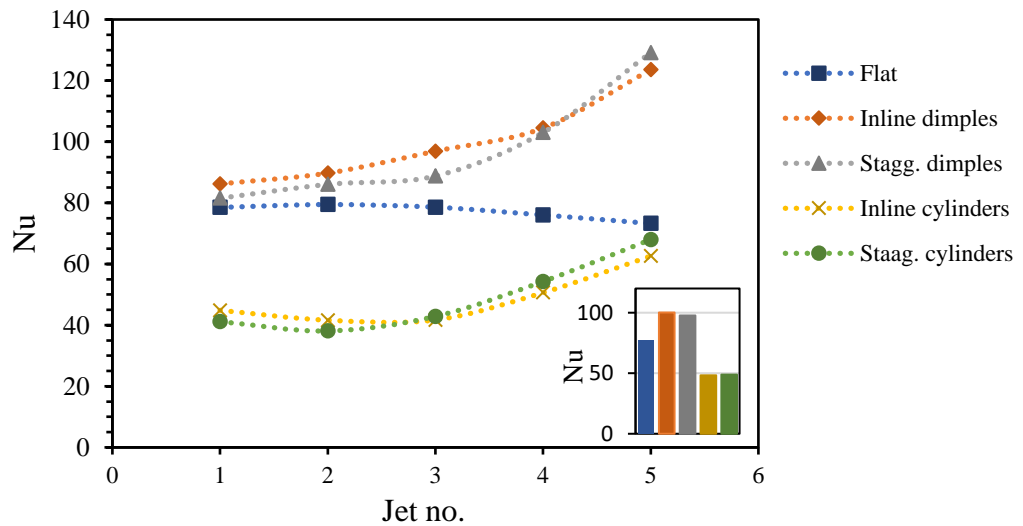


Figure 7.21 Comparison between average Nu of inline and staggered jet arrangement at $H/d=4$, $Re= 30,000$

Overall, the discharge coefficient can be seen to decrease for the reverse design relative to the flat plate baseline, as shown in Figure 7.22, due to the added complexity and pressure drop in the target plenum. However, the inline and staggered arrangements are shown to have very similar discharge coefficients.

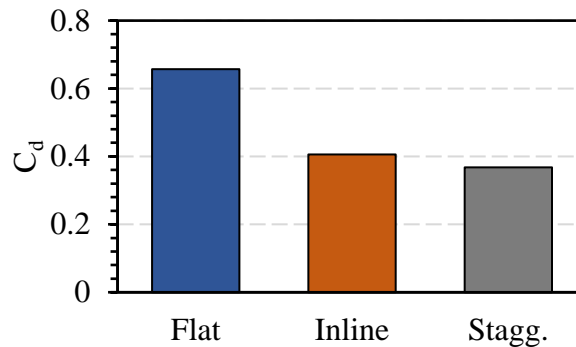


Figure 7.22 Target geometry influence on discharge coefficient at $H/d=4$, $Re=30,000$

7.5.2.2. Number of jets effect

The effects of crossflow were tested for a range of nozzles in an impingement row. This allows the cumulative effects to be shown dependent on overall jet number. Figure 7.23 shows how the jet number effects velocity distribution in the jet centreline. With three nozzles and targets, the crossflow effects can be seen to have relatively little impact on the jet deflection. When a row of seven jets is used, the crossflow effects are far more significant, with extreme deflection and recirculation occurring in jet 7. When comparing just the first three of seven jets to the three only jets, a very different potential core behaviour is observed. This difference is likely due to the downstream pressure differences in the outflow direction.

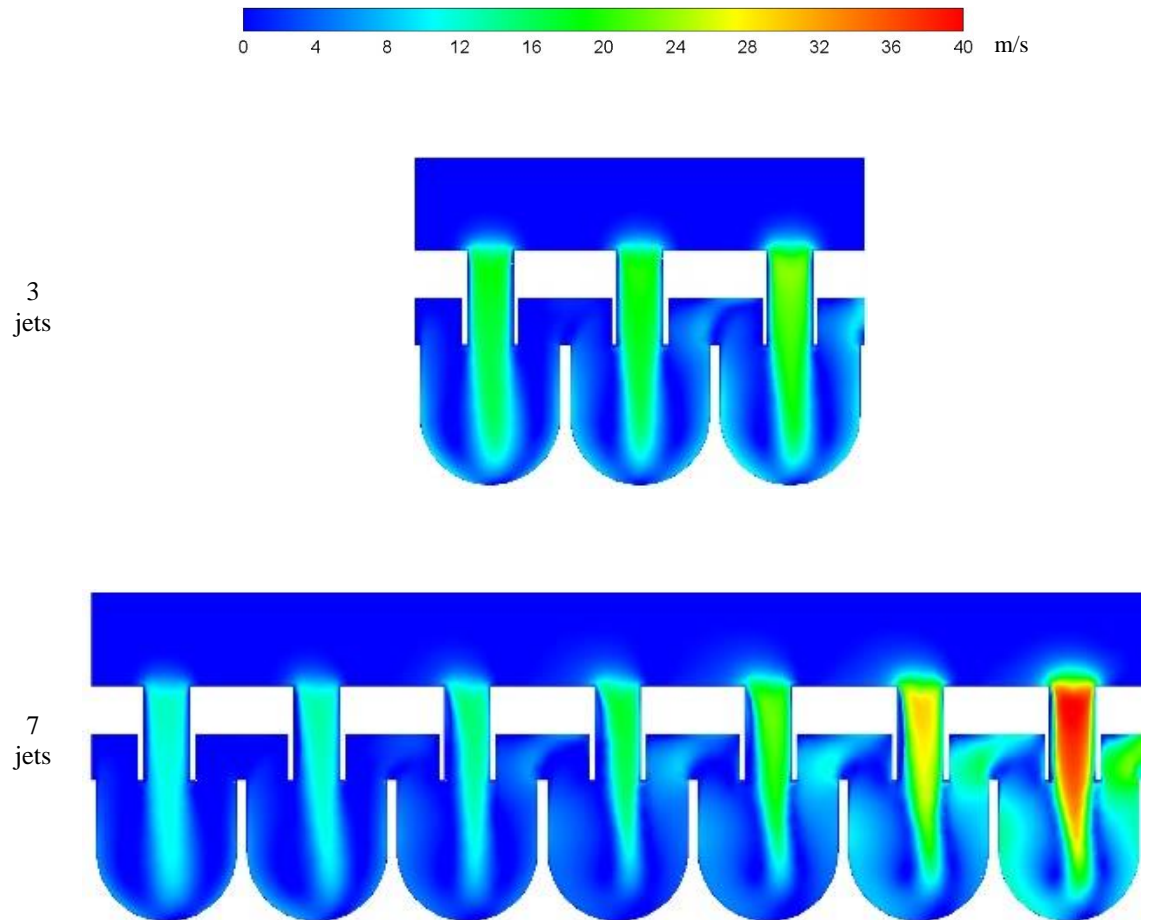


Figure 7.23 Number of jets influence on flow velocity contours at $H/d= 4$ and $Re= 30,000$

The effect of this jet nozzle number variation on Nusselt number distribution is shown in Figure 7.24. The nozzles in closer proximity to the outlet have greater Nu, this is due to the absence of any deflection effects, and the relatively large pressure drop between entrance and exit, cause by its proximity to the outlet. This effect is also apparent where seven jets are utilised, and additional distortion to the typical Nu distribution are clear with subsequent jet number.

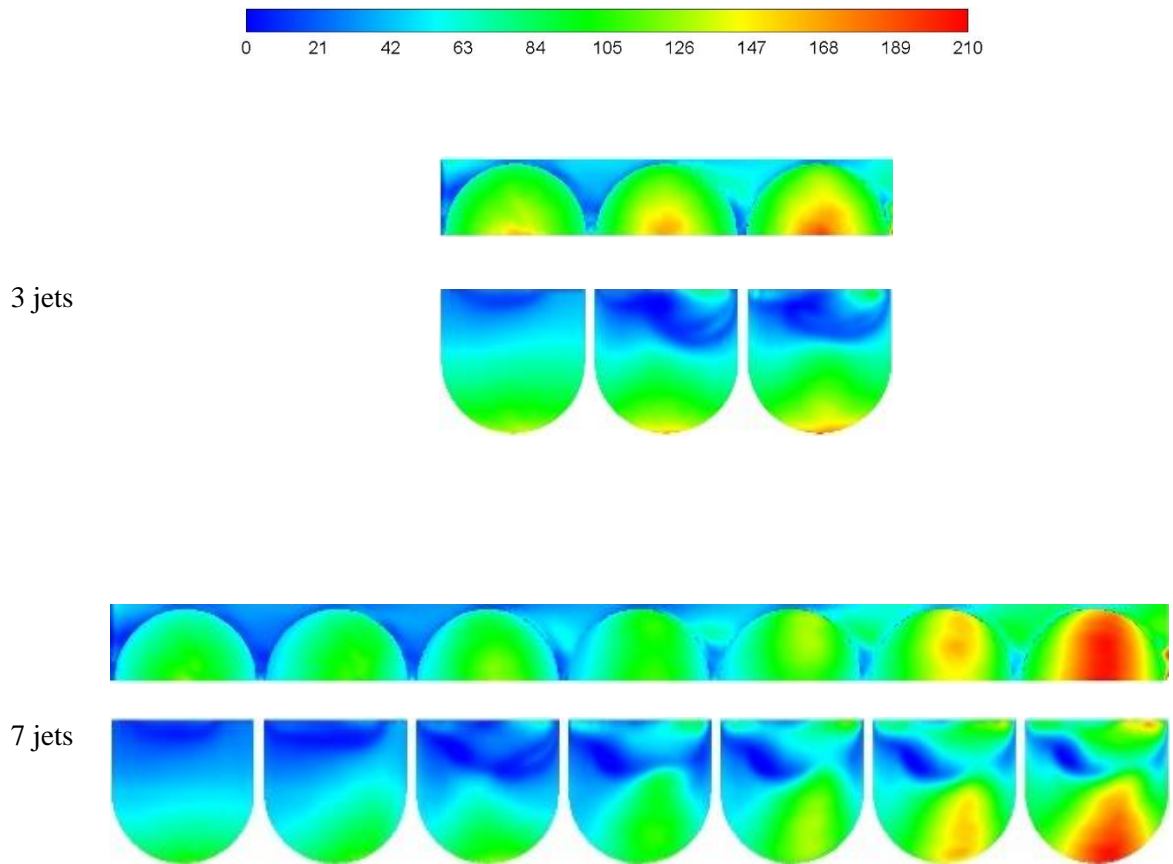


Figure 7.24 Number of jets influence on Nu contours at $H/d= 4$ and $Re= 30,000$

The overall impacts of this crossflow in increasing jet number to average target Nusselt number are shown in Figure 7.25. This plot clearly demonstrates that the trend of average Nu between jets is independent of jet number, with average Nu for each jet target increasing with proximity to the outlet, but the magnitude of this relationship decreases monotonically with jet number from three to seven. Although overall average Nu trends decrease in magnitude with increasing jet number, the maximum average value is always observed at the jet closest to the exit, and the number of jets increases the magnitude of this behaviour.

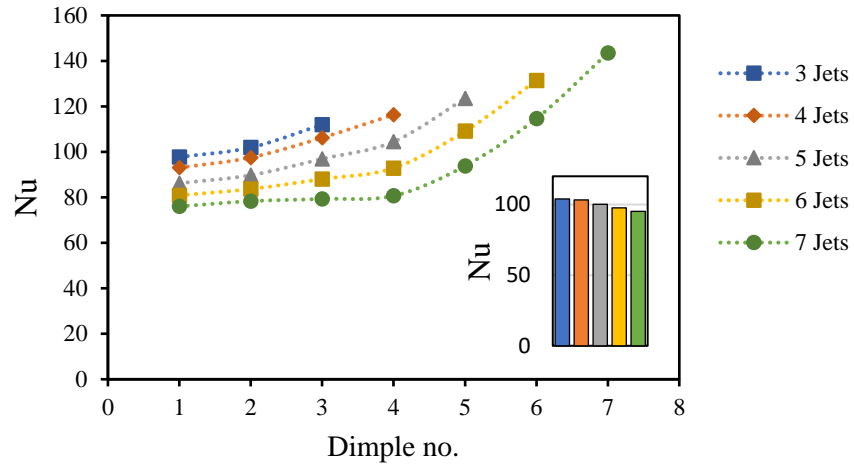


Figure 7.25 Number of jets influence on dimple average Nu at $H/d= 4$ and $Re= 30,000$

This same trend and characteristic can also mostly be observed in the heat transfer against the cylinder portion of the target walls in Figure 7.26. The key difference being that each trendline has a minimum overall Nusselt number at the third nozzle.

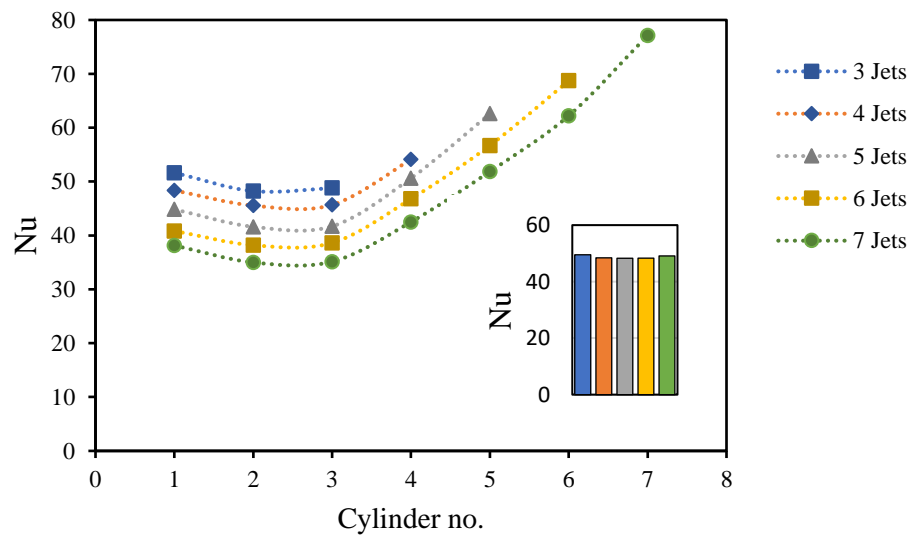


Figure 7.26 Number of jets influence on cylinder wall average Nu at $H/d= 4$ and $Re= 30,000$

Overall discharge coefficient can be seen, Figure 7.27, to decrease with the number of jets, this is due to the accumulated spent flow increasing through the crossflow channels with the increasing jet number.

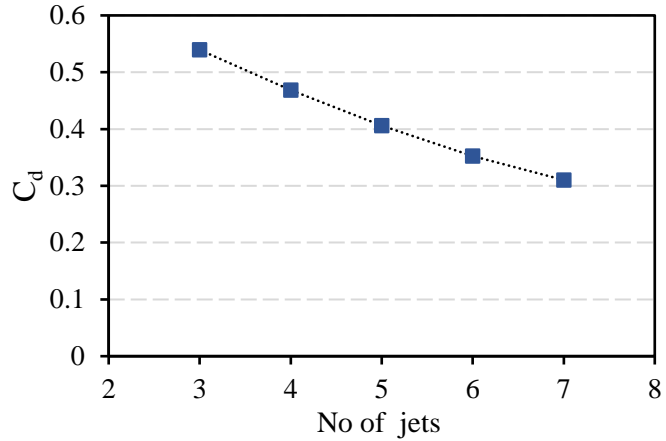


Figure 7.27 Number of jets influence on discharge coefficient at $H/d= 4$ and $Re= 30,000$

7.5.2.3. Dimple-to-nozzle effect

The effect of dimple diameter to nozzle diameter is shown in this section. In a traditional row of cooling jets, the spacing is determined by the pitch between nozzles. As each jet has a dimple target, it is appropriate to consider an increasing dimple diameter as pitch increases.

Figure 7.28 shows that as the dimple diameter increases, the target plenum increases in volume, and therefore the effects of crossflow on jet deflection are minimised, the increasing relative dimple diameter also boosts the surface area of the ‘dimple’ and increases the relative distance from the potential core to the cylinder walls.

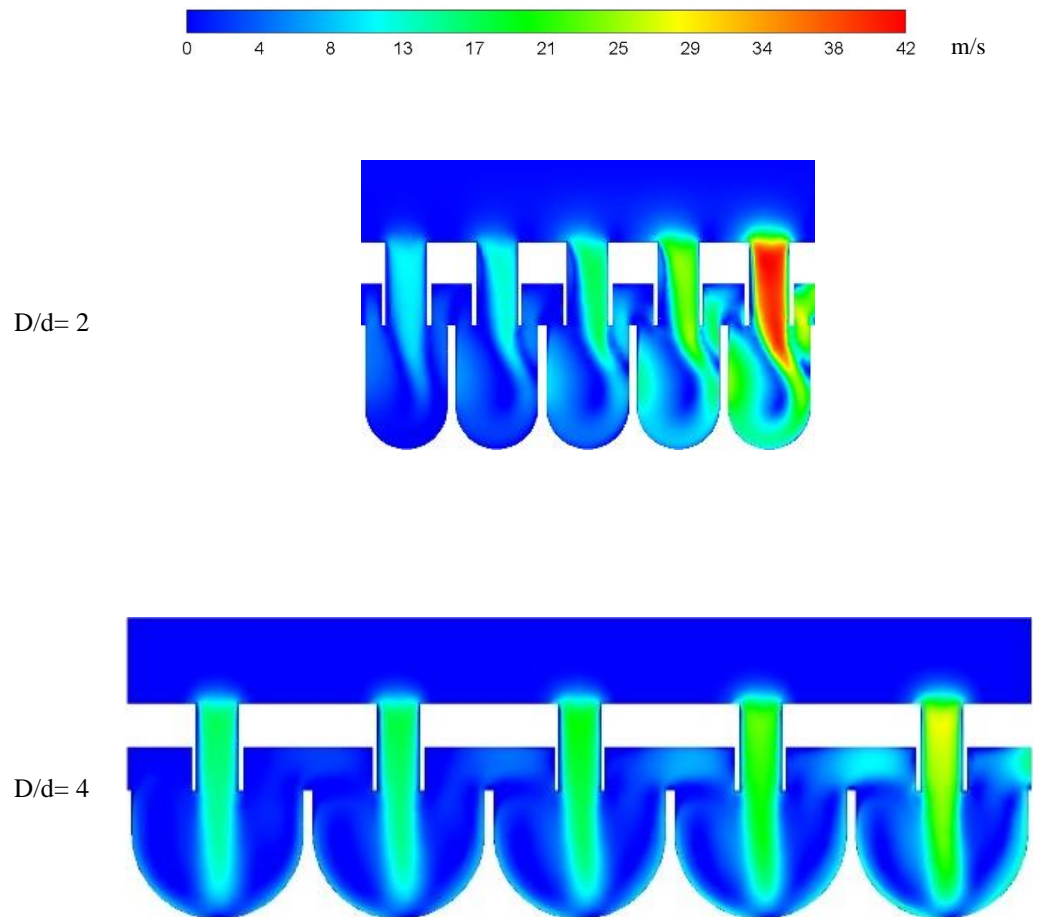


Figure 7.28 Nozzle-to-dimple influence on flow velocity contours at $H/d= 4$ and $Re= 30,000$

Due to the relatively lower jet deflection with larger dimple diameter, the migration of Nusselt number stagnation point is minimised, as observed in Figure 7.29. Where migration in the final jet of $D/d = 2$ is high on the cylinder wall, for $D/d = 4$, the deflection is still within 20 degrees of the dimple's stagnation target.

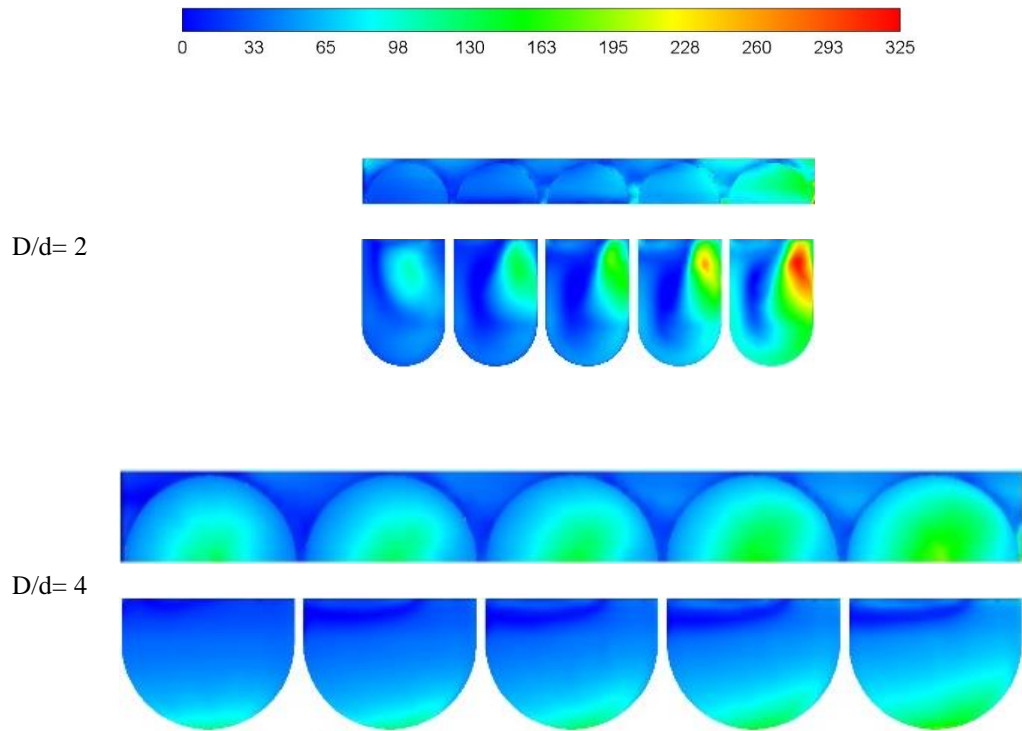


Figure 7.29 Nozzle-to-dimple influence on Nu contours at $H/d= 4$ and $Re= 30,000$

The average Nu distributions for each jet against the dimple target surface are shown in Figure 7.30 at 30,000 Reynolds number, these show that an optimum D/d is found at $D/d = 3$.

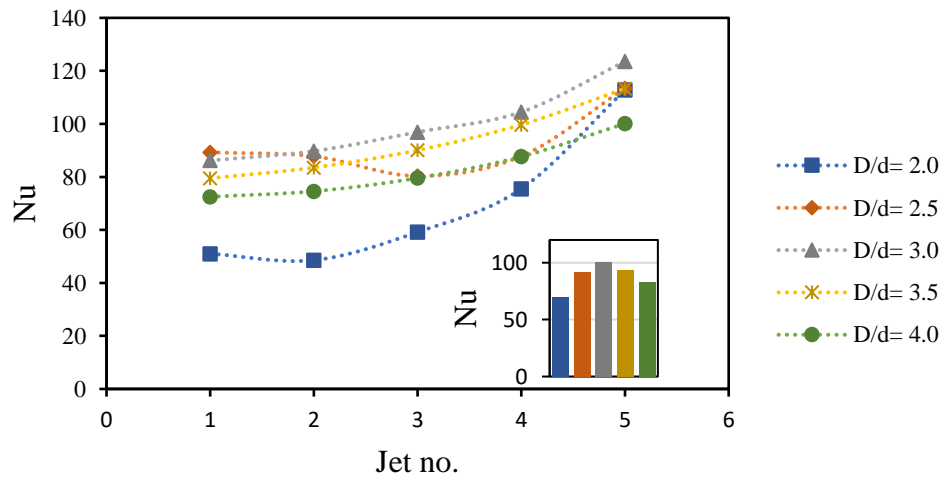


Figure 7.30 Nozzle-to-dimple influence on dimple average Nu at $H/d= 4$ and $Re= 30,000$

Figure 7.31 demonstrates the same Nusselt number against the cylinder wall portion under the same conditions. With very low D/d ($=2$), the effects of the deflection to the cylinder wall become more significant in subsequent jets, and although the overall average Nu is severely impacted, local Nu on the cylinder walls, especially those in proximity to the exit is highly enhanced. Therefore, an optimum for the cylinder walls was found at $D/d = 2$.

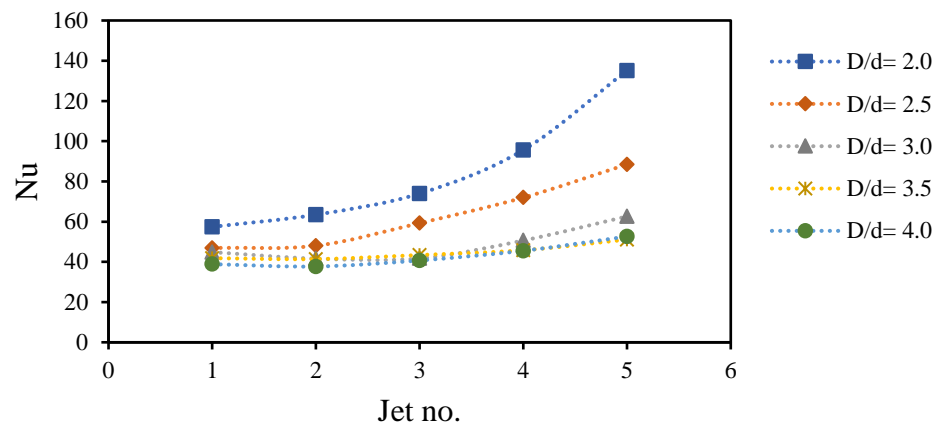


Figure 7.31 Nozzle-to-dimple influence on cylinder wall average Nu at $H/d= 4$ and $Re= 30,000$

At 30,000 Re , the discharge coefficient is shown to increase with D/d from 27% at $D/d = 2$ to 46% at $D/d = 4.5$, as shown in Figure 7.32.

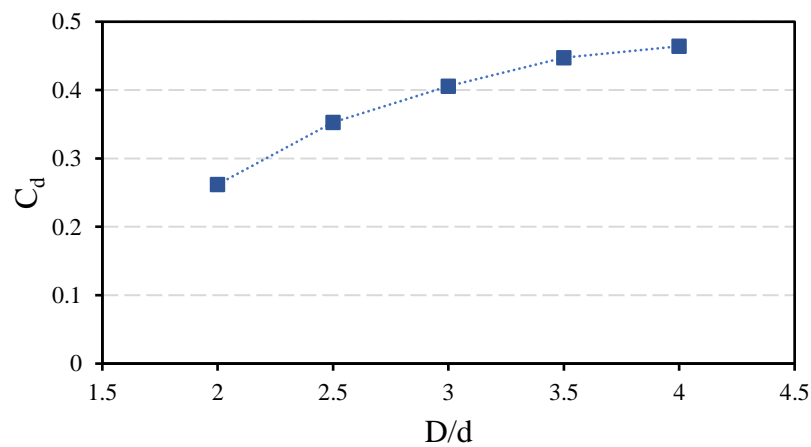


Figure 7.32 Nozzle-to-dimple influence on discharge coefficient at $H/d= 4$ and $Re= 30,000$

7.5.2.4. Reynolds number effect

The effect of Reynolds number was assessed from 10,000 to 70,000 Re at a H/d of 4, covering a range applicable to many industrial applications. Reynolds number is shown to have very little impact on the distribution of velocity, but magnitude of velocity is directly related to the Reynolds number, as shown in Figure 7.33.

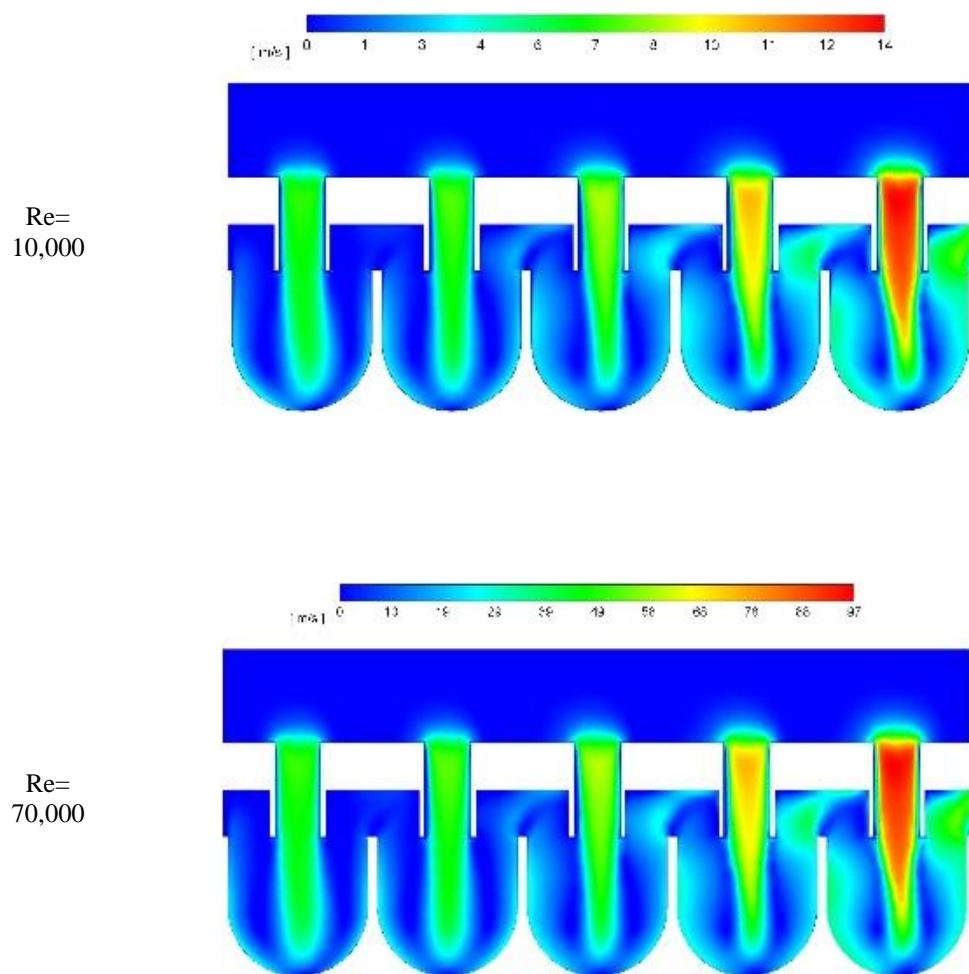


Figure 7.33 Reynolds number influence on flow velocity contours at H/d= 4, Re= 10,000 and 70,000

The effect of Reynolds number of the Nusselt number distribution was also investigated, as shown in Figure 7.34. Re is shown to have very little impact on the distribution of Nu, but with jets one to three having a relatively low share of the overall heat transfer, this is due to the relatively increased downstream back pressure.

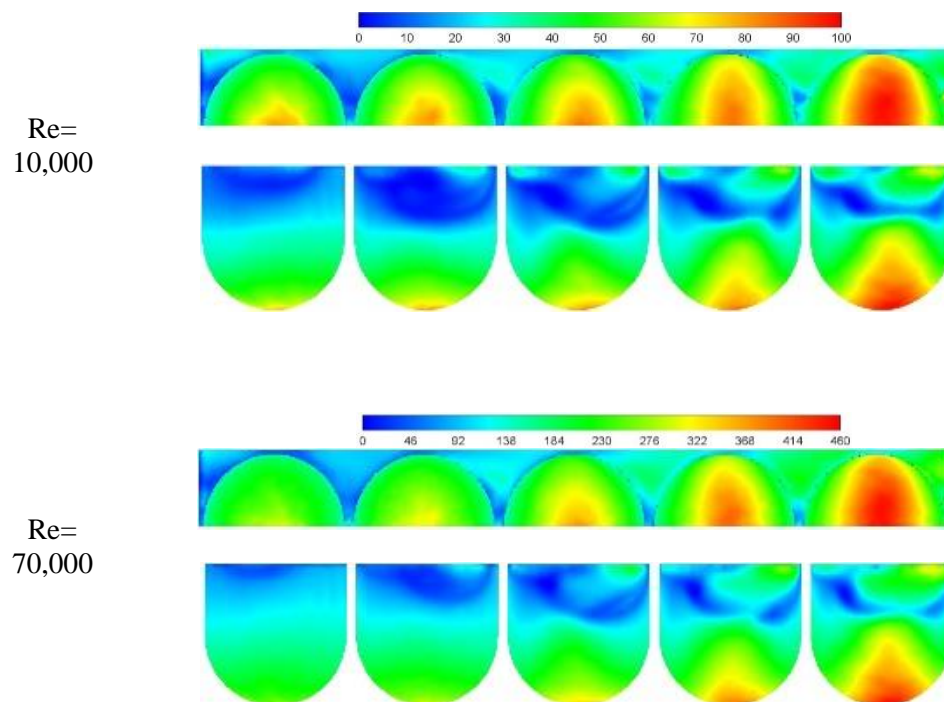


Figure 7.34 Reynolds number influence on Nu contours at $H/d= 4$, $Re= 10,000$ and $70,000$

Trends of Nu against the dimple target for varying Reynolds number show a consistent trend in Figure 7.35, with increasing Nu for subsequent jets, but with monotonically increasing overall magnitude of Nu as Re increases.

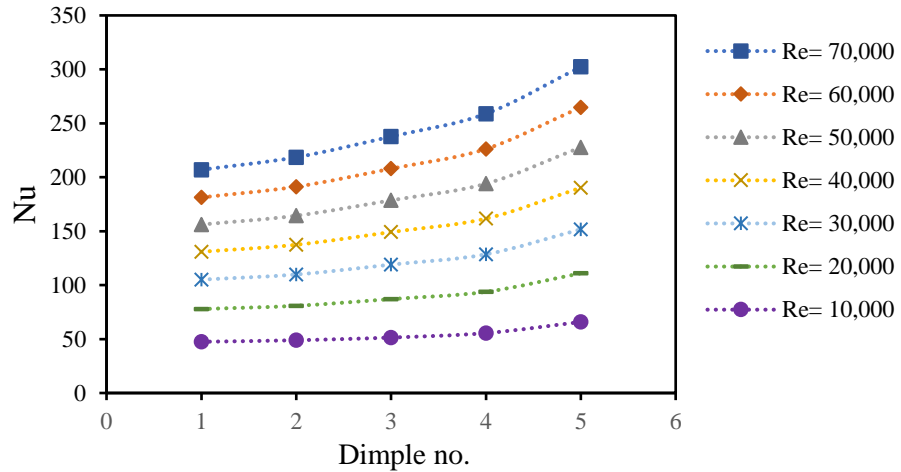


Figure 7.35 Reynolds number influence on dimple average Nu at $H/d=4$ and 70,000

Trends of Nu against the cylinder target for varying Re also show consistent trend in Figure 7.36, but with monotonically increasing magnitude as Re increases. An average jet minimum Nusselt number is again seen at jet number three for these cylinder walls.

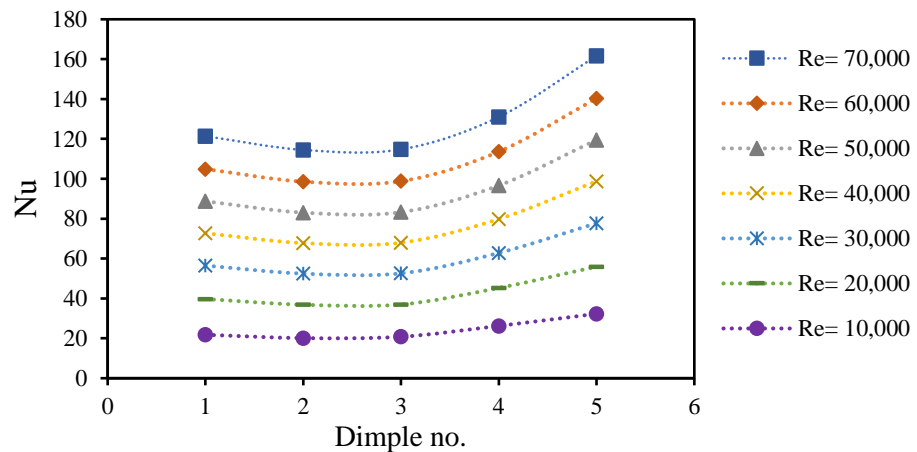


Figure 7.36 Reynolds number influence on cylinder wall average Nu at $H/d=4$

Figure 7.37 points out that the discharge coefficient was found to have a maximum of 40.6% at 20,000 Re. Followed by a decrease with increasing Re to 39% at 70,000 Re. C_d at 10,000 Re shows a lower value for C_d than 20,000 Re. But this is likely not statistically significant due to increasing uncertainty pressure measurements at lower flow rates.

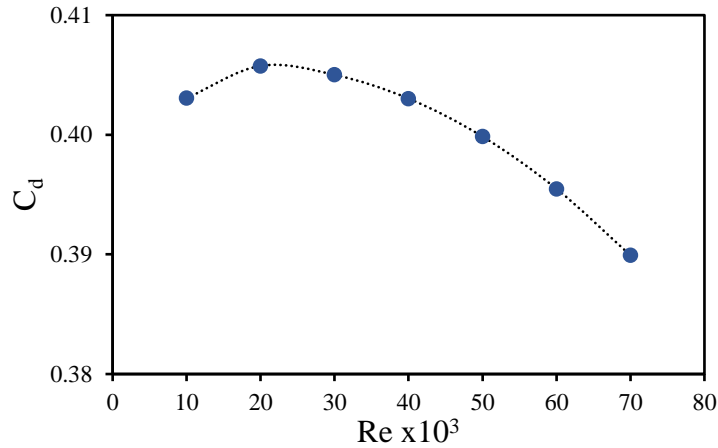


Figure 7.37 Influence of Reynolds number on discharge coefficient at $H/d= 4$

7.5.2.5. Crossflow channel height to nozzle effect

The effect of variation in the height of nozzle extension into the gas path, and therefore outflow channel height was investigated. The benefits are an increased outflow area to minimise crossflow pressure drop over the crossflow channels, but also a potential reduction in heat transfer surface area. For this study the cylinders height walls are kept constant, and therefore the overall height of the arrangement increases by the extension distance, with the heat transfer surface area being maintained. Due to the extended nozzle, the jet flow will also have increased flow development before exiting as a jet.

The variation in jet velocity profile is shown in Figure 7.38 which demonstrates that increasing nozzle extension length from 0.5 jet diameters to 2 jet diameters has a significant impact on reducing crossflow related jet deflection.

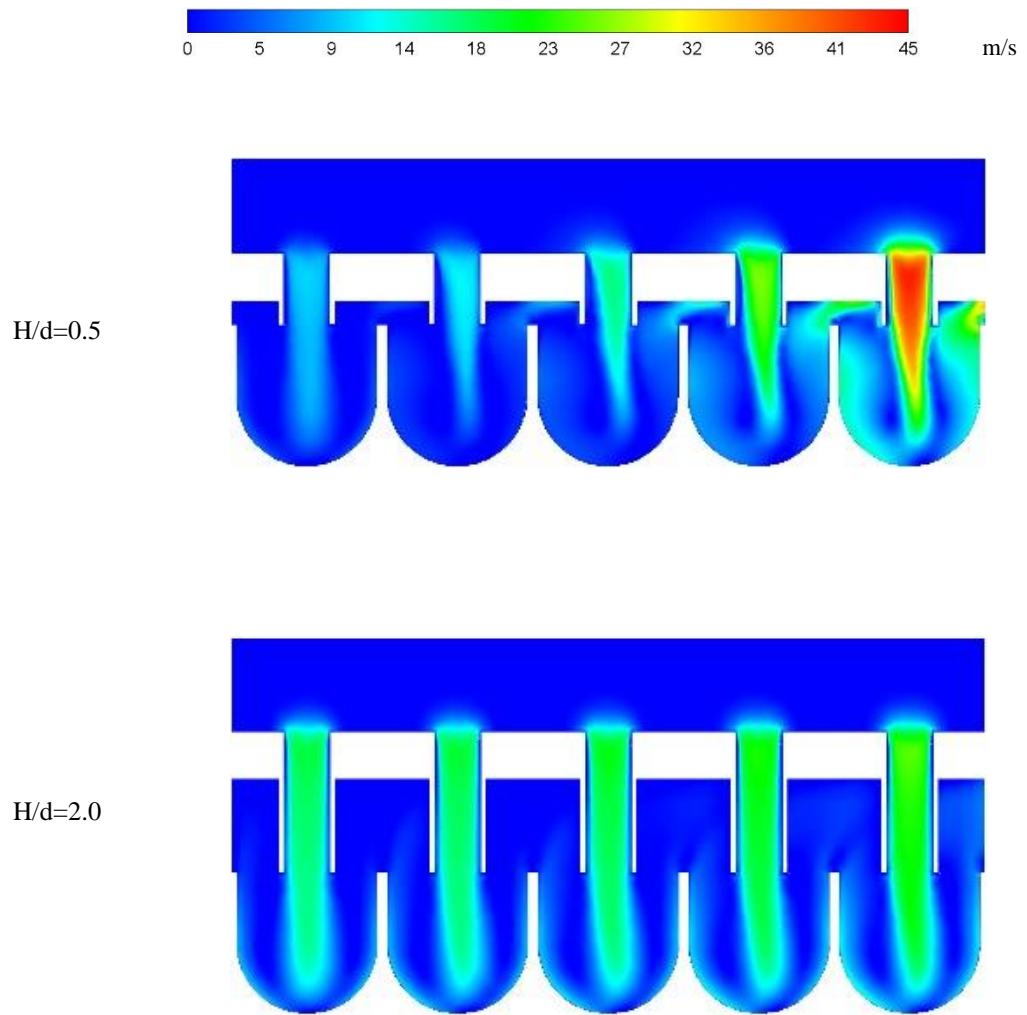


Figure 7.38 Influence of crossflow channel height to nozzle on flow velocity contours at $H/d=4$, $Re=30,000$

The impact of the extended nozzle to Nusselt number distribution is shown in Figure 7.39, and demonstrates that although crossflow is significantly reduced, the effects of increasing jet number on Nusselt number deterioration are not completely eliminated.

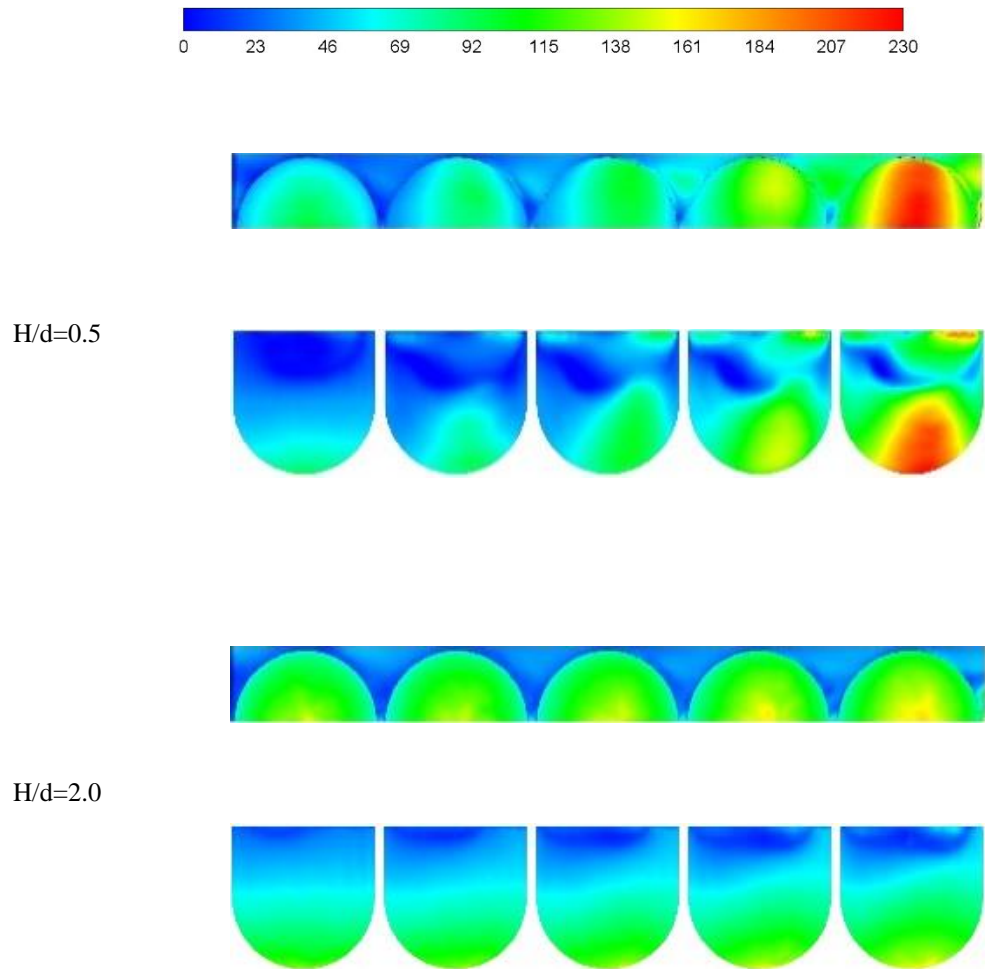


Figure 7.39 Influence of crossflow channel height to nozzle on Nu contours at $H/d=4$, $Re=30,000$

Overall, the impact on dimple surface Nusselt number of increasing h/d from 0.5 to 1 is very significant at 30,000 Re , as shown in Figure 7.40, both in trend of average Nu between nozzle targets, and overall heat transfer magnitude. Relatively little variation is observed between h/d of 1 and 2, so it is therefore recommended that a realistic optimum for the nozzle extension is found at $h/d = 1$.

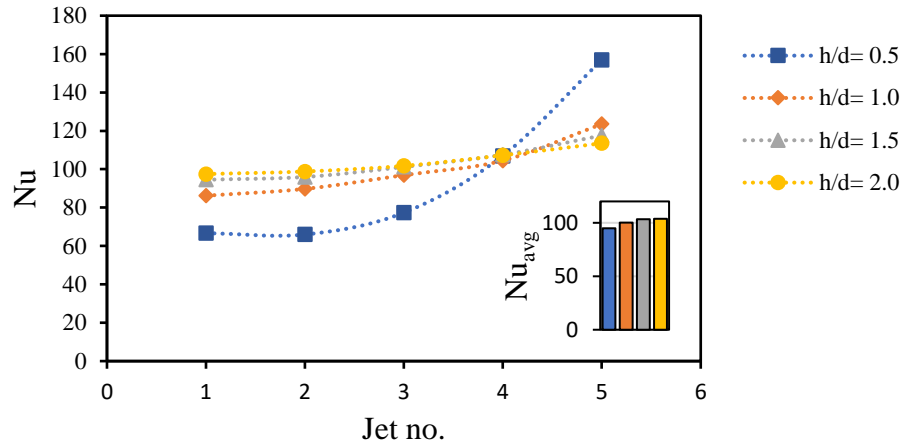


Figure 7.40 The effect of crossflow channel height to nozzle diameter (h/d) on dimple the average Nu at $H/d=4$, $Re=30,000$

When observing the change to cylinder wall average Nusselt number, the effect of increasing h/d from 0.5 to 1 is also significant, both in trend of average Nu between nozzle cylinder targets, and far more uniformity is observed at the larger length, with an overall optimum against this surface found at $h/d = 2$. In general, the relevance of heat transfer to the cylinder walls is comparatively lower than that to the dimple target. As such, an optimal H/d value of 4 and Reynolds number of 30,000 is recommended for a nozzle-to-target spacing ratio of $h/d = 1$, as shown in Figure 7.41.

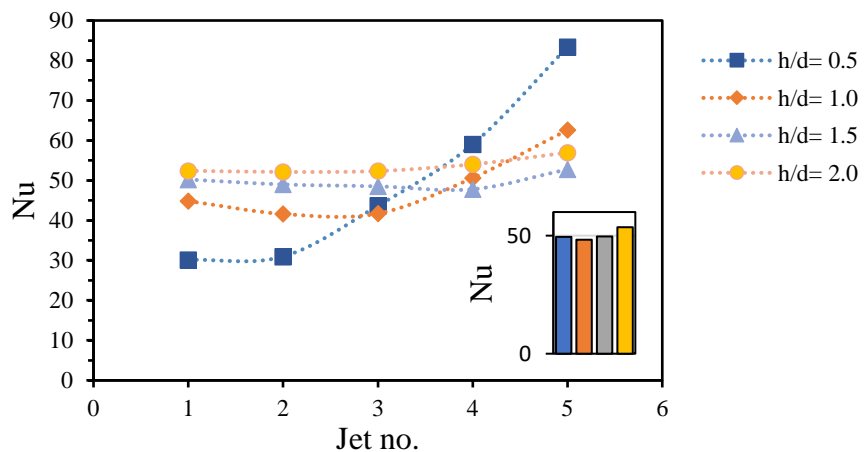


Figure 7.41 The effect of crossflow channel height to nozzle diameter (h/d) on cylinder average Nu at $H/d=4$, $Re=30,000$

Figure 7.42 demonstrates that the discharge coefficient was seen to increase with increasing h/d , from 22% at $h/d = 0.5$, to 53% at $h/d = 2$, as the flow through the nozzle tends towards a pipe flow and becomes more developed with increasing nozzle extension length, and the effective crossflow area becomes greater.

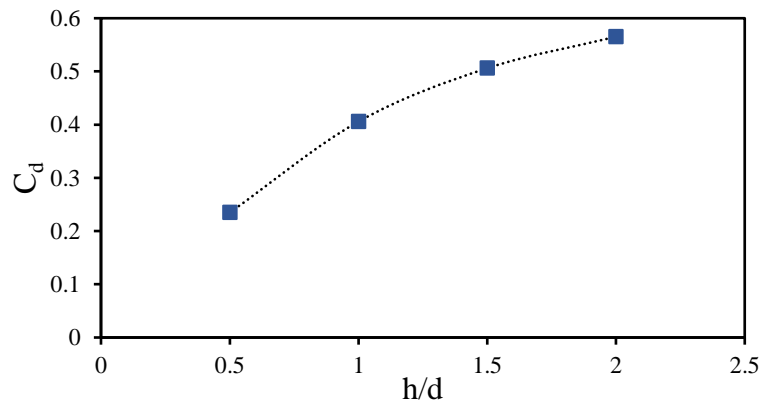


Figure 7.42 Crossflow channel height to nozzle influence on discharge coefficient at $H/d = 4$, $Re = 30,000$

7.5.3. Summary

A numerical evaluation was conducted for the novel reverse impingement geometry against experimental results. Assessing the impact of various geometrical and flow properties to enhance target heat transfer, extend the heat transfer surface, and to reduce the impacts of crossflow. The effects of inlet direction, outlet direction, jet to target spacing, jet to jet spacing, Reynolds number, nozzle extension, and the effect of inline vs staggered array variations have been evaluated numerically for detailed heat transfer distribution and discharge coefficient data.

- A row of five impinging jets was validated against experimental data, heat transfer contours and averages were provided, supported

by the experimental data, and detailed velocity distributions were developed to support these heat transfer measurements.

- For rows, both inline and staggered have been compared against baseline flat target.
- Jet to target spacing, H/D , has been evaluated, optimum for row at $H/d = 4$.
- A monotonic increase of Nu was observed against Re .
- Effect of crossflow was evaluated, reverse impingement design minimised the impacts, and the cylindrical target surface allowed for some recuperation for heat transfer from recirculation of the deflected jet.
- Novel extended nozzles were employed to further reduce the effects of crossflow, successfully, and an optimum nozzle extension length as found at h/d of 1.
- The effects of pitch to nozzle diameter ratio were evaluated, impacting the effective dimple diameter, an optimum was found for both the dimple and cylinder walls between $D/d = 2$ and 3.
- The effect of jet number on the overall and subsequent jet average Nu was evaluated, and a trend was developed which may be suitable for extrapolation to larger jet numbers.
- Staggered and inline dimples were shown to provide very similar enhancements to heat transfer and were significant compared to a traditional flat plate target.

Chapter 8. Conclusions and future work

8.1. Conclusions of current work

An experimental study was conducted to assess the effectiveness of a novel reverse jet impingement geometry in an impinging row, utilising the thermochromic liquid crystal technique. Overall, there is an enhancement of heat transfer uniformity to a dimple target surface, and additional heat transfer rate as the wall jet can transition to the ‘silo’ cylindrical wall. An optimum nozzle-to-target spacing was identified at $H/d = 4$, and Nusselt number was found to increase monotonically with Reynolds number.

Crossflow impacts the distribution of Nusselt number between each jet in the row, and the relatively large pressure drops generated over the crossflow channels cause an enhancement in the heat transfer for the impingement target closest to the outflow locations, becoming more significant when a maximum crossflow condition is imposed. Implementing an extension to the nozzles through the crossflow channels reduced negative effects of crossflow, especially the effects of jet deflection, but the effects of pressure drop variation remained significant. Discharge coefficient was shown to increase with larger H/d , and also increase with Reynolds number.

Additional experimental testing was conducted to assess the suitability of the novel geometry as part of an impinging array. Overall, there is an enhancement of heat transfer consistent to a dimple target surface, and additional heat transfer performed as the wall jet can transition to the ‘silo’ cylindrical wall.

An optimum H/d was identified between $H/d = 2.6 - 4$, and Nusselt number was found to increase monotonically with Reynolds number. The presence of film outlet holes between nozzle ‘silos’ is key to minimising the effects of crossflow, and some crossflow was still observed to impact the distribution of Nusselt number on the target surfaces of the outer six jets. Variation was observed between the seven jets. Discharge coefficient was shown to be independent of H/d and increase with Reynolds number.

A numerical analysis of the novel reverse jet impingement geometry was conducted, with validation against experimental results. In order to optimize the effectiveness of the arrangement, variations of inlet and outlet configurations and nozzle geometry were investigated

Initial tests indicate that crossflow effects are still significant in this geometry. As a result of extending the nozzle to the level of the crossflow channel, the effect of crossflow was significantly reduced and the Nu was increased. A detailed analysis of the variation of inlet conditions did not yield significant improvements. The spacing between the nozzle and target was optimized around three jet diameters.

The most significant variable in determining the nozzle discharge coefficient was the outlet condition, where a maximum flow area generated the highest discharge coefficient. Based on the results of the numerical study, an extended nozzle was determined to be the optimal reverse jet impingement arrangement. Due to its high resistance to crossflow, this design can be applied to a wide range of inlets and outlets configurations.

A numerical evaluation was conducted for the novel reverse impingement geometry against experimental results. Assessing the impact of various geometrical and flow properties to enhance target heat transfer, extend the heat transfer surface, and to reduce the impacts of crossflow.

The effects of inlet direction, outlet direction, jet to target spacing, jet to jet spacing, Reynolds number, nozzle extension, and the effect of inline vs staggered array variations have been evaluated numerically for detailed heat transfer distribution and discharge coefficient data.

The effects of Reynolds number were evaluated, with a monotonic increase of Nu was observed against Re. A row of five impinging jets was validated against experimental data, heat transfer contours and averages were provided, supported by the experimental data, and detailed velocity distributions were developed to support these heat transfer measurements.

The effects of crossflow were to significantly deflect the impinging jet, and to cause a circulation of flow through the reverse jet target, increasing in significance with each subsequent jet. By extending the nozzle to the level of the crossflow channel, the effects of crossflow could be significantly reduced and average Nu could be increased.

The effects of H/d were modelled, and impacts on the velocity contours were shown, demonstrating the ineffectiveness of the potential core to reach the target at greater H/d distances. There was an optimal spacing distance between the nozzle and target of approximately three to four jet diameters.

Despite an in-depth analysis of the inlet condition, no significant improvement was found. The most significant variable in analysing the

discharge coefficients was the outlet condition, i.e., a maximum crossflow scheme produced the highest discharge coefficients.

It was concluded from this numerical evaluation that the current optimised reverse jet impingement arrangement requires an extended nozzle. Due to this design's flexibility and high resilience to crossflow, it can be used with a wide range of inlet and outlet conditions.

When assessing the effectiveness of the novel reverse design in an array, both inline and staggered arrangements have been compared numerically against baseline flat target.

The effect of crossflow was evaluated, consistent with experimental results, the reverse impingement design minimised but not completely eliminated the impacts, and the cylindrical target surface allowed for some recuperation for heat transfer from recirculation of the deflected jet.

Novel extended nozzles were employed to further reduce the effects of crossflow, successfully, and an optimum nozzle extension length for heat transfer enhancement was found at h/d of 1, with discharge coefficient increasing with increasing h/d .

The effects of pitch to nozzle diameter ratio were evaluated, impacting the effective dimple diameter, an optimum was found for both the dimple and cylinder walls between $D/d = 2$ and 3. Moreover, The effect of jet number on the overall and subsequent jet average Nu was evaluated, and a trend was developed which may be suitable for extrapolation to larger jet numbers. In addition to, Staggered and inline dimples were shown to provide very similar

enhancements to heat transfer and were significant compared to a traditional flat plate target.

8.2. Future work

Some future investigations are recommended based on current work as:

- All the experimental investigations done for the row jet impingement was for 5 jets. Therefore it is recommended to investigate experimentally the effect of the jets number to find out the optimum number of jet and if the number of jets depends on the crossflow scheme and the nozzle-to target spacing distance.
- The experiments in this thesis were conducted with a constant ratio of the nozzle diameter to the dimple diameter. Further experiments are needed to investigate how varying this ratio affects heat transfer.
- SST K- ω turbulence model has been adapted for the numerical study after comparing it with other RANS turbulence models. The comparison indicated that SST K- ω turbulence model was the closest to the experimental results. It is suggested to use LES turbulence model for simulating the jet impingement and comparing the results with the SST K- ω turbulence model to determine how it could help in getting more accurate data which deserve the higher computational time.

- The target surface in all the study cases was smooth, so considering the surface roughness or corrugation as parameters would affect the heat transfer would need a future work.
- All the experimental work done on the film cooling was for a constant diameter film hole. So, it is recommended to reinvestigating the effect of the rotation and inclination angles on a film hole with different geometry, such as cone, fan, dumbbell, etc.
- Film cooling study in this thesis was for a single film hole. So, it is recommended to studying the film cooling for and row or array of film holes, to investigate how would be the interactions between the adjacent holes and the effect of the crossflow.

Chapter 9. REFERENCES

- [1] Y. A. Cengel and M. A. Boles, *Thermodynamics: An Engineering Approach*, Fifth edit. McGraw-Hill, 2005.
- [2] M. M. Rahman, T. K. Ibrahim, K. Kadirgama, R. Mamat, and R. A. Bakar, “Influence of operation conditions and ambient temperature on performance of gas turbine power plant,” *Adv. Mater. Res.*, vol. 189–193, pp. 3007–3013, 2011.
- [3] J. C. Han, S. Dutta, and S. V. Ekkad, *Gas Turbine Heat Transfer And Cooling Technology*, Second. New York: CRC Press, 2013.
- [4] S. Naik, “Basic Aspects of Gas Turbine Heat Transfer,” in *Heat Exchangers - Design, Experiment and Simulation*, no. April, Rijeka, Croatia: INTECH, 2017, pp. 111–143.
- [5] K. YERANEE and Y. RAO, “A review of recent studies on rotating internal cooling for gas turbine blades,” *Chinese J. Aeronaut.*, vol. 34, no. 7, pp. 85–113, 2021.
- [6] K. Takeishi, “Heat Transfer Research in High Temperature Industrial Gas Turbines,” Takasago City, Japan, 1994.
- [7] G. ZHANG, R. ZHU, G. XIE, S. LI, and B. SUNDÉN, “Optimization of cooling structures in gas turbines: A review,” *Chinese J. Aeronaut.*, vol. 35, no. 6, pp. 18–46, 2022.
- [8] J. C. Han and A. P. Rallabandi, “Turbine Blade Film Cooling Using

- PSP Technique,” *Front. Heat Mass Transf.*, vol. 1, no. 1, 2010.
- [9] G. A. Rao, Y. Levy, and M. Kitron-Belinkov, “Heat transfer characteristics of a multiple jet impingement system,” *49th Isr. Annu. Conf. Aerosp. Sci. 2009*, vol. 1, no. June 2016, pp. 314–328, 2009.
- [10] C. Liang, Y. Rao, J. Luo, and X. Luo, “Experimental and Numerical Study of Turbulent Flow and Heat Transfer in a Wedge-shaped Channel with Guiding Pin Fins for Turbine Blade Trailing Edge Cooling,” *Int. J. Heat Mass Transf.*, vol. 178, p. 121590, 2021.
- [11] K. Krishnaswamy and S. Sivan, “Improvement in thermal hydraulic performance by using continuous v and W-Shaped rib turbulators in gas turbine blade cooling application,” *Case Stud. Therm. Eng.*, vol. 24, no. January, 2021.
- [12] S. Rashidi, F. Hormozi, B. Sundén, and O. Mahian, “Energy saving in thermal energy systems using dimpled surface technology – A review on mechanisms and applications,” *Appl. Energy*, vol. 250, no. April, pp. 1491–1547, 2019.
- [13] F. Kebir and A. Azzi, “Study of wave number effect in wavy plate for improving the film cooling effectiveness at spanwise direction,” *Numer. Heat Transf. Part A Appl.*, vol. 73, no. 6, pp. 408–427, 2018.
- [14] R. S. Bunker, “Gas turbine cooling: Moving from macro to micro cooling,” *Proc. ASME Turbo Expo*, vol. 3 C, pp. 1–17, 2013.
- [15] M. Kim, D. H. Shin, B. J. Lee, and J. Lee, “Experimental and numerical investigation of micro-scale effusion and transpiration air cooling on

cascaded turbine blades,” *Case Stud. Therm. Eng.*, vol. 32, no. October 2021, p. 101892, 2022.

- [16] R. Nacke, B. Northcutt, and I. Mudawar, “Theory and experimental validation of cross-flow micro-channel heat exchanger module with reference to high Mach aircraft gas turbine engines,” *Int. J. Heat Mass Transf.*, vol. 54, no. 5–6, pp. 1224–1235, 2011.
- [17] S. C. Siw, N. Miller, M. K. Chyu, and M. A. Alvin, “Heat transfer and pressure loss characteristics of a narrow internal cooling passage at low reynolds number,” *Proc. ASME Turbo Expo*, vol. 5A, pp. 1–8, 2014.
- [18] H. Martin, “Heat and Mass Transfer between Impinging Gas Jets and Solid Surfaces,” *Adv. Heat Transf.*, vol. 106, pp. 34–41, 1984.
- [19] K. Jambunathan, E. Lai, M. A. Moss, and B. L. Button, “A review of heat transfer data for single circular jet impingement,” *Int. J. Heat Fluid Flow*, vol. 13, no. 2, pp. 106–115, 1992.
- [20] R. Viskanta, “Heat Transfer to Impinging Isothermal Gas and Flame Jets,” pp. 111–134, 1993.
- [21] R. J. Goldstein, A. I. Behbahani, and K. K. Heppelmann, “Streamwise distribution of the recovery factor and the local heat transfer coefficient to an impinging circular air jet,” *Int. J. Heat Mass Transf.*, vol. 29, no. 8, pp. 1227–1235, 1986.
- [22] D. W. Zhou and C. F. Ma, “Radial heat transfer behavior of impinging submerged circular jets,” *Int. J. Heat Mass Transf.*, vol. 49, no. 9–10, pp. 1719–1722, 2006.

- [23] S. S. Baughn, W. James, "Heat transfer measurement from a surface with uniform heat flux and a impingement jet," *Asme*, vol. 111, no. November, pp. 1096–1098, 1989.
- [24] C. O. Popiel and O. Trass, "Visualization of a free and impinging round jet," *Exp. Therm. Fluid Sci.*, vol. 4, no. 3, pp. 253–264, 1991.
- [25] G. C. Huang, "Investigations of heat-transfer coefficients for air flow through round jets impinging normal to a heat-transfer surface," *J. Heat Transfer*, vol. 85, no. 3, pp. 237–243, 1963.
- [26] C. D. Donaldson, R. S. Snedeker, and D. P. Margolis, "A study of free jet impingement: Part 2 Free jet turbulent structure and impingement heat transfer," *J. Fluid Mech.*, vol. 45, pp. 477–512, 1971.
- [27] J. C. Akfirat and F. M. Company, "The role of turbulence in determining the heat-transfer characteristics of impinging jets," *Int. J. Heat Mass Transf.*, vol. 8, pp. 1261–1272, 1965.
- [28] S. Polat, B. Huang, A. S. Mujumdar, and W. J. M. Douglas, "Numerical Flow and Heat Transfer Under Impinging Jets: A Review," *Annu. Rev. Heat Transf.*, vol. 2, pp. 157–197, 1993.
- [29] M. Angioletti, R. M. Di Tommaso, E. Nino, and G. Ruocco, "Simultaneous visualization of flow field and evaluation of local heat transfer by transitional impinging jets," *Int. J. Heat Mass Transf.*, vol. 46, no. 10, pp. 1703–1713, 2003.
- [30] J. Y. San and M. De Lai, "Optimum jet-to-jet spacing of heat transfer for staggered arrays of impinging air jets," *Int. J. Heat Mass Transf.*,

vol. 44, no. 21, pp. 3997–4007, 2001.

- [31] J. Lee and S. J. Lee, “The effect of nozzle configuration on stagnation region heat transfer enhancement of axisymmetric jet impingement,” *Int. J. Heat Mass Transf.*, vol. 43, no. 18, pp. 3497–3509, 2000.
- [32] N. T. Obot, A. S. Majumdar, and W. J. M. Douglas, “The effect of nozzle geometry on impingement heat transfer under a round turbulent jet,” 1979, p. 12.
- [33] S. V Garimella and R. A. Rice, “1995_Confined and Submerged Liquid jet impingement,” vol. 1, no. November 1995, 2016.
- [34] H. Chattopadhyay, “Numerical investigations of heat transfer from impinging annular jet,” *Int. J. Heat Mass Transf.*, vol. 47, no. 14–16, pp. 3197–3201, 2004.
- [35] S. J. Wang and A. S. Mujumdar, “A comparative study of five low Reynolds number k- ϵ models for impingement heat transfer,” *Appl. Therm. Eng.*, vol. 25, no. 1, pp. 31–44, 2005.
- [36] Q. Liu, A. K. Sleiti, and J. S. Kapat, “Application of pressure and temperature sensitive paints for study of heat transfer to a circular impinging air jet,” *Int. J. Therm. Sci.*, vol. 47, no. 6, pp. 749–757, 2008.
- [37] J. Badra, A. R. Masri, and M. Behnia, “Enhanced transient heat transfer from arrays of jets impinging on a moving plate,” *Heat Transf. Eng.*, vol. 34, no. 4, pp. 361–371, 2013.
- [38] N. T. Obot and T. A. Trabold, “Impingement heat transfer within arrays of circular jets: Part 1—effects of minimum, intermediate, and complete

- crossflow for small and large spacings,” *J. Heat Transfer*, vol. 109, no. 4, pp. 872–879, 1987.
- [39] L. W. Florschueiz, C. R. Truman, and D. E. Metzger, “Streamwise flow and heat transfer distributions for jet array impingement with crossflow,” *J. Heat Transfer*, vol. 103, no. 2, pp. 337–342, 1981.
- [40] J. C. Bailey and R. S. Bunker, “Gt-2002-30 of Dense and Sparse Extent,” pp. 1–10, 2002.
- [41] Y. Huang, S. V. Ekkad, and J. C. Han, “Detailed heat transfer distributions under an array of orthogonal impinging jets,” *J. Thermophys. Heat Transf.*, vol. 12, no. 1, pp. 73–79, 1998.
- [42] K. W. Van Treuren, Z. Wang, P. T. Ireland, and T. V. Jones, “Detailed measurements of local heat transfer coefficient and adiabatic wall temperature beneath an array of impinging jets,” *ASME 1993 Int. Gas Turbine Aeroengine Congr. Expo. GT 1993*, vol. 3A, no. July 1994, 1993.
- [43] R. J. Goldstein and A. I. Behbahani, “Impingement of a circular jet with and without cross flow,” *Int. J. Heat Mass Transf.*, vol. 25, no. 9, pp. 1377–1382, 1982.
- [44] B. R. Hollworth and R. D. Berry, “Heat Transfer From Arrays of Impinging Jets With Large Jet-To-Jet Spacing,” *Am. Soc. Mech. Eng.*, vol. 100, no. 78-GT-117, pp. 352–357, 1978.
- [45] N. Gao, H. Sun, and D. Ewing, “Heat transfer to impinging round jets with triangular tabs,” *Int. J. Heat Mass Transf.*, vol. 46, no. 14, pp.

2557–2569, 2003.

- [46] R. N. Koopman, “Local and average transfer coefficients for multiple impinging jets,” Minnesota University, Minneapolis, 1975.
- [47] L. W. Florschuetz, D. E. Metzger, and C. C. Su, “Heat Transfer Characteristics for Jet Array Impingement With Initial Crossflow.,” *Am. Soc. Mech. Eng. ASME*, vol. 106, no. 83, pp. 34–41, 1984.
- [48] S. V Ekkad, “Impingement Heat Transfer on a Target Plate,” vol. 13, no. 4, 1999.
- [49] Y. Xing, S. Spring, and B. Weigand, “Experimental and numerical investigation of heat transfer characteristics of inline and staggered arrays of impinging jets,” *J. Heat Transfer*, vol. 132, no. 9, pp. 1–11, 2010.
- [50] D. E. Metzger, L. W. Florschuetz, D. . I. Takeuchi, R. D. Behee, and R. A. Berry, “Heat Transfer Characteristics for Inline and Staggered Arrays of Circular Jets with Crossflow of Spent Air,” vol. 101, pp. 526–531, 1979.
- [51] J. Taborek, “Heat transfer of a cylinder in crossflow,” *Int. J. Heat Fluid Flow*, vol. 7, no. 2, p. 160, 1986.
- [52] M. Ashok Kumar and B. V. S. S. S. Prasad, “Computational investigations of flow and heat transfer on an effused concave surface with a single row of impinging jets for different exit configurations,” *Eng. Appl. Comput. Fluid Mech.*, vol. 3, no. 4, pp. 530–542, 2009.
- [53] Y. Q. Zu, Y. Y. Yan, and J. D. Maltson, “CFD prediction for multi-jet

- impingement heat transfer,” *Proc. ASME Turbo Expo*, vol. 3, no. PART A, pp. 483–490, 2009.
- [54] T. J. Craft, H. Iacovides, and N. A. Mostafa, “Modelling of three-dimensional jet array impingement and heat transfer on a concave surface,” *Int. J. Heat Fluid Flow*, vol. 29, pp. 687–702, 2008.
- [55] H. Iacovides, D. Kounadis, B. E. Launder, J. Li, and Z. Xu, “Experimental Study of the Flow and Thermal Development of a Row of Cooling Jets Impinging on a Rotating Concave Surface,” vol. 127, no. January 2005, pp. 222–229, 2005.
- [56] L. Luo, C. Wang, L. Wang, B. A. Sunden, and S. Wang, “A numerical investigation of dimple effects on internal heat transfer enhancement of a double wall cooling structure with jet impingement,” *Int. J. Numer. Methods Heat Fluid Flow*, vol. 26, no. 7, pp. 2175–2197, 2016.
- [57] R. Vinze *et al.*, “Effect of dimple pitch and depth on jet impingement heat transfer over dimpled surface impinged by multiple jets,” *Int. J. Therm. Sci.*, vol. 145, no. May, p. 105974, 2019.
- [58] N. Celik, “Effects of dimples’ arrangement style of rough surface and jet geometry on impinging jet heat transfer,” *Heat Mass Transf. und Stoffuebertragung*, vol. 56, no. 1, pp. 339–354, 2020.
- [59] S. M. Kim and K. Y. Kim, “Evaluation of cooling performance of impinging jet array over various dimpled surfaces,” *Heat Mass Transf.*, vol. 52, no. 4, pp. 845–854, 2016.
- [60] Y. Xing and B. Weigand, “Experimental investigation of impingement

heat transfer on a flat and dimpled plate with different crossflow schemes,” *Int. J. Heat Mass Transf.*, vol. 53, no. 19–20, pp. 3874–3886, 2010.

- [61] A. Bolek and S. Bayraktar, “Flow and heat transfer investigation of a circular jet issuing on different types of surfaces,” *Sadhana - Acad. Proc. Eng. Sci.*, vol. 44, no. 12, 2019.
- [62] Y. Xie, P. Li, J. Lan, and D. Zhang, “Flow and Heat Transfer Characteristics of Single Jet Impinging on Dimpled Surface,” *J. Heat Transfer*, vol. 135, pp. 1–15, 2013.
- [63] H. Xing, W. Du, P. Sun, S. Xu, D. He, and L. Luo, “Influence of surface curvature and jet-to-surface spacing on heat transfer of impingement cooled turbine leading edge with crossflow and dimple,” *Int. Commun. Heat Mass Transf.*, vol. 135, no. 0735–1933, pp. 106–116, 2022.
- [64] S. W. Chang and H. F. Liou, “Heat transfer of impinging jet-array onto concave- and convex-dimpled surfaces with effusion,” *Int. J. Heat Mass Transf.*, vol. 52, no. 19–20, pp. 4484–4499, 2009.
- [65] A. M. El-Jumrah, G. E. Andrews, and J. E. J. Staggs, “Predictions of Impingement Heat Transfer with Dimples, Pin-fins and zig-zag rib Obstacles: Conjugate Heat Transfer Computational Fluid Dynamics Predictions,” in *Proceedings of ASME Turbo Expo 2019*, 2019, pp. 1–12.
- [66] LCRHallcrest, “TLC PRODUCTS FOR USE IN RESEARCH AND TESTING APPLICATIONS,” 2022.

- [67] N. Abdullah, A. R. Abu Talib, A. A. Jaafar, M. A. Mohd Salleh, and W. T. Chong, “The basics and issues of Thermochromic Liquid Crystal Calibrations,” *Exp. Therm. Fluid Sci.*, vol. 34, no. 8, pp. 1089–1121, 2010.
- [68] R. Wiberg and N. Lior, “Errors in thermochromic liquid crystal thermometry,” *Rev. Sci. Instrum.*, vol. 75, no. 9, pp. 2985–2994, 2004.
- [69] Y. Rao and S. Zang, “Calibrations and the measurement uncertainty of wide-band liquid crystal thermography,” *Meas. Sci. Technol.*, vol. 21, no. 1, 2010.
- [70] V. U. Kakade, G. D. Lock, M. Wilson, J. M. Owen, and J. E. Mayhew, “Accurate heat transfer measurements using thermochromic liquid crystal. Part 1: Calibration and characteristics of crystals,” *Int. J. Heat Fluid Flow*, vol. 30, no. 5, pp. 939–949, 2009.
- [71] M. Parsley, “Personal Communication, Managing Director, Hallcrest Technologies Limited, UK.” 2019.
- [72] S. Bakrania and A. M. Anderson, “A TRANSIENT TECHNIQUE FOR CALIBRATING THERMOCHROMIC LIQUID CRYSTALS: THE EFFECTS OF SURFACE PREPARATION, LIGHTING AND OVERHEAT,” in *Proceedings of IMECE2002 ASME*, 2018, pp. 1–7.
- [73] M. Behle, K. Schulz, W. Leiner, and M. Fiebig, “Color-based image processing to measure local temperature distributions by wide-band liquid crystal thermography,” *Appl. Sci. Res.*, vol. 56, pp. 113–143, 1996.

- [74] N. Abdullah, A. R. Abu Talib, H. R. Mohd Saiah, A. A. Jaafar, and M. A. Mohd Salleh, "Film thickness effects on calibrations of a narrowband thermochromic liquid crystal," *Exp. Therm. Fluid Sci.*, vol. 33, no. 4, pp. 561–578, 2009.
- [75] J. von Wolfersdorf, P. Ott, and B. Weigand, "Temperature and pressure sensitive coatings," *Flow Phenom. Nat.*, vol. 4, pp. 747–766, 2006.
- [76] A. C. Chambers, D. R. H. Gillespie, P. T. Ireland, and G. M. Dailey, "A novel transient liquid crystal technique to determine heat transfer coefficient distributions and adiabatic wall temperature in a three-temperature problem," *J. Turbomach.*, vol. 125, no. 3, pp. 538–546, 2003.
- [77] J. P. C. W. Ling, P. T. Ireland, and L. Turner, "A technique for processing transient heat transfer, liquid crystal experiments in the presence of lateral conduction," *J. Turbomach.*, vol. 126, no. 2, pp. 247–258, 2004.
- [78] C. Paper, B. Sunden, and G. Tanda, "On liquid crystal thermography for determination of the heat transfer coefficient in rectangular ducts," no. May, 2011.
- [79] R. Poser, J. Von Wolfersdorf, and E. Lutum, "Advanced evaluation of transient heat transfer experiments using thermochromic liquid crystals," vol. 221, pp. 793–801, 2007.
- [80] K. Li, "Experimental Study of Heat Transfer Coefficient and Film Cooling Effectiveness," KTH School of Industrial Engineering and Management, 2019.

- [81] B. A. Brigham and G. J. Vanfossen, "Length to Diameter Ratio and Row Number Effects in Short Pin Fin Heat Transfer," *J. Eng. Gas Turbines Power*, vol. 106, no. 83, pp. 241–244, 2016.
- [82] G. J. Vanfossen, "Heat-Transfer Coefficients for Staggered Arrays of Short Pin Fins," *J. Eng. Power*, vol. 104, no. April 1982, 2016.
- [83] T. L. Bergman, T. L. Bergman, F. P. Incropera, D. P. DeWitt, and A. S. Lavine, *Fundamentals of Heat and Mass Transfer*. Wiley, 2011.
- [84] LCRHallcrest, "Handbook of Thermochromic Liquid Crystal Technology," Glenview, United States, 2019.
- [85] J. C. Simonich and R. J. Moffat, "Liquid Crystal Visualization of Surface Heat Transfer on a Concavely Curved Turbulent Boundary Layer," *J. Heat Transfer*, vol. 106, no. 83, pp. 619–627, 2016.
- [86] S. A. Hippensteele, L. M. Russell, and F. S. Stepka, "Evaluation of a Method for Heat Transfer Measurements and Thermal Visualization Using a Composite of a Heater Element and Liquid Crystals," *J. Heat Transfer*, vol. 105, no. 1983, pp. 184–189, 2016.
- [87] R. J. Clifford, T. V. Jones, and S. T. Dunne, "Techniques for Obtaining Detailed Heat Transfer Coefficient Measurements Within Gas Turbine Blade and Vane Cooling Passages," in *THE AMERICAN SOCIETY OF MECHANICAL ENGINEERS*, 2018, pp. 1–6.
- [88] C. Camci, K. Kim, and S. A. Hippensteele, "A new hue capturing technique for the quantitative interpretation of liquid crystal images used in convective heat transfer studies," *J. Turbomach.*, vol. 114, no. 4,

pp. 765–775, 1992.

- [89] A. Terzis, J. Von Wolfersdorf, B. Weigand, and P. Ott, “DETAILED HEAT TRANSFER DISTRIBUTIONS OF NARROW IMPINGEMENT CHANNELS WITH VARYING JET DIAMETER Alexandros,” *ASME J. Turbomach.*, pp. 1–11, 2016.
- [90] J. W. Baughn, “Liquid crystal methods for studying turbulent heat transfer,” no. 1989, 1990.
- [91] P. T. Ireland and T. V. Jones, “Liquid crystal measurements of heat transfer and Liquid crystal measurements of heat transfer and surface shear stress,” *Meas. Sci. Technol.*, vol. 11, pp. 969–986, 2000.
- [92] Z. Wang, P. T. Ireland, and T. V Jones, “An Advanced Method of Processing Liquid Crystal Video Signals From Transient Heat Transfer Experiments,” vol. 117, no. January 1995, 2016.
- [93] A. R. Abu Talib, A. J. Neely, P. T. Ireland, and A. J. Mullender, “A Novel Liquid Crystal Image Processing Technique Using Multiple Gas Temperature Steps to Determine Heat Transfer Coefficient Distribution and Adiabatic Wall Temperature,” *J. Turbomach.*, vol. 126, pp. 587–596, 2015.
- [94] Z. Wang, P. T. Ireland, T. V Jones, and R. Royce, “A Color Image Processing System for Transient Liquid,” vol. 1, no. July 1996, 2015.
- [95] M. Wilson, B. J. Syson, and J. M. Owen, “Image processing techniques applied to wide – band thermochromic liquid crystals,” Bath, UK, 1993.
- [96] T. L. Chan, S. Ashforth-frost, and K. Jambunathan, “Calibrating for

viewing angle effect during heat transfer measurements on a curved surface,” vol. 44, pp. 2209–2223, 2001.

[97] J. L. Hay and D. K. Hollingsworth, “Calibration of micro-encapsulated liquid crystals using hue angle and a dimensionless temperature,” vol. 18, pp. 0–6, 1998.

[98] P. Chen, P. Ding, and D. Ai, “An improved data reduction method for transient liquid crystal thermography on film cooling measurements,” vol. 44, pp. 1379–1387, 2001.

[99] D. E. Metzger, B. A. Berry, and J. P. Bronson, “Developing Heat Transfer in Rectangular Ducts With Staggered Arrays of Short Pin Fins,” *J. Heat Transfer*, vol. 104, no. November 1982, 2016.

[100] C. S. Fan and S. W. Haley, “Effects of Pin Shape and Array Orientation on Heat Transfer and Pressure Loss in Pin Fin Arrays,” *J. Eng. Gas Turbines Power*, vol. 106, no. January 1984, pp. 251–258, 2016.

[101] J. K. Hector, Z. Xu, H. Iacovides, D. Kounadis, and B. Launder and Li, “Effects of Rotation on Cooling Performance of an Impinging Jet Row,” in *3rd Symposium on Turbulent Shear Flow Phenomena, TSFP3, Sendai, Japan, 2003*.

[102] ISO5167-1, “Measurement of fluid flow by means of pressure differential devices inserted in circular cross-section conduits running full,” *Int. Stand.*, vol. 2003, no. Second edition, 2003.

[103] L. Guo, “Numerical And Experimental Study On Turbine Blade Cooling, Turbulent Flow And Surface Heat Transfer,” University of

Nottingham, 2011.

- [104] A. Terzis, J. Von Wolfersdorf, B. Weigand, and P. Ott, “Thermocouple thermal inertia effects on impingement heat transfer experiments using the transient liquid crystal technique,” *Meas. Sci. Technol.*, vol. 23, no. 11, 2012.
- [105] S. A. Strieg and T. E. Diller, “An analysis of the effect of entrainment temperature on jet impingement heat transfer,” *J. Heat Transfer*, vol. 106, no. 4, pp. 804–810, 1984.
- [106] K. KIM and C. CAMCI, “Fluid dynamics and convective heat transfer in impinging jets through implementation of a high resolution liquid crystal technique,” *Int. J. Turbo Jet Engines*, vol. 19, pp. 13–19, 1995.
- [107] A. Ahmed, E. Wright, F. Abdel-Aziz, and Y. Yan, “Numerical investigation of heat transfer and flow characteristics of a double-wall cooling structure: Reverse circular jet impingement,” *Appl. Therm. Eng.*, vol. 189, no. January, p. 116720, 2021.
- [108] R. S. Amano, “Turbulence Effect on the Impinging Jet on a Flat Plate,” *Bull. JSME*, vol. 25, no. 221, pp. 1891–1899, 1983.
- [109] E. M. Sparrow, R. J. Goldstein, and M. A. Rouf, “Effect of Nozzle - Surface Separation Distance on Impingement Heat Transfer for a Jet in a Crossflow.,” *J. Heat Transf. Am. Soc. Mech. Eng.*, no. 76-HT-F, pp. 528–533, 1976.
- [110] R. J. Moffat, “Describing the uncertainties in experimental results,” *Exp. Therm. Fluid Sci.*, vol. 1, no. 1, pp. 3–17, 1988.

- [111] J. Lee and S. Lee, “The effect of nozzle configuration on stagnation region heat transfer enhancement of axisymmetric jet impingement,” *Int. J. Heat Mass Transf.*, vol. 43, pp. 3497–3509, 2000.
- [112] ISO 5167, “Orifice Plates (ISO 5167-2: 2003),” vol. 2, 2003.
- [113] T. Gal-Chen and R. C. J. Somerville, “Numerical Solution of the Navier-Stokes,” *J. Comput. Phys.*, vol. 17, no. 104, pp. 276–310, 1975.
- [114] G. K. Batchelor, *An Introduction to Fluid Dynamics*. Cambridge, England: Cambridge Univ. Press, 1967.
- [115] T. J. Barth and D. Jespersen, “The design and application of upwind schemes on unstructured meshes,” *AIAA 27th Aerosp. Sci. Meet.*, 1989.
- [116] A. J. Chorin, “Numerical solution of navier-stokes equations,” *Math. Comput.*, vol. 22, p. 745–762, 1968.
- [117] T. R. Society, P. Transactions, R. Society, C. Papers, and P. Character, “The Deferred Approach to the Limit,” *Soc. R. Trans. Philos. Soc. R. Pap. Contain. Character, Phys.*
- [118] D. C. Wilcox, “Turbulence Modeling for CFD,” . *DCW Ind. Inc. La Canada*, 1998.
- [119] F. R. Menter, “Two-Equation Eddy-Viscosity Turbulence Models for Engineering Applications,” *AIAA J.*, vol. 32, no. 2, p. 1598–1605, 1994.
- [120] B. E. Launder and D. B. Spalding, “Lectures in Mathematical Models of Turbulence,” *Acad. Press. London, England*, 1972.
- [121] T. H. Shih, W. W. Liou, A. Shabbir, Z. Yang, and J. Zhu, “A New

Eddy-Viscosity Model for High Reynolds Number Turbulent Flows-Model Development and Validation,” *Comput. Fluids*, vol. 24, no. 3, p. 227–238, 1995.

[122] Y. Rao, Y. Liu, and C. Wan, “Multiple-jet impingement heat transfer in double-wall cooling structures with pin fins and effusion holes,” *Int. J. Therm. Sci.*, vol. 133, no. June, pp. 106–119, 2018.

[123] L. Guo, Y. Yan, and J. D. Maltson, “Performance of 2D scheme and different models in predicting flow turbulence and heat transfer through a supersonic turbine nozzle cascade,” *Int. J. Heat Mass Transf.*, vol. 55, no. 23–24, pp. 6757–6765, 2012.

Appendix: Experimental study on Film hole

Film cooling is a commonly used technique, and whilst the downstream film effectiveness is well understood, the internal heat sink effect, caused by heat transfer coefficients within the entry length to the cylinder are often not well understood.

This study was conducted to experimentally evaluate detailed heat transfer coefficients within a representative geometry, provide contours of internal surface Nusselt number, circumferentially averaged Nusselt number along the entry length of the channels, and provide discharge coefficient data.

9.1. Test section

The test section representing the film cooling hole is a cylindrical channel with an inclination angle (α) between the cooling plenum and 'hot-gas' plenum wall, and rotation angle (β) relative to the axial/radial direction angle as shown in Figure 9.1, where X axis represent the mainstream flow direction.

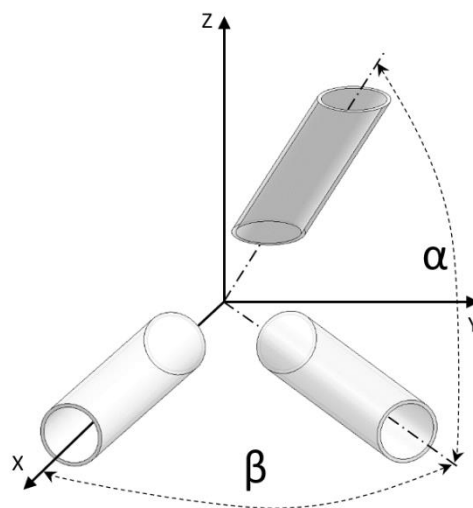


Figure 9.1 schematic diagram for the inclination (α) and rotation (β)

angles

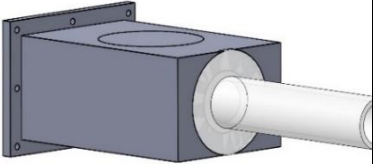
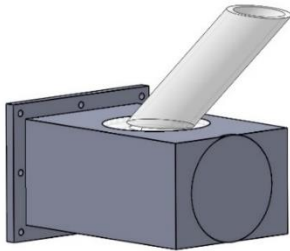
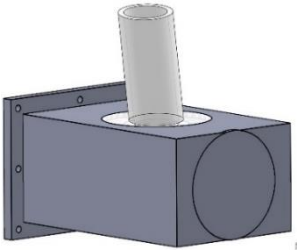
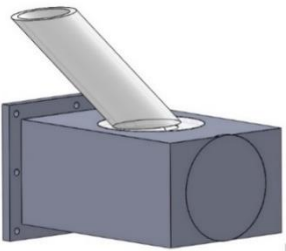
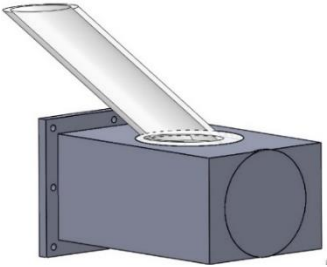
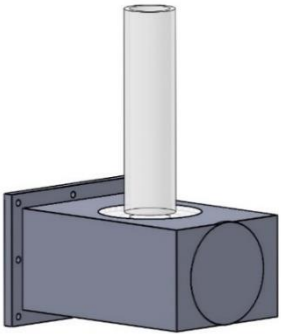
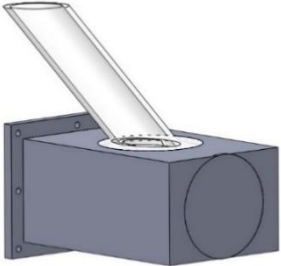
The Reynolds number was varied between 30,000 and 60,000 and the complete test schedule is shown in table.

Table 9.1 Film hole study cases

	Re	Inlet configuration	α	β
1	30,000	Sharp	0	0
2	45,000	Sharp	0	0
3	60,000	Sharp	0	0
4	45,000	Chamfer	0	0
5	45,000	Flited	0	0
6	45,000	Sharp	45	0
7	45,000	Sharp	90	0
8	45,000	Sharp	135	0
9	45,000	Sharp	45	45
10	45,000	Sharp	45	90
11	45,000	Sharp	45	135

The scheme of variations of inclination and rotation angles tested experimentally for this study are shown in Table 9.1 Film hole study cases.

Table 9.2 scheme of variations of inclination and rotation angles

$\alpha \backslash \beta$	0	45	90	135
0				
45				
90				
135				

9.2. Results and discussion

9.2.1. Reynolds number effect

With inclination and rotation angles of 0 degrees, the detailed distributions of entry length heat transfer enhancement effects against the channels side wall, for Re between 30,000 and 60,000 are shown in Figure 9.2. The distribution of Nusselt number demonstrate similar distributions independent of Reynolds number, but with increasing magnitude.

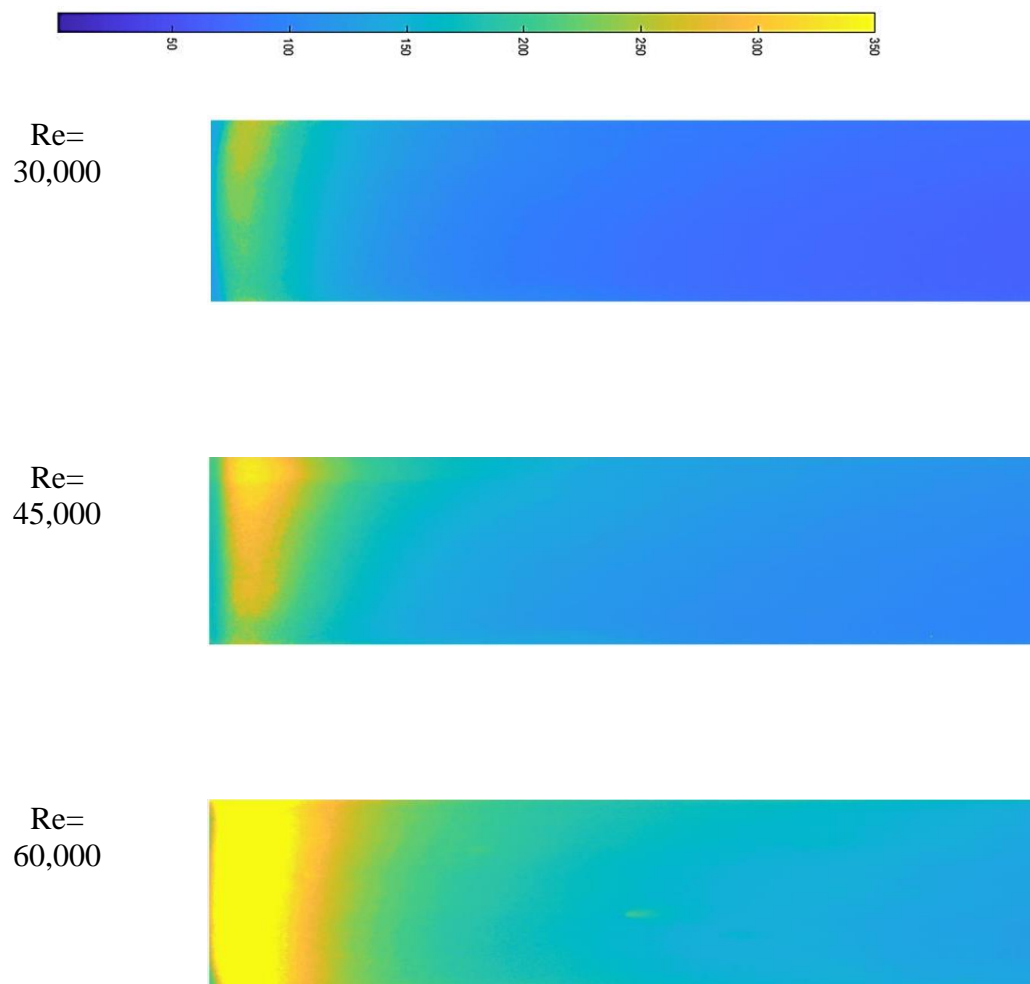


Figure 9.2 Reynolds number influence on local Nu distribution at $\alpha = 0^\circ$,

$$\beta = 0^\circ$$

The circumferentially averages plots for Nu are shown in Figure 9.3, demonstrating an initial enhancement due to both the thermal boundary development, and a trip in the fluid boundary layer. This is consistent with literature and shows a trend towards fully developed flow along the channel.

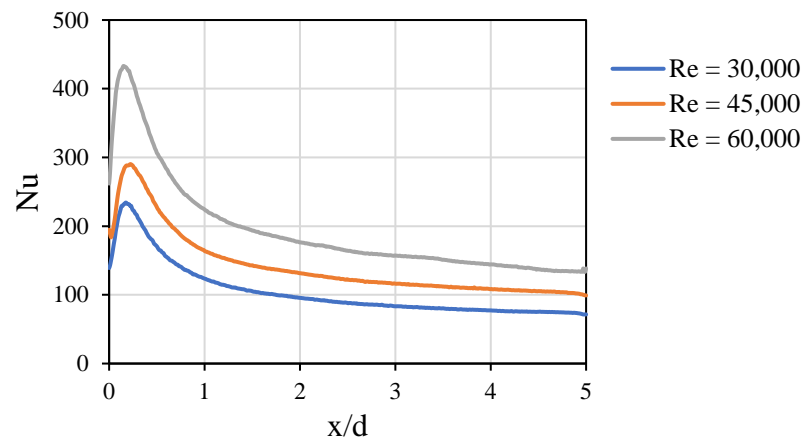


Figure 9.3 Reynolds number influence on average Nu distribution at $\alpha=0^\circ$, $\beta=0^\circ$

9.2.2. Inlet configuration effect

Variations in inlet condition were varied between a sharp entry, a filleted entry, and a chamfered entry at 45,000 Reynolds number. Nu distributions for each are shown in Figure 9.4. Enhancement can be seen to be more significant in the sharper entry, due to a larger disruption and mixing in the boundary layer. All cases show an initial area of low Nusselt number, as the flow separates followed by reattachment. The severity of the Nusselt number variation is proportional to the sharpness of the entry condition.

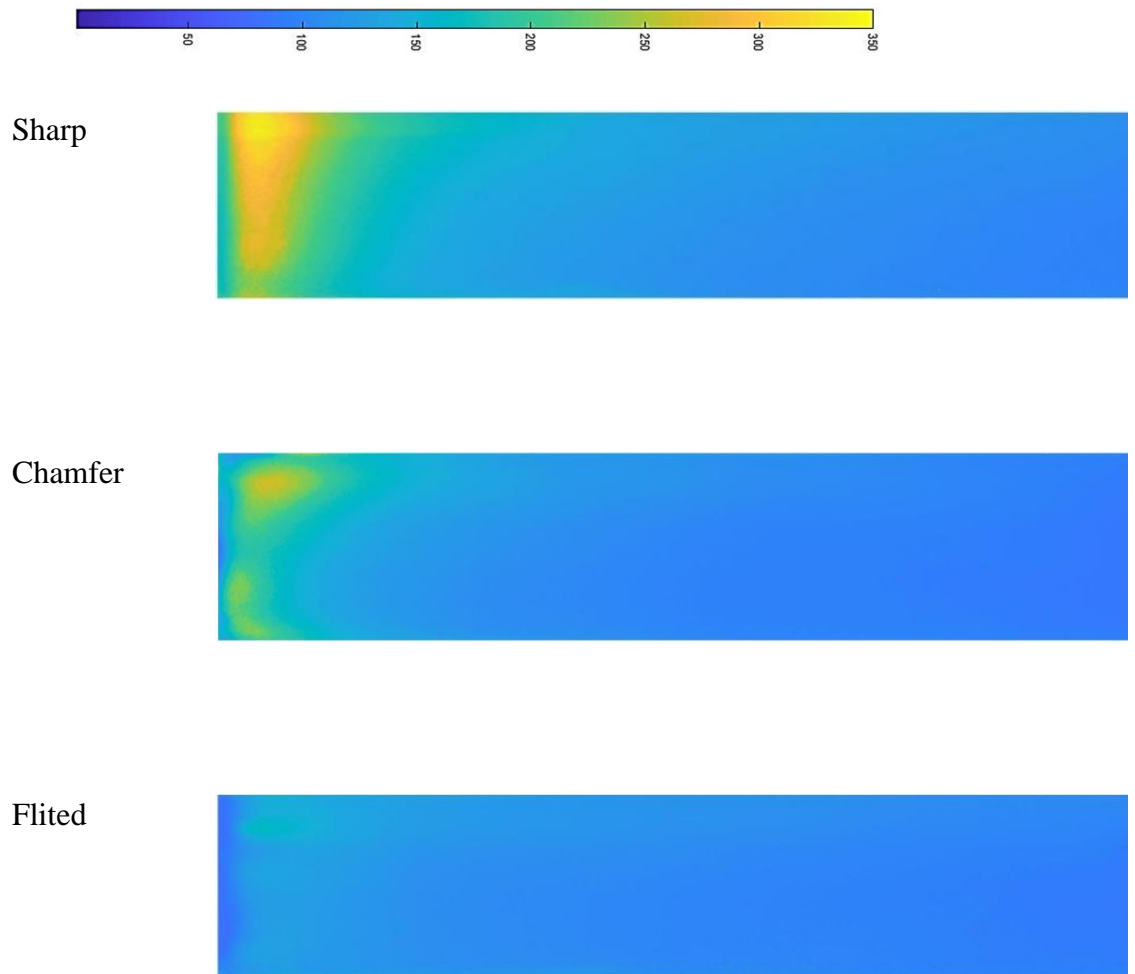


Figure 9.4 Inlet configuration influence on local Nu distribution at $\alpha= 0^\circ$,
 $\beta= 0^\circ$

The circumferentially averaged plots for Nu are shown in Figure 9.5, the enhancement is seen to be larger with a sharper entry, but all three converge as the flow develops towards x/d of 5. The initial separation is seen in all three, but the reattachment of the flow is more significant for a sharper entry, and so it the magnitude of the subsequent decrease, demonstrating a more severe magnitude and rate of this phenomena.

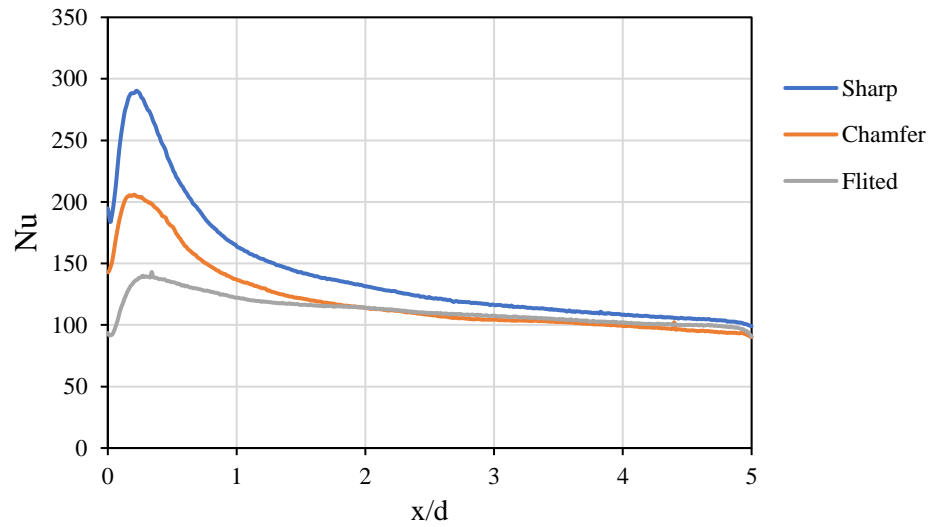
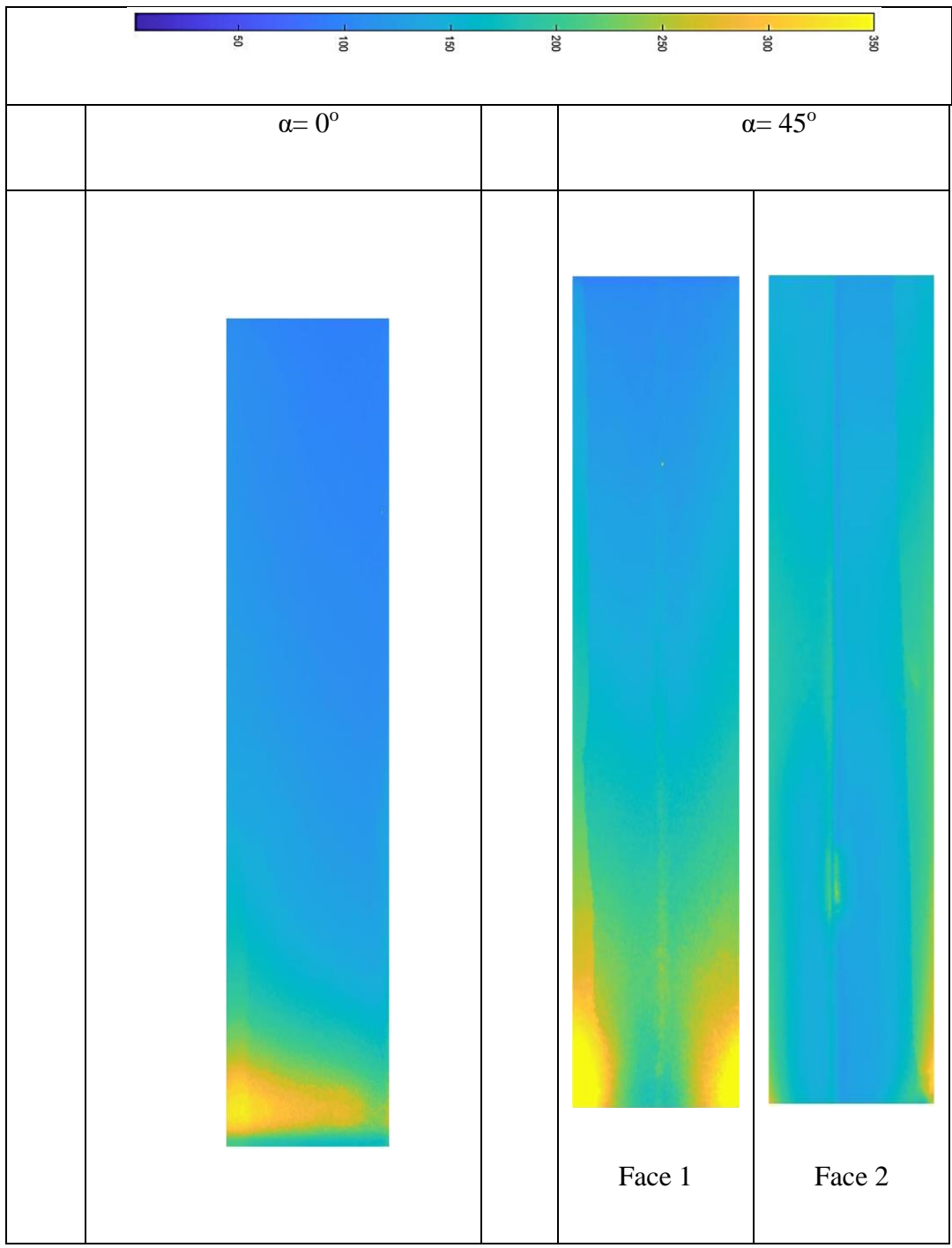


Figure 9.5 Inlet configuration influence on average Nu distribution at $\alpha= 0^\circ$, $\beta= 0^\circ$ and $Re= 45,000$

9.2.3. Alpha angle effect

The effect of inclination (α) angle is shown against the constituent heat transfer surfaces in Figure 9.6. At 45° , the flow can be seen to bias towards face 1, with secondary flows generating signs of high heat transfer, these signs are seen to be most significant at 45° and cause a larger variation in heat transfer around the circumference between faces 1 and 2. At 90° the flow is seen to bias towards the wall, as the flow turned around the inclination angle, and at 135° reversal in the flow direction reduces the impact of enhancement.



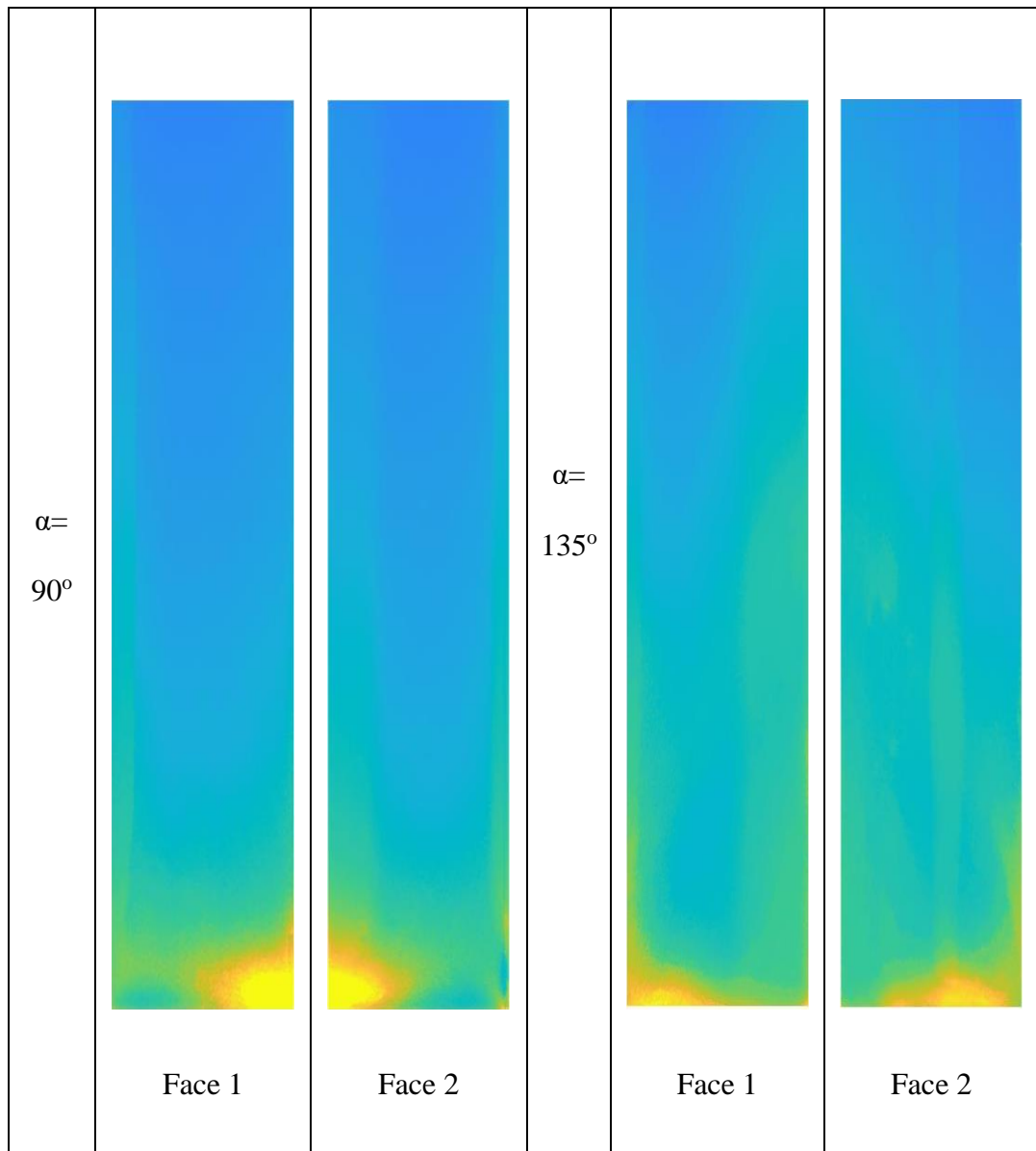


Figure 9.6 Influence of α angle on local Nu distribution at $\beta = 0^\circ$, $Re =$

45,000

The variation between the ‘faces’ is shown to be most significant at 45° , with all other variations in inclination angle producing very similar distributions between faces 1 and 2, as shown in Figure 9.7. At greater inclination angles, the initial separation and reattachment produces a less significant decrease after the reattachment.

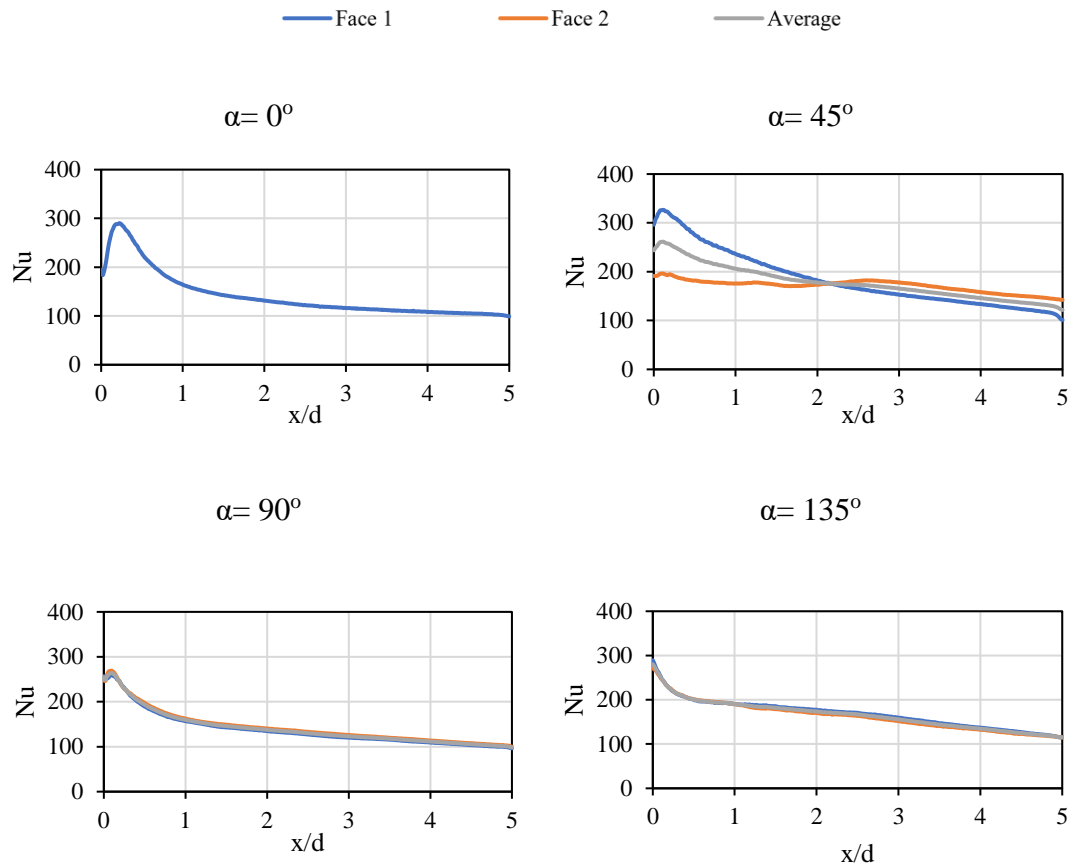


Figure 9.7 Influence of α angle on average Nu distribution at $\beta = 0^\circ$, $Re = 45,000$

Considering the overall circumferentially averaged Nusselt number along the entry length of the cylindrical film cooling channel, as shown in Figure 9.8, at 0° rotation angle, and 45,000 Reynolds number, figure further demonstrates the reduced impact of the separation and reattachment at increasing inclination angle. Overall, the impact of the secondary flow signs of high heat transfer in the 45° are significant in enhancing the overall Nusselt number.

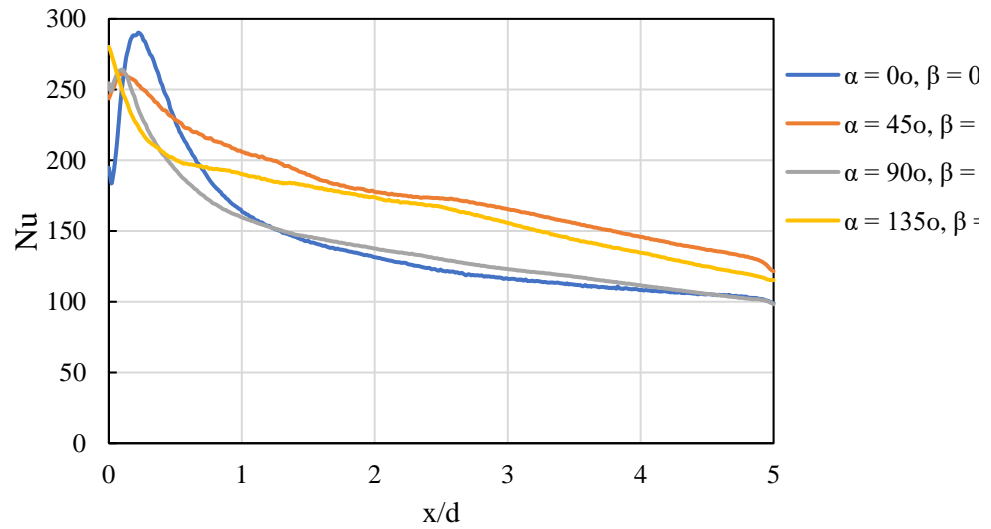


Figure 9.8 Influence of α angle on total average Nu distribution at $\beta = 0^\circ$,
 $Re = 45,000$

9.2.4. Beta angle effect

In common turbomachinery cooling applications, the rotation angle may be adjusted to compensate for a non 90° difference between the cooling plenum and the hot gas streamlines. Rotation angle was varied between 0° and 135° at $40,000$ Re and inclination angle of 45° .

Secondary flows are again seen to be significant in all cases where an angle is introduced, and the flow turns through the channel, with significant enhancement for 45° angles. At larger rotation angles, 90° and 135° , less significant, but very similar distributions of Nusselt number are observed, as shown in Figure 9.9.



$\beta = 0^\circ$

$\beta = 45^\circ$



Face 1

Face 2

Face 1

Face 2

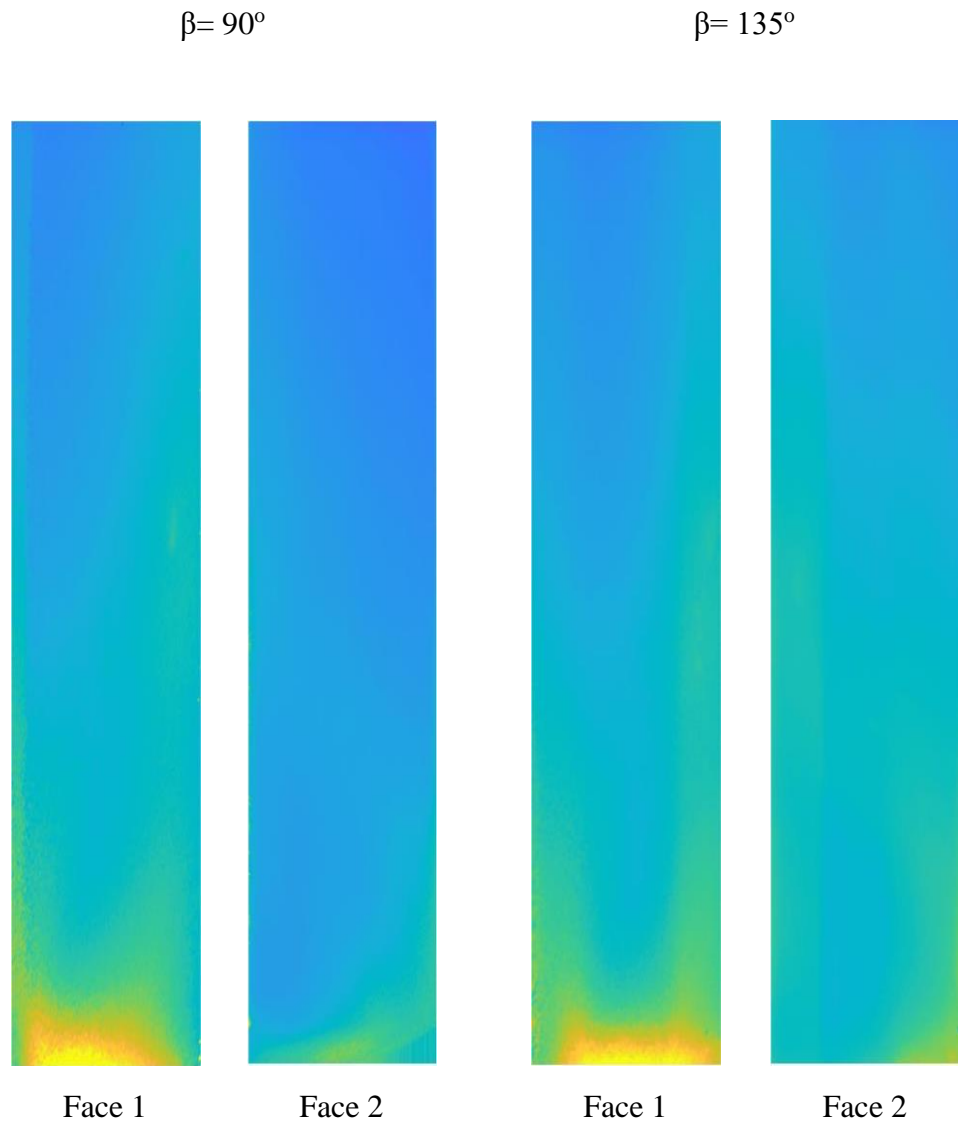


Figure 9.9 Influence of β angle on local Nu distribution at $\alpha= 45^\circ$, $Re= 45,000$

When comparing the circumferentially averaged entry length effects for variation in rotation angle between face 1 and face 2, as shown in Figure 9.10, most variation between faces is observed for 0° , where variation extends to $x/d = 2$, for all other cases, significant variation is limited to the region between the entry and $x/d = 1$. In all cases of turning, face 1, the face which has the turning flow impinging against it, has an initial enhancement of heat transfer, as the boundary layer is thinned.

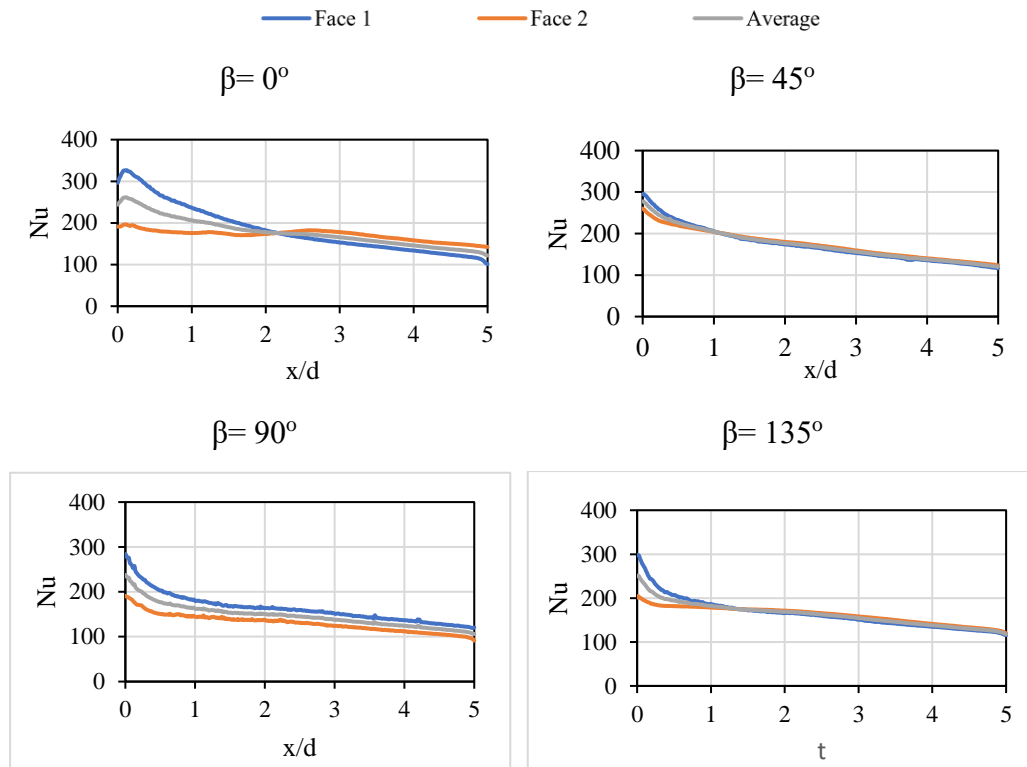


Figure 9.10 Influence of β angle on average Nu distribution at $\alpha = 45^\circ$,
 $Re = 45,000$

When assessing the circumferentially averaged entry length effects for variation in rotation angle, Figure 9.11 demonstrates that only the 0° case shows an initial area of sufficient separation, this is likely due to the existing impact of the 45° inclination angle, and that the biased enhancement against the right face compensates for the average initial separation. All rotation angles otherwise follow a similar trend, with the highest overall rates of heat transfer in the 0° rotation angle case.

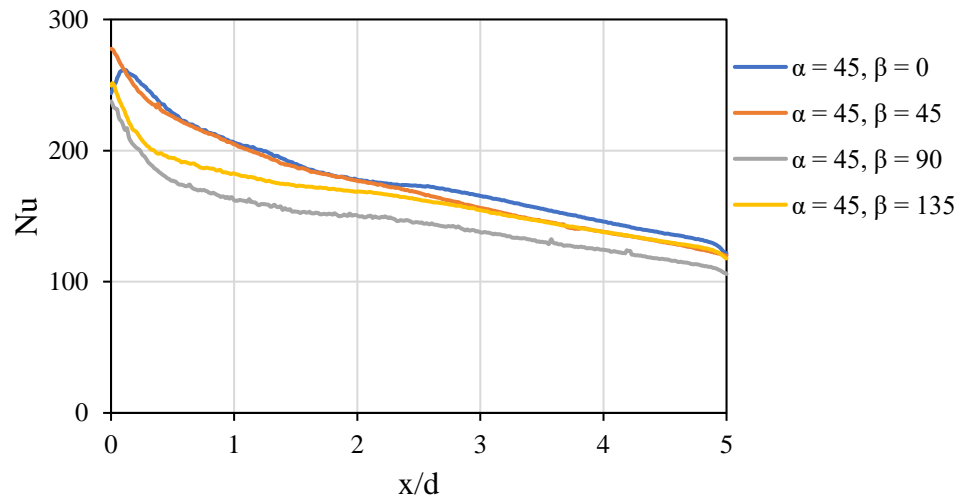


Figure 9.11 Influence of β angle on total average Nu distribution at $\alpha = 45^\circ$, $Re = 45,000$

9.2.5. Discharge Coefficient

Figure 9.12 indicates that the discharge coefficient is proportional to the Reynolds number, regardless of the inlet configuration. Through comparing the discharge coefficient for three different inlet configurations, i.e. sharp, chamfered, and filleted, the C_d values for the chamfered and filleted inlets are very close, while the C_d values for the sharp inlet are about 9% less than the filleted inlet configuration.

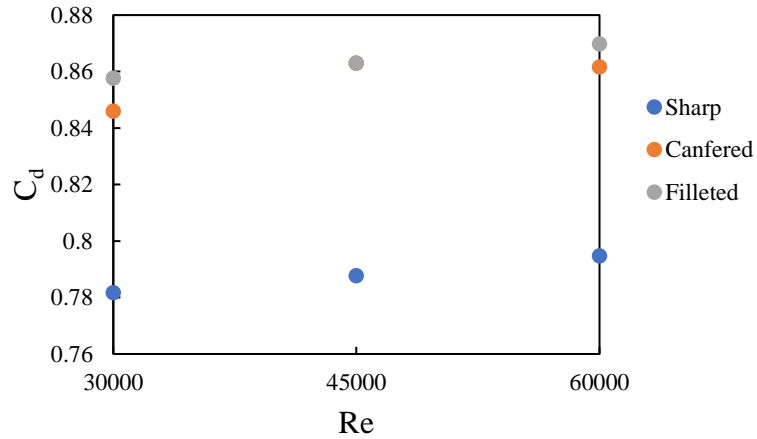


Figure 9.12 Reynolds number influence on discharge coefficient at different inlet configurations at $\alpha=0^\circ$, $\beta=0^\circ$

At a rotation angle of 0° , and 45,000 Reynolds number, the discharge coefficient was shown to decrease with increasing inclination angle, from 80% at 0° to 61% at 135° , as illustrated in Figure 9.13. This is due to the increased angle of turning, and therefore greater acceleration required to maintain the flow.

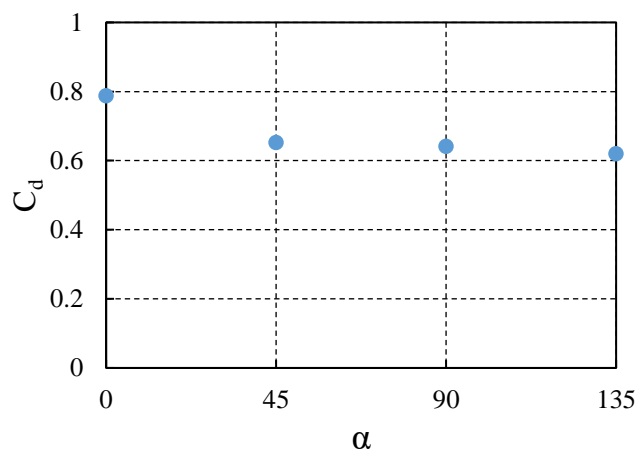


Figure 9.13 Influence of α angle on discharge coefficient at $\beta=0^\circ$, $Re=45,000$

As with inclination angle, discharge coefficient naturally also decreases with increasing rotation angle, as demonstrated in Figure 9.14. Decreasing from 80% at 0°, to 62% at 135°, this is consistent with the relative impact of inclination angle.

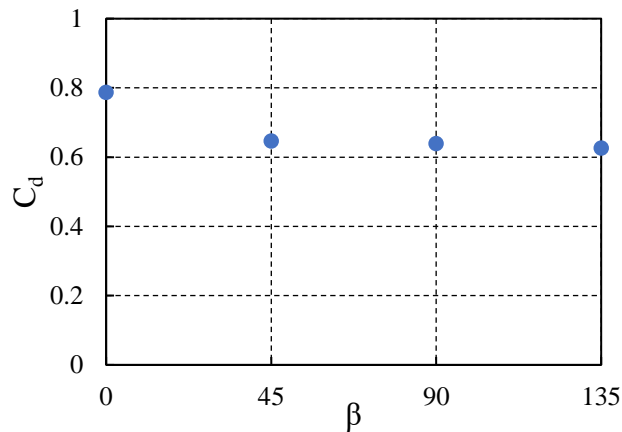


Figure 9.14 Influence of β angle on discharge coefficient at $\alpha = 45^\circ$, $Re = 45,000$

9.3. Conclusion

Heat transfer distributions and discharge coefficients were evaluated experimentally within a model of a scaled cylindrical film cooling channel. The geometries of the holes had no expansion, with constant cylindrical cross-section. In all variations, the film channel had a length of 5 jet diameters.

Initial testing was conducted with no rotation or inclination angle, varying Reynolds number between 30,000 and 60,000. Nusselt number distribution was independent of Reynolds number, but Nusselt number magnitude increases monotonically with Reynolds number. For Reynolds numbers, an

initial entry length separation was observed, followed by a heat transfer enhancement with reattachment. Throughout the remaining entry length, the heat transfer tends to unity as in fully developed Dittus-Boelter.

In the zero rotation and inclination angle case, for 45,000 Re, the effect of channel entry was also varied between sharp, filleted, and chamfered. Results showed that the sharpness of the nozzle was directly related to the magnitude of the entry length separation and reattachment heat transfer enhancement.

When inclination angles were introduced, and varied between 0 and 135°, it was discovered that there was a reduction of the reattachment heat transfer enhancement, but that an overall increase in heat transfer could be achieved, with most enhancement shown for inclination angles of 45° and 135°. Particularly for the 45° inclination angle case, the secondary flows became very significant, introducing ‘fingers’ of enhancement.

Rotation angle was also varied between 0 and 90 degrees, showing the most significant impact between the channel entry, and 1 diameter in length, with overall reductions in heat transfer when varied by more than 90°.

When assessing the impact of geometry and flow variations on discharge coefficient, it was observed that discharge coefficient decreases with increasing entry sharpness, increasing inclination angle, and increasing rotation angle.